Study of the blur, ringing and aliasing artifacts in numerical imaging : application to restoration

Gwendoline Blanchet

THÈSE DE DOCTORAT
DE L'ÉCOLE NORMALE SUPÉRIEURE DE CACHAN

Présentée par
Mademoiselle Gwendoline BLANCHET

pour obtenir le grade de

DOCTEUR DE L'ÉCOLE NORMALE SUPÉRIEURE DE CACHAN

Domaine : Mathématiques appliquées

Étude des artefacts de flou, ringing et aliasing en imagerie numérique. Application à la restauration.

Study of the blur, ringing and aliasing artifacts in numerical imaging. Application to restoration.

Thèse présentée et soutenue à Cachan le 17 novembre 2006 devant le jury composé de :

Andrés ALMANSA	Université de la République, Uruguay	Rapporteur
Michel AVIGNON	Centre National d'Études Spatiales	Examinateur
Vicent CASELLES	Université Pompeu Fabra, Espagne	Rapporteur
Sylvain DURAND	Faculté de Math/Info d'Amiens	Rapporteur
Frédéric GUICHARD	DXOLabs	Invité
Yves MEYER	École Normale Supérieure de Cachan	Président du jury
Lionel MOISAN	Université Paris V	Directeur de thèse
Jean-Michel MOREL	École Normale Supérieure de Cachan	Invité
Bernard ROUGÉ	Centre National d'Études Spatiales	Directeur de thèse

Laboratoire du Centre de Mathématiques et de Leurs Applications
ENS CACHAN/CNRS/UMR 8536
61, avenue du Président Wilson, 94235 CACHAN CEDEX, FRANCE.

Remerciements

Mes premières pensées iront à mes deux directeurs de thèse, Lionel Moisan et Bernard Rougé, qui ont accepté de co-encadrer celle-ci et qui m'ont ainsi accordé leur confiance. Leur gentillesse, leur exigence et leur attention ont été primordiales dans son accomplissement. Les discussions communes ainsi que leurs expériences ont été une réelle chance et m'ont offert la possibilité d'avancer mon travail de recherche pendant ces trois années. Je souhaite leur adresser ici toute ma reconnaissance.

Je tiens à remercier Yves Meyer de m'avoir fait l'honneur de présider mon jury de thèse. Je n'oublierai jamais son enthousiasme communicatif pour nous expliquer le monde merveilleux du traitement d'images et de la vision humaine. Merci à Andrés Almansa, Vicent Caselles et Sylvain Durand d'avoir accepté d'être rapporteurs de ma thèse. Je veux leur assurer toute ma reconnaissance pour l'effort important qu'ils ont fourni pour lire la thèse ainsi que pour tout l'intérêt qu'ils y ont apporté. Michel Avignon, Frédéric Guichard et Jean-Michel Morel m'ont fait grand honneur en participant à mon jury de thèse. Je les remercie d'avoir bien voulu prendre le temps de s'intéresser au travail effectué et d'avoir pu ouvrir les discussions grâce à leurs expériences respectives.

Les conditions de travail au laboratoire du Centre de Mathématiques et de Leurs Applications de l'ENS de Cachan ont été excellentes, et je tiens à en remercier ici tous les membres. La thèse s'est déroulée dans un contexte scientifique de grande qualité sans lequel la finalisation de ce travail n'aurait pas été possible. Je salue l'esprit convivial de Véronique, Micheline, Virginie et Pascal ainsi que celui des doctorants qui ont donné une atmosphère chaleureuse à nos bureaux. Je pense tout particulièrement à plusieurs membres de ce laboratoire: Stéphanie, Yen, Sébastien, Diego, Jean-Pascal, Julie, Jérémie, Rafael, Christophe et les autres . . . que je souhaite encore remercier.

Durant ma thèse, j'ai aussi été très bien accueillie à l'université Paris V au sein de laquelle j'ai effectué mon monitorat. Les discussions avec ses membres ont été riches en enseignements et m'ont permis d'avancer dans mes recherches. Je voudrais leur exprimer toute ma gratitude. Je tiens aussi à remercier ceux avec qui j'ai eu le plaisir de partager mon bureau: Amandine, Bénédicte, Cécile, Claire J., Claire L., Gaëlle, Neus, Sylvain, sans oublier ceux du septième étage: Béatrice, Javiera, Mohamed, Olivier . . .

Mes amis ont toujours été présents. Je pense tout particulièrement à Cathy, Charlotte, Claire, Delphine, Pierre et Jérôme. Plus qu'à quiconque, je dédie cette thèse à ma famille sans laquelle rien n'aurait été possible. Je pense à mes parents, qui m'ont permis d'arriver à cet accomplissement, ainsi qu'à mon frère Guilhem. Enfin merci à Alexandre pour m'avoir accompagnée dans mes doutes et mes joies.

Contents

Introduction

Cette thèse porte sur une thématique fondamentale en traitement d'image : la qualité des images numériques. Les images numériques sont une représentation discrète des images continues. Cependant le passage d'une représentation continue à une représentation discrète conduit généralement à un compromis entre différents types de dégradations d'image. Ce sont ces dégradations, liées à l'échantillonnage d'une image continue, que nous étudions dans cette thèse, et notamment leur impact sur la qualité image. L'évaluation de la qualité image est essentielle à la validation de tout traitement, par exemple pour les algorithmes de restauration dont le but est d'exprimer le mieux possible l'image continue à partir de l'image discrète. L'œil humain perçoit très bien la qualité visuelle d'une image, telle que le niveau de bruit et le niveau de flou, mais il en est tout autrement pour l'ordinateur. La grande majorité des algorithmes de restauration sont paramétrés et nécessitent un choix des paramètres optimaux. Afin de faire le choix d'une manière automatique, il est nécessaire d'avoir des critères de qualité fiables et universels. De plus, l'automatisation est primordiale dès lors que l'on veut traiter un grand nombre d'images. L'être humain ne pouvant évaluer autant d'images, il convient d'utiliser des outils mathématiques généraux qui soient capables de le faire. Pour atteindre ce but, nous avons découpé ce problème en trois sous-problèmes, qui constituent les trois premières parties de ce mémoire. Des applications sont étudiées dans la quatrième partie.

La première partie définit exactement les critères que nous utilisons pour l'évaluation de la qualité de l'image. Pour ce faire nous caractérisons trois dégradations fondamentales de l'image numérique, c'est à dire liées au caractère discret de la représentation d'un monde continu, nommées *aliasing*, *flou* et *ringing*. La deuxième partie propose un traitement de réduction d'images, c'est-à-dire une diminution de la taille de l'image tout en conservant l'information essentielle, lors duquel la qualité image est contrôlée. La troisième partie définit pour chaque critère des mesures qui soient applicables à tout type d'image. Enfin en quatrième partie de ce mémoire, nous proposons des applications concrètes de l'évaluation automatique de la qualité image à des enjeux majeurs en traitement d'image tels que ceux de la restauration. Nous étudions plus spécifiquement les problèmes de déconvolution aveugle et de débruitage.

Artefacts dans les images numériques

Une image numérique est une matrice de valeurs codant l'intensité lumineuse en chaque pixel (de l'anglais *picture element*). Dans cette thèse, nous ne traitons que les images en niveaux de gris. Chaque pixel code un niveau de gris, généralement compris entre 0 et 255. L'image numérique est la représentation discrète d'une image continue sous-jacente. Dans tout système de prise de vue, tels que l'appareil photo numérique ou bien le satellite, l'image géométrique u_g est obtenue par projection du paysage observé (en trois dimensions) sur le plan du capteur. La réponse impulsionnelle de l'optique h_{opt}, puis celle du capteur h_{capteur} modifient l'image géométrique idéale en $u = h_{\text{capteur}} \star h_{\text{opt}} \star u_g$,

où $\star$ est l'opérateur de convolution. Son échantillonnage construit l'image discrète u_d, c'est à dire que des points de l'image continue u sont sélectionnés selon une grille régulière. Si l'échantillonnage n'est pas adapté à u, il peut introduire différents types de dégradations dans l'image. La structure de la grille d'échantillonnage est déterminée par la géométrie du système du capteur. Il existe plusieurs types de grille, telles que la grille hexagonale ou la grille carrée. Si la grille est carrée, alors l'image discrète associée est $u_d[m,n] = u(m \cdot s, n \cdot s)$, où n et m sont des nombres entiers et s représente le pas d'échantillonnage de la grille, c.à.d. la distance entre les points de la grille dans la direction horizontale et verticale. Par exemple, la matrice de détecteurs des appareils photo numériques est une grille carrée. Il existe différents types de matrices telles que les matrices C.C.D. (charge coupled device) ou C.M.O.S. (complementary metal-oxide semiconductor). Dans l'œil humain, le réseau de capteurs situés sur la rétine a une distribution spécifique non régulière, proche du réseau hexagonal en forme de nid d'abeille [11] [34]. Dans ce mémoire, nous nous limitons au cas de la grille carrée, qui est caractéristique de très nombreux capteurs industriels.

Le passage entre le continu et le discret peut détériorer la qualité de l'image si la discrétisation est trop grossière, c'est-à-dire si les points de la grille sont trop éloignés. La théorie fondamentale sous-jacente est celle de la transformée de Fourier, qui exprime un signal comme une somme de sinusoïdes. Shannon a utilisé par la suite la transformée de Fourier pour trouver la finesse minimale de la grille de sorte à avoir un processus d'échantillonnage réversible [45]. Le passage de l'image discrète u_d vers l'image originale u n'est possible que si l'image discrète est échantillonnée sur une grille suffisamment fine. La finesse requise dépend bien évidemment du contenu de l'image continue que l'on souhaite retrouver. Si l'image contient de nombreux détails, alors la grille doit être fine, et vice versa. Si la condition du théorème de Shannon est satisfaite, alors l'image continue est retrouvée exactement par interpolation avec un sinus cardinal.

Si la condition du théorème de Shannon n'est pas satisfaite, alors il devient impossible de distinguer certaines fréquences de l'image originale à cause du repliement fréquentiel. La Figure 1 montre comment un échantillonnage trop grossier modifie une fréquence originale en sa version basse fréquence.

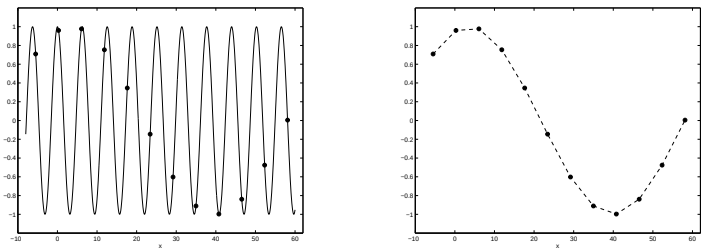

(a) (b)

FIG. 1 – (a) Graphe de la fonction $x \mapsto \cos(x)$ et sa version discrétisée ($\bullet$) avec un pas d'échantillonnage $s = 5.7$. (b) Signal discret associé. Sa fréquence est plus basse que la fréquence originale de la fonction cosinus.

Le problème de l'échantillonnage est relié aux trois artefacts que nous étudions dans cette thèse et qui constituent des facteurs majeurs de dégradation d'image. Le premier de ces artefacts est l'aliasing. Il est une conséquence directe du non respect de la condition du théorème de Shannon. Le repliement fréquentiel caractéristique de l'aliasing déforme l'image originale en créant des textures nouvelles ou

bien en crénelant les contours des objets. L'aspect non naturel de l'aliasing est dévastateur du point de vue qualité visuelle. L'aliasing a été essentiellement supprimé dans les filtres proposés dans la deuxième partie. Les deux autres artefacts, à savoir le ringing et le flou, sont reliés car il s'agit souvent de faire un compromis entre ces deux dégradations pour respecter les conditions du théorème de Shannon. En effet, pour remplir ces conditions, il s'agit de ne conserver que les fréquences qui pourront être exprimées dans l'image discrète, c.à.d. les basses fréquences. Les hautes fréquences sont atténuées par un filtrage passe-bas. Selon la forme du filtre près de la fréquence de coupure, l'image a du ringing et/ou du flou. Il n'existe aucun filtre passe-bas qui n'introduise ni ringing ni flou, puisque conserver toutes les fréquences intactes jusqu'à la fréquence de coupure ajoute du ringing et qu'au contraire atténuer les hautes fréquences avant la fréquence de coupure floue l'image. Le flou se manifeste par un adoucissement des transitions. Les contours des objets de l'image paraissent estompés. Le ringing se caractérise quant à lui par une réplication des contours des objets de l'image. Souvent associé avec le phénomène de Gibbs, le ringing se différencie pourtant du cadre du théorème de Gibbs [20]. La présence d'oscillations décrites par le théorème de Gibbs se justifie par la non-convergence uniforme des séries de Fourier des fonctions discontinues. Alors que pour le ringing, les oscillations peuvent apparaître pour des fonctions régulières, et même C^∞.

Filtrage adapté à la qualité image souhaitée

Plusieurs facteurs peuvent intervenir dans la mesure de la qualité image. Dans cette partie, la qualité image est estimée dans le cadre d'un filtrage passe-bas précédant un échantillonnage. Une telle procédure peut être utilisée dans deux situations bien différentes. La première situation est la capture d'un paysage par un système optique, tel que celui décrit précédemment. L'image discrète u_d est obtenue par filtrage puis échantillonnage de l'image géométrique continue u_g. Le filtre est imposé par la lentille et le capteur utilisés ($k = h_{\text{capteur}} \star h_{\text{opt}}$), et l'échantillonnage est celui de la grille de capteur. La deuxième situation envisageable est la réduction d'une image, c'est à dire le passage d'une image discrète u_d à une autre image discrète v_d plus petite. Contrairement à la première situation, le filtre passe-bas précédant le sous-échantillonnage n'est pas imposé : il n'est plus lié à la physique des éléments de la chaîne optique. Selon le filtre choisit, l'image obtenue v_d sera plus ou moins dégradée. Dans cette partie, nous nous plaçons uniquement dans le cadre de la réduction d'image : nous proposons une méthode pour choisir un filtre k adapté à la nouvelle grille d'échantillonnage tout en contrôlant la dégradation introduite. Le filtre et la grille d'échantillonnage constituent deux des éléments utilisés par Rougé dans [42] pour définir la qualité image dans le cadre de la première situation (capture d'un paysage par un système optique). Il note FTM (Fonction de Transfert de Modulation) la transformée de Fourier de k et R le réseau local d'échantillonnage auxquels il ajoute un troisième élément : la statistique du bruit du système. Il note σ_b l'écart-type du bruit (qui est fonction de la fréquence) et forme ainsi le *triplet instrument-échantillonnage*

$$(FTM, \sigma_b, R)\,.$$

Dans cette thèse, nous étudions uniquement les artefacts liés à l'échantillonnage (FTM, R) et pas le bruit instrumental (σ_b). Il est important de noter la différenciation faite ici entre les artefacts et le bruit : les artefacts représentent une perturbation structurée du signal à la différence du bruit de type bruit blanc. Le détérioration de la qualité image par le bruit n'a pas été l'axe de recherche principal de cette thèse bien que le cas des images légèrement bruitées ait été analysé.

Réduire la taille d'une image discrète d'un facteur s dans les deux directions (horizontale et verticale) est un problème directement relié au théorème de Shannon. Pour éviter les artefacts causés par l'aliasing,

le sous-échantillonnage d'une image u_d de taille $N \times N$ à une image v_d de taille $\frac{N}{s} \times \frac{N}{s}$ nécessite en amont un filtrage passe-bas : $v_d = (k \star u_d) \downarrow s$, où k est le filtre discret et $\downarrow s$ le sous-échantillonnage discret d'un facteur s dans les deux directions. Une coupure fréquentielle brute dans le domaine de Fourier correspond au filtre sinus cardinal de Shannon dans le domaine spatial. Le caractère très oscillant de ce filtre introduit un fort ringing. Les filtres classiques tels que la prolate [48] ou la gaussienne introduisent moins de ringing mais en contrepartie rendent l'image plus floue que le filtre de Shannon. Étonnamment, la littérature ne donne aucune table de référence du niveau de flou et de ringing que ces filtres introduisent. Nous proposons de répondre à cet oubli en suggérant une classification de filtres classiques selon le double critère : ringing et flou. Cette table a un double avantage. Tout d'abord elle permet d'évaluer quantitativement les niveaux d'artefacts introduit par le filtre. Mais elle permet aussi en pratique de comparer les performances de différentes familles de filtres de sorte à choisir le meilleur filtre pour les niveaux d'artefacts autorisés. L'étude est menée d'abord en une dimension et s'étend simplement au cas bidimensionnel par produit tensoriel. Comme dans d'autres travaux, le contour est modélisé par la fonction de Heaviside H.

Les deux artefacts s'ajoutent au niveau des contours rendant difficile leurs mesures indépendantes. Nous définissons une mesure jointe par un système géométrique de boîte montré sur les Figures 2 et 3. Le paramètre S mesure l'étalement du signal (en anglais *spread*) et R le ringing. Pour chaque filtre, la mesure se définit par une courbe flou/étalement. La norme L^∞ permet de contrôler le rebond maximal de $k \star H$, car l'œil est très sensible aux fortes variations de niveaux de gris. D'autres mesures, telles que la norme L^1 et L^2, sont aussi testées. Cette modélisation permet de construire des *filtres optimaux* selon notre définition de R et S. C'est-à-dire que pour une valeur donnée d'étalement S, le filtre optimal donne la plus petite valeur de ringing R atteignable par n'importe quel autre filtre passe-bas imaginable respectant la même fréquence de coupure. De manière générale, la classification montre que les filtres dont la transformée de Fourier est voisine du cosinus sont de bons filtres, proches de l'optimalité. De plus ils ont l'avantage d'être simple d'utilisation puisque leur expression analytique est connue, à la différence d'autres filtres classiques.

La mesure jointe du ringing et du flou nous a permis d'étudier la dégradation de filtres classiques, mais aussi la dégradation de systèmes optiques réels. La construction de la courbe flou/étalement pour le système optique positionné sur un des satellites du Centre National d'Études Spatiales (CNES) met en évidence l'optimalité du filtre pour des couples (S, R) par rapport aux filtres appartenant à la même famille de filtres, bien que le filtre du CNES soit imposé par les instruments du système d'acquisition d'image installé sur le satellite.

Les expériences numériques montrent que la mesure des artefacts associés à un filtre n'est pas suffisante pour les contrôler sur les images filtrées. Ces observations proviennent du caractère additif du ringing. En effet, des oscillations provenant de différents contours de l'image se croisent et peuvent localement s'ajouter si elles sont en phase, créant à cet endroit de plus grandes oscillations. Une évaluation directe basée sur les zones homogènes, où le ringing est particulièrement visible, permet de confirmer les bons résultats des *filtres optimaux*.

Mesure de la qualité image

Par association avec les trois artefacts étudiés dans cette thèse : flou, ringing et aliasing, nous définissons trois détecteurs. Le premier est un détecteur de netteté, par opposition avec le flou. Nous basons notre approche sur les mesures de cohérence de phase introduites par Morrone [37]. L'idée principale se fonde sur le fait que les composantes de la transformée de Fourier dans le voisinage d'un

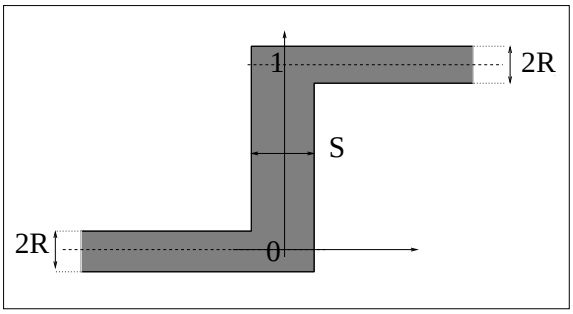

FIG. 2 – Domaine $D_{S,R}$

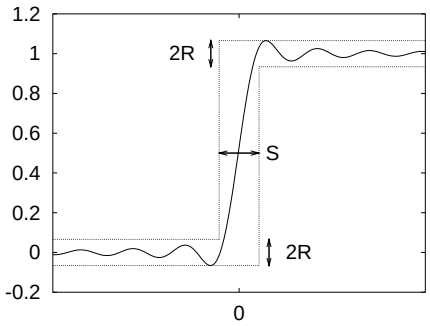

FIG. 3 – Le graphe de $k \star H$ est inclus dans $D_{S,R}$

contour sont en phase. Notre mesure de netteté est basée sur la sensibilité de l'image à la destruction, c'est à dire au déphasage aléatoire. Un contour prononcé est très sensible à une telle destruction, puisque le déphasage d'une seule sinusoïde fait apparaître des oscillations sur le signal reconstruit. La sensibilité est mesurée en terme de variation totale (VT), classiquement utilisée pour évaluer le ringing.

$$VT(u) = \int |Du|$$

où Du est la différentielle de u. Une approximation discrète de la VT est la moyenne de la somme des sauts de l'image en chaque pixel dans les deux directions. De sorte à s'affranchir de paramètre, nous avons utilisé une approche probabiliste. La cohérence de phase notée $F_\varepsilon(u)$ est ainsi mesurée par

$$F_\varepsilon(u) = -\log_{10} \ \mathbb{P}\left(VT(U_\varepsilon) \leq VT(u)\right),$$

où U_ε est l'image construite par le déphasage aléatoire des phases de u dans $[-\varepsilon\pi, \varepsilon\pi]$. Une image nette a des phases cohérentes, donc la variation totale des images déphasées aura tendance à augmenter, ce qui implique une forte valeur de $F_\varepsilon(u)$. Lorsque ε tend vers zéro, $F_\varepsilon(u)$ évalue la sensibilité de l'image à un très faible déphasage :

$$F_{0^+}(u) = \lim_{\substack{\varepsilon \to 0 \\ \varepsilon > 0}} F_\varepsilon(u).$$

Cette mesure s'avère être un bon détecteur puisque nous avons pu vérifier que les images nettes ont une très grande valeur de $F_{0^+}(u)$ contrairement aux images floues.

Le deuxième détecteur est spécifique au ringing. Les mesures existantes de ringing mesurent les rebonds de chaque côté des discontinuités [31]. D'autres comparent la variance des niveaux de gris autour des contours [39]. Ici, nous ne nous intéressons pas au caractère perceptuel du ringing, mais plutôt à la présence d'une période particulière d'oscillations sur toute l'image. La détection est faite *a contrario* sous l'hypothèse *a priori* qu'il n'y a pas de période particulière d'oscillations sur une image de bruit blanc ou sans ringing. De telles images ne contiennent pas d'oscillations et ne seront alors pas détectées. Nous nous basons ici sur la méthode générale de détection *a contrario* [12] que nous rendons spécifique au ringing. La longueur maximale des oscillations est calculée sur une ligne perpendiculaire au contour de sorte à se placer dans la direction du ringing (Figure 4). Les expériences montrent une période hautement représentée dans les images avec ringing ce qui permet de les distinguer des images sans ringing. Les textures périodiques faussement détectées comme étant du ringing sont facilement exclues car la détection est localisée sur la texture et n'est pas généralisée à l'ensemble de l'image.

(a) (b) (c)

FIG. 4 – (a) image original u (b) image avec du ringing (c) l'étude du ringing ne s'effectue pas selon les axes X et Y de l'image mais dans la direction v perpendiculaire au contour.

Le troisième détecteur est spécifique à l'aliasing. La littérature n'offre pas de consensus pour la détection de cet artefact. Or dans de nombreuses applications, les images sont aliasées. Il est donc important de le détecter pour essayer de le supprimer. Dans ce mémoire, nous étudions dans ce but trois approches : une approche fréquentielle, une approche géométrique et une approche basée sur la sensibilité de la variation totale à la translation. Ces trois approches utilisent les différentes manifestations de l'aliasing. Quelques unes sont montrées sur la Figure 5.

1. La première approche est basée sur l'étude fréquentielle puisque l'aliasing est défini comme un recouvrement fréquentiel. De manière générale, l'approche fréquentielle est difficile car la transformée de Fourier est une opération globale. Le phénomène de repliement spectral, typique de l'aliasing, est souvent caché par le contenu fréquentiel déjà riche de l'image de départ. Cependant pour des cas très particuliers d'images, telles que les images contenant un seul contour la détection est visuellement possible sur sa transformée de Fourier. Si l'image n'est pas aliasée, la transformée de Fourier a son énergie maximale selon une ligne dans la direction orthogonale au contour. Si le contour est mal échantillonné, l'aliasing se visualise par un repliement fréquentiel dans le domaine spectral de l'image : des lignes secondaires apparaissent parallèles à la ligne de forte énergie spectrale.
2. La deuxième approche est basée sur l'étude géométrique des lignes de niveau de l'image le long des contours. Ces derniers paraissent hachurés et les lignes de niveau associées sont crénelées. Une étude statistique sur des lignes de niveau des images aliasées et non aliasées permet de mettre en évidence la forte concentration de contours de type *escaliers* sur les images aliasées. La détection est rendue systématique grâce à la prise en compte de la longueur de la ligne de niveau crénelée.
3. La troisième approche est basée sur le postulat de Shannon qu'une image est équivalente à ses versions translatées. Comme une image aliasée ne respecte pas le critère de Shannon, nous mettons en évidence la non équivalence des images aliasées avec leurs translatées. De nouveau, le critère employé est basé sur la variation totale puisque la translation ajoute des oscillations. Le détecteur d'aliasing est défini de la même manière que le détecteur de netteté $F_\varepsilon(u)$ pour lequel nous avons proposé une méthode probabiliste sans paramètre basée sur le calcul des variations totales :
$$G(u) = -\log_{10} \ \mathbb{P}\left(TV(U_t) \leq TV(u)\right),$$
où U_t est l'image translatée de u avec une translation aléatoire uniforme dans $[0,1[^2$ (translation sous-pixelliques).

(a) (b) (c) (d) (e) (f)

FIG. 5 – Exemples d'aliasing : (a-b) exemple de changement de texture (c-d) exemple de pixellisation des éléments filaires (e-f) exemple de contours de type *escaliers*. A chaque fois sont représentées l'image originale et l'image aliasée à sa droite. L'image aliasée est construite par sous-échantillonnage spatial d'un facteur 2 de l'image originale de taille 64×64. Pour la visualisation, l'image aliasée est zoomée d'un facteur 2 avec une spline d'ordre 3.

Applications

Les applications de tels détecteurs sont nombreuses. Les détecteurs de netteté, de ringing ou d'aliasing sont directement utilisables dans toute méthode de restauration d'image paramétrée nécessitant une automatisation. Les paramètres optimaux sont obtenus en détectant la meilleure image parmi toutes celles obtenues avec les différents jeux de paramètres. L'application testée est la déconvolution aveugle. Il s'agit de retrouver le filtre k et l'image originale u_0 à partir du résultat $u = k \star u_0$. Ce problème a été étudié dans la littérature et connaît un engouement particulier dans l'imagerie astronomique. Un algorithme classique est celui de Lucy-Richardson [27][41], que nous comparons avec l'approche proposée. Nous étudions deux familles de filtres positifs : les filtres à support compact 3×3 et à support non compact de type gaussienne. Ces filtres sont classiquement étudiés car ils ont de bonnes propriétés et possèdent peu de paramètres [8]. Nous montrons que le détecteur de netteté permet de retrouver le filtre k lors d'une simple déconvolution régularisée. Les résultats obtenus permettent de considérer que dans le cadre de l'analyse, le détecteur de netteté ouvre des possibilités nouvelles pour la déconvolution aveugle.

La deuxième application testée est le débruitage automatique. Pour cela, nous testons un algorithme de débruitage fort efficace basé sur la redondance spatiale dans les images appelé *Non-Local Means Algorithm*, introduit par Buades *et al.* dans [6]. Il calcule la moyenne des niveaux de gris des pixels qui ont un voisinage semblable. La distance entre ces pixels peut être grande. Cet algorithme de moyennes non locales débruite particulièrement bien les structures périodiques. Cette méthode a quatre paramètres pour lesquels les auteurs nous donnent des suggestions d'initialisation basées sur l'évaluation visuelle de ses résultats. Nous montrons que le détecteur de netteté permet d'optimiser d'une façon très fiable et automatique les paramètres pour obtenir le meilleur résultat possible.

D'autres applications peuvent être étudiées dès lors que l'optimisation automatique de la procédure de restauration d'images est nécessaire. D'une façon plus générale, les mesures de qualité proposées peuvent être utilisés dans toute problématique liée à la mesure d'efficacité d'un algorithme, ou bien dans sa comparaison avec d'autres algorithmes.

Part I

Formation and processing of numerical images. Artifacts

Introduction

The formation of a numerical image is the process of storing an observed scene on a numerical support by using some optical devices. It can be modeled as governed by two major principles. The first one is the geometry, which explains how the light rays coming from the scene points converge by passing through the optical device. The second one is related to the sampling stage, which builds the discrete image. We shall now describe successively these two stages.

We assume that the optical device is a simple convex lens of negligible thickness characterized by its focal distance f and its diameter D when considering a circular lens. Its focal plane P is positioned at a distance f from the lens optical center $O = (0, 0, 0)$. It is defined as the plane where the image of an object at an infinite distance focus. If one considers light rays coming from an object located at a distance $Z_0 > f$ from the lens, they all converge at a certain distance S behind the lens. Thus, we speak about the geometrical image u_g of the object, which is formed on the plane $z = -S$ (Fig.6).

Let us consider the images formed on the focal plane P. They are represented by a two dimensional signal which indicates the density of energy received at the position (x, y) on the plane P. A bright spot in the scene yields a large value of $u_g(x, y)$. The three dimensional scene is thus projected onto a plane. At that stage some background objects might be either totally or partially occluded by some other objects closer to the lens. Some light rays coming from the background objects are stopped by the foreground objects, so that they do not reach the lens. This is an important phenomenon, especially the partial occlusion, since it is a major key of the human vision. Our eye is very sensible to large intensity differences, such as the ones along the boundary between two objects.

This simple introduction of the geometrical principle is a theoretical approach which is valid only for *perfect* lenses. Most of the lenses, including the lenses of the human eye, have some limitations that deteriorate image quality. So the image observed on P is not u_g, the image obtained by the projection of the 3D scene on P, but a degraded version u. The limitations of the lens due to focal length f and diameter D degrade u_g in the two following ways.

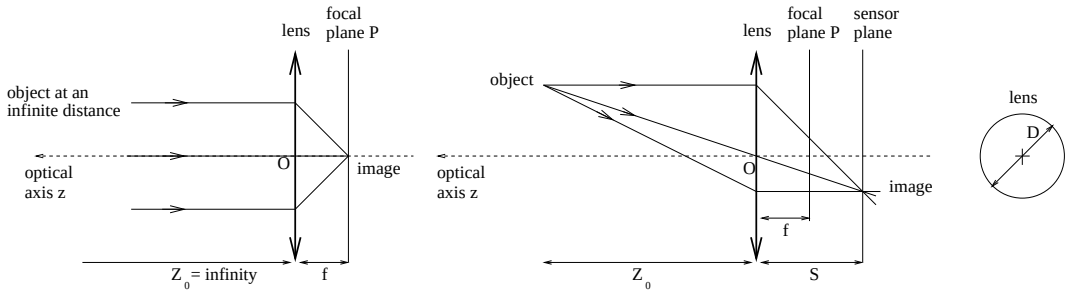

Figure 6: The geometrical principle of image formation and the lens properties.

1. The image in the focal plane is focused for parallel light rays only, i.e. for objects at an infinite distance. Points that are not at infinity are not focused in the plane $z = f$: they appear blurry. This is the reason why the recording surface S of the camera (a charge coupled device C.C.D. for a digital camera or a photographic film for classical ones) does not generally coincide with the focal plane. As all objects of the scene do not have the same depth, the photographer adapts the relative position of the sensor plane S with respect to the objects of interest. Its position is given by the Gauss' Formula:
$$\frac{1}{f} = \frac{1}{S} + \frac{1}{Z_0}$$
where Z_0 is the depth of the object to focus. As a consequence, all objects at a depth $z = Z_0$ will be focused. Objects with a smaller or larger depth will appear more or less blurry.

2. Since we consider a circular lens, its aperture is a disc of diameter D. When D is small, the lens introduces diffraction, slightly spreading the paths of the light rays. It means that the image of a point source in the scene will not give a single point on S but a central bright point surrounded by bright rings: the light rays spread out a little bit. This pattern is known as the Airy disc. Its size depends on the wavelength λ of the light and of the parameter D. The smaller the disc is, the bigger the light ray spreading is. Less details of the original scene can be reproduced on S since the image of two close bright points might overlap. The image of a point source is given by the Point Spread Function (PSF) of the optical system, which represents the impulse response of the system. Such a function is linked to the aperture size of the optical device and degrades the geometrical image u_g into u. This transformation can be approximated by the convolution of u with the PSF of the device.

The sampling stage is usually performed by a matrix of small sensors that transforms u into its digitalized version u_d, such as C.C.D. sensors. A numerical value is associated to the average luminance received by each sensor. The discrete image has the same size as the number of sensors in the C.C.D. matrix. Note that when the C.C.D is a line sensor, such as in modern satellite imaging systems, the discrete image is obtained by the combination of several C.C.D line sensors, each one building a row of the image. The signal u_d is the discretized version of the continuous original scene (Fig.7). A small sampling step s is crucial to obtain good quality images. However it is technically difficult to reduce the sampling step because it is directly related to the physical size of the sensors. If s is too large, the discretized version u_d has poor quality because details of u are lost. The optimal s is given by the Shannon sampling theorem. It is related to the maximal frequency component describing u. Before analyzing the theorem, let us first recall some elements of Fourier theory.

Fourier transform of functions in L^1

Let f be a real-valued function defined on $\mathbb{R}^n$. Assume $f \in L^1$ which means that $\int_{\mathbb{R}^n} |f(x)|dx < \infty$. The Fourier transform of f is the continuous function $\widehat{f} \in L^1$ defined by
$$\widehat{f}(\xi) = \int_{\mathbb{R}^n} e^{-i<\xi,x>} f(x)dx$$
where $< \xi, x >= \sum_{i=1}^{n} \xi_i x_i$ is the inner product in $\mathbb{R}^n$. When $\widehat{f} \in L^1$, the function f can be reconstructed from $\widehat{f}$ with the following formula
$$f(x) = \frac{1}{(2\pi)^n} \int_{\mathbb{R}^n} e^{i<\xi,x>} \widehat{f}(\xi)d\xi\,.$$

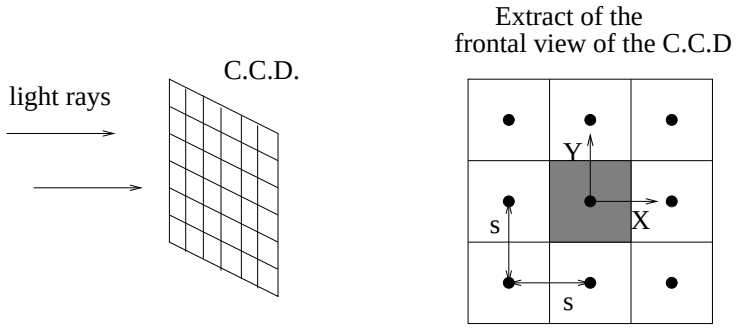

Figure 7: The light rays coming from the lens hit the C.C.D matrix. The sampling step s is the distance between the centers of the adjacent sensors. As the grid is square, the sampling step is identical in the X and Y directions.

A very useful property of the Fourier transform is the fact that the convolution calculus, which is relatively difficult to perform, in the space domain becomes a mere multiplication in the Fourier domain. The computation of any convolution is time consuming especially when the convolution kernel K is large. Note that this convolution kernel is also called filter in this thesis, and $\star$ denotes the convolution operator.

$$\forall x \in \mathbb{R}^n, \quad f \star K(x) = \int_{\mathbb{R}^n} K(y) f(x-y) dy$$

$$\widehat{f \star K} = \widehat{f} \cdot \widehat{K} \quad \text{and} \quad \widehat{f \cdot K} = \frac{1}{(2\pi)^n} \widehat{f} \star \widehat{K} \,. \tag{1}$$

The definition of the Fourier transform given above for functions in L^1 is also true for functions in the Schwartz space $\mathcal{S}$. Let us recall that $\mathcal{S} \subset L^1$ and that it is the space of functions with fast decay at infinity for all derivatives, i.e. it contains the functions $f \in C^\infty$ such that $x^\alpha \, \partial^\beta f(x) \to 0$ as $|x| \to \infty$ for any multi-indices $\alpha, \beta \in \mathbb{N}^n$. The Fourier transform operation is an isomorphism of $\mathcal{S}$ so if $f \in \mathcal{S}$ then $\widehat{f} \in \mathcal{S}$, and reversely. As v is an image, let us set the dimension $n = 2$. The frame of the sampling theorem is now defined.

Theorem 0.1 (Shannon sampling theorem) *Let $f \in \mathcal{S}$ and $s > 0$. If supp$(\widehat{f}) \subset \left[-\frac{\pi}{s}, \frac{\pi}{s}\right]^2$, then*

$$\forall (x,y) \in \mathbb{R}^2, \quad f(x,y) = \sum_{(k,l)} f(ks, ls) \; \mathit{sinc}\left(\frac{x}{s} - k\right) \; \mathit{sinc}\left(\frac{y}{s} - l\right) .$$

supp$(\widehat{f})$ is the support of the function $\widehat{f}$ and $\text{sinc}(x) = \frac{\sin(\pi x)}{\pi x}$ for $x \neq 0$, and $\text{sinc}(0) = 1$ by continuous extension. The proof is given in [32]. In other words, the theorem says that any continuous function $f(x,y)$ can be exactly reconstructed from its samples $f(ks, ls)$ as long as its spectrum $\widehat{f}(\xi_x, \xi_y)$ is included in $\left[-\frac{\pi}{s}, \frac{\pi}{s}\right]^2$. Note that in this configuration, i.e. when $\widehat{f}$ has compact support, f is said to be band-limited. From the theorem, we know that the coarsest grid necessary to perfectly reconstruct f has the critical sampling step s. Any smaller sampling step, corresponding to a finer grid, is also accepted but it is not necessary since it would reconstruct exactly the same function f than with the

grid with the large sampling step s. A similar formulation of the theorem is given by Unser in [53] which presents an account of the current state of sampling, 50 years after Shannon's formulation of the sampling theorem. It recalls the classical sampling theorem. It is important to note here that this formulation is a weak version of the Shannon theorem, and that there is an other formulation that adds a degree of freedom in the hypothesis of the theorem: the constraint $\text{supp}(\widehat{f}) \subset \left[-\frac{\pi}{s}, \frac{\pi}{s}\right]^2$ is replaced by $\text{supp}(\widehat{f}) \subset R$, where R is called the reciprocal cell. If Γ is the regular sampling grid in the space domain and Γ^* is the dual grid in the Fourier domain (for example the case of the square grid is explicitly defined by Almansa in [2]: $\Gamma = \mathbb{Z}\binom{1}{0} + \mathbb{Z}\binom{0}{1}$ and $\Gamma^* = 2\pi\left(\mathbb{Z}\binom{1}{0} + \mathbb{Z}\binom{0}{1}\right)$), then by definition the reciprocal cell R is a tile of Γ^*. Let us now give the complete formulation following the one given by Morel *et al.* in [34] and Almansa in [2] in the two dimensional case:

Theorem 0.2 (Shannon-Whittaker in $\mathcal{S}$) *Given a function $f \in \mathcal{S}(\mathbb{R}^2)$, a 2-dimensional sampling grid Γ and a compact reciprocal cell $R \subset \mathbb{R}^2$. If the following conditions are met*

(S1) *(R, Γ^*) is a packing,*

(S2) *supp$(\widehat{f}) \subset R$ (i.e. f is band-limited),*

then f can be completely recovered from its samples in Γ, i.e. from

$$g = \{f_\gamma\}_{\gamma \in \Gamma}$$

by the following convolution

$$f = s \star g$$

of the sampled image g with the generalized sinc kernel $s = \frac{1}{S^*} \cdot \mathcal{F}^{-1}(\mathbb{1}_R)$.

Notations:

- $\mathcal{F}^{-1}$ is the inverse Fourier transform,
- S^* is the area of a cell of Γ^*,
- by definition: given a grid Γ^* and a set $R \subset \mathbb{R}^2$, (R, Γ^*) is a *packing*, if

$$\forall \gamma \in \Gamma,\ \gamma \neq 0 \Longrightarrow R \cap (R + \gamma) = \varnothing\,.$$

Now that we have recalled the Shannon theorem, let us go back to u and u_d. We have seen that the continuous function u is obtained by the convolution of the geometrical image u_g with the lens PSF and the captor filter. Since this operation is a low-pass filtering, u is band-limited. The spectral support of u can be deduced when the PSF is known. In the end, the sampling step s can be optimized to satisfy the Shannon sampling theorem. However, when the spectral support of u is large, which requires a very small sampling step to satisfy Shannon theorem, the actual technology might not be able to produce sensors of such small size. This unavoidable physical limit may have disastrous effects on images. However the sensor grid can still be used if the spectrum of v is forced to be band-limited prior to sampling.

The band-limitation of an image is a classical processing, that is required in many cases. In order to correctly define the band-limitation of an image, let us first specify the band-limited space.

Definition 0.3 *We define the space of band-limited functions in the L^2 sense by*

$$B_W = \{f \in L^2(\mathbb{R}), \textit{supp}(\hat{f}) \subset [-W, W]\}$$

where supp$(\hat{f})$ is the support of $\hat{f}$.

Fig.8 shows one example of function $f \in B_W$, and one example of the projection onto B_W of a function g, which is not initially in B_W. The band-limitation is done with a hard frequency cut-off:

$$\widehat{g_W}(\xi) = \begin{cases} \hat{g}(\xi) & \text{for } |\xi| \leq W \\ 0 & \text{for } |\xi| > W \end{cases} .$$

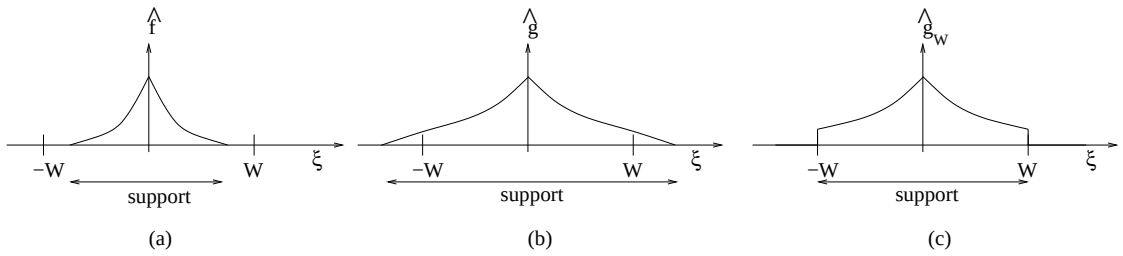

Figure 8: (a) $f \in B_W$ (b) $g \notin B_W$ (c) the hard cut-off of high frequencies of g yields $g_W \in B_W$.

Band-limiting a signal prior to sampling may degrade image visual quality since it may introduce two artifacts called *ringing* and *blur* in the literature, whereas avoiding the band-limitation prior to sampling creates another artifact called *aliasing*. These three artifacts are fundamental degradations linked to the sampling stage. It is essential to minimize them although we show that there is an avoidable trade-off between those three artifacts in most cases. This is the reason why we study the three of them in this thesis. Let us now recall some basic facts concerning these artifacts.

Chapter 1

Aliasing artifact

Since the sampling stage may introduce aliasing, let us formalize it. Preserving each value of f on an uniform grid with element size equal to s can be rewritten by using the theory of distribution

$$g = f \cdot \Pi_s$$

or equivalently in the Fourier domain

$$\widehat{g} = \frac{1}{(2\pi)^2} \widehat{f} \star \widehat{\Pi_s}$$

where Π_s is the Dirac comb defined by $\Pi_s = \sum_{(k,l)\in\mathbb{Z}^2} \delta_{(ks,ls)}$. Let $\mathcal{S}'$ be the space of tempered distributions, dual space of $\mathcal{S}$. We note δ the Dirac distribution defined in $\mathcal{S}'$ by $< \delta_{(x,y)}, \varphi >= \varphi(x,y)$ for any test function $\varphi \in \mathcal{S}$. As $\widehat{\Pi_s} = \left(\frac{2\pi}{s}\right)^2 \Pi_{2\pi/s}$, then from (1) it is clear that sampling a signal is equivalent to the periodization of its spectrum. The periodized versions of $\widehat{f}$ are called aliases. When the spectral support length is larger than the period, the alias will interfere, creating the so called *aliasing* artifact. The Fourier transform of the aliased version g is defined by

$$\forall (\xi_x, \xi_y) \in \left[-\frac{\pi}{s}, \frac{\pi}{s}\right]^2, \quad \widehat{g}(\xi_x, \xi_y) = \sum_{(k,l)\in\mathbb{Z}^2} \widehat{f}\left(\xi_x + \frac{2k\pi}{s}, \xi_y + \frac{2l\pi}{s}\right).$$

The addition of the Fourier transform components results in overlapping high and low component values. Fig.1.1 shows the representation of the phenomenon in one dimension , which has a simpler expression

$$\forall (\xi) \in \left[-\frac{\pi}{s}, \frac{\pi}{s}\right], \quad \widehat{g}(\xi) = \sum_{k\in\mathbb{Z}} \widehat{f}\left(\xi + \frac{2k\pi}{s}\right).$$

Note that values of $\widehat{f}$ are complex. For the clarity of the presentation the ordinate in Fig.1.1 represents the real part of the Fourier transform. The same figure we would also be correct for the imaginary part of the Fourier transform. Fig.1.2 shows the same phenomenon in two dimensions. The periodization results in disastrous visual effects on images, especially on textures. It may create textures with a very different aspect (Fig.1.3). Some other negative visual aspects of the aliasing are discussed in detail in Chapter 12.

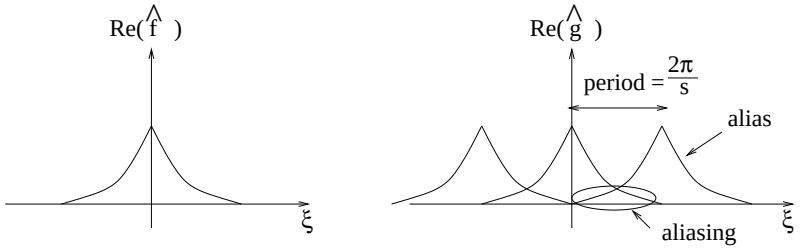

Figure 1.1: The aliasing process in 1D. The aliases are obtained by the $\frac{2\pi}{s}$-periodization of $\widehat{f}$.

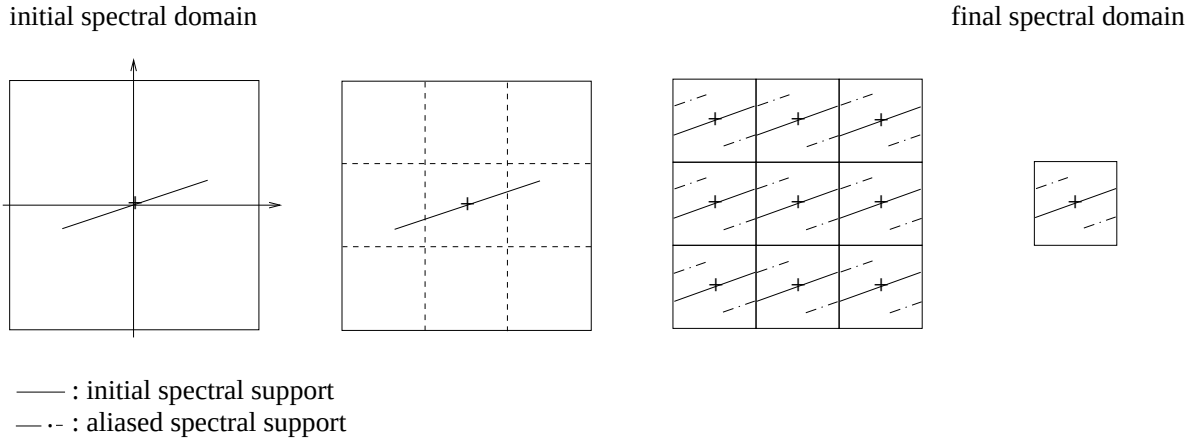

Figure 1.2: The aliasing process in 2D. Example of a downsampling by a factor three in both the x and y directions: the frequency support is reduced by a factor three in the ξ_x and ξ_y directions.

The aliasing artifact may occur at two stages. The first stage is the formation of the discrete signal on the C.C.D. grid from the continuous version. If the sampling step is too large, the conditions of the Shannon sampling theorem are not satisfied. Consequently, the high frequencies are replicated into low ones yielding aliasing. The second stage when the aliasing may occur is the post-processing of the discrete signal. For some applications, it is useful to have smaller images. For example, one may want to reduce the cost of the transmission of the signal, or its storage space. One can reduce the signal size by downsampling it. During this operation one preserves only one sample over s in each direction. It transforms an original discrete image of size $N \times N$ to another one of size $\lfloor \frac{N}{s} \rfloor \times \lfloor \frac{N}{s} \rfloor$ (Fig.1.4). The replication of the high frequencies into low ones can be seen on real images when the original image has a highly represented high frequency. For example, the oscillatory structure of the roof in Fig.1.3 changes orientation after downsampling. The structure of the roof in the sampled image has a lower frequency than in the original image and the orientation is nearly perpendicular to the original one.

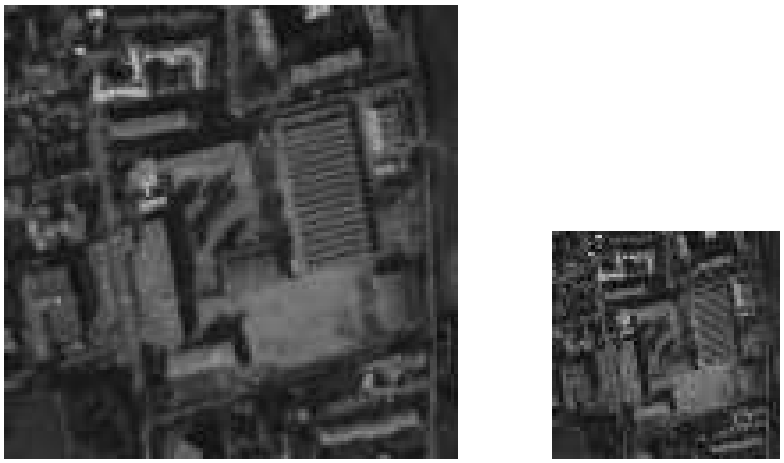

(a) (b)

Figure 1.3: Aliasing example on a real image: (a) original 128×128 image (b) its sub-sampled version ($s = 2$). Observe the texture orientation change on the roof: the parallel lines have different orientations in (a) and (b).

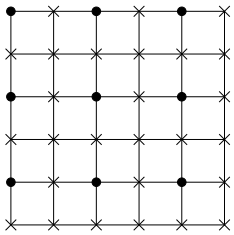

Figure 1.4: Original discrete grid on which the preserved samples are marked by $\bullet$ and the samples marked by $\times$ are discarded. The downsampling by a factor 2 in both directions reduces the image size from 6×6 to 3×3.

As we said above, there is no contradiction with the hypothesis of the Shannon sampling theorem as soon as the signal is band-limited. Then one can assert the absence of aliasing after the sampling stage. However if the projection is done with a hard frequency cut-off, it introduces the ringing artifact which we will study in detail in Chapter 3. But let us first give some comments on the blur artifact, since we will see that it is directly related to the ringing.

Chapter 2

Blur artifact

We have seen that a hard frequency cut-off makes zero the frequencies above the cut-off frequency W and preserves the others. By comparison, a smooth frequency cut-off suppresses the discontinuity at $|\xi| = W$ by regularizing the transition to zero for $|\xi| \leq W$ and preserving the zero aliasing condition: $\hat{f}(\xi) = 0$ for $|\xi| > W$. This can be done by applying a smoothing window on $\hat{f}$.

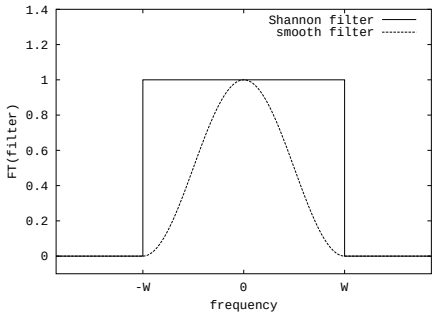

Figure 2.1: The Shannon filter (hard frequency cut-off) and a smooth filter represented in the Fourier domain.

Fig.2.1 shows the hard frequency cut-off and an example of a smooth one. In latter one attenuates high frequencies close to the cut-off. This artifact degrades the image quality, reducing its sharpness and discarding small details that were initially present in the original image. Fig.2.2 shows the original image and the resulting filtered images before their downsampling by a factor $s = 3$. The Fourier transform modulus shown in Fig.2.3 featuring hard and smooth band-limitation illustrates the results. The original image (a) has a wide spread Fourier Transform. Only few frequency coefficients are equal to zero. On the contrary, both band-limited images (b-c) have a small frequential support. However they do not have the same visual impact: image (b) looks sharp but has ringing around edges, whereas image (c) is blurry since only the low frequency coefficients are kept: most of the textures and details are lost. But it has no ringing. This example shows the possible trade-off between these two artifacts. The second part of this thesis is devoted to this problem and we try to answer the crucial question: which filter gives the best trade-off? One immediately remarks that there are filters whose Fourier transform graph are between the two tested in the example in Fig.2.1 (the hard and the smooth ones). Such filters would give a better spread/ringing trade-off. But choosing the best one is not obvious. In fact, we show in Part II that there is not one single best filter for any spread/ringing trade-off, but

that there is a family of best filters. Each of them is the best one for either a given spread value or a given ringing value. In order to formalize the criteria of choice, let us define in detail the ringing artifact. This is done in the following chapter.

(a) (b) (c)

Figure 2.2: (a) Original image (b) Image filtered with the Shannon filter (c) Image filtered with a filter with smooth Fourier transform.

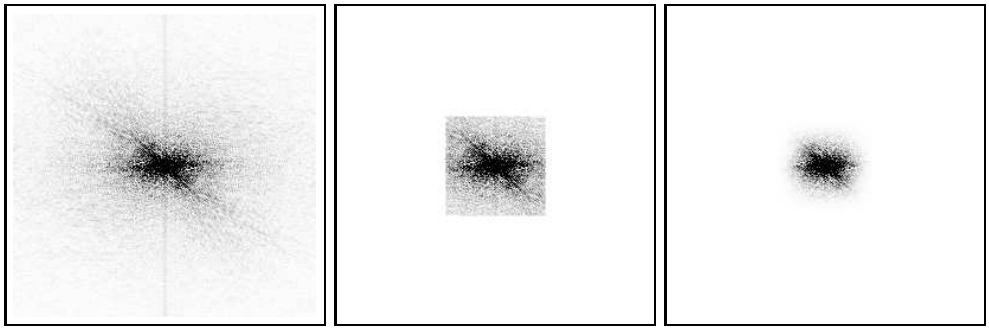

(a) (b) (c)

Figure 2.3: Fourier transform modulus of the images in Fig.2.2. The representation here is unusual since in these figures white pixels mean that the modulus is equal to zero and darker ones indicate higher values of the modulus. As always in natural images, most of the energy is contained in low frequencies. This is indicated by the dark spot in the center of the three spectral images.

Chapter 3

Ringing artifact

Origin and description of the phenomenon

We keep the notations of the introduction. In order to satisfy Shannon theorem conditions, the continuous signal f is band-limited prior to sampling. A hard frequency cut-off of f is defined by

$$\widehat{g} = \widehat{f} \cdot \mathbb{1}_{\left[-\frac{\pi}{s},\frac{\pi}{s}\right]^2}$$

where s is the sampling step. Thanks to (1), the equivalent formulation in the space domain is given by

$$g = f \star K\,,$$

where K is a convolution kernel defined as the inverse Fourier transform ($\mathcal{F}^{-1}$) of $\mathbb{1}_{\left[-\frac{\pi}{s},\frac{\pi}{s}\right]^2}$:

$$K(x,y) = \frac{1}{s^2} \cdot \mathrm{sinc}\left(\frac{x}{s}\right) \cdot \mathrm{sinc}\left(\frac{y}{s}\right)\,. \tag{3.1}$$

Proof of (3.1): Let us note ξ_x and ξ_y the frequencies in the x and y directions, respectively.

$$\begin{aligned}
\mathcal{F}^{-1}\left(\mathbb{1}_{\left[-\frac{\pi}{s},\frac{\pi}{s}\right]}(\xi_x,\xi_y)\right)(x,y) &= \frac{1}{(2\pi)^2}\int_{\mathbb{R}}\int_{\mathbb{R}} \mathbb{1}_{\left[-\frac{\pi}{s},\frac{\pi}{s}\right]^2} \cdot e^{i(x\,\xi_x + y\,\xi_y)}\,d\xi_y\,d\xi_x \\
&= \frac{1}{(2\pi)^2}\int_{-\pi/s}^{\pi/s} e^{i\,x\,\xi_x}\,d\xi_x \;\cdot\; \int_{-\pi/s}^{\pi/s} e^{i\,y\,\xi_y}\,d\xi_y\,.
\end{aligned}$$

The first integral is equal to

$$\int_{-\pi/s}^{\pi/s} e^{i\,x\,\xi_x}\,d\xi_x = \left[\frac{e^{i\,x\,\xi_x}}{i\,x}\right]_{-\pi/s}^{\pi/s} = \frac{1}{i\,x}\left(e^{i\,x\,\pi/s} - e^{-i\,x\,\pi/s}\right) = \frac{2\,\sin(x\,\pi/s)}{x}$$

if $x \neq 0$. Hence,

$$\begin{aligned}
\mathcal{F}^{-1}\left(\mathbb{1}_{\left[-\frac{\pi}{s},\frac{\pi}{s}\right]}(\xi_x,\xi_y)\right)(x,y) &= \frac{1}{(2\pi)^2} \cdot \frac{2\,\sin(x\,\pi/s)}{x} \cdot \frac{2\,\sin(y\,\pi/s)}{y} \\
&= \frac{\sin(x\,\pi/s)}{\pi\,x} \cdot \frac{\sin(y\,\pi/s)}{\pi\,y} \\
&= \frac{1}{s^2} \cdot \mathrm{sinc}\left(\frac{x}{s}\right) \cdot \mathrm{sinc}\left(\frac{y}{s}\right)\,. \qquad \square
\end{aligned}$$

The sinc function oscillates and even has negative values (Fig.3.1-(a)). As we will see, the convolution with such a function might also oscillate if f has sharp transitions. (In images, sharp transitions are located at the border between two objects. We shall call such borders equally well edges and contours. It refers to the occlusion principle we described in the previous chapter.) The perceptual impact on images is the edge replication. In the literature, this artifact is called *ringing*: objects seem surrounded by rings. There are different intensities of ringing. The length and the amplitude of the oscillations change the visual impact. A long oscillation is more noticeable than a short one. The ringing is called an artifact since it adds to the image information that does not exist in the original scene. The replications are spaced by a constant value $2s$, which is directly related to the zeros of the sinc function. Ringing is particularly disastrous for the post-processing as oscillations might be amplified (Fig.3.1-(b)). The ringing is sometimes called "Gibbs phenomenon" in the literature because of the oscillations. However, in Chapter 4 we will see that the ringing is not a consequence of the Gibbs theorem. In an image, transition sharpness may be of different orders. However the sharper the transition is, the more ringing occurs. In order to have a good understanding of the phenomenon, it is essential to define the projection onto B_W of a discontinuous function in 1D such as the Heaviside function (Fig.3.2-(a)).

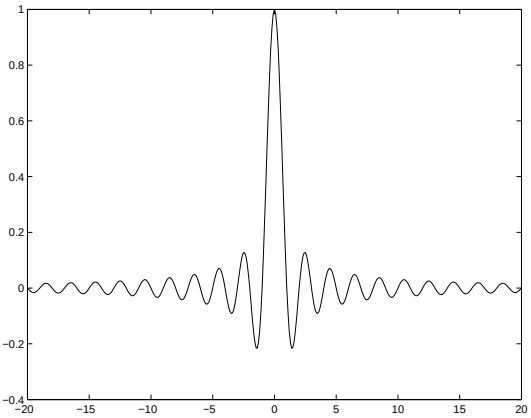

(a)

(b)

Figure 3.1: (a) Graph of the $x \mapsto \text{sinc}(x)$ function (b) Example of ringing on a real image. The replications of the plane's edges come from the sharp transition between the plane bright value and its shadow.

Definition 3.1 *The step function (also called Heaviside function) in 1D is defined by*

$$\forall x \in \mathbb{R}, \quad H(x) = \begin{cases} 1 & \text{for } x \geq 0 \\ 0 & \text{for } x < 0 \end{cases} \quad . \tag{3.2}$$

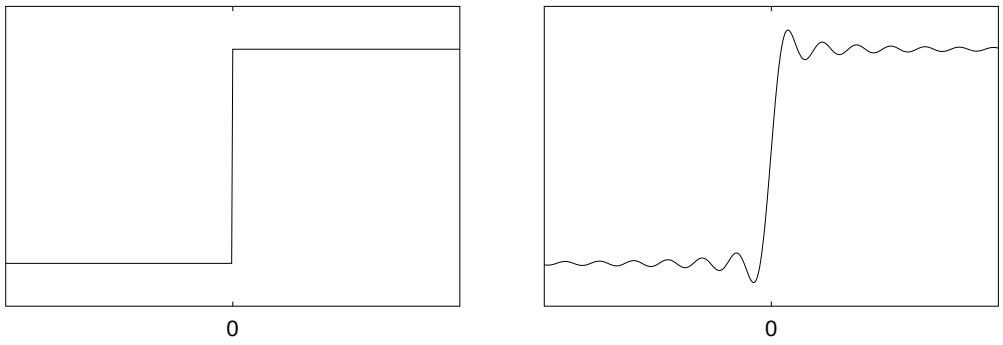

Figure 3.2: (a) Graph of H (b) Graph of H_W. The projection of the Heaviside function H onto B_W oscillates.

Unfortunately, H belongs to $L^1_{\text{loc}}(\mathbb{R})$ but not to $L^1(\mathbb{R})$. We recall that $L^1 \subset L^1_{\text{loc}}$. So the classical definition of the projection onto the band-limited space (in the L^1 sense) is not adapted to H. Since H is slowly increasing, it is also in $\mathcal{S}'$, the space of tempered distributions. So let us recall the definition of the Fourier transform in $\mathcal{S}'$.

Fourier transform of function in $\mathcal{S}'$ [5]

Let $f \in \mathcal{S}'(\mathbb{R}^n)$. The Fourier transform of f is the tempered distribution defined by

$$\forall \varphi \in \mathcal{S}(\mathbb{R}^n), < \widehat{f}, \varphi > = < f, \widehat{\varphi} >$$

where $\mathcal{S}$ is the Schwartz class of functions with fast decay at infinity for all derivatives ($\mathcal{S} \subset \mathcal{S}'$).
Remark: $\mathcal{S}'$ is closed under Fourier transform. If $f \in \mathcal{S}'$ then $\widehat{f} \in \mathcal{S}'$.

Proposition 3.2 *H is equivalently defined in the Fourier domain by*

$$\forall \xi \in \mathbb{R},\ \hat{H}(\xi) = \frac{1}{i} PV(\frac{1}{\xi}) + \pi\delta(\xi) \tag{3.3}$$

where PV stands for Cauchy principal value, defining $1/\xi$ as a distribution.

By definition, for any test function φ,

$$< PV(\frac{1}{\xi}), \varphi > = \lim_{\varepsilon \to 0} \int_{|\xi| \geq \varepsilon} \frac{\varphi(\xi)}{\xi} d\xi = \lim_{\varepsilon \to 0} \int_{\varepsilon}^{+\infty} \frac{\varphi(\xi) - \varphi(-\xi)}{\xi} d\xi \,.$$

Proof: H is equivalently defined in the space domain by

$$H(x) = \frac{1}{2}(\text{sign}(x) + 1),$$

where $\mathrm{sign}(x)$ is the sign function:

$$\forall x \in \mathbb{R}, \quad \mathrm{sign}(x) = \begin{cases} 1 & \text{for } x \geq 0 \\ -1 & \text{for } x < 0 \end{cases} . \tag{3.4}$$

Since the Fourier transform is linear, we have $\forall \xi \in \mathbb{R}$

$$\widehat{H}(\xi) = \frac{1}{2}\widehat{\mathrm{sign}(x) + 1} = \frac{1}{2}\widehat{\mathrm{sign}(x)} + \widehat{\left(\frac{1}{2}\right)} . \tag{3.5}$$

It is well known that the Fourier transform of a constant is a Dirac distribution δ

$$\widehat{\left(\frac{1}{2}\right)} = \frac{1}{2} \cdot 2\pi\delta(\xi) = \pi\delta(\xi) \tag{3.6}$$

and that the calculus of $\widehat{\mathrm{sign}(x)}$ is done by using the Cauchy principal value, to avoid the problem of $\xi = 0$

$$\widehat{\mathrm{sign}(x)}(\xi) = \frac{2}{i}\,\mathrm{PV}(\frac{1}{\xi}) .$$

Let us give some more details on the computation of $\widehat{\mathrm{sign}(x)}$.

- First we give the expression of the Fourier transform of the derivative of $\mathrm{sign}(x)$. For any test function φ

$$\begin{aligned} < \mathrm{sign}', \varphi > &= < \mathrm{sign}, \varphi' > \\ &= -2\int_0^{+\infty} \varphi'(x)dx = 2 \cdot \varphi(0) \end{aligned}$$

  So $\forall x \in \mathbb{R}$, $\mathrm{sign}'(x) = 2 \cdot \delta(x)$. Consequently, $\forall \xi \in \mathbb{R}$, $\widehat{\mathrm{sign}'(x)} = 2 \cdot \widehat{\delta(x)} = 2$.

- The value of $\widehat{\mathrm{sign}(x)}$ is obtained by integrating the previous expression. To that aim, we recall some properties of the Fourier transform. Let $f \in \mathcal{S}$, we have $\widehat{\partial f} = i\xi \cdot \widehat{f}$ [5]. So by integration we have

$$\forall \xi \in \mathbb{R}, \quad \widehat{\mathrm{sign}(x)} = \frac{2}{i}\,\mathrm{PV}(\frac{1}{\xi}) . \tag{3.7}$$

In the end, substituing (3.6) and (3.7) in (3.5) yields $\forall \xi \in \mathbb{R}$

$$\widehat{H}(\xi) = \frac{1}{2}\left(\frac{2}{i}\,\mathrm{PV}(\frac{1}{\xi})\right) + \pi\delta(\xi) = \frac{1}{i}\,\mathrm{PV}(\frac{1}{\xi}) + \pi\delta(\xi) .$$

□

This framework allows us to define the band-limited space B_W and the projection on this space in a new sense.

Definition 3.3 *We define the space of band-limited function in the $\mathcal{S}'$ sense by*

$$\widetilde{B}_W = \{f \in \mathcal{S}' \mid \mathit{supp}(\widehat{f}) \subset [-W, W]\}$$

where $\mathit{supp}(\widehat{f})$ is the support of $\widehat{f}$.

Proposition 3.4 *Let $F \in \mathcal{S}'$. The projection of F in $\widetilde{B}_W$ is the distribution $F_W \in \widetilde{B}_W$ such that*

$$F_W := \underset{\{f:\, f\in B_W \text{ and } F-f\in L^2\}}{\arg\min} ||F - f||_2 \,.$$

The band-limited expression of F is explicitly given by

$$\widetilde{F}_W(x) =< \widehat{F}\,,\, \frac{1}{2\pi}\mathbb{1}_{[-W,W]}\, e^{ix\cdot} > \,.$$

Proof:

1. We first demonstrate the existence of F_W.
   Assume $f \in B_W$ such that $g = F - f \in L^2$ then

   $$g = F - f = F - F_W + F_W - f \,.$$

   The function g is the sum of $F - F_W$ and $F_W - f$. We shall now determine to which space they belong.

   - First we prove that $F - F_W \in {B_W}^\perp \cap L^2$, where ${B_W}^\perp$ is the orthogonal complement to B_W. Indeed on the one hand, $F_W \in B_W$ and $F = F_W + F_{W^\perp}$, so $F - F_W = F_{W^\perp} \in {B_W}^\perp$. On the other hand, F_W is one of the function f such that $F - f \in L^2$, so $F - F_W \in L^2$.
   - Second, the demonstration of $F_W - f \in B_W$ is immediate since $F_W \in B_W$ and $f \in B_W$.

   We have

   $$\underbrace{g}_{\in L^2} = \underbrace{F - F_W}_{\in {B_W}^\perp \cap L^2} + \underbrace{F_W - f}_{\in B_W} \,.$$

   It means that g can be decomposed into the sum of an element in B_W and an element in ${B_W}^\perp$. Consequently, g has a projection in B_W. We conclude that any element $f + g$ with $f \in B_W$ and $g \in L^2$ has a projection in B_W.

2. We now demonstrate the uniqueness of F_W with a proof by contradiction.
   Assume there are two possible decompositions:

   (i) $F = f_0 + g_0$ with $f_0 \in B_W$ and $g_0 \in L^2$,

   (ii) $F = f_1 + g_1$ with $f_1 \in B_W$ and $g_1 \in L^2$.

   From (i) and (ii), we have $F = f_0 + (g_1 - f_0 + f_1)$. Then $g_0 = g_1 - f_0 + f_1$. Since $g_0 \in L^2$, then $g_1 - f_0 + f_1 \in L^2$.
   Since

   $$\underbrace{f_1 - f_0}_{\in B_W} = \underbrace{g_0 - g_1}_{\in L^2}$$

   then $f_1 - f_0 \in B_W \cap L^2$. So $(f_1 - f_0)_W = (f_1 - f_0)$. This result is useful to prove that $g_0 - (g_0)_W = g_1 - (g_1)_W$.

   $$\begin{aligned} g_0 - (g_0)_W &= g_1 - f_0 + f_1 - (g_1 - f_0 + f_1)_W \\ &= g_1 - f_0 + f_1 - (g_1)_W - (f_1 - f_0)_W \\ &= g_1 - (g_1)_W + f_1 - f_0 - (f_1 - f_0)_W = g_1 - (g_1)_W \,. \end{aligned}$$

To conclude, since $g_0 - (g_0)_W = g_1 - (g_1)_W$, whatever the initial decomposition of F, the projection is unique.
Let us give some more details:

$$\begin{aligned} F &= f_1 + g_1 = f_1 + g_1 - (g_1)_W + (g_1)_W \\ &= \underbrace{f_1 + (g_1)_W}_{\in B_W} + \underbrace{g_1 - (g_1)_W}_{\in {B_W}^\perp} \end{aligned}$$

$$\begin{aligned} F_W &= F - [g_1 - (g_1)_W] \\ &= F - [g_0 - (g_0)_W] \end{aligned}$$

As $g_1 - (g_1)_W = g_0 - (g_0)_W$, the projection F_W is unique.

□

By Proposition 3.4, it is clear that the projection of H onto the band-limited space B_W exists and is unique. Fig.3.2-(b) shows the graph of H_W. A devoted study of H_W is given in Section 4.4, however the presence of oscillations, typical characteristic of the ringing phenomenon, can be explained here. We have seen in (3.1) that the Shannon filter is a sinc function. The convolution of H with a sinc function reduces to a very simple form:

$$\begin{aligned} \text{sinc} \star H(x) &= \int_{\mathbb{R}} H(x-y)\ \text{sinc}(y)dy = \int_{\mathbb{R}} \mathbb{1}_{\mathbb{R}^+}(x-y)\ \text{sinc}(y)dy \\ &= \int_{-\infty}^{x} \text{sinc}(y)dy \end{aligned} \tag{3.8}$$

From the graph of sinc, it is not surprising that its integral from $-\infty$ to x oscillates.

Proposition of the ringing definition

We propose to define the ringing in both the continuous and discrete cases. Let us first explain the motivation before giving the definitions. We observed that the ringing phenomenon adds oscillations when band-limiting a signal. However the term "oscillations" is not well defined. They can be observed either on a continuous function g, either on its discretized version $g(k\pi/W)$. If we suppose here it means that the function is alternatively increasing and decreasing (as commonly assumed), then there are *"continuous"* and *"discrete oscillations"*. Continuous oscillations are the alternation of maximal and minimal local extrema with a certain period. A good example is the sine or cosine function. For the discrete oscillations, extrema are chosen among the samples and thus depend on the sampling grid. They might not coincide with the extrema of the continuous function. There might even exist a grid configuration for which a very oscillating function has very small discrete oscillations. (For example, the sine function has no discrete oscillations if the sampling step is equal to 2π.) The sampling step is in general fixed by W, however the grid can be translated. So translated versions of the grid result in different configurations of oscillation. Such an example is given in Fig.3.4.

Let us now define the continuous and discrete ringing. Before giving the definitions let us first give some preliminary explanations. We have seen that the word *ringing* means that the band-limited signal oscillates while the original signal is not oscillating. Since we can work either with continuous signal/oscillation or with discrete signal/oscillation for the original and band-limited signals, we formalize for both signals the type of considered oscillations. The original reference will always be the

discrete signal $f(k\pi/W)$. So the discrimination between the *continuous and discrete ringing* is done with the band-limited signal. This leads to the two following definitions.

Definition 3.5 *When we approximate a function $f(\mathbb{R} \to \mathbb{R})$ by a band-limited function $g(g \in B_W)$, g may have additional oscillations the sampled function $f(k\pi/W)$ does not have: this is the* **continuous ringing phenomenon**.

Definition 3.6 *When we approximate a function $f(\mathbb{R} \to \mathbb{R})$ by a band-limited function $g(g \in B_W)$, the sampled function $g(k\pi/W)$ may have additional oscillations the sampled function $f(k\pi/W)$ does not have: this is the* **discrete ringing phenomenon**.

Examples of *continuous* and *discrete ringing* are shown in Fig.3.3 and 3.4, respectively.

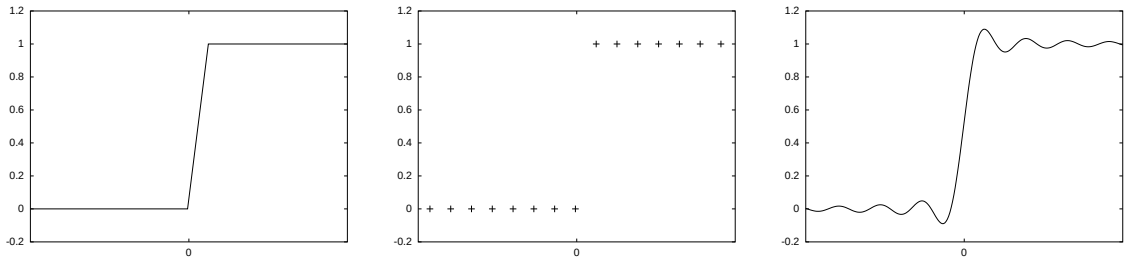

Figure 3.3: Example of the *continuous ringing phenomenon*: (a) original non-oscillating function f (b) its sampled version $f(k\pi/W)$ does not oscillate (c) the band-limited version g of f oscillates. The function g has *continuous ringing* since it is a continuous functions and it oscillates by comparison with $f(k\pi/W)$ which has no (discrete) oscillation: there is no discrete ringing in (b).

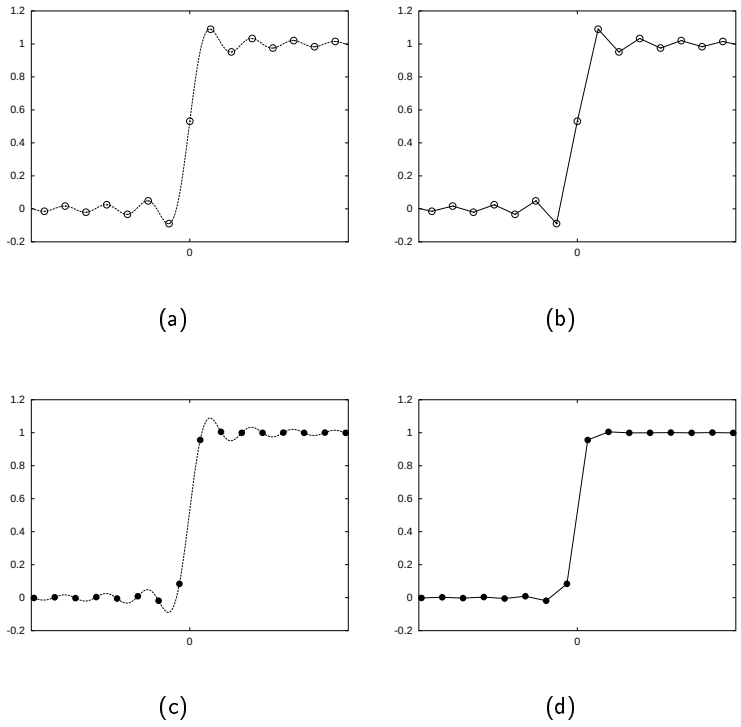

Figure 3.4: Two examples of the *discrete ringing phenomenon*: (a) band-limited oscillating function g and samples ($\circ$) (b) $g(k\pi/W)$ This is an example of the *discrete ringing phenomenon* since $g(k\pi/W)$ has discrete oscillations on the contrary to the original discrete signal $f(k\pi/W)$. Furthermore, the *discrete ringing* value is maximal since $g(k\pi/W)$ has the same local minima and maxima than the continuous signal g. The second line displays another discretization of g which shows small *discrete ringing* because the samples ($\bullet$) are located between the extrema of g.

Chapter 4

Ringing and the Gibbs theorem

4.1 Gibbs theorem

The Gibbs phenomenon is associated with the overshoots and undershoots of the truncated Fourier series or integrals when approximating functions with jump discontinuities. This phenomenon comes from the lack of uniform convergence of the Fourier series in the vicinity of sharp transitions. A more detailed historical note on the Gibbs phenomenon is given in [20]. Even if the phenomenon is named according to the mathematician J. Willard Gibbs in 1906, H.Wilbraham was the first to discover the phenomenon in 1848. The Wilbraham discovery was almost forgotten for about eighty years. It was not until 1925 that Carlslaw brought it to light. In reference to its two discoverers, the phenomenon is sometimes named "The Gibbs-Wilbraham phenomenon".

Gibbs proved the presence of overshoots and undershoots in order to explain the experimental results of Michelson and Stratton. Their "harmonic analyzer" was built to reduce the labor of the Fourier analysis computations. This machine computed the Fourier coefficients given the function to be represented. They tested the 1D square wave

$$f(x) = \begin{cases} \frac{\pi}{4} & \text{for } |x| < \frac{\pi}{2} \\ -\frac{\pi}{4} & \text{for } \frac{\pi}{2} < |x| < \pi \end{cases} \quad . \tag{4.1}$$

"They were surprised when their (such perfect) machine did not predict the square wave shape near the jump discontinuities, but rather added an overshoot and undershoot on each side of the jump discontinuities at $x = \pm\frac{\pi}{2}$ ..."[20]
Gibbs gave the full explanation of the phenomenon in a letter to the Nature journal and described exactly the limit curve of the graphs of some functions. He brought the attention to the difference between the *graph of the limit* and the *limit of the graph* of the Fourier series partial sum. When a function has a discontinuity, the graphs of the partial sum oscillates. On the limit of the graph remains a single overshoot and undershoot which is localized at the discontinuity. In 1906, Bôcher gave a complete proof of Gibbs's assertion and greatly extended it as follows [16].

Theorem 4.1 (Bôcher) *Let f be a real-valued function on the real line $\mathbb{R}$ with period 2π, and suppose that f and its derivative f' are both continuous except for a finite number of finite jump discontinuities in the interval $[0, 2\pi]$. Let $S_n(x)$ be the n^{th} partial sum of the Fourier series of the function f, computed at the point x. The graphs of the function $y = S_n(x)$ converge to curves as sketched in Fig.4.1-(b): in this figure, a is a generic point of discontinuity of f. The vertical segments are of length $\frac{2}{\pi}Si(\pi)\,|f(a+0) - f(a-0)|$ and are centered at $\frac{1}{2}(f(a+0) + f(a-0))$.*

Note: $Si(x) := \int_0^x \frac{\sin(t)}{t} dt$ for $0 < x < \infty$. $Si(\pi) = \int_0^\pi \frac{\sin(t)}{t} dt \simeq 1.851$

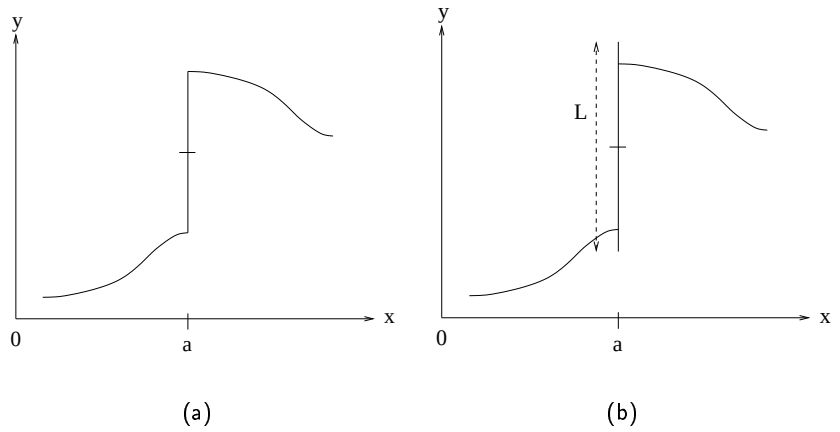

(a) (b)

Figure 4.1: (a) graph of the limit (b) limit of the graph. The limit of the graph has a taller vertical segment than the graph of the limit. At $x = a$, the vertical segment is of length $L = \frac{2}{\pi} Si(\pi) \, |f(a + 0) - f(a - 0)|$ and centered at $\frac{1}{2}(f(a + 0) + f(a - 0))$.

4.2 Is ringing a consequence of Gibbs theorem ?

Overshoots and undershoots are visible in two phenomena: the Gibbs phenomenon and the ringing. These artifacts are both a consequence of the hard frequency cut-off. However, even if these two phenomena have oscillations (we shall call them *Gibbs effect*), it is important to understand that they are not equivalent.

- The Gibbs phenomenon, as given by Gibbs in his theorem and even after by Bôcher, refers to the overshoots and undershoots of a **discontinuous function**, such as the Heaviside function or the 1D square wave. The oscillation amplitude cannot be reduced even with a large number of Fourier coefficients. This phenomenon is characterized by considering the **limit behavior**: the graph of the limit and the limit of the graph are not the same.

- We have seen in Chapter 3 that the ringing phenomenon oscillations are of different kind. According to Definition 3.5, the ringing oscillations come from the hard frequency cut-off of a C^k function, with $k \in [0, +\infty]$. They may appear on a **continuous function**, as long as transitions are sharp enough. **The limit behavior is not considered anymore**. These considerations allow us to state that the ringing is not a consequence of the Gibbs theorem.

In the following section, we consider ringing on a C^∞ function, which does not match the frame of the Gibbs theorem.

4.3 Example of ringing on a C^∞ function

4.3.1 Theorem

Theorem 4.2 *Let G_σ be the increasing function defined by*

$$\begin{array}{rccl} G_\sigma: & \mathbb{R} & \to & \mathbb{R} \\ & t & \mapsto & \int_{-\infty}^{t} e^{-\frac{x^2}{\sigma^2}} dx \end{array}$$

with $\sigma \in \mathbb{R}$. Let $(G_\sigma)_W$ be its projection onto B_W ($W \in \mathbb{R}$) with a hard frequency cut-off. Then

i) *$(G_\sigma)_W$ is not monotone on $\mathbb{R}$,*

ii) *$(G_\sigma)_W$ is increasing on $[-\tau, \tau]$, where τ is a positive constant which only depends on σ.*

(see proof in Appendix 1)

Remark: note that G_σ is related to the standard "error function" $\text{erf}(t) = \frac{2}{\sqrt{\pi}} \int_0^t e^{-x^2} dx$ by the following expression

$$\frac{\text{erf}\left(\frac{x}{\sigma}\right) + 1}{2} = \frac{G_\sigma(x)}{\sigma\sqrt{\pi}} \, .$$

4.3.2 Discussion

In the proof of Theorem 4.2, we defined two constant values α_0 and α_1, the values of which we shall state later in the paragraph. Now let us make several important observations on the theorem.

- We have considered an error function G_σ. Whatever its sharpness controlled by the parameter σ, its band-limitation always lead to the creation of oscillations. One should note that for $t > t_0 = \frac{\sigma}{2\sqrt{\alpha_0}}$, oscillations start at the position of the local maximum and persist as $t \to +\infty$, although their amplitude grows smaller as t increases. The value of t_0 depends only on σ but the position of the local maximum depends on both σ and W.

- The interval $[-\tau, \tau]$, where $(G_\sigma)_W$ is proved to be monotone, only depends on σ ($\tau = \frac{\sigma}{2\sqrt{\alpha_1}}$). Even for small W, which corresponds to keeping only the lowest frequencies, the underlying regularity imposed by the small spectral support $[-W, W]$ forces $(G_\sigma)_W$ to be very smooth. It also implies that the abscissa of the first extrema does not go to 0 (Fig. 4.2).

- We can estimate numerically the values of α_0 and α_1. Theorem 4.2(i) states that $(G_\sigma)_W$ is not monotone on $\mathbb{R}$. We showed that the sign of $((G_\sigma)_W)'$ is related to the sign of $h_\alpha(Wt)$ where $\alpha = \frac{\sigma^2}{4t^2}$. The function h_α has the two following properties

$$\begin{array}{rcl} h_0(2\pi) & = & 0 \, , \\ \left(\frac{d}{d\alpha} h_\alpha(2n\pi)\right)_{\alpha=0} & < & 0 \, . \end{array}$$

  Then $h_\alpha(2\pi) < 0$ for $\alpha \in [0, \alpha_0)$, where α_0 is defined as the smallest α such that $h_\alpha(2\pi) = 0$. The constant value α_1 is also given by the sign of $h_\alpha(Wt)$, which is positive on $(0, \frac{3\pi}{2})$. So the largest t such that $(G_\sigma)_W$ remains monotone around 0 is $\frac{3\pi}{2W}$. Since $h_\alpha(\frac{3\pi}{2}) > 0$ for $\alpha \geq \alpha_1$, then α_1 is defined as the smallest α such that $h_\alpha(3\pi/2) = 0$.
  Numerically, we find $\alpha_0 = 0.0588$ and $\alpha_1 = 0.0753$ (Fig. 4.3).

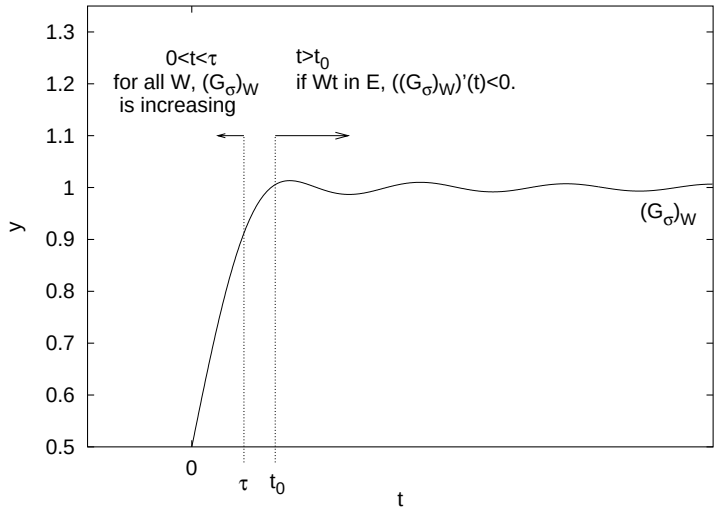

Figure 4.2: Behavior of $((G_\sigma)_W)(t)$ for $t \geq 0$. The spread of the monotone zone around zero depends on σ but not on W. From Theorem 4.2, $(G_\sigma)_W$ is increasing on $[-\tau, \tau]$. Moreover there is at least one overshoot for $t > t_0$ and $Wt \in E$.

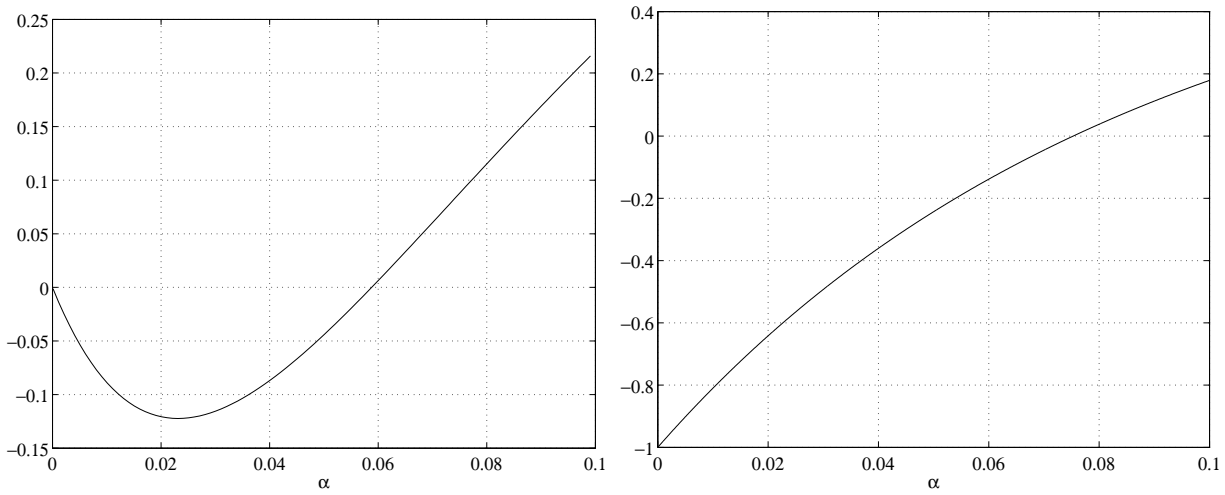

Figure 4.3: Graphs of the function (a) $h_\alpha(2\pi)$ (b) $h_\alpha(\frac{3\pi}{2})$. The values of α_0 and α_1 are determined such that $h_\alpha(2\pi) = 0$ and $h_\alpha(\frac{3\pi}{2}) = 0$. We obtain $\alpha_0 = 0.0588$ and $\alpha_1 = 0.0753$.

- The band-limitation of a monotone function does not necessarily introduce oscillations. It depends on both the filter and the function itself. If the function has no frequency higher than the frequency cut-off then the projection on B_W does not change the spectrum of the function. Thus, if the original function is monotone, then the projected function remains monotone. On the contrary, if the function has frequencies higher than the frequency cut-off, then the projection on B_W may or may not add oscillations, it depends on the projection filter.

- We have seen with the G_σ function an example of a monotone C^∞ function which oscillates after being band-limited. We shall now wonder if there are some C^∞ functions f which are both monotone and band-limited. Assume f is an increasing function, then we have to prove that there is such a C^∞ function that is band-limited and respects $f'(x) > 0$ for all $x \in \mathbb{R}$. For example the function defined by

$$\forall \xi \in \mathbb{R}, \quad \hat{T}(\xi) = \left(1 - \frac{|\xi|}{W}\right) \cdot \mathbb{1}_{[-W,W]}(\xi) = \frac{1}{W} \cdot \mathbb{1}_{[-\frac{W}{2},\frac{W}{2}]} \star \mathbb{1}_{[-\frac{W}{2},\frac{W}{2}]}(\xi)$$

or equivalently by

$$\forall x \in \mathbb{R}, \quad T(x) = \frac{2\pi}{W} \cdot \left(\frac{\sin(\frac{W}{2}x)}{\pi x}\right)^2$$

is both positive in space ($\forall x \in \mathbb{R}, T(x) \geq 0$) and band-limited thanks to the multiplication by $\mathbb{1}_{[-W,W]}(\xi)$. Consequently, we have found one possible f by setting $f'(x) = T(x)$. The function f is monotone, because $\forall x \in \mathbb{R}, f'(x) = T(x) \geq 0$, and it is also band-limited since the property of being band-limited is inherited from its derivative. Here we have

$$f(x) = \int_{-\infty}^{x} T(t)\, dt \; = \; T \star H(x)$$

where H is the Heaviside function, so from (1) we deduce that

$$\widehat{f}(\xi) = \widehat{T}(\xi) \cdot \widehat{H}(\xi) = \widehat{T}(\xi) \cdot \left(\frac{1}{i} \cdot PV\frac{1}{\xi} + \pi\delta(\xi)\right).$$

Since $\widehat{T}(\xi)$ has non zero values only on $[-W, W]$, this also true for $\widehat{f}(\xi)$, which is then said to be band-limited. It is now clear that there are functions that are both band-limited and monotone.

Let us remark here that the previously defined function $f = T \star H(x)$ can also be interpreted as the band-limitation of the Heaviside function by a filter with triangle shape in the Fourier domain. We have already seen in (3.8), the band-limitation of H with the Shannon filter, which represents a hard-frequency cut-off filter, and we observed that ringing occurs. It came from the oscillations of the sinc function along the x-axis. Now, with the filter T, the ringing is avoided because T is positive, then its integral is positive and increases with x.

Remark: for any non-negative function $f \in C^\infty$, the function $T \star f$ is band-limited and non-negative.

4.3.3 Numerical experiments

Theorem 4.2 is validated experimentaly in Fig.4.4. The projection of G_1 onto B_W is represented for different values of W. As expected, we can see that

- $((G_1)_W)(t)$ is increasing on $[-\tau, \tau]$ with

$$\tau = \frac{\sigma}{2\sqrt{\alpha_1}} \simeq \frac{1}{2\sqrt{0.0753}} \simeq 1.822 \ ,$$

- the abscissa of the first overshoot reaches a minimum at τ,

- for the tested values of W, all the function have at least one overshoot at the position $t > t_0$ with

$$t_0 = \frac{\sigma}{2\sqrt{\alpha_0}} \simeq \frac{1}{2\sqrt{0.0588}} \simeq 2.062 \ .$$

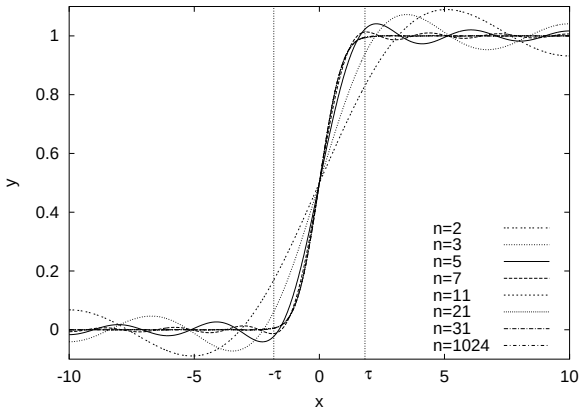

Figure 4.4: Example of functions $((G_1)_W)(t)$ for $t \in [-10, 10]$. Different values of W are tested. Since the signal size is 1024, the frequency associated to each integer n is given by $W = n \cdot W_0$ where $W_0 = \frac{2\pi}{1024}$.

Note that for any fixed σ, there is a value of W that minimizes the abscissa of the first overshoot. We observe that for small values of W, which means that the signal is reconstructed only with small frequency coefficients, the position of the first overshoot is far from the transition (Fig.4.5(a)). This is not surprising since the oscillations of those sinusoids have large period, which directly fix the position of the overshoot far from the transition.
When W increases of a small amount, which means preserving some high frequencies, the abscissa of the overshoot decreases and goes to τ (Fig.4.5(b-c-d-e)). However, when W increases two much, we observe that the position of the first overshoot is pushed away to larger t values (Fig.4.5(f-g)). In fact, the addition of higher frequencies succeeds in canceling the first overshoot, but this is not the case for other overshoots. The sharp transition of the signal is better reconstructed, but there are still oscillations, more far away from the transition, which cannot be avoided because of the lack of the highest frequencies. Note that this phenomenon is very different from the Gibbs phenomenon: here the abscissae of the first overshoots do not tend to 0 as $W \to \infty$ and their amplitudes depend on W, whereas for the Gibbs phenomenon, as we will see in the next section, the amplitude of the first overshoot is independent of W and its abscissa tends to 0.

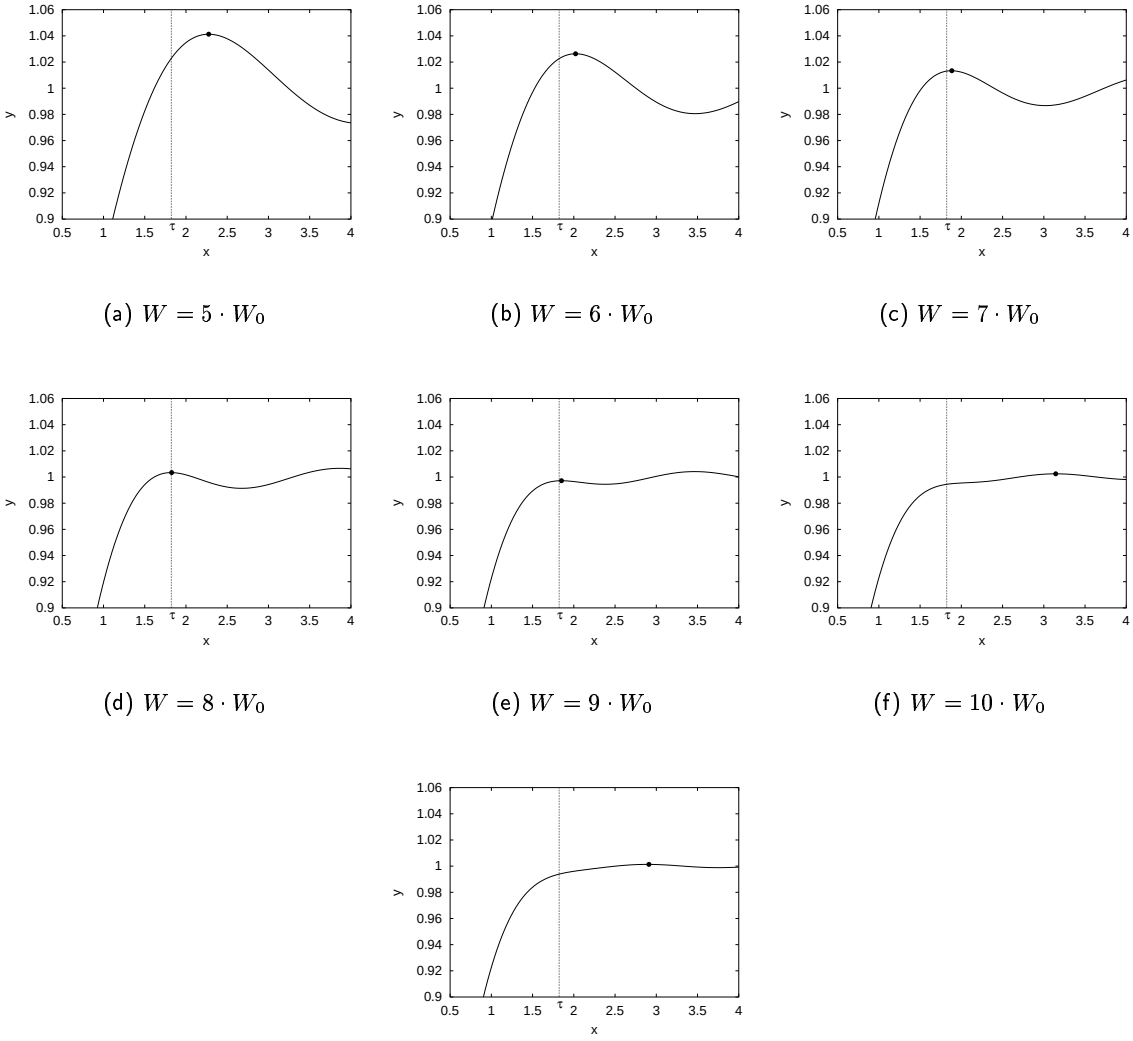

(a) $W = 5 \cdot W_0$ (b) $W = 6 \cdot W_0$ (c) $W = 7 \cdot W_0$

(d) $W = 8 \cdot W_0$ (e) $W = 9 \cdot W_0$ (f) $W = 10 \cdot W_0$

(g) $W = 11 \cdot W_0$

Figure 4.5: Zoom of Fig.4.4 around the first overshoot. (a) $n = 5$ (b) $n = 6$ (c) $n = 7$ (d) $n = 8$ (e) $n = 9$ (f) $n = 10$ (g) $n = 11$. For each function $(G_1)_W$, the first overshoot is marked by (•). Their abscissae are 2.275, 2.021, 1.884, 1.826, 1.850, 3.144 and 2.910, respectively. They satisfy the condition of the theorem $|t| > \tau = 1.822$.

4.4 Gibbs effect on the Heaviside function

Consider the Heaviside function H. The projection of this discontinuous function onto the band-limited space is described by Bôcher theorem. This implies the first part of the following property.

Property 4.3 *Let H_W be the projection of H onto B_W, then*

(i) $H_W \xrightarrow[W\to\infty]{\text{not uniformly}} H$,

(ii) *the maximal overshoot of H_W is located at $x = \frac{\pi}{W}$. Its value is $y_0 \simeq 1.0892$ and is independent of W,*

(iii) *the maximal undershoot of H_W is located at $x = -\frac{\pi}{W}$. Its value is $y_u \simeq -0.0892$ and is independent of W,*

(iv) $H_W(x) = H_{kW}\left(\frac{x}{k}\right)$.

(see proof in Appendix 2). The graph of H_W is drawn in Fig.4.6. The positions of the maximal overshoot and minimal undershoot correspond to those predicted by Property 4.3.

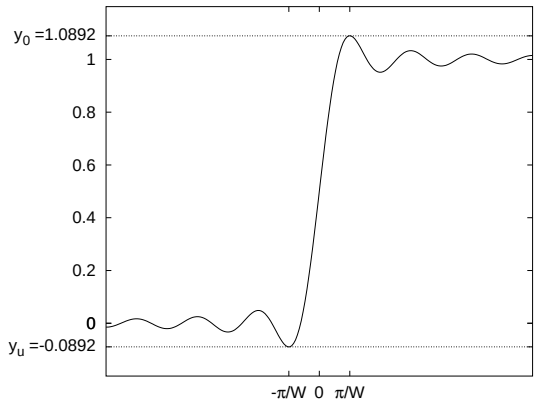

Figure 4.6: Graph of H_W. The overshoot and undershoot values do not depend on W.

4.5 Appendix 1

Proof of Theorem 4.2

Let us first recall the theorem.

Theorem 4.4 *Let G_σ be the increasing function defined by*

$$\begin{array}{rccc} G_\sigma: & \mathbb{R} & \to & \mathbb{R} \\ & t & \mapsto & \int_{-\infty}^{t} e^{-\frac{x^2}{\sigma^2}} dx \end{array}$$

with $\sigma \in \mathbb{R}$. Let $(G_\sigma)_W$ be its projection onto B_W ($W \in \mathbb{R}$) with a hard frequency cut-off. Then

i) *$(G_\sigma)_W$ is not monotone on $\mathbb{R}$,*

ii) *$(G_\sigma)_W$ is increasing on $[-\tau, \tau]$, where τ is a positive constant which only depends on σ.*

Let us now prove it.
Proof of **(i)**:

- It is equivalent to prove that the derivative of $(G_\sigma)_W$ with respect to t changes sign. By definition

$$((G_\sigma)_W)(t) = \frac{1}{2\pi} \int_{-W}^{+W} \widehat{(G_\sigma)}(\xi)\ e^{i\xi t} d\xi.$$

From Fourier transform properties, we have

$$\frac{d((G_\sigma)_W)(t)}{dt} \quad = \quad ((G_\sigma)_W)'(t) = \frac{1}{2\pi} \int_{-W}^{+W} i\ \xi\ \widehat{(G_\sigma)}(\xi)\ e^{i\xi t} d\xi \tag{4.2}$$

Let us define $g_\sigma(t)$, the derivative of $G_\sigma(t)$ with respect to t:

$$g_\sigma(t) = \frac{d}{dt} G_\sigma(t) = \frac{d}{dt} \int_{-\infty}^{t} e^{-\frac{x^2}{\sigma^2}}\, dx = e^{-\frac{t^2}{\sigma^2}}\,.$$

So, thanks to the well known property

$$\widehat{g_\sigma}(\xi) = i\ \xi\ \widehat{(G_\sigma)}(\xi)\,,$$

(4.2) can be rewritten

$$((G_\sigma)_W)'(t) \quad = \quad \frac{1}{2\pi} \int_{-W}^{+W} \widehat{g_\sigma}(\xi)\ e^{i\xi t} d\xi\,.$$

From [5], we know that the Fourier transform of $g_\sigma(x) = e^{-\frac{t^2}{\sigma^2}}$ is $\widehat{g_\sigma}(\xi) = \sqrt{\pi}\ \sigma\ e^{-\sigma^2\xi^2/4}$, then

$$\begin{aligned} ((G_\sigma)_W)'(t) &= \frac{\sigma}{2\sqrt{\pi}} \int_{-W}^{+W} e^{-\frac{\sigma^2\xi^2}{4}} (\cos(\xi t) + i \sin(\xi t)) d\xi \\ &= \frac{\sigma}{\sqrt{\pi}} \int_{0}^{+W} e^{-\frac{\sigma^2\xi^2}{4}}\ \cos(\xi t) d\xi. \end{aligned} \tag{4.3}$$

- With the new variables $u = \xi t$, $s = Wt$ and $\alpha = \frac{\sigma^2}{4t^2}$, the study of the sign of $((G_\sigma)_W)'(t)$ with respect to $t > 0$ is simplified to the study of the sign of

$$h_\alpha(s) = \int_0^s e^{-\alpha u^2} \cos u\, du$$

with respect to s. First we show that $h_\alpha(2n\pi) \ \leq\ 0$ for small values of α and $n > 0$.
Let us set $n > 0$, we will discuss the case $n = 0$ later.

As $h_0(2n\pi) = 0$ and
$\left(\frac{d}{d\alpha}h_\alpha(2n\pi)\right)_{\alpha=0} = -\int_0^{2n\pi} u^2 \cos u\, du = \int_0^{2n\pi} 2\,u\, \sin u\, du = -4n\pi < 0,$
we obtain

$$\exists \alpha_0 > 0, \forall \alpha, 0 < \alpha \leq \alpha_0\ , h_\alpha(2n\pi) < 0. \tag{4.4}$$

As $\cos u$ is positive for $u \in (2n\pi - \pi/2, 2n\pi)$, we deduce from (4.4) that $\forall \alpha \leq \alpha_0, \forall s \in E$,

$$h_\alpha(s) < 0 \text{ with } E = \bigcup_{n\in\mathbb{N}^*} [2n\pi - \frac{\pi}{2}, 2n\pi]. \tag{4.5}$$

Now let us go back to $((G_\sigma)_W)'$. For any given σ and W, there is a value of t such that $\frac{\sigma^2}{4t^2} < \alpha_0$ and $Wt \in E$. From (4.5), we get $((G_\sigma)_W)'(t) < 0$. Since $((G_\sigma)_W)'(0) = \frac{\sigma}{\sqrt{\pi}} \int_0^W e^{-\frac{\sigma^2\xi^2}{4}} d\xi > 0$ and $((G_\sigma)_W)'$ is continuous, we conclude that $(G_\sigma)_W$ is not monotone in $\mathbb{R}$. This proves Theorem 4.2-i).

□

Remark: the proof is done for $n > 0$. We have shown that there is at least one value of $t > 0$ where $((G_\sigma)_W)$ has an overshoot. Since we have not studied the smaller values of t, corresponding to the case $n = 0$, there might exist another overshoot with small abscissa. So the overshoot obtained with $n > 0$ might not be the first one (we will see in (ii) that the position of this first overshoot is bounded from above by τ). We shall not prove here whether there is or not an overshoot for the small values of t, since we have shown that there is at least one, which is enough to prove (i).

Proof of **(ii)**:

1) We first prove that

$$\forall \alpha \geq \alpha_1, \forall s > \frac{3\pi}{2}\ \ h_\alpha(s) \geq 0. \tag{4.6}$$

For this purpose, we write

$$h_\alpha(s) = h_\alpha(\frac{3\pi}{2}) + \sum_{m=0}^{m_0-1} q_m(2\pi) + q_{m_0}(s - 2m_0\pi - \frac{3\pi}{2}) \tag{4.7}$$

with $q_m(t) = \int_A^{A+t} e^{-\alpha u^2} \cos u\ du$, $m_0 = \left\lfloor \frac{s-\frac{3\pi}{2}}{2\pi} \right\rfloor$, where $\lfloor x \rfloor$ is the floor function, and $A = 2m\pi + \frac{3\pi}{2}$.

- Let us prove that

$$\forall m \in \mathbb{N}, \forall t \in (0, 2\pi], \quad q_m(t) > 0 \tag{4.8}$$

  - For $t \in (0, \pi]$, the proof is immediate as $\cos u \geq 0$ on $[A, A + \pi]$.
  - For $t \in (\pi, 2\pi]$,

$$\begin{aligned} q_m(t) =& \int_A^{A+t-\pi} e^{-\alpha u^2} \cos u\, du + \int_{A+t-\pi}^{A+\pi} e^{-\alpha u^2} \cos u\, du + \int_{A+\pi}^{A+t} e^{-\alpha u^2} \cos u\, du \\ =& \int_A^{A+t-\pi} (e^{-\alpha u^2} - e^{-\alpha(u+\pi)^2}) \cos u\, du + \int_{A+t-\pi}^{A+\pi} e^{-\alpha u^2} \cos u\, du \end{aligned}$$

As $e^{-\alpha u^2} - e^{-\alpha(u+\pi)^2} \geq 0$ and $\cos u \geq 0$ on both $(A, A+t-\pi)$ and $(A+t-\pi, A+\pi)$, $q_m(t) \geq 0$.

- Let us prove that

$$\exists \alpha_1 > 0,\ \forall \alpha \geq \alpha_1,\ h_\alpha(\frac{3\pi}{2}) > 0. \tag{4.9}$$

By definition $h_\alpha(\frac{3\pi}{2}) = \int_0^{\frac{3\pi}{2}} e^{-\alpha u^2} \cos u \ du$. Thus by Lebesgue's dominated convergence theorem we have

$$\lim_{\alpha \to \infty} h_\alpha(\frac{3\pi}{2}) = 0. \tag{4.10}$$

Furthermore

$$\begin{aligned}
\frac{d}{d\alpha} h_\alpha(\frac{3\pi}{2}) =& -\int_0^{\frac{3\pi}{2}} u^2 e^{-\alpha u^2} \cos u \ du \\
=& -\int_0^{\frac{\pi}{2}} u^2 e^{-\alpha u^2} \cos u \, du \\
&+ \int_0^{\frac{\pi}{2}} \cos t((\pi - t)^2 e^{-\alpha(\pi - t)^2} + (\pi + t)^2 e^{-\alpha(\pi+t)^2}) \, dt
\end{aligned}$$

  - On one hand, for $\frac{1}{\sqrt{\alpha}} \leq \frac{\pi}{2}$,

$$\begin{aligned}
\int_0^{\frac{\pi}{2}} u^2 e^{-\alpha u^2} \cos u \, du \geq & \int_0^{\frac{1}{\sqrt{\alpha}}} u^2 e^{-\alpha u^2} \cos(\frac{1}{\sqrt{\alpha}}) \, du \\
= & \frac{1}{\alpha\sqrt{\alpha}} \cos(\frac{1}{\sqrt{\alpha}}) \int_0^1 t^2 e^{-t^2} dt \underset{\alpha \to \infty}{\sim} \frac{C}{\alpha\sqrt{\alpha}}
\end{aligned}$$

    for some positive constant C. Hence

$$-\int_0^{\frac{\pi}{2}} u^2 e^{-\alpha u^2} \cos u \, du \leq -r(\alpha) \qquad \text{with} \qquad r(\alpha) \underset{\alpha \to \infty}{\sim} \frac{C}{\alpha\sqrt{\alpha}}.$$

  - On the other hand, we bound from above the second term

$$\int_0^{\frac{\pi}{2}} \cos t((\pi - t)^2 e^{-\alpha(\pi - t)^2} + (\pi + t)^2 e^{-\alpha(\pi+t)^2}) dt$$

    by

$$8\pi^2 e^{-\frac{\alpha\pi^2}{4}} = \underset{\alpha \to \infty}{o}(\frac{1}{\alpha\sqrt{\alpha}}).$$

Consequently,

$$\exists \alpha_1 > 0,\ \forall \alpha \geq \alpha_1,\ \frac{d}{d\alpha} h_\alpha(\frac{3\pi}{2}) < 0 \ . \tag{4.11}$$

From (4.10) and (4.11), we deduce (4.9).

- From (4.8) and (4.9), we know that

1. $h_\alpha(\frac{3\pi}{2}) \geq 0$,
2. $\forall m \in \{0, 1, \ldots, m_0 - 1\} \quad q_m(2\pi) > 0$,
3. $q_{m_0}(s - 2m_0\pi - \frac{3\pi}{2}) \geq 0$
   (> 0 if $m_0 = 0$, $s > \frac{3\pi}{2}$).

With (4.7), this ends the proof of (4.6).

2) Now let us study the sign of h_α on the interval $(0, \frac{3\pi}{2})$. First, we have proven in (4.9) that $h_\alpha(\frac{3\pi}{2}) > 0$ for $\alpha \geq \alpha_1$ and by definition we have $h_\alpha(0) = 0$. Then, from the sign of the cosine function we know that $h_\alpha(s)$ is increasing on $[0, \pi/2]$ and decreasing on $[\pi/2, 3\pi/2]$. Consequently,

$$h_\alpha(s) > 0 \quad \text{on} \quad \left(0, \frac{3\pi}{2}\right). \tag{4.12}$$

3) From (4.6) and (4.12), we deduce that

$$\forall \alpha \geq \alpha_1 \quad \forall s \in (0, +\infty) \quad h_\alpha(s) > 0. \tag{4.13}$$

4) Now let us go back to $((G_\sigma)_W)'$. By definition $s = Wt$ and $\alpha = \dfrac{\sigma^2}{4t^2}$. Thus

$$((G_\sigma)_W)'(t) = C \cdot h_{\frac{\sigma^2}{4t^2}}(Wt)$$

with a constant C positive. The condition $\alpha \geq \alpha_1$ is equivalent to $t \leq \tau$ with $\tau = \frac{\sigma}{2\sqrt{\alpha_1}}$. From (4.13) — and (4.3) for the case $t = 0$ — we conclude that

$$\forall t \in [-\tau, \tau] \quad ((G_\sigma)_W)'(t) > 0.$$

This proves Theorem 4.2-ii). □

4.6 Appendix 2

Proof of Property 4.3

Let us first recall the property.

Property 4.5 *Let H_W be the projection of H onto B_W, then*

(i) $H_W \xrightarrow[W\to\infty]{\text{not uniformly}} H$,

(ii) *the maximal overshoot of H_W is located at $x = \frac{\pi}{W}$. Its value is $y_0 \simeq 1.0892$ and is independent of W,*

(iii) *the maximal undershoot of H_W is located at $x = -\frac{\pi}{W}$. Its value is $y_u \simeq -0.0892$ and is independent of W,*

(iv) $H_W(x) = H_{kW}\left(\frac{x}{k}\right)$.

Let us now prove it.
Proof of **(i)**: It is proved by Bôcher theorem.
Proof of **(ii)**: The inverse Fourier transform ($\mathcal{F}^{-1}$) of $\widehat{H}$ is by definition

$$\tilde{H}(x) = \mathcal{F}^{-1}\left[\widehat{H}(\xi)\right](x) = \frac{1}{2\pi}\int_{-\infty}^{\infty} e^{i\xi x}\,\hat{H}(\xi)d\xi\,.$$

From (3.3), $\forall x \in \mathbb{R}, \varepsilon > 0$,

$$\begin{aligned}\tilde{H}(x) &= \frac{1}{2\pi}\int_{-\infty}^{\infty} e^{i\xi x}\cdot\left(\frac{1}{i}\ \mathrm{PV}\ \frac{1}{\xi} + \pi\delta\right)\,d\xi \\ &= \frac{1}{2\pi}\lim_{\varepsilon\to 0}\int_{-\infty}^{-\varepsilon}\frac{e^{i\xi x}}{i\xi}d\xi + \frac{1}{2\pi}\lim_{\varepsilon\to 0}\int_{\varepsilon}^{+\infty}\frac{e^{i\xi x}}{i\xi}d\xi + \frac{1}{2\pi}\int_{-\infty}^{\infty} e^{i\xi x}\,\pi\delta d\xi \qquad (4.14)\end{aligned}$$

From [5], we know that $\mathcal{F}(1) = (2\pi)\cdot\delta$, so $\mathcal{F}^{-1}(\delta) = \frac{1}{2\pi}$. In the end, the last term of (4.14) is simply

$$\mathcal{F}^{-1}(\pi\delta) = \frac{1}{2\pi}\int_{-\infty}^{\infty} e^{i\xi x}\,\pi\delta d\xi = \frac{\pi}{2\pi} = \frac{1}{2}\,.$$

Thus

$$\tilde{H}(x) = \frac{1}{2\pi}\lim_{\varepsilon\to 0}\int_{-\infty}^{-\varepsilon}\frac{e^{i\xi x}}{i\xi}d\xi + \frac{1}{2\pi}\lim_{\varepsilon\to 0}\int_{\varepsilon}^{+\infty}\frac{e^{i\xi x}}{i\xi}d\xi + \frac{1}{2}\,.$$

Let H_W be its projection onto B_W. $\forall x \in \mathbb{R}, \varepsilon > 0$,

$$H_W(x) \quad = \frac{1}{2\pi}\lim_{\varepsilon\to 0}\int_{-W}^{-\varepsilon}\frac{e^{i\xi x}}{i\xi}d\xi + \frac{1}{2\pi}\lim_{\varepsilon\to 0}\int_{\varepsilon}^{+W}\frac{e^{i\xi x}}{i\xi}d\xi + \frac{1}{2} = \quad \frac{1}{\pi}\int_0^W \frac{\sin(\xi x)}{\xi}d\xi + \frac{1}{2}\,.$$

By changing the variable $t = \xi\,x$, we obtain $\forall x \in \mathbb{R}$,

$$H_W(x) = \frac{1}{\pi}\int_0^{Wx}\frac{\sin(t)}{t}dt + \frac{1}{2}. \qquad (4.15)$$

This last expression proves **(iv)**. Now let $g(t) = \frac{\sin(t)}{t}$ be the function defined for all $t \in [0, +\infty)$. We seek Wx, such as H_W is maximal. Let us consider the integral:

$$\int_0^{Wx}\frac{\sin(t)}{t}dt = A_{0,Wx} \qquad (4.16)$$

$$A_{0,Wx} = A_{0,\pi} + A_{\pi,2\pi} + A_{2\pi,3\pi} + A_{3\pi,4\pi} + \ldots + A_{k\pi,Wx}$$

where $k \in \mathbb{Z}$ and $A_{n\pi,(n+1)\pi} = \int_{n\pi}^{(n+1)\pi}\frac{\sin(t)}{t}dt$ with $n \in \mathbb{Z}$.
As $\mathrm{sign}(g(t)) > 0$ for $t \in [0,\pi] + k\cdot 2\pi$ and $\mathrm{sign}(g(t)) < 0$ for $t \in [\pi, 2\pi] + k\cdot 2\pi$ $(k > 0)$, then the sign of $A_{n\pi,(n+1)\pi}$ in (4.16) alternates: $A_{0,\pi} > 0$, $A_{\pi,2\pi} < 0$, $A_{2\pi,3\pi} > 0$, ... (Fig. 4.7). Let us compare the values of two successive integral values $A_{n\pi,(n+1)\pi}$ and $A_{(n+1)\pi,(n+2)\pi}$.
Let $t_1 \in [n\pi, (n+1)\pi]$ and $t_2 \in [(n+1)\pi, (n+2)\pi]$ be such as $t_2 = t_1 + \pi$, and let us compare their associated values $g(t_1)$ and $g(t_2)$

$$g(t_1) = \frac{\sin(t_1)}{t_1} \quad , \quad g(t_2) = \frac{\sin(t_2)}{t_2}.$$

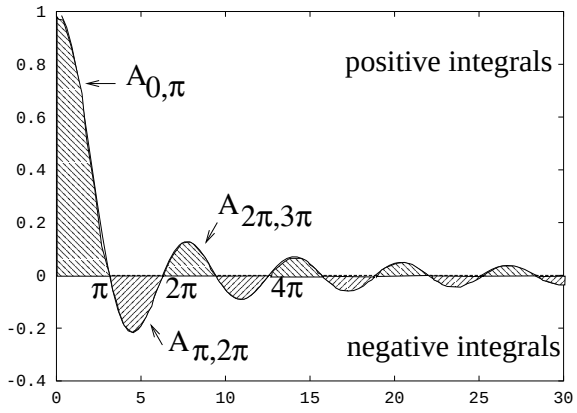

Figure 4.7: Graph of $g(t)$. The sign of the integral of $g(t)$ on each interval $[0,\pi]+2k\pi$ and $[\pi,2\pi]+2k\pi$ alternates.

As the sine function is odd and $0 < t_1 < t_2$,

$$\left|\frac{\sin(t_1)}{t_1}\right| > \left|\frac{\sin(t_2)}{t_2}\right|.$$

Indeed $|\sin(t_1)| = |\sin(t_1+\pi)|$ and $|1/t_1| > |1/(t_1+\pi)|$. Moreover by taking all possible $t_1 \in [n\pi,(n+1)\pi]$ and $t_2 = t_1+\pi$, we cover the whole integration space. We deduce:

$$|A_{n\pi,(n+1)\pi}| > |A_{(n+1)\pi,(n+2)\pi}|.$$

We have also demonstrated that $A_{n\pi,(n+1)\pi}$ and $A_{(n+1)\pi,(n+2)\pi}$ have opposite signs. If $A_{n\pi,(n+1)\pi} < 0$, then $A_{(n+1)\pi,(n+2)\pi} > 0$, then $A_{n\pi,(n+1)\pi} + A_{(n+1)\pi,(n+2)\pi} < 0$. Consequently, the right term of (4.16) is an alternate series of terms with the following particular property: the first negative integral is not canceled by the next one, which is positive inevitably.

$$\underbrace{A_{0,\pi}}_{>0} + \underbrace{A_{\pi,2\pi} + A_{2\pi,3\pi}}_{<0} + \underbrace{A_{3\pi,4\pi} + A_{4\pi,5\pi}}_{<0} + \ldots + A_{k\pi,Wx}$$

Consequently, as $A_{0,\pi} > 0$ and $A_{0,x}$ is increasing for $x \in [0,\pi]$ (because $\text{sign}(g(t)) > 0$ on $[0,\pi]+k\cdot 2\pi$) then the maximal value of H_W is reached when $Wx = \pi$. So from (4.15), the maximal value is given by

$$H_W(x) = \frac{1}{\pi}\int_0^{Wx} \frac{\sin(t)}{t}dt + \frac{1}{2} = \frac{1}{\pi}\int_0^{\pi} \frac{\sin(t)}{t}dt + \frac{1}{2}$$

which is independent of W.

Proof of **(iii)**: As H is odd, then H_W is also odd. Consequently, from (ii), H_W is minimal when $Wx = -\pi$. The overshoot value is independent of W. This *property* is also valid for the undershoot value.

Now let us consider a transition from 0 to T. From Bôcher theorem, the amplitude of the transition is increased due to the band-limitation. We know that

$$L = \frac{2}{\pi}\cdot Si(\pi)\cdot T \simeq 1.1783804\cdot T\,.$$

Hence,

- the overshoot has ordinate

$$y_o = \frac{T}{2} + \frac{L}{2} = \frac{T}{2} + \frac{1}{2} \cdot \frac{2}{\pi} \cdot Si(\pi) \cdot T\,.$$

  In our case $T = 1$, because H is a transition from 0 to 1, so

$$y_o = \frac{1}{2} + \frac{1}{2} \cdot \frac{2}{\pi} \cdot Si(\pi) \cdot 1 \simeq \frac{1}{2} + \frac{1}{2} \cdot 1.1783804 \simeq 1.0891902\,.$$

  Since $H = 1$ at the overshoot, H_W increases the original value of H at this point by $1 - 1.0891902 \simeq 0.0892$.

- symmetrically with respect to the origin, the undershoot has ordinate

$$y_u = \frac{T}{2} - \frac{L}{2} = \frac{1}{2} - \frac{1}{2} \cdot \frac{2}{\pi} \cdot Si(\pi) \simeq -0.0891902\,. \tag{4.17}$$

Proof of **(iv)**: It is already done in the proof of **(ii)**.

□

Conclusion

This part presented the origin of the three artifacts studied in this thesis: aliasing, blur and ringing. For this, we recalled some properties of Fourier transform theory. We stated that

- aliasing, defined as the overlapping of high frequencies onto lower ones, is perfectly predicted by the Shannon sampling theorem,
- blur is understood as a lack of high frequencies, especially for the reconstruction of edges,
- ringing comes from a sharp low-pass filtering, which creates oscillations around edges.

Even if the three artifacts have their own definition and characterization, we have seen that they are all linked to the sampling stage and that there is a trade-off between the three of them. Let us recall here the main contributions of this part.

First, we extended the definition of the projection onto the band-limited space B_W in the L^1 sense to the projection in the $\mathcal{S}'$ sense, where $\mathcal{S}'$ is the space of tempered distributions. This has the great advantage for formalizing the projection of the Heaviside function into B_W, which is not possible in the classical definition of the projection since this function does not belong to L^1. This preliminary formalization is important for the second part of this thesis, which is dedicated to the study of the low-pass filtering of the Heaviside function.

Second, we proposed two definitions of the ringing phenomenon, depending on whether the oscillations of the band-limited function are analyzed in the continuous or in the discrete sense. This distinction is inherent to the two possible definitions of the not well defined term "oscillation", which is associated to a visual feeling. We showed that there are continuous and discrete oscillations, which might not coincide for the same continuous function.

Third, we showed that the ringing phenomenon is not a consequence of the Gibbs theorem. We recalled that the Gibbs theorem refers to the overshoots and undershoots of the hard frequential cut-off of a discontinuous function. Moreover, the Gibbs theorem analyses the non uniform convergence of functions and shows that the graph of the limit and the limit of the graph are not the same. Thus there are two reasons why the ringing phenomenon is not explained by the Gibbs theorem. First, the ringing phenomenon may appear on a C^k function. Second, the uniform convergence is not analyzed. We are interested in the presence of oscillations for a given band-limiting projection, and not by its limit behavior.

Fourth, we gave a complete study of an example of the ringing phenomenon. In order to prove that the discontinuity of the function is not required, the chosen example is the C^∞ *error function*. Theorem 4.2 states the non-monotonicity of its projection onto B_W and gives the smallest possible abscissa of its first overshoot. Numerical experiments confirm the theorem.

Finally, we concluded with the Gibbs theorem by studying H_W: the projection of the discontinuous Heaviside function onto B_W. As expected, H_W oscillates. Property 4.3 gives the position and the

value of its first overshoot. This result is the mathematical justification of some results of the next part, since the first overshoot is closely related to the *level of ringing* associated to this low-pass filtering. The next part shows that the hard frequency cut-off gives very bad results in terms of the level of ringing for a given blur level. This leads to the challenging goal of building new low-pass filters with smaller ringing values.

Part II

Ringing and blur control in the sampling process

Introduction

This part is dedicated to the ringing control in the sampling process. Since it is essential to band-limit the signal before sampling to avoid aliasing, we consider low-pass filters. Moreover the blur/ringing artifacts are not specific to images, in comparison with one-dimensional signals, so the whole study is done in one dimension and is generalized to the 2D case in Chapter 7. Some examples of one-dimensional low-pass filters have already been given in the previous part. One of them is the sinc function which is the optimal low-pass filter in the L^2 sense since it preserves all the frequencies in the bandwidth. But it also has a major drawback: large ringing oscillations in the space domain. As this artifact degrades image quality and might even be increased after a post-processing, it is a paramount to reduce it as much as possible. Some filters such as prolates or splines introduce less ringing. However in the Fourier domain they result in the loss of high frequencies, which blurs edges. These filters allow a trade-off between blur and ringing. However in practice, we know neither how much blur and ringing they add, nor which one is the best.

For example, in some applications, one may allow some ringing. It is the case in a noisy image because the noise may hide the ringing. Since there is a blur/ringing trade-off and since the ringing has to be under the level of noise in the image, the best filter is the one that adds small ringing (not noticeable for this level of noise) and little blur. The zero ringing filter is not adapted, because this unnecessary strong constraint on the ringing adds more blur in the image.

In this part we propose a unified approach of the ringing and blur measure. We control the level of artifacts of a filter by its *Spread-Ringing curve*. This curve is interesting at different levels.

level 1 (the filter level) : the *Spread-Ringing curve* of a filter measures simultaneously its level of ringing and blur. It is the trade-off curve.

level 2 (the filter family level) : the *Spread-Ringing curve* of a family of filter enables to choose the best filter within a family.

level 3 (the filter family comparison level) : the comparison of the *Spread-Ringing curve* of filter families enables to choose the best filter family out of classical ones.

A practical application of this joint measure of the ringing and blur artifacts to a real optical system is given in Chapter 8. This is a special constrained case where the filter is fixed by the instruments of the optical device and is optimal for a given blur/ringing trade-off among the associated filter family. Finally in Chapter 9, some numerical experiments are presented for image reduction. This represents the unconstrained case where the filter can be freely chosen. The filtered numerical images with the optimal filter are compared to the results obtained with other classical filters.

Classical filters

As mentioned before, we recall here some one-dimensional classical low-pass filters. This is not meant to be an exhaustive review of the literature, but more an indication of aliasing-free filters. For example we do not consider the splines typically used for image resizing (enlargement or reduction) [38] [54] [51]. In this study, we focus on even filters because they are the most commonly used and enforce the classical assumption that there are no privileged directions. It is well known that such filters have a real and even Fourier transform. Some filters are already band-limited such as the Shannon filter. Some others becomes band-limited by simply windowing the Fourier domain by $\mathbb{1}_{[-W,W]}(\xi)$, where W is the frequency cut-off. The considered filter families are parametrized by α. Here are the definition of the filters in the Fourier domain, the graphs of which are shown in Fig.4.8:

1. the Shannon filter $\quad \forall \xi \in \mathbb{R}, \quad \widehat{\mathrm{sinc}}(\xi) = \mathbb{1}_{[-W,W]}(\xi)$.
2. the frequency truncated trapezoid ($\alpha = (\alpha_1, \alpha_2)$ with $\alpha_1 \in [0,1]$ and $\alpha_2 \in [0, W]$):

$$\widehat{T_\alpha}(\xi) = \mathbb{1}_{[-\alpha_2,\alpha_2]}(\xi) + \left(1 + \frac{\alpha_1 - 1}{W - \alpha_2}(|\xi| - \alpha_2)\right) \cdot \mathbb{1}_{(-W,-\alpha_2]\cup[\alpha_2,W)}(\xi)$$

The parameter α_1 determines the level of discontinuity at $|\xi| = W$. If $\alpha_1 > 0$, then the modulus is discontinuous, whereas if $\alpha_1 = 0$, then $\widehat{T_\alpha} \in C^0$. Note that we obtain the Shannon filter for $\alpha_1 = 1$ or $\alpha_2 = W$. Assume the ringing is correlated to the discontinuity amplitude in the Fourier domain. Then the larger α_1 is, the more ringing the reduced image has.

The parameter α_2 determines the level of continuity at $\xi = 0$. For $\alpha_2 = 0$ and $\alpha_1 \neq 1$, the first derivative of $\widehat{T_\alpha}(0)$ does not exist. The parameter α_2 is interesting because it refers to the assumption of J.Buzzi and F.Guichard [8] that the blur is uniquely defined by the second derivative at the origin of the Fourier transform ($\xi = 0$) of the filter. Here we have two parameters α_2 and α_1 to measure both the blur and the ringing.

The case $\alpha_1 = \alpha_2 = 0$ build a special filter called "frequency triangle".

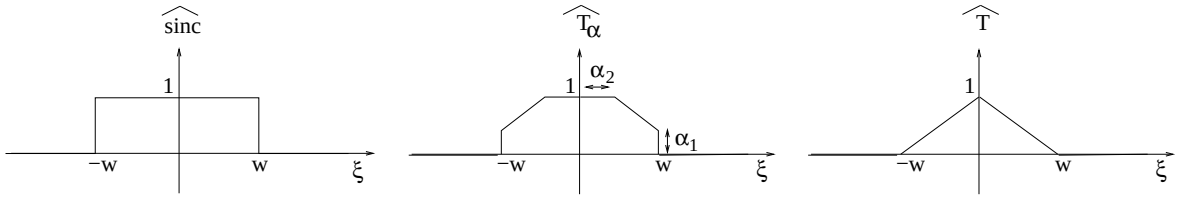

Figure 4.8: Visualization of low-pass filters in frequency space: sinc, T_α and T filters. As filters are even, $\mathcal{I}(\widehat{T_\alpha}) = 0$ and $\mathcal{R}(\widehat{T_\alpha}) = \widehat{T_\alpha}$ (idem for $\widehat{\mathrm{sinc}}$ and $\widehat{T}$).

Theorem 4.6 *The frequency triangle filter T is equivalent to the Cesàro filter.*

Proof: The Cesàro mean of a sequence $\{a_j\}_{j=0}^{\infty}$ is defined to be the average of the n first partial sums. Let $S_k = \sum_{j=0}^{k} a_j$ be the partial sum and $c_n = \frac{1}{n}\sum_{k=0}^{n-1} S_k$ the Cesàro mean. Then

$$c_n = \sum_{k=0}^{n-1}(1 - \frac{k}{n}) \;\; a_k.$$

Denote by g_N the truncated Fourier series

$$g_N(\theta) = \frac{a_0}{2} + \sum_{k=1}^{N} [a_k \ \cos(k\theta) \ + \ b_k \ \sin(k\theta)].$$

The Cesàro regularization (h_N) is a mean of the successive coefficients $g_N(\theta)$

$$h_N(\theta) = \frac{a_0}{2} \ + \ \sum_{k=1}^{N} \frac{N-k}{N} \ [a_k \cos k\theta \ + \ b_k \sin k\theta].$$

The Fourier coefficients are weighted by the factor $C(N,k) = \dfrac{N-k}{N} = 1 - \dfrac{k}{N}$.
This factor is equal to the weight of filter T which can be rewritten by definition

$$\widehat{T}(\xi) = \left(1 - \frac{|\xi|}{W}\right) \cdot \mathbb{1}_{[-W,W]}$$

□

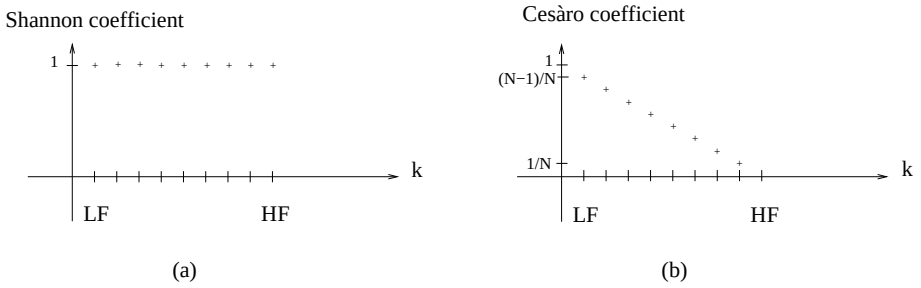

Figure 4.9: (a) Shannon filter (b) Cesàro filter. For both filters, the Fourier coefficients are set to zero for high frequency $\xi > W$. The Shannon filter preserves Fourier coefficient from the low (LF) to the high (HF) frequencies whereas the Cesàro filter has a triangle shape: it preserves better low frequency coefficients.

This equivalence between the frequency truncated triangle filter T and the Cesàro filter is interesting, because the Cesàro filter is often proposed in the literature to reduce the ringing artifact [20]. But as we will see in the filter classification, the counterpart of this zero ringing filter is the large amount of blur in the images. Most of the time, the perceptual results are better when allowing some ringing and so preserving transition sharpness.

3. the frequency truncated cosine filter ($\alpha \in \mathbb{R}$):

$$\widehat{C_\alpha}(\xi) = \left(\frac{1 + \cos(\alpha\xi)}{2}\right) \cdot \mathbb{1}_{[-W,W]}(\xi)$$

Notice that $\widehat{C_\alpha}(0) = 1$, as usually chosen for filter to preserve the mean of an image. This filter is different from classical windows (Hamming, Van Hann, Blackman [29], Chebyshev...) which have a similar definition in the space domain. For example, the Hann window (also called Hanning window, in analogy to the Hamming window) is defined by

$$\forall x \in \mathbb{R}, \quad \mathrm{Ha}(x) = \cos^2\left(\frac{\pi x}{2\tau}\right) \cdot \mathbb{1}_{[-\tau,\tau]}(x) = \left(\frac{1 + \cos(\pi x/\tau)}{2}\right) \cdot \mathbb{1}_{[-\tau,\tau]}(x)\,.$$

4. the band-limited Gaussian filters for which α is the scaling factor. Let us recall that the not band-limited Gaussian filter defined by

$$g_\sigma(x) = \frac{1}{\sigma\sqrt{2}}\, e^{-\frac{x^2}{2\sigma^2}}$$

optimizes the spatial/spectral concentration according to Heisenberg inequality [32]:

Theorem 4.7 (Heisenberg inequality) *If $f \in L^2(\mathbb{R})$, then*

$$\underbrace{\int_{\mathbb{R}} t^2 f^2(t)dt}_{\text{spatial concentration}} \cdot \underbrace{\int_{\mathbb{R}} \xi^2 |\widehat{f}(\xi)|^2 d\xi}_{\text{frequential concentration}} \geq \frac{\pi}{2} \cdot \left(\int_{\mathbb{R}} f^2(t)dt\right)^2 ,$$

with equality if and only if $f(t) = \alpha e^{-\beta t^2}$ for some $\alpha \in \mathbb{R}$ and $\beta > 0$.

The Fourier transform of an non band-limited Gaussian is also a Gaussian [5]

$$\widehat{g_\sigma}(\xi) = \sqrt{\pi}\, e^{-\frac{\sigma^2\xi^2}{2}} .$$

The associated band-limited Gaussian filter is defined by

$$\widehat{G_\sigma}(\xi) = e^{-\frac{\sigma^2\xi^2}{2}} \cdot \mathbb{1}_{[-W,W]}(\xi)$$

to satisfy both the band-limiting constraint and the image mean preservation ($\widehat{G_\sigma}(0) = 1$). However we will see that the blur/ringing trade-off will be measured on the graph of the function resulting from the convolution of the Heaviside function and the filter, which in the case the Gaussian filter can be expressed using the error function

$$\begin{array}{rccl} \text{erf}\colon & \mathbb{R} & \to & [-1,1] \\ & t & \mapsto & \frac{2}{\sqrt{\pi}} \int_0^t e^{-x^2} dx \end{array}$$

by using the following function

$$\frac{\text{erf}(\alpha x) + 1}{2} , \tag{4.18}$$

the Fourier transform of which will be band-limited to $[-W, W]$. Its derivative with respect to x is the associated filter called G_α. Note that for this filter, the parameter α is directly related to the sharpness of the transition of $G_\alpha \star H$ as shown in Fig.4.10. Large values of α yield sharper transitions which have a larger spectral support than smooth transitions. Consequently the band-limitation in $[-W, W]$ adds more artifacts for large values of α.

5. and the prolate spheroidal function defined by Slepian, Pollak and Landau in [49] [25] [26] [47] [48], also called simply *prolate* in this thesis. This filter does not optimize the spatial/spectral concentration according to Heisenberg inequality, as the Gaussian does, but it maximizes the concentration of its energy in a given spectral support, which is here $D_\xi = [-W, W]$. The spatial support is fixed and parametrized here by α to build the prolate family. Let us call $D_x = [-\alpha, \alpha]$ The energy being maximized in the given spectral support is

$$\frac{1}{||\widehat{P_\alpha}||^2} \int_{D_\xi} |\widehat{P_\alpha}(\xi)|^2 d\xi = \chi^2 ,$$

where P_α is the prolate parametrized by α and $\chi \in [0, 1]$ as close to 1 as possible. The iterative algorithm to build the filter is given by Rougé in [42].

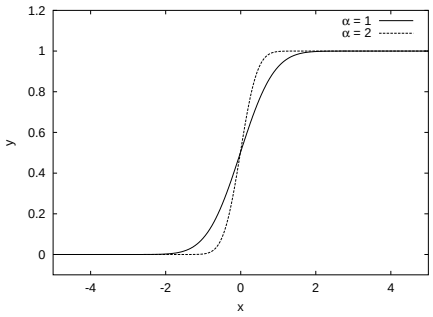

Figure 4.10: Curve $G_\alpha \star H(x)$ for $\alpha = 1, 2$.

It is also interesting to compute the inverse Fourier transform of those filters in order to have an idea of the oscillating behavior of the filter in the space domain. The more oscillating the filter is, the more ringing it may add. The band-limitation, achieved with a multiplication by $\mathbb{1}_{[-W,W]}(\xi)$, is equivalent to a convolution by a sinc function ($\frac{\sin(xW)}{\pi x}$) (replace $\frac{\pi}{s}$ by W in (3.1)). So we expect oscillating filters.

The expression of the filters in the space domain is well known in the literature. The prolate is defined in [48]. The Gaussian case is studied in Theorem 4.2. Now let us give the explicit expression of the truncated cosine filter.

Proposition 4.8 *The inverse Fourier transform of* $\widehat{C_\alpha}(\xi)$ *is*

$$(C_\alpha)_W(t) = \frac{1}{2\pi} \cdot \frac{\sin(Wt)}{t} + \frac{1}{4\pi} \cdot \left(\frac{\sin((\alpha+t)W)}{\alpha+t} + \frac{\sin((\alpha-t)W)}{\alpha-t} \right) \tag{4.19}$$

Proof: By definition

$$\begin{aligned} (C_\alpha)_W(t) &= \frac{1}{2\pi} \int_{-W}^{W} \widehat{(C_\alpha)}(\xi) \cdot e^{i\xi t} d\xi = \frac{1}{2\pi} \int_{-W}^{W} \frac{1}{2}(1+\cos(\alpha\xi)) \cdot e^{i\xi t} d\xi \\ &= \frac{1}{4\pi} \int_{-W}^{W} e^{i\xi t} d\xi + \frac{1}{4\pi} \int_{-W}^{W} \cos(\alpha\xi) e^{i\xi t} d\xi = \frac{1}{4\pi} \cdot \frac{2}{t} \sin(Wt) + \frac{1}{4\pi} \int_{-W}^{W} \cos(\alpha\xi) e^{i\xi t} d\xi \end{aligned}$$

Assume A is the last integral of the previous equation, then

$$A = \int_{-W}^{W} \cos(\alpha\xi) e^{i\xi t} d\xi = \int_{-W}^{W} \cos(\alpha\xi)(\cos(\xi t) + i\sin(\xi t)) d\xi = \int_{-W}^{W} \cos(\alpha\xi)\cos(\xi t) d\xi$$

as the function $\cos(\alpha\xi)\sin(\xi t)$ is odd with respect to ξ. Moreover $\cos(\alpha\xi)\cos(\xi t)$ is even, hence

$$\begin{aligned} A &= 2\int_0^W \cos(\alpha\xi)\cos(\xi t) d\xi = \int_0^W (\cos(\alpha\xi+\xi t) + \cos(\alpha\xi-\xi t)) d\xi \\ A &= \left[\frac{\sin(\alpha\xi+\xi t)}{\alpha+t} + \frac{\sin(\alpha\xi-\xi t)}{\alpha-t} \right]_0^W = \left(\frac{\sin((\alpha+t)W)}{\alpha+t} + \frac{\sin((\alpha-t)W)}{\alpha-t} \right) \end{aligned}$$

This ends the proof of the proposition. □

From (4.19) can be deduced a very simple form of $(C_\alpha)_W$ that show the oscillating characteristic of

this filter. So let us remark that (4.19) is the sum of three sinc functions. Indeed

$$\frac{\sin(Wt)}{t} = W\text{sinc}(T) \text{ with } \text{sinc}(t) = \frac{\sin(\pi t)}{\pi t} \text{ and } T = \frac{Wt}{\pi}.$$

So

$$\begin{aligned}(C_\alpha)_W(t) &= \frac{1}{2\pi}\cdot\frac{\sin(Wt)}{t} + \frac{1}{4\pi}\cdot\left(\frac{\sin((\alpha+t)W)}{\alpha+t} + \frac{\sin((\alpha-t)W)}{\alpha-t}\right)\\ &= \frac{W}{2\pi}\cdot\text{sinc}\left(\frac{Wt}{\pi}\right) + \frac{W}{4\pi}\cdot\left(\text{sinc}\left(\frac{W(\alpha+t)}{\pi}\right) + \text{sinc}\left(\frac{W(\alpha-t)}{\pi}\right)\right)\end{aligned}$$

This last equation shows that $(C_\alpha)_W$ is the sum of three sinc functions, centered in $t=0$, $t=-\alpha$ and $t=\alpha$, respectively. Note also that the central sinc function (centered in $t=0$) has a twice larger weight than the side ones (centered in $t=-\alpha$ and $t=\alpha$). Fig.4.11 displays $(C_\alpha)_W$ with $W=5$ and $\alpha=6$.

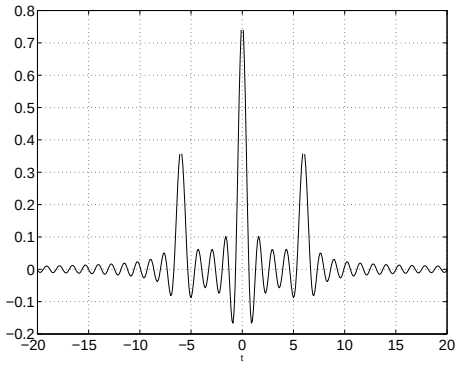

Figure 4.11: Curve $(C_\alpha)_W(t)$ for $\alpha=6$ and $W=5$. The function $(C_\alpha)_W(t)$ is the result of the addition of three sinc functions centered in $t=0$, $t=\alpha=6$ and $t=-\alpha=-6$, respectively.

As you can see from Fig.4.11, a large value of α, such as shown in the example, does not produce an interesting function $g=\varphi\star H$ since it has visually three big steps where we wished a single one. The side sinc functions are far from $t=0$. This result is confirmed in Chapter 6, where $\alpha\simeq 0$ yields the best blur/ringing trade-off for $(C_\alpha)_W\star H$.
Going back to the case $\alpha\simeq 0$, the position of the first overshoot can be deducted from (4.19). Considering the filter, it is equivalent to find the abscissa of its zeros. Since, the three sinc functions are centered in points very close to $t=0$, their zeros are very close. In Property 4.3, we saw that the first overshoot of the sinc function centered in $t=0$ has abscissa $t_0=\frac{\pi}{W}$.

Remark: it coincides with the zeros of the sine function. For $T>0$, the smallest T such that $\text{sinc}(T)=0$ is also the smallest T such that $\sin(\pi T)=0$, that is $T=1$. Since $T=\frac{Wt}{\pi}$, it yields $t=\frac{\pi}{W}$.
Since α is very small, the position of the overshoot of the sinc function centered in $t=\pm\alpha$, is also very close to t_0. Consequently, the first overshoot of the function $g(t)=(C_\alpha)_W\star H(t)$ has its abscissa close $t=t_0$ (Fig.4.12). This property is also satisfied for large values of α, because the oscillations of the side sinc functions have nearly no impact on $g(t)$ for t around zero. The case $\alpha\in[\varepsilon,4t_0]$ with

ε a small positive number, is the most difficult case, since the side sinc functions are centered close enough to $t = 0$ to interact with the overshoot of the central sinc function in $t = t_0$. Fig.4.13 shows the filter $(C_\alpha)_W$ and its Fourier transform used in Fig.4.12.

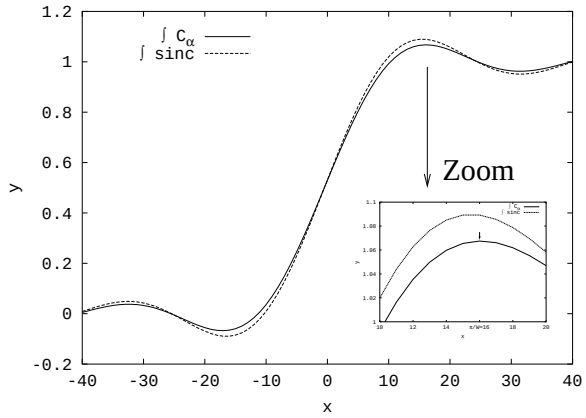

Figure 4.12: Graphs of the function $g(t) = (C_\alpha)_W \star H(t)$ and $H_W(t)$ with $\alpha = 0.03$. Both have the first overshoot in t close to t_0. As expected, the filter $(C_\alpha)_W$ adds less ringing (smaller overshoot) than the sinc one.

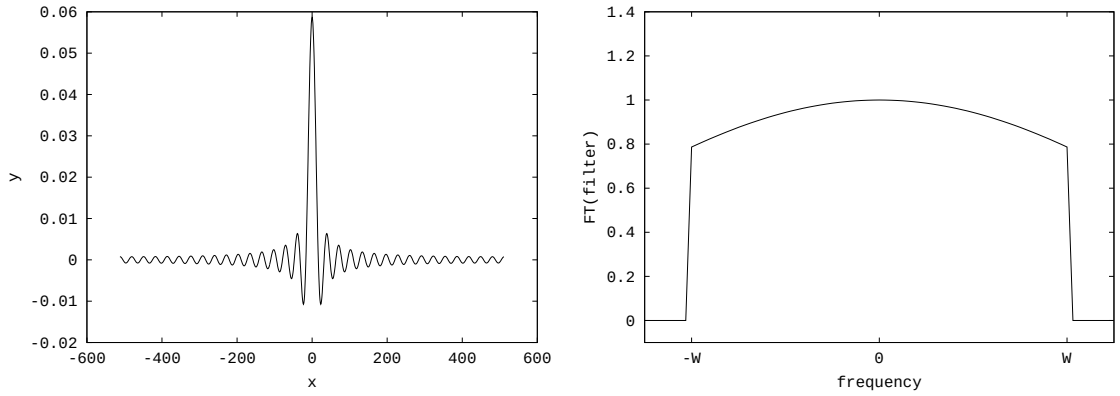

(a) (b)

Figure 4.13: Graph of $(C_\alpha)_W$ (a) in the space domain (b) in the Fourier domain, with $\alpha = 0.03$.

The reduction method

In order to measure the amount of ringing after a low-pass filtering, we model image transitions by the Heaviside function. Let us consider a filter $\varphi \in B_W$, such as a classical filter mentioned above. Applying this filter to the Heaviside function (H), yields a new signal $g = \varphi \star H$. This is the signal the ringing of which we will now measure.

Chapter 5

Joint measure of ringing and blur produced by a family of filters

5.1 The Spread-Ringing curve with the L^∞ norm

A sharp edge, such as the Heaviside function, has neither blur nor ringing. There is no blur because this function is discontinuous in $x = 0$ with $\lim_{x\to 0^-} H(x) = 0$ and $\lim_{x\to 0^+} H(x) = 1$. So the transition from 0 to 1 has zero spread. There is no ringing because H is monotonic. The filtered signal $g = \varphi \star H$ may have both artifacts. Blur is localized at the transitions. They are smoothed yielding a non-zero spread. The ringing phenomenon is localized around the transitions, adding some spurious oscillations. Since it is difficult to define the distance from the edge where blur stops and where ringing begins, we choose to measure simultaneously the spread of the transition (S) and the amplitude of the oscillations outside the transition domain (R) by constraining the graph of g, $\Gamma_g = \{(x, g(x));\ x \in \mathbb{R}\}$ to be contained in the domain $D_{S,R}$ (Fig. 5.1).

Definition 5.1 *We denote $D_{S,R}$ the subset of $\mathbb{R}^2$ defined by*

$$D_{S,R} = \left\{ (x,y) \;\middle|\; \begin{array}{rcl} x \le -\frac{S}{2} & \text{and} & |y| \le R \\ \text{or } |x| \le \frac{S}{2} & \text{and} & -R \le y \le 1+R \\ \text{or } x \ge \frac{S}{2} & \text{and} & |1-y| \le R \end{array} \right\}.$$

We observe that a small R prevents too large oscillations of g, while a small S ensures a sharp edge approximation of the discontinuity of H. Hence, the couple (S, R) reflects the blur/ringing trade-off to be satisfied by g. This leads to the following definition.

Definition 5.2 *The Spread-Ringing domain associated to a filter $\varphi \in B_W$ is*

$$D(\varphi) = \{(S,R) \in (0,+\infty)^2;\ \Gamma_{\varphi\star H} \subset D_{S,R}\}. \tag{5.1}$$

The Spread-Ringing curve associated to φ is the boundary of $D(\varphi)$.

If $(S, R) \in D(\varphi)$, so does $(S + p, R + q)$ for any non-negative p and q. So the boundary of $D(\varphi)$ is obtained by taking the minimal possible value of R for any fixed S, or the minimal value of S for a fixed R. The Spread-Ringing curve can be described by the graph of a function

$$r_\varphi(S) = \min\{R \in (0,+\infty); (S,R) \in D(\varphi)\}$$

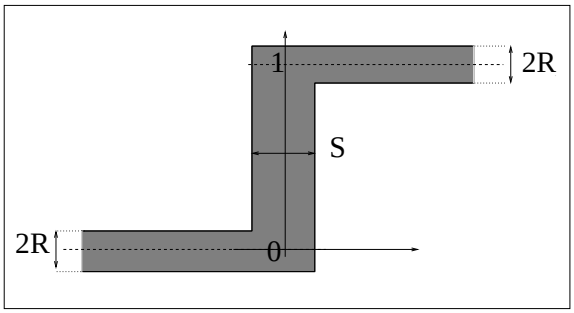

Figure 5.1: $D_{S,R}$ domain

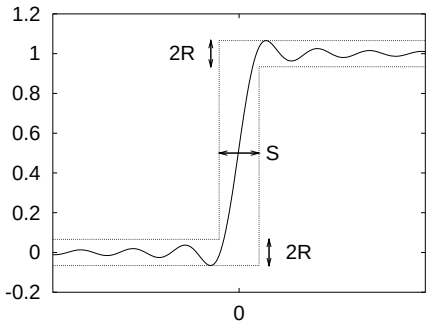

Figure 5.2: Γ_g is included in $D_{S,R}$

except when the Spread-Ringing curve has vertical edges, which never occurs with the filters we consider. An example of the Spread-Ringing curve is shown in Fig.5.3 and Fig.5.4.

This definition of ringing has the drawback that no unique value of S and R are associated to a given filter since, as we mentioned before, it is difficult to distinguish the edge from the ringing near the transition. However, this construction has the advantage to remain very general, since it does not rely on any arbitrary threshold.

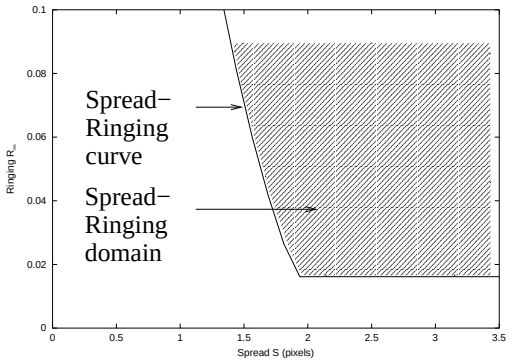

Figure 5.3: The Spread-Ringing curve and the Spread-Ringing domain associated to the filter $(C_\alpha)_W$ with $\alpha = 0.066$.

Definition 5.2 can be generalized to a *family* of filters φ_α (α being in general a real parameter) and still yields a single *Spread-Ringing curve*, as specified in the following definition.

Definition 5.3 *The Spread-Ringing domain associated to a family of filters $(\varphi_\alpha)_{\alpha\in A}$ is*

$$D\left((\varphi_\alpha)_{\alpha\in A}\right) \;=\; \bigcup_{\alpha\in A} D(\varphi_\alpha). \tag{5.2}$$

Its Spread-Ringing curve is the associated boundary.

Remarks:

1. From Definition 5.3, we can construct the Spread-ringing curve associated to each filter φ_α. Consequently, the Spread-ringing curve of a family of filters $(\varphi_\alpha)_{\alpha\in A}$ is

$$r_{(\varphi_\alpha)_{\alpha\in A}}(S)= \min\{R \in (0,+\infty); (S,R) \in D\left((\varphi_\alpha)_{\alpha\in A}\right)\}. \tag{5.3}$$

2. The curve r_φ is decreasing with S. The larger the spread is, the smaller the oscillations, and then the ringing, are likely to be outside the spread domain, because the amplitude of the oscillations decays with the distance to the edge. This curve explains the trade-off between ringing and blur, as no point on r_φ achieves minimum ringing and blur simultaneously. The curve r_φ provides the smallest reachable S by the tested filter φ for a given R value. Conversely, it provides the smallest R associated to a fixed S. The curve $r_{(\varphi_\alpha)}$ provides the smallest reachable S among all tested filters φ_α. The filter, that minimizes S for a given R, is the filter φ_α that preserves the best sharp transitions for this level of noise. An example of the Spread-Ringing curve of the cosine filter family is shown in Fig.5.4. In order to explain the construction of this curve, it also shows some Spread-Ringing curves of four cosine filter with $\alpha = 0.03, 0.038, 0.051, 0.066$, which have worst or same results than the Spread-Ringing curve of the cosine filter family. The comparison of the Spread-Ringing curves of all the filter families studied in this thesis is presented in Section 6.2.

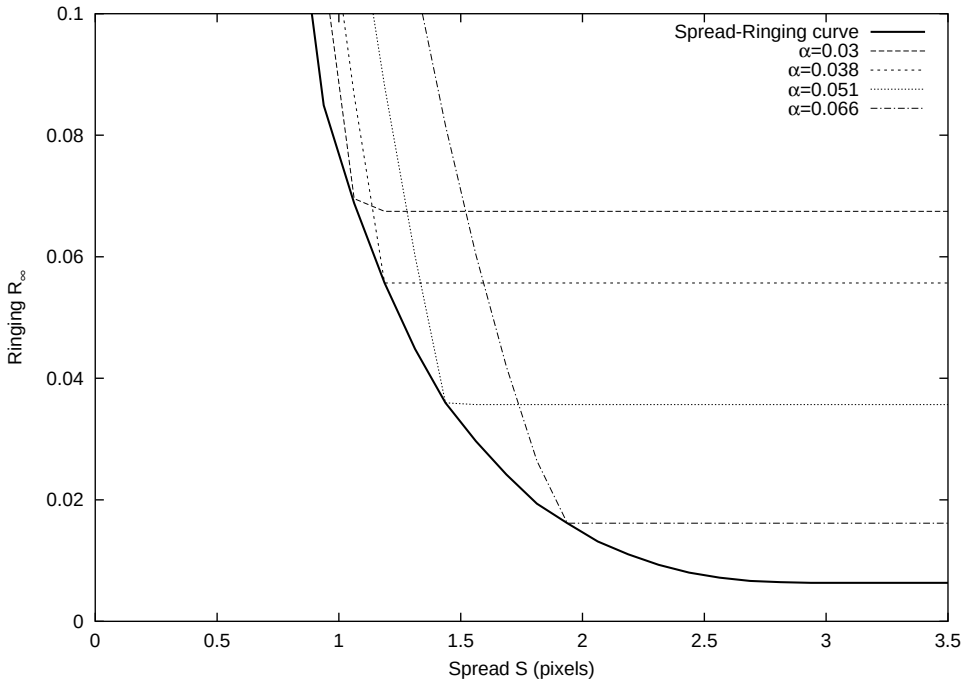

Figure 5.4: The Spread-Ringing curve of the family of $(C_\alpha)_W$ filters is the boundary of the union of the Spread-Ringing domain over all the α, some boundaries of which are plotted for $\alpha = 0.03, 0.038, 0.051, 0.066$.

3. Since the value of the parameter α is not the same for all the couples (S,R) of the Spread-Ringing curve $r_{(\varphi_\alpha)}$, it is interesting to plot the curve of the associated couples (α,R). In

practical applications it gives the values of α that gives the expected value of ringing. Fig.5.5 shows the couples (α, R) for the cosine filter family $(C_\alpha)_W$.

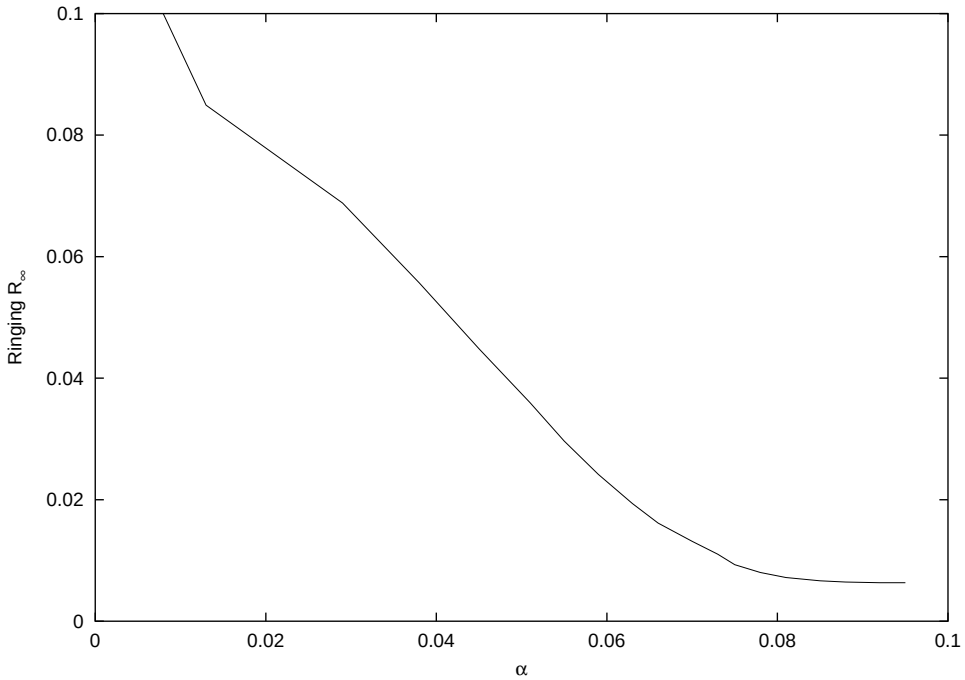

Figure 5.5: The curve of the parameter α associated to the Spread-Ringing curve of the cosine filter $(C_\alpha)_W$ shown in Fig.5.4.

5.2 Other possible measures

This approach to define the ringing has been finalized after realizing that other direct measures of ringing and spread were not satisfactory. Let us describe some of them.

The easy way is to decorrelate the estimation of S and R. For instance, one possibility is to evaluate S with $g'(g^{-1}(\frac{1}{2}))$, the slope of the function $g = \varphi \star H$ at the transition, which is related to the value of $\varphi(g^{-1}(\frac{1}{2}))$. But this definition is not satisfactory in practice because it is too local to the transition center $g^{-1}(\frac{1}{2})$ and does not give the global transition speed from 0 to 1. This measure is adapted to filters φ with spatial unimodal shape, whose maximal value is $\varphi(g^{-1}(\frac{1}{2}))$. But this measure is not satisfactory for the filters with non spatial unimodal shape, because the point $g^{-1}(\frac{1}{2})$ may not have the largest slope and then the spread estimation is corrupted by the local low value of the filter in $g^{-1}(\frac{1}{2})$.

A similar approach is the one proposed by Ladjal: the blur is measured locally around sharp transitions [23]. It is based on the study of the tangent of the inflection point of the transition g. Let us recall the blur definition given by Ladjal and the corresponding figure (Fig.5.6). This method has the same drawback than the previous one since it is localized to the inflection point and does not take into account the behavior far from the edge, which could amplify or reduce the subjective blur.

Definition 5.4 *Let g be a real differentiable function on $\mathbb{R}$, not constant and bounded. The blur*

measure associated to g is defined by

$$F(g) = \frac{\max_{x\in\mathbb{R}} g(x) - \min_{x\in\mathbb{R}} g(x)}{\max_{x\in\mathbb{R}} |g'(x)|}$$

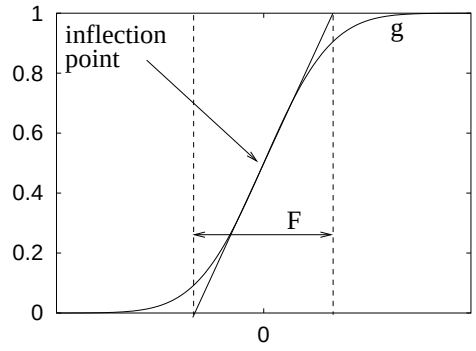

Figure 5.6: Definition of blur proposed by Ladjal: here the blur F is the abscissa spread of the tangent to reach the transition height.

The approach proposed by Marziliano *et al.* [30] also measures the spread of sharp transitions. The start and end positions of the edge are defined as the local extrema locations closest to the edge. However this measure is not adapted to the our case since they did not consider the ringing phenomenon, whose oscillations may change the local extrema locations.

Another possibility to measure S is to consider the value $\inf\{x, g(x) = 1-\gamma\} - \sup\{x, g(x) = \gamma\}$ parameterized with γ, or to compare the spread of the given function g with a parameterized function, the spread of which we can estimate. Both possibilities were rejected as the choice of the parameter γ, the choice of the reference function and the choice of the parameter to measure the distance between g and the reference function are arbitrary.

In order to have a parameter-free definition, here are two possibilities for a joined definition of S and R using the local monotony of g.

1. The first one is to consider for S the value

$$S_1(g) = x^+ - x^- = \arg\max_{x\in\mathbb{R}} g(x) - \arg\min_{x\in\mathbb{R}} g(x)$$

   and the associated ringing value $R_1(g) = \max(|g(x^-)|, |1 - g(x^+)|)$.

2. The second one is based on the upper and lower envelope.

$$g^+(x) = \inf(h(x); h \text{ non decreasing}; h \geq g).$$

$$g^-(x) = \sup(h(x); h \text{ non decreasing}; h \leq g).$$

   The associated spread S_2 is the maximal interval $[x^-, x^+]$ such that $g^-(I) = g^+(I)$. The ringing value is then $R_2(g) = \max(\sup_{x\leq x^-} |g(x)|, \sup_{x\geq x^+} |1 - g(x)|)$.

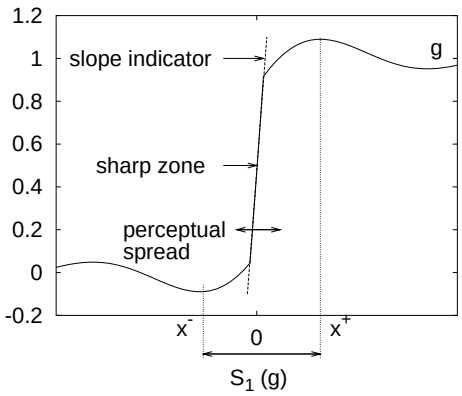

Figure 5.7: Example of function with a perceptual spread smaller than $S_1(g)$.

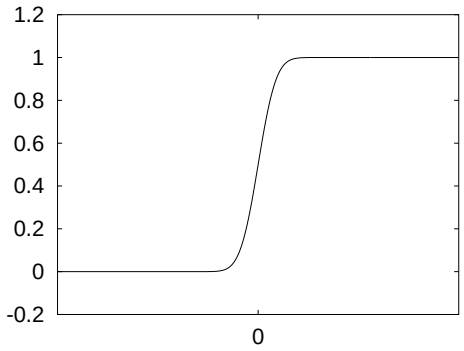

Figure 5.8: Graph of the function $g(x) = \int_{-\infty}^{x} \text{sinc}^2(t)dt$. This increasing function has a perceptual finite spread.

The first possibility is not satisfactory as the transition may look sharper than S (Fig. 5.7). The second one returns an infinite spread value and no ringing ($S_1(g) = +\infty$ and $R = 0$) if g is monotone. This is not coherent with the perceptual spread value (Fig. 5.8). We prefer to tolerate a positive ringing value for monotone functions than an infinite spread value.

The Spread-Ringing curve has the advantage of avoiding this kind of problem. Moreover, it is parameter-free and characterizes the ringing with the L^∞ norm. We chose naturally to control the ringing with the L^∞ norm (rather than with the L^2 norm for example) because our perception of images is more sensitive to large local overshoots than to small oscillations (hidden by image noise or textures) spread on a large domain. However experimental results (see Chapter 9) showed that this norm has perceptual drawbacks. At equivalent L^∞ norm, the eye detects the ringing where long oscillations are. So it is also interesting to define the *Spread-Ringing curve* for other norms, such as the L^2 or L^1 norms.

5.3 L^2 and L^1 norms to measure the ringing

In the previous section, the ringing was measured with the L^∞ norm. We shall call SR_∞ the associated *Spread-Ringing curve*. Let us now define SR_2 and SR_1 which are the *Spread-Ringing curve* built with the L^2 and L^1 norms, respectively.

Definition 5.5 *The Spread-Ringing curve SR_2 associated to a filter $\varphi \in B_W$ is*

$$SR_2(\varphi) = \left\{ (S, R_2) \in (0, +\infty) \text{ where } R_2 = \int_{-\infty}^{-S} (f(x) - H(x))^2 \, dx \; + \; \int_{+S}^{+\infty} (f(x) - H(x))^2 \, dx \right\}. \tag{5.4}$$

Definition 5.6 *The Spread-Ringing curve SR_1 associated to a filter $\varphi \in B_W$ is*

$$SR_1(\varphi) = \left\{ (S, R_1) \in (0, +\infty) \text{ where } R_1 = \int_{-\infty}^{-S} |f(x) - H(x)| \, dx \; + \; \int_{+S}^{+\infty} |f(x) - H(x)| \, dx \right\}. \tag{5.5}$$

Now that we have defined the Spread-Ringing measures, we shall propose three algorithms, associated to the three previously defined Spread-Ringing curves (SR_∞, SR_2, SR_1) to design the three corresponding optimal filters.

Chapter 6

Optimal filters for the Spread-Ringing curves

6.1 Definition and construction

Optimal filters for the SR_∞ curve

We now build a family of band-limited filters (φ_S), called *SR filters*, having the best possible *Spread-ringing curve*. These filters have minimal ringing R for a fixed spread S, or equivalently, minimal spread S for a fixed ringing R. The algorithm proposed here sets S while minimizing R. We recall here the two constraints that should be satisfied:

1. the filter is band-limited ($\varphi \in B_W$),
2. the signal $\varphi \star H$ minimizes R when S is set.

The design of the filter is based on the Alternative Projection Onto Convex Sets (POCS) [19]. This method is commonly used for image restoration [59]. The filter contains the two latter desirable properties by alternatively projecting onto the convex constraint sets. Let us now explain why the two constraint sets are convex:

1. the first constraint is related to the band-limitation property of the filter. The convex signal sets include the space of band-limited signals [19], so the sets of band-limited signals are convex sets.
2. the second constraint requires the projection of the graph of the function $f = \varphi \star H$ in the domain $D_{S,R}$. The set of functions

$$A = \{\ f \mid \Gamma_f \subset D_{S,R}\ \}$$

is a convex set because for every $f \in A$ and every $g \in A$, the function $\alpha \cdot f + (1-\alpha) \cdot g \in A$ for all $\alpha \in [0,1]$. Indeed from Definition 5.1, if $f \in A$, then for $x \leq -\frac{S}{2}$, $f(x) \in [-R,R]$. Moreover if $g \in A$, then $g(x) \in [-R,R]$ too. By linearity, we obtain $\alpha \cdot f(x) + (1-\alpha) \cdot g(x) \in [-R,R]$. The property is preserved for all $x \leq -\frac{S}{2}$. The same reasoning can be applied for $|x| \leq \frac{S}{2}$ and $x \geq \frac{S}{2}$. So the property is satisfied for $x \in \mathbb{R}$.

For convexity reasons, this family exists and is unique. For each S, φ_S can be computed by the following iterative algorithm:

Algorithm 1 (SR_∞ optimal filter)

set $\varphi = \delta_0$ (Dirac)
assign a large value to R
repeat
  set $\varphi_S = \varphi$
  set $N = 1$
  repeat
    force $\Gamma_{\varphi \star H} \subset D_{S,R}$ by thresholding
    force $\varphi \in B_W$, that is $\hat{\varphi}(\xi) = 0$ for $\xi \notin [-W, W]$
    set $N = N + 1$
  until *convergence test* or $N > N_{max}$
  reduce R
until $N > N_{max}$

The thresholding of g, where $g = \varphi \star H$, produces g' such that $\Gamma_{g'} \subset D_{S,R}$ and $||g - g'||_2$ is minimum. This is achieved by projecting Γ_g onto $D_{S,R}$. The convergence test is satisfied when the two forcing steps have small enough effects on φ, that is, when the first forcing step changes φ by less than ε_1 (according to L^∞ norm) and the second forcing step changes φ by less than ε_2 (according to the L^2 norm). In practice, we checked that convergence was undoubtedly attained with $N_{\max} = 10000$ and $\varepsilon_1 = \varepsilon_2 = 0.001$.

When looking at SR filters (obtained with this algorithm), we noticed that their Fourier transform was real symmetric (as expected), but not unimodal (that is, not increasing on $\mathbb{R}^-$ and decreasing on $\mathbb{R}^+$), due to large weights on the frequencies near the cut-off frequency W. This phenomenon, due to the fact that the ringing is controlled through a L^∞ norm, can be undesired in some applications (since for example, natural images generally have unimodal spectra). It can be avoided by building *unimodal SR filters*, that is, whose Fourier spectrum is non decreasing on $\mathbb{R}^-$ and non increasing on $\mathbb{R}^+$, obtained by adding a third forcing step in the algorithm (between the $D_{S,R}$ forcing step and the B_W one) which changes $\hat{\varphi}$ into its L^2 unimodal regression. This is a isotonic regression problem, also called monotonic regression in the literature. It involves finding the least square fit y to a vector x with weight vector w subject to monotonicity constraints. A standard algorithm for isotonic regression that find a piecewise constant solution is the pool adjacent violators (PAV) algorithm [3].

Algorithm 1bis (unimodal SR_∞ optimal filter)

set $\varphi = \delta_0$ (Dirac)
assign a large value to R
repeat
  set $\varphi_S = \varphi$
  set $N = 1$
  repeat
    force $\Gamma_{\varphi \star H} \subset D_{S,R}$ by thresholding
    force $\varphi \in B_W$, that is $\hat{\varphi}(\xi) = 0$ for $\xi \notin [-W, W]$
    force unimodality of $\hat{\varphi}$ by isotonic regression
    set $N = N + 1$
  until *convergence test* or $N > N_{max}$
  reduce R
until $N > N_{max}$

Some results obtained with Algorithm 1 and 1bis are illustrated in Fig.6.1 and 6.2. The signal φ has $N = 1024$ samples and the frequency cut-off corresponds to a reduction by a factor 16, i.e. $W = N/2 \cdot 1/16 = 32$. The tested spread values are $S = 1, 1.5, 2, 2.5$ pixels because we consider that transitions larger than 2.5 pixels are very blurry.
Remarks:

- The value of W is arbitrary since different values of W simply mean different scales.
- In the algorithm, the projection onto B_W is performed after the thresholding, because the constraint of band-limitation is more important than the ringing performance of the filter. After convergence, one has to be sure the filter is in B_W to avoid aliasing. The unimodality constraint has no influence on the filter's bandpass once it is band-limited.

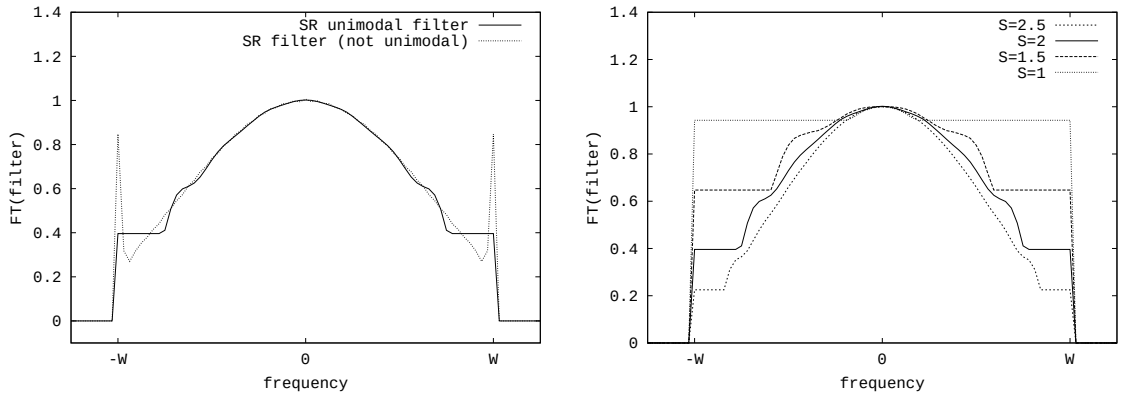

(a) (b)

Figure 6.1: Some SR filters in Fourier domain (a) with and without unimodal constraint for $S = 2$ pixels (b) with unimodal constraint for different S. Note that the filter without unimodal constraint has an unnatural shape.

Optimal filters for the SR_2 and SR_1 curve

The optimal filter for the SR_∞ curve is calculated by constraining the spread value S while minimizing the ringing R. A reverse approach could have been used: setting R while minimizing S. For the L^∞ norm, both approaches are equivalent because the ringing is related to the extremal values of the signal, which are easily detected with the adopted geometrical definition of the ringing. For the L^2 and L^1 norms, the "box" approach is only adapted to measure the spread and not the ringing. Consequently the design of the optimal filters for the SR_2 and SR_1 curves is done by setting the spread while minimizing the ringing. We used a gradient descent with a small step size ε.

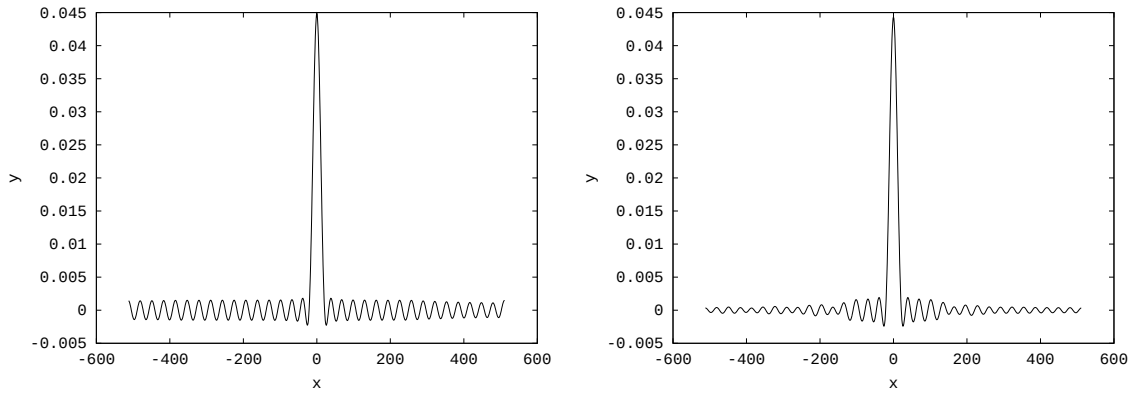

(a) (b)

Figure 6.2: Filters of Fig.6.1-(a): $S = 2$ pixels. (a) SR filter (not unimodal) (b) SR unimodal filter. Oscillations decay faster with the SR unimodal filter.

Algorithm 2 (SR_2 optimal filter)

set $\varphi = \delta_0$ (Dirac)
fix S
fix ε
repeat
  minimize the L^2 error

$$\forall x \in \mathbb{R}, \quad \varphi \star H(x) = \begin{cases} \varphi \star H(x) - \varepsilon(\varphi \star H(x) - H(x)) & \text{for } |x| \geq S \\ \varphi \star H(x) & \text{otherwise} \end{cases}$$

  force $\varphi \in B_W$, that is $\hat{\varphi}(\xi) = 0$ for $\xi \notin [-W, W]$
until convergence

The design of the optimal filters for the SR_1 can be obtained with an algorithm similar to the SR_2 case, except that it minimizes the L^1 error. As the SR_1 curves did not give a clearer classification than the SR_2 curves we did not proceed further: we did not compute the associated optimal filter but the SR_1 classification for the classical filters is given in Fig.6.12. The optimal filters for the SR_2 curve are shown in Fig.6.3. Note that the Fourier transform of φ is already unimodal. This is the reason why we did not add a monotonicity constraint as in Algorithm 1bis.

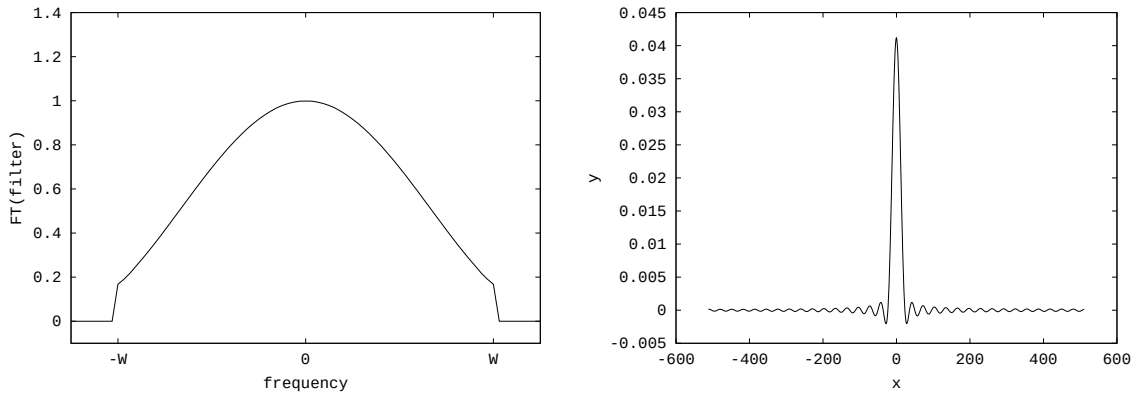

(a) (b)

Figure 6.3: SR_2 optimal filters φ for $S = 2$ pixels (a) in Fourier domain (b) in space domain.

R_∞	SR_∞ opt. fil.	SR_∞ unimod. opt. fil.	Gaussian	prolate	cos	T_α	sinc
S=1	0.0555	0.0699	**0.0766**	0.0786	0.0769	0.0772	0.0892
S=1.5	0.0212	0.0247	0.0314	0.0339	0.0328	**0.0289**	0.0892
S=2	0.0086	0.0096	**0.0118**	0.0155	0.0146	0.0160	0.0892
S=2.5	0.0036	0.0039	0.0070	**0.0062**	0.0076	0.0115	0.0892

Table 6.5: R_∞ ringing table for $S = 1$, 1.5, 2 and 2.5 pixels. A smaller ringing value indicates that the filter adds less noise in the filtered image. "opt. fil." stands for "optimal filter".

6.2 Comparison with the Spread-Ringing curves of classical filters

6.2.1 SR_∞ curves

One of the main contribution of this thesis is to give a blur/ringing measure to compare different filters. Fig. 6.4 shows the *Spread-Ringing curves* of the prolate, Gaussian and *sinc* filter. The *Spread-Ringing curves* of the Cosine and Frequency truncated trapezoid are not displayed for the sake of clarity, but Table 6.5 shows some characteristics of all the filters.

We observe that for any S, the Shannon filter have the highest ringing value. This is not surprising as this filter is highly discontinuous in the Fourier domain. Note that the ringing value is coherent with Bôcher theorem (Theorem 4.1). We recall from Property 4.3-iii that a Heaviside function has a ringing value of $\frac{Si(\pi)}{\pi} - \frac{1}{2} \simeq 0.0891902$.

We observe that the band-limited Gaussian filter yields better results than the prolate: for small spreads, i.e. $S \leq 2.5$ pixels, the ringing value with the Gaussian is smaller. If we consider that a transition with a spread larger than 2.5 pixels is very blurry, then the band-limited Gaussian should be preferred to the prolate in practice. On the same interval, the cosine and the prolate gives very similar results. This unexpected result is interesting because the cosine has an analytic expression, unlike the prolate, which is easy to use in practice and allows some mathematical calculus thanks to its continuity

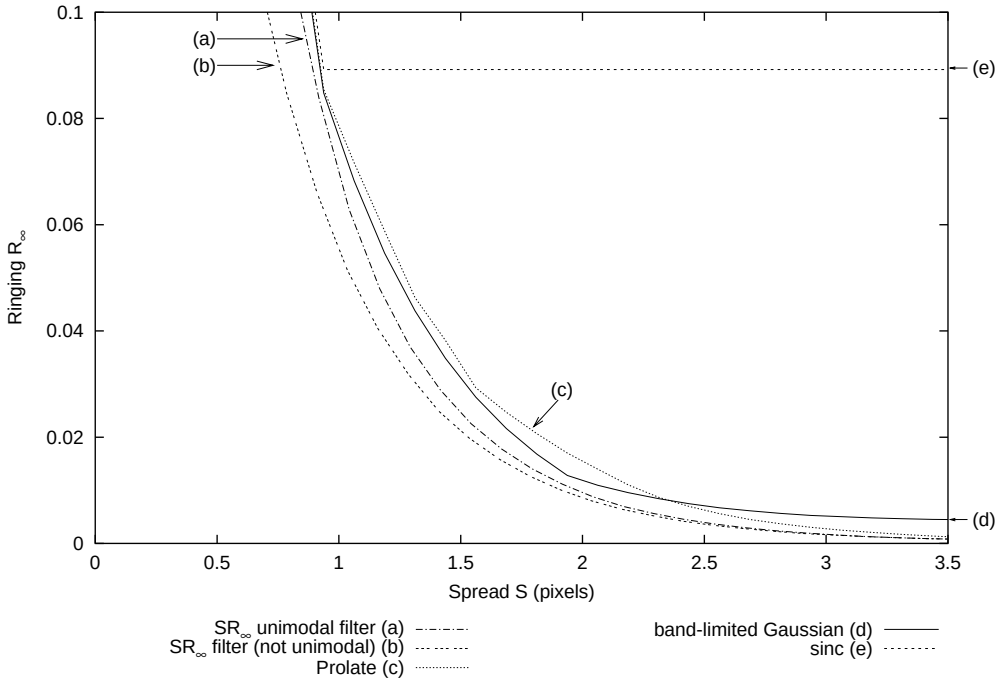

Figure 6.4: SR_∞ *Spread-Ringing curves*. The unimodal and not unimodal SR_∞ filters perform better than the other tested filters.

property.

However for larger spreads, the cosine is no longer optimal since it adds more ringing than the prolate. The trapezoid filter in the Fourier domain T_α is the only tested filter that performs better than the band-limited Gaussian for small spread values $S \in [1.1, 1.7]$: this filter produces a slightly less noisy image than a band-limited Gaussian, however it performs very badly for other spreads (Fig.6.6).

As expected, the SR_∞ filter shows optimal results, which confirms its optimality. It proposes the smallest ringing measure. Of course the SR_∞ unimodal filter shows worst results than the SR_∞ filter since it is more constrained. For small S, this difference gets magnified. The unimodal constraint penalizes the ringing performance as the spread of the resulting function is larger for equivalent R.

For practical applications, we shall give now the (α, R) curves associated to two commonly used filters: the band-limited Gaussian family G_α (Fig.6.7) and the prolate family P_α (Fig.6.8). The curve of the cosine family C_α has already been given in Fig.5.5. As expected, the band-limitation in $[-W, W]$ with the filter G_α has better results for small values of α since the large values of α correspond to sharp transitions, which are more affected by the band-limitation in $[-W, W]$ (i.e. adds more ringing) than a smooth transition. We recall here that for the prolate filter P_α, the parameter α does not measure the sharpness of the transition as for G_α, but it gives the size of the spatial support. A small spatial support is a bigger constraint than a large one. This is the reason why large α introduce less ringing. Note that the spatial support is discretized so that the values of α are integer. In this experiment, the tested signal P_α has size 1024 and the tested values of α go from 3 to 150 which represent a spatial spread support of $[3 \cdot 2 + 1, 150 \cdot 2 + 1] = [7, 301]$ samples.

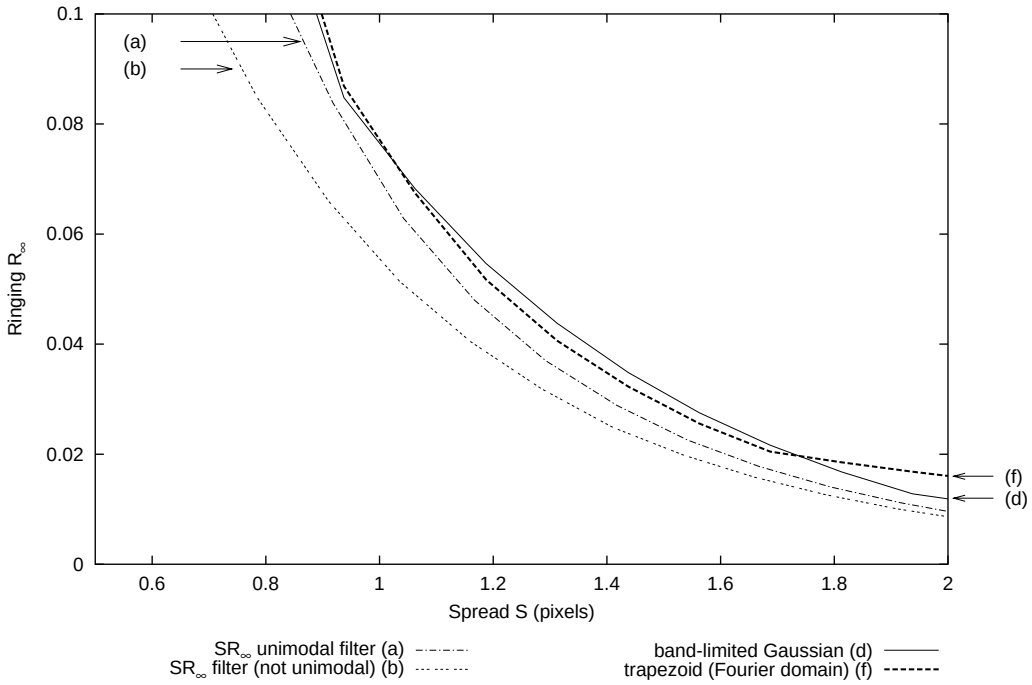

Figure 6.6: SR_∞ *Spread-Ringing curves*. The trapezoid filter in the Fourier domain performs better than the band-limited Gaussian for small spread values $S \in [1.1, 1.7]$.

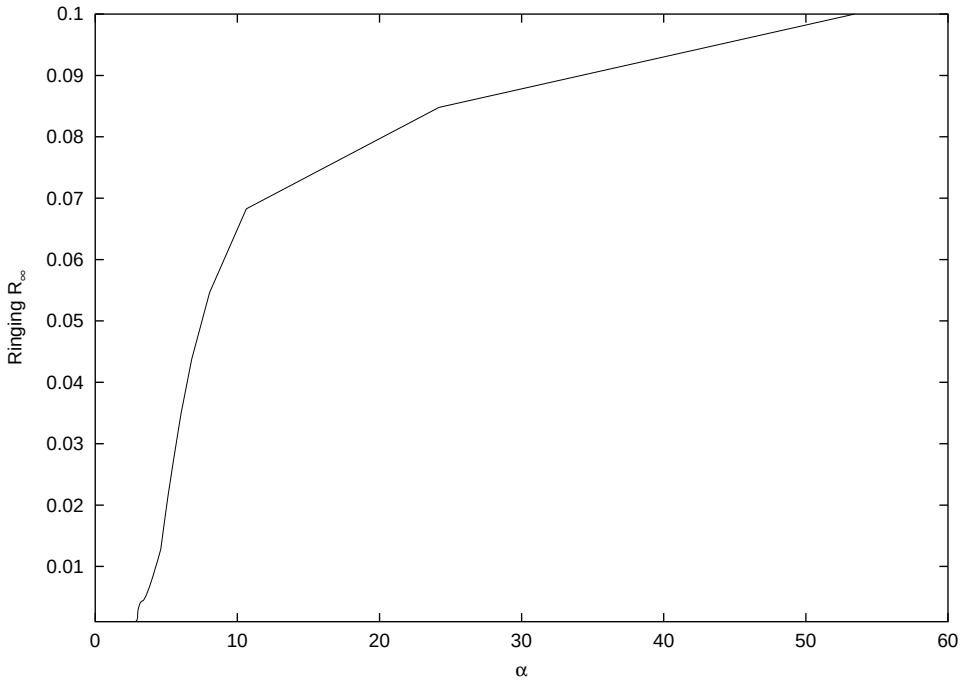

Figure 6.7: Curve of the parameter α associated to the Spread-Ringing curve of the Gaussian G_α.

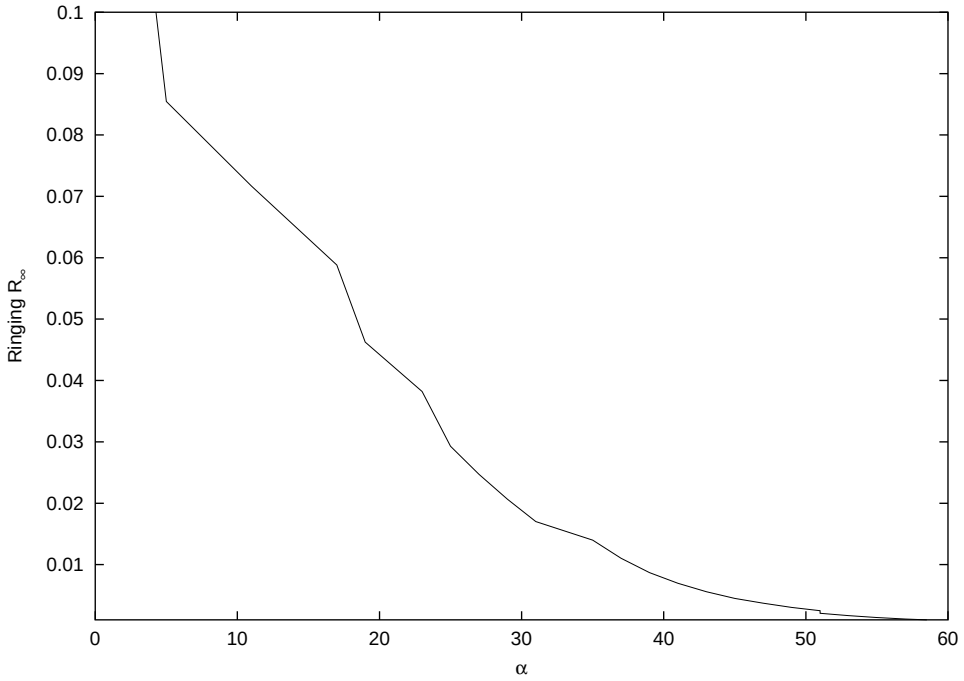

Figure 6.8: Curve of the parameter α associated to the Spread-Ringing curve of the Prolate filter P_α.

R_2	SR_2 opt. fil.	SR_∞ opt. fil.	SR_∞ unimod. opt. fil.	Gaussian	prolate	cos	T_α	sinc
S=1	0.0519	0.0817	0.0591	0.0552	**0.0551**	**0.0551**	0.0600	0.1162
S=1.5	0.0115	0.0202	0.0143	0.0120	**0.0117**	**0.0116**	0.0157	0.1093
S=2	0.0023	0.0046	0.0033	0.0030	**0.0024**	**0.0024**	0.0064	0.0873
S=2.5	0.0004	0.0009	0.0007	0.0012	**0.0005**	**0.0005**	0.0046	0.0594

Table 6.10: Ringing table for $S = 1$, 1.5, 2 and 2.5 pixels.

6.2.2 SR_2 curves

Fig.6.9 shows the SR_2 curves and Table 6.10 gives some values for specific spread. As expected the SR_2 filter gives the best results, i.e. the smallest R_2 for any fixed S.

The prolate and cosine filter have similar ringing values for small spread values, i.e. for $S \in [0, 2.5]$. This confirms the previous results that a cosine filter might be a judicious filter choice since its SR_2 curve is very close to the optimal one. However for larger spread values $S > 2.5$, the prolate should be used instead of the cosine, because the prolate performs better in that case.

Conversely to the conclusion for the SR_∞ curve, the SR_∞ unimodal optimal filter introduces less ringing R_2 than the not unimodal one. The faster decay of the oscillations of the unimodal filter reduces R_2, whereas this decay was no help for R_∞ as only the maximum value did count.

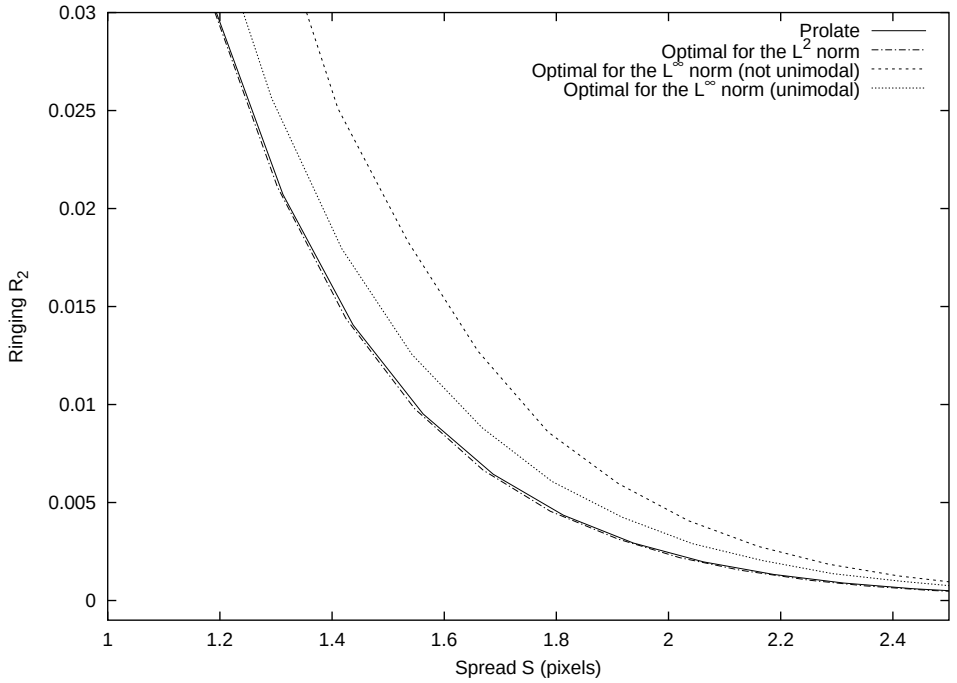

Figure 6.9: SR_2 *Spread-Ringing curves*. The SR_2 filter performs better than the other tested filters.

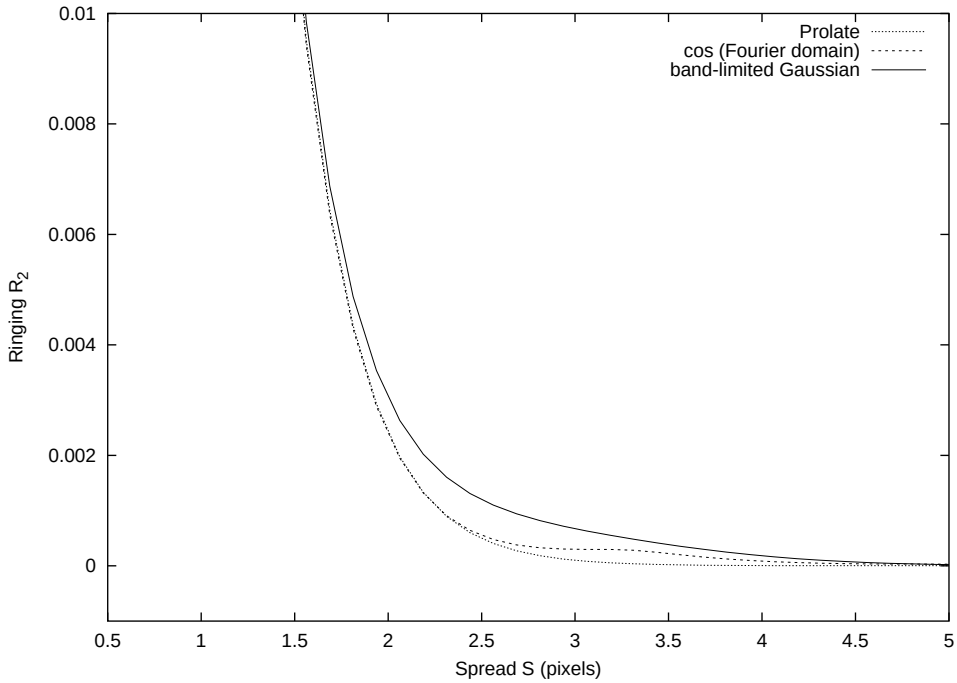

Figure 6.11: SR_2 *Spread-Ringing curves*. Comparison of the cosine and prolate filters.

6.2.3 SR_1 curves

The good results of the cosine filter are validated by the SR_1 curves (Fig.6.12). A zoom is given in Fig.6.13.

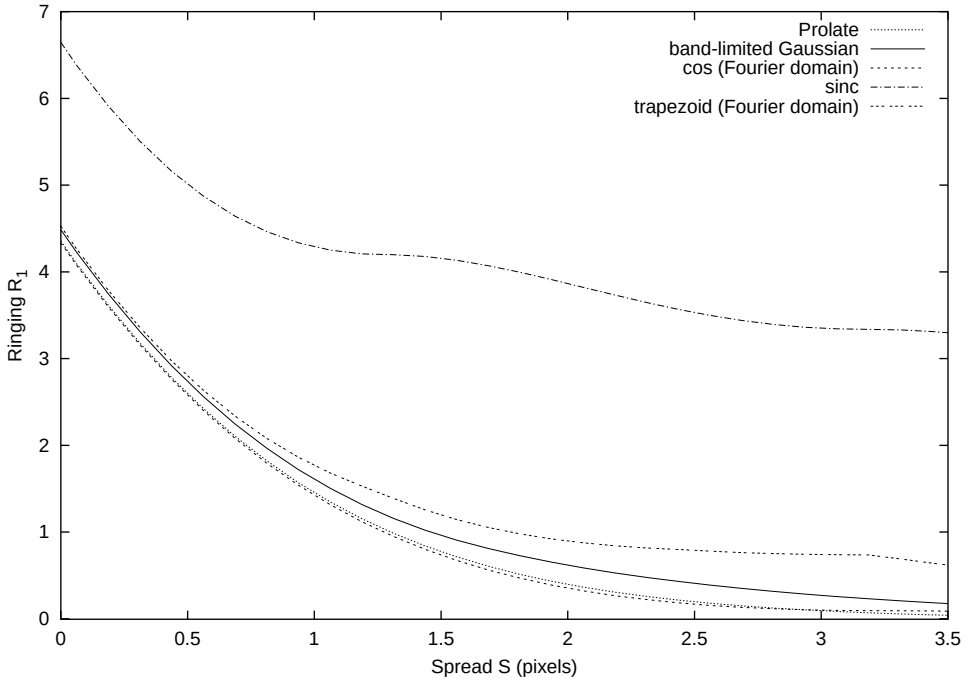

Figure 6.12: SR_1 *Spread-Ringing curves*. For small spread, the cosine filter offers a Spread-Ringing trade-off similar to the one of the prolate.

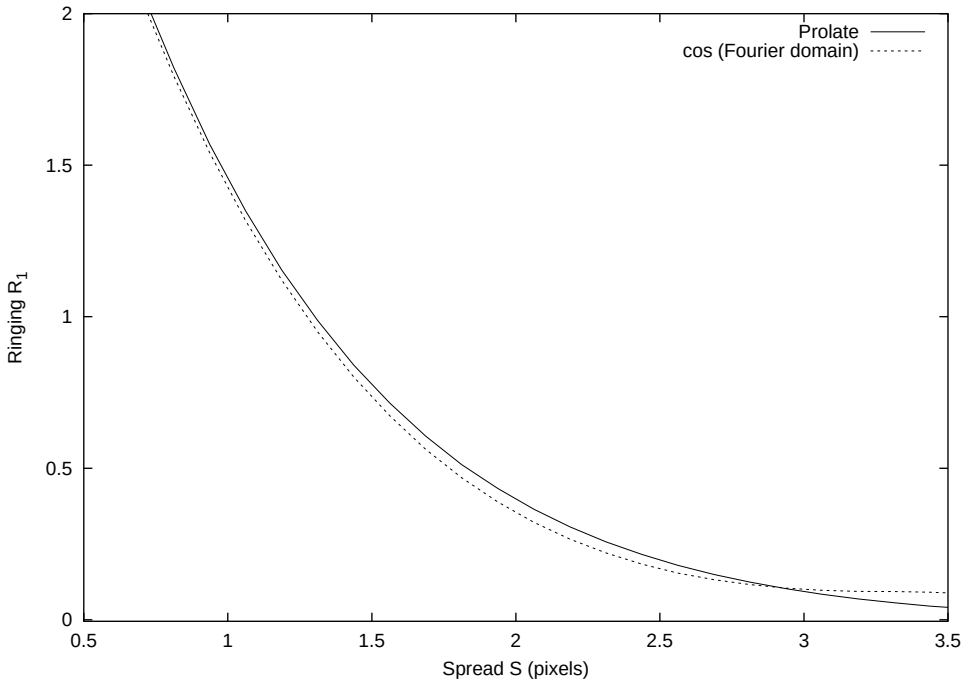

Figure 6.13: SR_1 *Spread-Ringing curves*. Comparison of the cosine and prolate filters.

Chapter 7

Filter generalization to the 2D

There are several ways to generalize 1D filters to 2D. The most common one is to use the separable convolution in both directions. This is how we reduced the images in the numerical experiments (Chapter 9). Another possibility is to determine the 2D filter directly from the 1D filter. We note k the 1D filter and l its generalization to two dimensions. The aim of this chapter is to determine the 2D filter l from the known filter k, such as the filter described in the previous chapters. This approach requires some additional hypothesis on l. First we shall consider an additional isotropic constraint on the spatial behavior of l in order to have an identical filter response in all directions. In this chapter the isotropic filters are also called radial shaped filters. Second, the result of the convolution of the filter k and the Heaviside function (1D step function), which is $k \star H$, is generalized to two dimensions by considering the result of the convolution of the filter l and the 2D step function M_{2D}.

Definition 7.1 *The step function in 2D is defined by*

$$\forall (x,y) \in \mathbb{R}^2, \quad M_{2D}(x,y) = \begin{cases} 1 & \text{for } x \geq 0 \\ 0 & \text{for } x < 0 \end{cases} \tag{7.1}$$

The associated constraint is that the result in one dimension $k \star H$ should be equal to any line y of the result in two dimensions $l \star M_{2D}(:,y)$. In practice, we use the following equivalent constraint in two dimensions:

$$\forall (x,y) \in \mathbb{R}^2, \quad \mathrm{M}_{2D} \star l(x,y) = (k \star H) \otimes \mathbb{1}_{\mathbb{R}}(x,y) \tag{7.2}$$

where $\otimes$ denotes the tensor product.

In the first section, we present some mathematical results obtained on the Fourier transform of those radial shaped filters. In the second section, we design the filter l from a given filter k.

7.1 Radial shaped filter's Fourier transform property

In this part, we use another definition of the Fourier transform which is equivalent to the one given in Part I because we write now the transform in terms of oscillation frequency (u,v) instead of the angular frequency $(\xi_x, \xi_y) = (2\pi u, 2\pi v)$. This definition is more convenient than the one given at the first place because the computations have a simpler form. In this section, we shall prove that the Fourier transform of a radial function can be written with the Hankel function of its associated polar expression. Let us first recall the considered Fourier transform and the Hankel transform pairs.

Let $f : \mathbb{R} \times \mathbb{R} \to \mathbb{R}$ be a function and F its Fourier transform

$$F(u,v) = \int_{-\infty}^{\infty} \int_{-\infty}^{\infty} f(x,y) e^{-2\pi i(ux+vy)} dx\, dy \tag{7.3}$$

with $u \in \mathbb{R}$ and $v \in \mathbb{R}$ the oscillation frequencies associated to directions x and y. We note $\mathcal{H}$ the zeroth order Hankel transform. By definition, the Hankel transform pairs are

$$\mathcal{H}[f_{pol}](\rho) = 2\pi \int_0^{\infty} f_{pol}(r) \cdot J_0(2\pi\rho r)\ r\ dr$$

$$f_{pol}(r) = 2\pi \int_0^{\infty} \mathcal{H}[f_{pol}](\rho) \cdot J_0(2\pi\rho r)\ \rho\ d\rho$$

where J_0 is the zeroth order Bessel function of the first kind defined by

$$J_0(r) = \frac{1}{\pi} \int_0^{\pi} \cos(-r \sin\theta)\, d\theta\,.$$

Property 7.2 (Fourier transform of a radial function) *If f is a radial function, $f(x,y) = f_{pol}(r)$, with $r = \sqrt{x^2+y^2}$ and f_{pol} the associated polar function*

$$\begin{array}{rccc} f_{pol}: & \mathbb{R}^+ & \to & \mathbb{R} \\ & r & \mapsto & f_{pol}(r) \end{array}$$

then F is radial and defined with the Hankel function ($\mathcal{H}$):

$$\mathbf{F}(\mathbf{u},\mathbf{v}) = \mathbf{C}[\mathbf{F_{pol}}(\rho)] = \mathbf{C}[\mathcal{H}[\mathbf{f_{pol}}](\rho)]$$

where $\rho = \sqrt{u^2+v^2}$ and the transformation

$$C^{-1}: \quad f(x,y) \quad \mapsto \quad f_{pol}(r).$$

Proof: We introduce the polar coordinates defined

- in the space domain by $x = r\cos(\theta)$, $y = r\sin(\theta)$
- in the Fourier domain by $u = \rho\cos(\varphi)$, $v = \rho\sin(\varphi)$.

Let note $\tilde{F}$ the expression of F in polar coordinates

$$\begin{array}{rccc} \tilde{F}: & \mathbb{R}\times\mathbb{R} & \to & \mathbb{R} \\ & (\rho,\varphi) & \mapsto & \tilde{F}(\rho,\varphi) \end{array}$$

and P the transformation from any function $\tilde{g}(\rho,\varphi)$ in polar coordinates to its expression $g(u,v)$ in Cartesian coordinates

$$\begin{array}{rccc} P: & \mathbb{R} & \to & \mathbb{R} \\ & \tilde{g}(\rho,\varphi) & \mapsto & g(u,v). \end{array}$$

In polar coordinates, (7.3) becomes

$$F(u,v) = P[\tilde{F}(\rho,\varphi)] \tag{7.4}$$

with

$$\tilde{F}(\rho,\varphi) = \int_0^\infty \int_0^{2\pi} \tilde{f}(r,\theta) e^{-2\pi i r\rho(\cos(\varphi)\cos(\theta)+\sin(\varphi)\sin(\theta))}\, r\, dr\, d\theta. \tag{7.5}$$

If f has radial shape, then $\tilde{f}(r,\theta) = f_{pol}(r)$.

$$\begin{aligned}\tilde{F}(\rho,\varphi) &= \int_0^\infty \int_0^{2\pi} f_{pol}(r) e^{-2\pi i r\rho(\cos(\theta-\varphi))}\, r\, dr\, d\theta \\ &= \int_0^\infty \int_{-\varphi}^{2\pi-\varphi} f_{pol}(r) e^{-2\pi i r\rho(\cos(\theta))}\, r\, dr\, d\theta \\ &= \int_0^\infty \int_0^{2\pi} f_{pol}(r) e^{-2\pi i r\rho\cos(\theta)}\, r\, dr\, d\theta\end{aligned}$$

as the cosine function is 2π-periodic. Hence, $\forall\varphi$

$$\begin{aligned}\tilde{F}(\rho,\varphi) &= C^{-1}[F(u,v)] = F_{\mathsf{pol}}(\rho) \\ &= \int_0^\infty f_{pol}(r)\left[\int_0^{2\pi} e^{-2\pi i r\rho\cos(\theta)} d\theta\right] r\, dr \\ &= 2\pi \int_0^\infty f_{pol}(r) J_0(2\pi\rho r)\, r\, dr \\ &= \mathcal{H}[f_{\mathsf{pol}}](\rho)\end{aligned}$$

This result shows that $\tilde{F}(\rho,\varphi)$ is independent of φ. □

7.2 Application to 2D radial filter design

In this section, we shall use Property 7.2 to design the desired 2D radial filter l from the expression of the 1D filter k. It is explicitly given in Property 7.3.

Property 7.3 *Let k be the known 1D filter and K its Fourier transform. Let l be the desired 2D radial filter: $l(x,y) = l_{pol}(r)$ satisfying (7.2). The filter is obtained by applying the inverse Hankel Transform on K.*

$$\boxed{l_{pol}(r) = \mathcal{H}^{-1}[K](r)} \tag{7.6}$$

Proof: The constraint on both l and k is (7.2), that is

$$\forall (x,y) \in \mathbb{R}^2, \quad \mathsf{M}_{2D} \star l(x,y) = (k \star H) \otimes \mathbb{1}_{\mathbb{R}}(x,y)\,.$$

Since M_{2D} is the 2D step function and H the 1D step function, (7.2) can be written

$$\forall (x,y) \in \mathbb{R}^2, \quad \mathbb{1}_{\mathbb{R}^+\times\mathbb{R}} \star l(x,y) = (k \star \mathbb{1}_{\mathbb{R}^+}) \otimes \mathbb{1}_{\mathbb{R}}(x,y)\,.$$

Taking Fourier Transform (FT) on both sides yields

$$\forall (u,v) \in \mathbb{R}^2, FT(\mathbb{1}_{\mathbb{R}^+\times\mathbb{R}} \star l)(u,v) = FT((k \star \mathbb{1}_{\mathbb{R}^+}) \otimes \mathbb{1}_{\mathbb{R}})(u,v)\,. \tag{7.7}$$

Thanks to Fourier Transform's properties,

$$\begin{aligned}(7.7) \quad &\Leftrightarrow \quad \forall (u,v) \in \mathbb{R}^2, FT(\mathbb{1}_{\mathbb{R}^+\times\mathbb{R}})(u,v) \cdot \quad L(u,v) = FT((k \star \mathbb{1}_{\mathbb{R}^+}) \otimes \mathbb{1}_{\mathbb{R}})(u,v) \\ &\Leftrightarrow \quad \forall (u,v) \in \mathbb{R}^2, \quad L(u,v) = \frac{FT((k \star \mathbb{1}_{\mathbb{R}^+}) \otimes \mathbb{1}_{\mathbb{R}})(u,v)}{FT(\mathbb{1}_{\mathbb{R}^+\times\mathbb{R}})(u,v)}\,. \end{aligned} \tag{7.8}$$

From Property 7.2, we deduce that the Fourier Transform L of l is radial and we have

$$L(u,v) = C\left[\mathcal{H}\left[l_{\mathsf{pol}}\right](\rho)\right]. \tag{7.9}$$

Equation (7.8) only depends on the parameter u because

$$FT(\mathbb{1}_{\mathbb{R}^+\times\mathbb{R}})(u,v) = \frac{1}{i}\mathrm{PV}\ \frac{1}{u} + \pi\delta(\xi)$$

$$FT((k \star \mathbb{1}_{\mathbb{R}^+}) \otimes \mathbb{1}_{\mathbb{R}})(u,v) = (\frac{1}{i}\mathrm{PV}\ \frac{1}{u}\ +\ \pi\delta(\xi))\ \cdot\ K(u)$$

where K is the Fourier Transform of the 1D kernel k. Hence, (7.8) becomes

$$\forall (u,v) \in \mathbb{R}^2,\ \ L(u,v) = K(u)\,. \tag{7.10}$$

The right term in (7.10) is independent of v then one can choose $v = 0$. It simplifies equations by setting $u = \rho$ and then (7.9) yields

$$L(u,0) = C\left[l_{\mathsf{pol}}(u)\right]\ = C\left[\,\mathcal{H}\left[l_{\mathsf{pol}}\right](u)\,\right].$$

Finally

$$l_{\mathsf{pol}}(u) = \mathcal{H}\left[l_{\mathsf{pol}}\right](u)$$

and (7.10) is now

$$\forall u \in \mathbb{R},\ \ \mathcal{H}\left[l_{\mathsf{pol}}\right](u) = K(u).$$

7.3 Numerical computations

In this section, a 2D kernel l is computed from a known kernel k by using Property 7.3. Moreover we check if k and the obtained filter l satisfy the constraint (7.2).

Fig.7.1 and 7.2 show the chosen 1D filter k (it is a prolate of size 512) and the obtained 2D filter l, respectively. The validation of the constraint (7.2) is done in Fig.7.3. In this last experiment, the transition is from 0 to 100 for visualization reasons and not from 0 to 1 as it is for both H and M_{2D}. The comparison of one line of the image $\mathsf{M}_{2D} \star l$ with the signal $k \star H$ shows very similar results. Note that theoretical expression of l given by Property 7.3 suppose that H and M_{2D} have infinite support, which is not possible in the experiments.

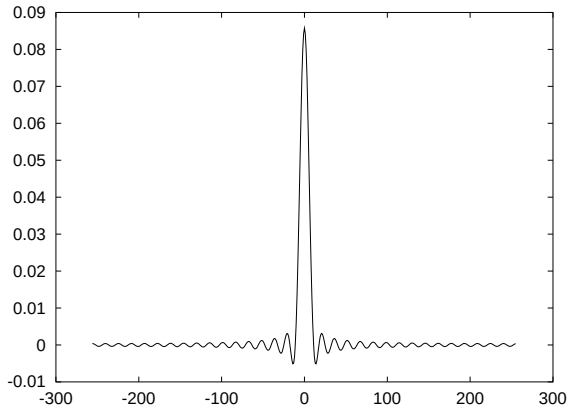

Figure 7.1: Example of a 1D prolate kernel in the space domain.

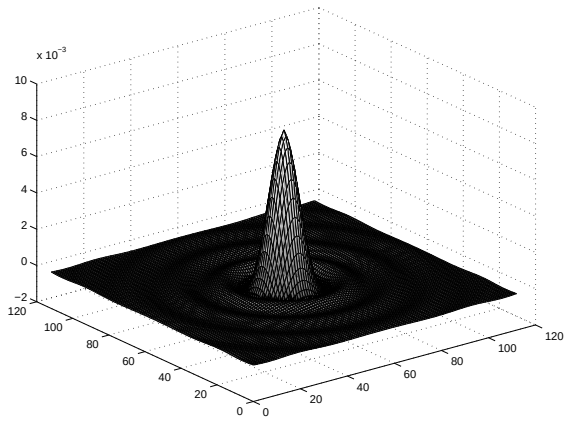

Figure 7.2: The associated 2D prolate kernel in the space domain obtained with Property 7.3.

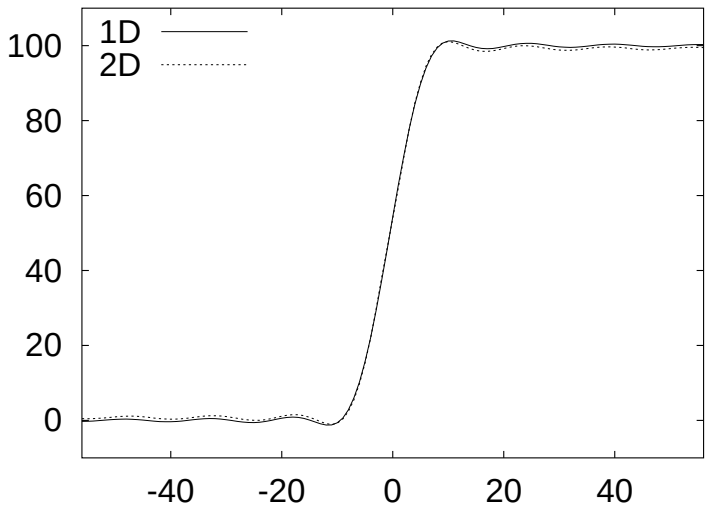

Figure 7.3: Comparison of $k \star H$ (1D) and a line of $\mathrm{M}_{2D} \star l$ (2D). Both signals are very similar as imposed by the constraint (7.2) of Property 7.3.

Chapter 8

Application to a real optical system

8.1 Description of the system

In this chapter, we study one of the satellite optical system launched by the CNES. The two contributions we will consider here are the optical and the physical sampling device. The optical system is an isotropic low-pass filter. The sampling system is a CCD array which has a regular sampling grid. There are possible other distortions due for example to the motion blur of the satellite, but we will not take them into account. We keep the notations of the previous chapter and we set the frequency cut-off $W = \frac{1}{2}$ for normalization reasons. The Fourier transform of the filter family (parametrized by $\alpha \in \mathbb{R}^+$) is modeled by

$$\widehat{\varphi_\alpha}(\xi_x, \xi_y) = \underbrace{\mathrm{sinc}(\xi_x) \cdot \mathrm{sinc}(\xi_y)}_{\text{physical sampling device}} \cdot \underbrace{e^{-\alpha\sqrt{(\xi_x)^2+(\xi_y)^2}}}_{\text{optical device}} \tag{8.1}$$

with $(\xi_x, \xi_y) \in \mathbb{R}^2$. For the CNES satellite, the parameter α is given by the lens geometry of the satellite optical chain: $\alpha = 3.702$.

In order to study the amount of ringing and blur of the filter family φ_α, we compute its *Spread-Ringing curve*. It also adds a new filter family into the filter classification and it shows that the filter chosen by the CNES ($\alpha = 3.702$) inside the (φ_α) family has its own *Spread-Ringing curve*, that is optimal for a given (S, R) couple.

In order to keep the framework of the previous chapter, we do not study φ_α but its 1D band-limited version (to avoid aliasing) called h_α. The Fourier transform of the filter is then set to

$$\widehat{h_\alpha}(\xi) = \mathrm{sinc}(\xi) \cdot e^{-\alpha\xi} \cdot \mathbb{1}_{[-W,W]}\,. \tag{8.2}$$

Note that the CNES's filter defined by $\widehat{\varphi_{3.702}}$ in (8.1) adds aliasing since the modulus of $\widehat{\varphi}$ is not zero at the frequency cut-off. Indeed at the frequency cut-off $(\xi_x, \xi_y) = (W, 0)$, we have

$$\begin{aligned} \widehat{\varphi_\alpha}\,(W,0) &= \widehat{\varphi_\alpha}\left(\frac{1}{2}, 0\right) = \mathrm{sinc}\left(\frac{1}{2}\right) \cdot e^{-\frac{\alpha}{2}} \\ &= \frac{\sin(\pi/2)}{\pi/2} \cdot e^{-\frac{3.702}{2}} \approx 0.1 \neq 0\,. \end{aligned}$$

Its band-limited version $(h_{3.702})$ is shown in Fig.8.1.

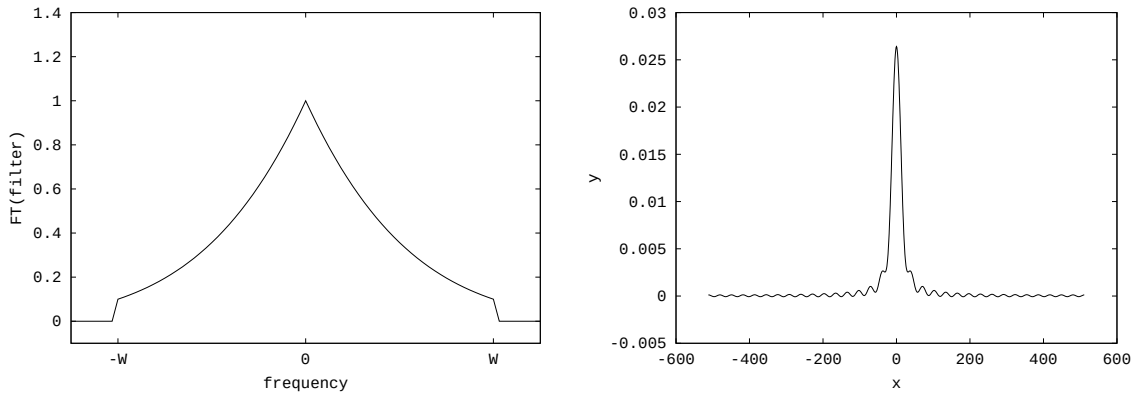

(a) (b)

Figure 8.1: The band-limited filter h_α with $\alpha = 3.702$ (a) in the Fourier domain. (b) in the space domain.

In this model, the high value of α enhances the exponential decrease of the Fourier modulus. Prefiltering with such a filter creates a blurry image. Another example of h_α is shown in Fig.8.2 with $\alpha = 0.6$. In this case, the shape of the filter Fourier transform is close to the triangle filter T. The quantity of blur due to the prefiltering stage might be similar to the one of the trapezoid filter $T_{(\alpha_1,0)}$.

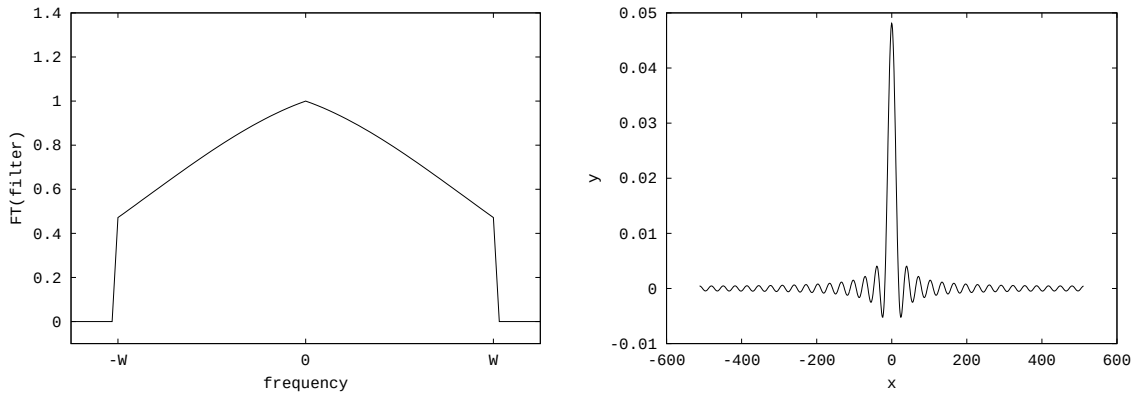

(a) (b)

Figure 8.2: The band-limited filter h_α with $\alpha = 0.6$ (a) in the Fourier domain (b) in the space domain

8.2 The Spread-Ringing curve of the system

The SR_∞ curve of the h_α filter family is compared to the one of the optimal SR filter and the prolate (Fig.8.3). As expected the optimal filter has the best blur/ringing trade-off. The new filter family h_α performs better than the prolate on a small spread interval $S = [1.24, 1.5]$. Fig.8.4 shows the Fourier transform of one of this optimal filter. Note how close to a cosine shape it is. This result is not surprising since the cosine filter C_α performs better than the prolate for small spread values. However this filter family h_α gives bad results for small ringing values since it requires very large spread values.

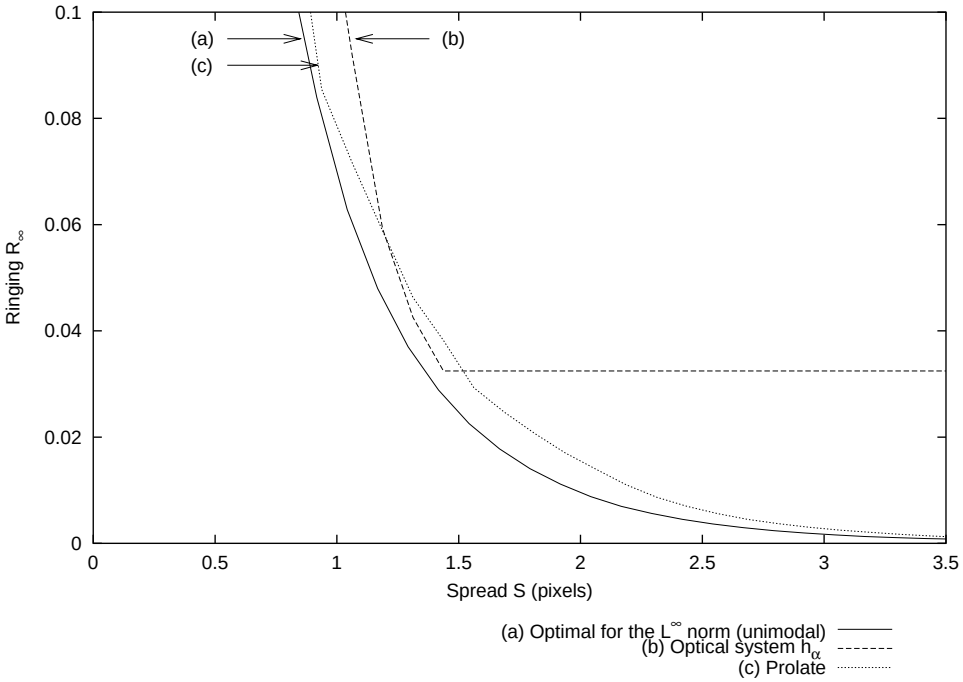

Figure 8.3: SR_∞ *Spread-Ringing curves*

Fig.8.5 shows the optimal parameter α for each ringing value. Small α values give the best trade-off. The value $\alpha = 3.702$ is not optimal in the considered spread range $S \in [0, 3.5]$. It is not surprising since it is not exactly the configuration of the filter used by the CNES. First, the band-limitation of the filter increases the blur, and consequently the spread. Second, this study is done only in 1D, and the optimality of $\alpha = 3.702$ should be measured in 2D. The results are even worse for the SR_2 curves (Fig.8.6) since the spread/ringing trade-off of the h_α family is far from the trade-off of the optimal filter family (Fig.6.9). In this study, we allow no aliasing and we measure ringing. This is not exactly the CNES configuration where the constraints of the optical devices introduce aliasing and no ringing. Using h_α instead of φ_α is swapping aliasing for ringing. To be closer to the CNES configuration, which is limited by the constraints of the instruments, and to show the optimality of the CNES filter, we ought to plot a Spread-Aliasing curve instead of the Spread-Ringing curve. But such a measure has not been defined in this thesis. Hence in this example, the approach with one dimensional filters and no aliasing does not match the CNES filter case. We do not really answer to the evaluation of the φ_α filters used by the CNES. However this example is an illustration of how the *Spread-Ringing curve* can be applied to any practical application. The *Spread-Ringing curve* is a generic tool which can be used

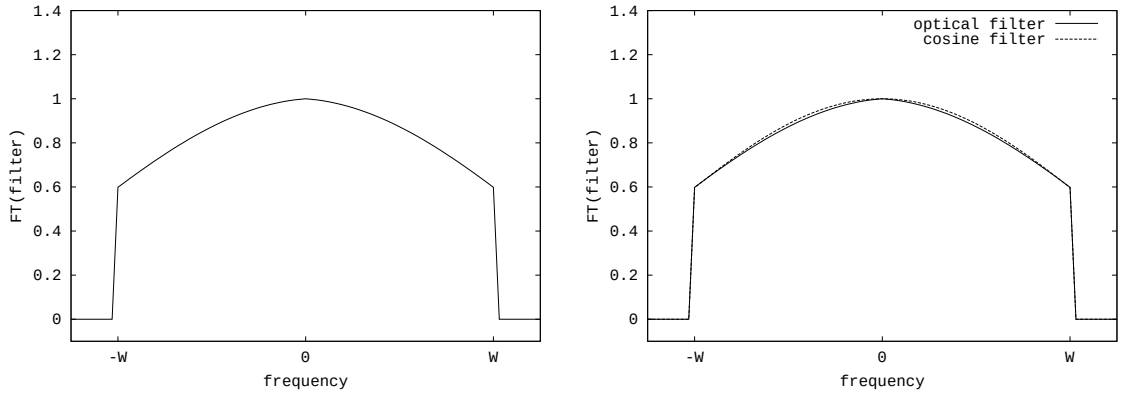

(a) (b)

Figure 8.4: (a) The band-limited filter with $\alpha = 0.123$ in the Fourier domain. This filter has a best ringing trade-off than the prolate for the same spread value. (b) Comparison with the cosine filter. Note how $\widehat{h_{\alpha=0.123}}$ is very close to the cosine filter $\widehat{C_{\alpha=0.043}}$.

to characterize any filter of a real system.

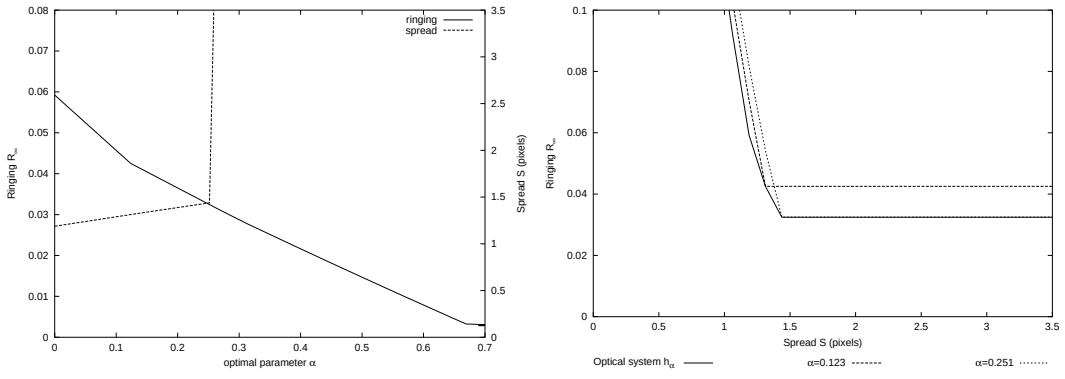

(a) (b)

Figure 8.5: (a) Optimal parameter α for each ringing and spread value (b) SR_∞ curves for $\alpha = 0.123$ and $\alpha = 0.251$ and the SR_∞ curve of the family h_α. The case $\alpha = 3.702$ is not shown here since the amount of blur introduced by the filter is bigger than $S = 3.5$ pixels. The curves of (a) can be directly used in applications: when the maximum level of ringing is set then there is a unique value of the filter parameter α, indicated by the curve "ringing". Then this value of α gives the level of blur introduced by this filter thanks to the "spread" curve.

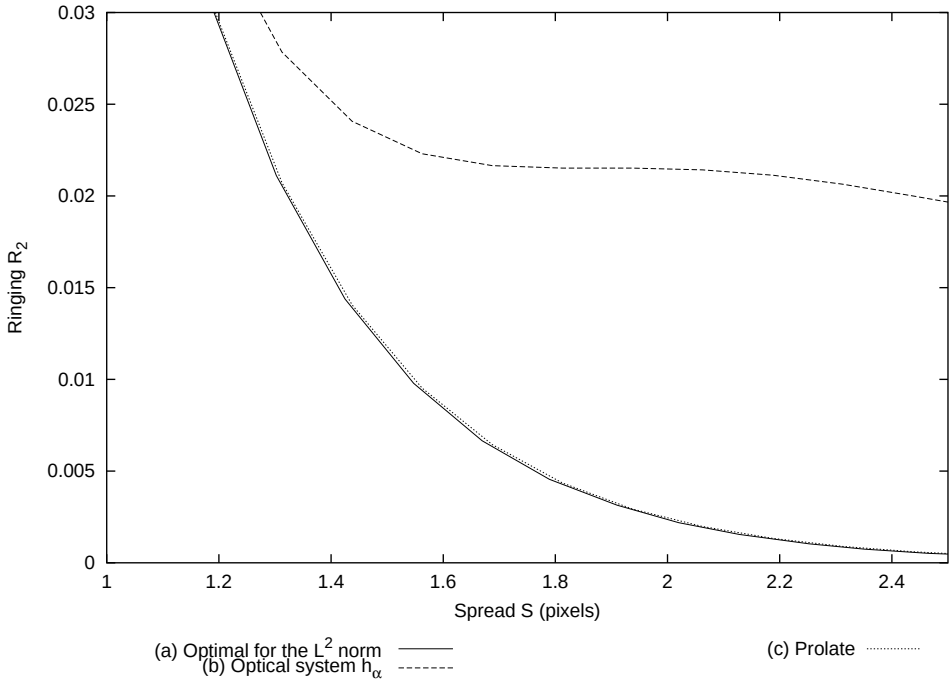

Figure 8.6: SR_2 *Spread-Ringing curves*. The spread/ringing trade-off of h_α measured with the L^2 norm is far from the optimal results and even far from the results obtained with classical filters such as the prolate.

Chapter 9

Numerical experiments

Experiments are performed on synthetic and natural images. We compare the results between an "optimal" filter and a classical one. Hence we consider two filters: the SR filter and the prolate filter. We set the ringing level and we compare the blur of the filtered images. In each experiment, the low-pass filtering reduce the frequency domain by a factor 16.

9.1 Text images

Text images are good test images to evaluate filters. The black letters on a white surface are discontinuity examples. The white surface shows the visual impact of the ringing artifact. In this experiment, we set the level of ringing R and we compare the sharpness of the images. Note that by definition the ringing R is measured for a transition from 0 to 1, because it is the amplitude of the Heaviside function. Since we consider now images with gray levels in $[0, 255]$, and not in $[0, 1]$, the corresponding ringing on the text images is $255 \cdot R$. On Fig. 9.1, we set $R = 0.003$, which means a ringing of less than one gray level ($255 \cdot 0.003 = 0.765$), that is bellow the perceptible ringing level. Can you read the following text ? [1]

9.2 Natural images

In this part we consider two satellite images. Such images are usually corrupted with noise coming from the instruments, unlike the synthetic *text images*. Since noise may hide the ringing phenomenon, we allow a larger ringing value than in the previous experiments. On Fig. 9.2 and 9.5, the level of ringing is fixed to $R = 0.0124$, because a higher value of R would be visible. For this value of R the image noise hide the ringing phenomenon. Let us compare the sharpness of the transitions. We note u the reference original image, u_P and u_{SR} the prefiltered images with respectively the prolate and the optimal SR_∞ filter. In all experiments, the size of u is 512×512. Consequently, the prefiltered images have same size. The downsampled versions of the prefiltered images are not presented. We only evaluate here the prefiltering process. The regions of interest and the gradient norm are shown in Fig.9.3 and 9.4, respectively.

The amplitude of the transitions are better preserved with the SR filter than with the prolate (Fig.9.6-(b)). The difference between u and both prefiltered images u_P and u_{SR} confirms the improvement:

[1] Solution: *The rain in Spain stays mainly in the plain! Henry in Hartford, Hereford and Hampshire ...? Eliza Hurricanes hardly happen How kind of you ...*, which is a quote from "My fair lady".

(a) (b)

Figure 9.1: (a) prolate (b) SR filter. The text is more readable with the SR filter than with the prolate.

(a) (b) (c)

Figure 9.2: Harbor: (a) u (b) u_P (c) u_{SR}. Details (boats) are better preserved with the SR filter.

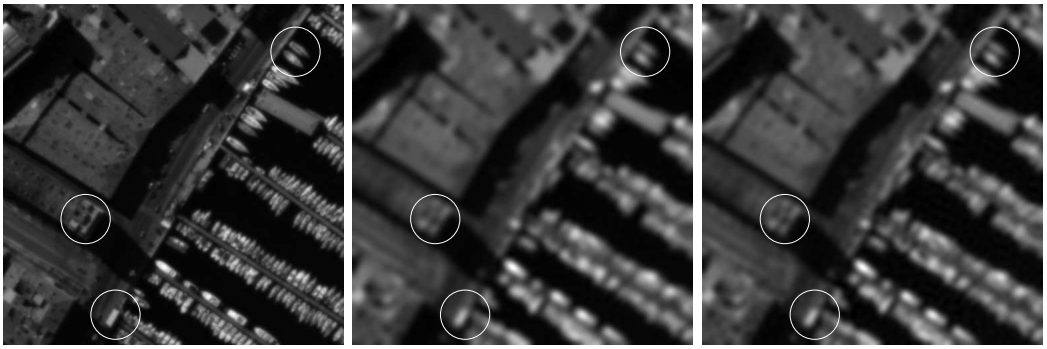

(a)

Figure 9.3: Images from Fig.9.2 with regions of interest.

(a) (b) (c)

Figure 9.4: Gradient norm of the images from Fig.9.2.

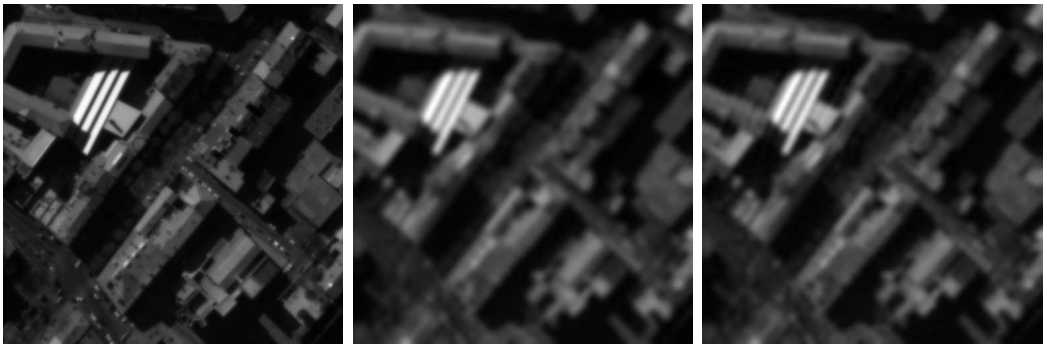

(a) (b) (c)

Figure 9.5: Town: (a) u (b) u_P (c) u_{SR} . The white roof is better preserved with the SR filter: sharper transitions.

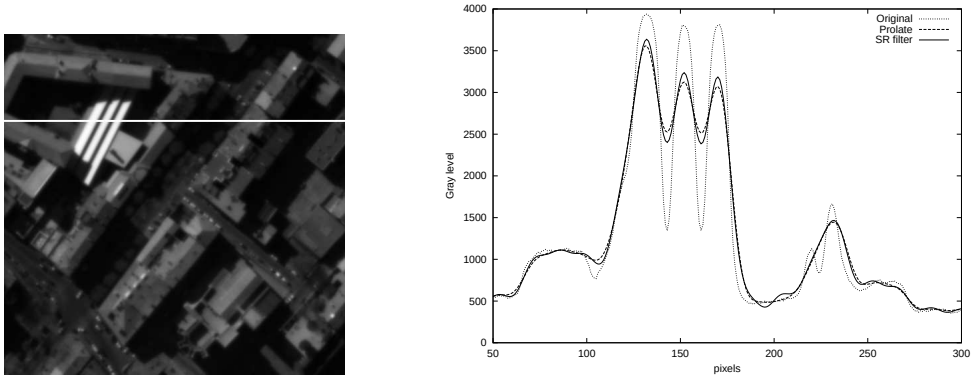

(a) (b)

Figure 9.6: (a) Image u with the line 130 in white (b) Line 130 near the white roof. Note how the prolate smoothes more sharp transitions than the SR filter.

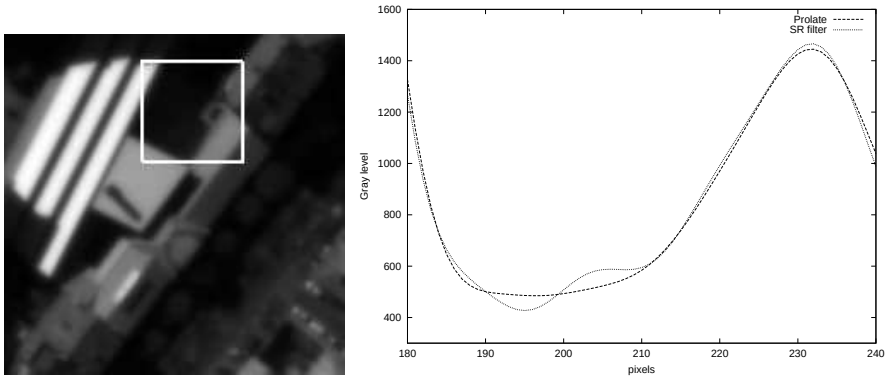

(a) (b)

Figure 9.7: (a) Subpart of the image u with the region of interest defined by $x \in [180, 240]$ and $y \in [100, 160]$ shown with the white square (b) zoom of u_P and u_{SR} along line 130, showing an undesired oscillation of u_{SR} near the column 200. This effect is not related to the 2D filtering since the image (a) shows no sharp transition in the vertical direction y.

$||u-u_P||_1 = 90$, $||u-u_{SR}||_1 = 83$, $||u-u_P||_2 = 150$, $||u-u_{SR}||_2 = 137$. However we observed some oscillations on u_{SR}, even though the ringing level was chosen below the image noise level. Fig.9.7-(b) and 9.8 show two oscillation examples on u_{SR} which does not exist on u and u_P. This problem comes from the additivity of the ringing. An image contains several edges. Each one may produce ringing. At some points the overshoot of the oscillations coming from different edge locations may be in phase. The addition of those overshoots creates larger ringing values than expected with the chosen filter. This observation leads to evaluating the ringing directly on prefiltered images prior to sampling and not from the filter. The evaluation cannot only rely on the filter model. However the ringing evaluation on natural images obtained with the evaluation on filters is not generic, since it is specific to the tested images.

9.3 Ringing evaluation on natural images

Procedure

We propose to measure the ringing by comparing the original image u with the prefiltered images u_{SR} and u_P. The comparison is done with a simple difference: $||u - u_P||$ and $||u - u_{SR}||$, that will be specified later. This operation is not done on the whole image but on subparts where ringing effects are easily detected. For example, we shall select uniform zones where in general the presence of oscillations are visually detected, since it adds a structure on a quasi-constant area. On the contrary, we shall not select subparts with textures since they often hide the phenomenon (Fig.12.25). Let us note M the mask of the selected subparts, which include as we have seen mainly uniform zones.

Before describing the procedure to build M, let us give some preliminary remarks. The mask is built to compare the original image with the prefiltered ones. In order to have comparable results for $||u-u_P||_M$ and $||u-u_{SR}||_M$, the mask is computed from u and not from the prefiltered images. This

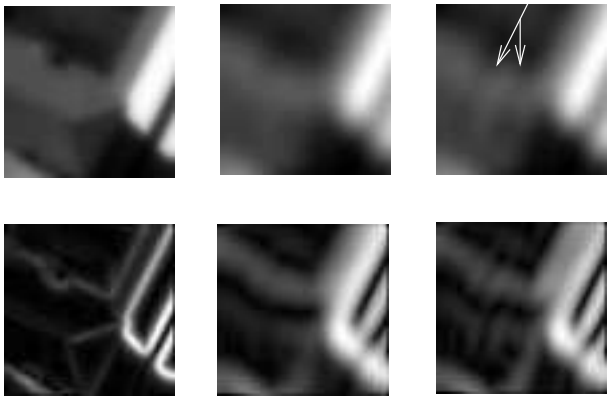

Figure 9.8: Subpart of Fig.9.5. First line: u, u_P and u_{SR}. Second line: the norm of their derivative. Example of oscillations on u_{SR}.

ensures that u_P and u_{SR} are analyzed on the same regions. Let us now describe the construction of M.

The first idea for finding homogeneous zones is to compute the gradient of the image and to keep the pixels that have a gradient norm smaller than a threshold value. However, the construction of this mask depends on the level of noise in u. Since noise increases the gradient norm on constant zones, the mask does not contain those zones. Furthermore, the threshold value is a parameter that can be avoided.

This leads to a second idea. Instead of measuring directly the gradient, which can be very chaotic in noisy images, it is more judicious to measure the contrast level of the level sets of u. The level set is defined by

$$B_{\lambda,\lambda'} = \{x; \lambda \leq u(x) \leq \lambda'\}$$

where x is any pixel of u and λ, λ' are two gray-level that satisfy $\lambda < \lambda'$. Setting $\lambda' = \lambda + \alpha$ defines α as the contrast measure. The smaller α is, the more homogeneous the region $B_{\lambda,\lambda'}$ is. The selection of all the pixels having a contrast measure of α is the following three stage process:

1. the level set $B_{\lambda,\lambda'}$ is cleaned by erosion, which suppresses pixels close to the boundary of $B_{\lambda,\lambda'}$. The eroded level set is defined by

   $$E_r(B_{\lambda,\lambda'}) = \{x \in B_{\lambda,\lambda'} \, ; \, D(x,r) \subset B_{\lambda,\lambda'}\}$$

   with $D(x,r)$ a disc with center x and radius r.

2. the mask of all the image regions with small contrast α is the union of the mask $E_r(B_{\lambda,\lambda'})$ for all $\lambda \in [0, 255]$. This collection of disjoint pixel sets is defined by

   $$R := \bigcup_{\lambda} E_r(B_{\lambda,\lambda'}) \, .$$

   Since this mask is obtained by the union of eroded masks, the distance between edges and mask elements is generally more than r, i.e. pixels near edges are not selected. This is not optimal to study the ringing since this phenomenon occurs near sharp transitions. The ringing oscillations may decay very fast, so pixels near edges bring more information than pixels far from the discontinuity. In order to include pixels near edges, the final mask is obtained by dilating R.

3. the mask final, called M, is defined by

$$M := D_{r'} R$$

where R is dilated with a disc shaped structuring element of radius r'. Setting $r' \leq r$ ensures that the mask does not dilate further than the edge lines. Dilating with $r' \geq r$ may add pixels in M that belong to other objects. These objects may hide the ringing phenomenon. So it is not judicious to chose these pixels to measure the ringing. The image M is a binary image where $M(u)(x) = 1$ means that the pixel x is selected, otherwise $M(u)(x) = 0$.

In practice, the image M is obtained with two basic operators of mathematical morphology called erosion and dilation [44].

Definition 9.1 (Erosion and dilation) *Let $u(x)$ be an image and F a shape, i.e. a subset of $\mathbb{R}^2$, then the erosion of u by the structuring element F is the image v defined by*

$$v(x) = \inf_{\delta \in F} u(x + \delta)\,.$$

The "inverse" operation, called dilation, is defined by

$$v(x) = \sup_{\delta \in F} u(x + \delta)\,.$$

The mask R is obtained with the following proposition.

Proposition 9.2 *Let $u(x)$ be an image and $\lambda \leq \lambda'$ two real numbers in $[0, 255]$. Let R be the collection of pixels defined by*

$$R = \bigcup_{\lambda} E_r(B_{\lambda,\lambda'})$$

where $B_{\lambda,\lambda'}$ is the level set defined by

$$B_{\lambda,\lambda'} = \{x; \lambda \leq u(x) \leq \lambda'\}$$

and $E_r(B_{\lambda,\lambda'})$ its eroded version defined by

$$E_r(B_{\lambda,\lambda'}) = \{x \in B_{\lambda,\lambda'}\,;\, D(x,r) \subset B_{\lambda,\lambda'}\}\,.$$

Then

$$R = \{x; D_r(u)(x) - E_r(u)(x) \leq \alpha\}\,. \tag{9.1}$$

Proof: By definition of $E_r(B_{\lambda,\lambda'})$, the structuring element is the disc of radius r. $E_r(B_{\lambda,\lambda'})$ contains the pixels $x \in B_{\lambda,\lambda'}$, such that $D(x,r) \subset B_{\lambda,\lambda'}$ which means that $\forall \delta \in D(0,r)$, $x + \delta \in B_{\lambda,\lambda'}$. Then $x + \delta$ satisfies

$$\lambda \leq u(x + \delta) \leq \lambda'\,. \tag{9.2}$$

From Definition 9.1, the erosion and the dilation of u are

$$E_r(u)(x) = \inf_{\delta \in D(0,r)} u(x + \delta)\,,$$

$$D_r(u)(x) = \sup_{\delta \in D(0,r)} u(x + \delta)\,.$$

The erosion darkens images since it preserves the $\inf$ value of the gray levels in the neighborhood of x. Conversely the dilation brightens images. Satisfying $\lambda \leq u(x+\delta)$ for all values of $\delta \in D(0,r)$ in (9.2) is equivalent to satisfy that the inf value of $u(x+\delta)$ with respect to δ is bigger or equal to λ. So

$$\forall \delta \in D(0,r), \lambda \leq u(x+\delta) \Longleftrightarrow \lambda \leq E_r(u)(x)\,.$$

The same reasoning can be applied to the inequality of (9.2) yielding

$$E_r(B_{\lambda,\lambda'}) = \{x; E_r(u)(x) \geq \lambda \text{ and } D_r(u)(x) \leq \lambda'\}\,.$$

Since R is the collection of E_r for all the values of λ, the expression of R can be rewritten with $\alpha = \lambda' - \lambda$ instead of the two values λ and λ'. We obtain (9.1). Indeed If x belongs to $E_r(B_{\lambda,\lambda'})$ then it satisfies $E_r(u)(x) \geq \lambda$ and $D_r(u)(x) \leq \lambda'$ which can be rewritten

$$D_r(u)(x) - E_r(u)(x) \leq \lambda' - \lambda = \alpha\,.$$

□

Notation: We define $Z(u)$ the image u restricted to the set of pixels corresponding to a constant zone: $M(u)(x) = 1$.

Choice of α

In the experiments, we compute $|Z(u) - Z(u_P)|$ and $|Z(u) - Z(u_{SR})|$. Images u, u_P and u_{SR} are images from Fig.9.5. In order to have a global understanding of the influence of the parameter α, we test different values of α in $[0, 255]$ with step $\Delta\alpha = 1$. Plotting directly the curves $(\alpha, |Z(u) - Z(u_P)|)$ and $(\alpha, |Z(u) - Z(u_{SR})|)$ shows locally constant values when the mask does not change between two steps of α (Fig.9.9-(a)). This drawback shows that α is not the best abscissa choice and it should be replaced by another parameter that takes into account the evolution of the mask, that is the number of points in M. For this purpose, we note $P(\alpha)$ the proportion of points in the mask

$$P(\alpha) = \frac{\sum_{k\in\Omega} M(k)}{|\Omega|}$$

where

- Ω is the image domain and $|\Omega|$ its cardinality. It is equal to the number of pixels in u or equivalently in u_{SR} or u_P. Its value is independent of α.
- $\sum_{k\in\Omega} M(k)$ is the number of pixels in M belonging to an uniform zone, i.e. satisfying $M(u)(x) = 1$. For small α values, only pixels in a poorly contrasted region belong to the mask. In this case, $\sum_{k\in\Omega} M(k)$ is small. For larger α, the mask may contain contrasted regions. So $\sum_{k\in\Omega} M(k)$ increases with α and tends to $|\Omega|$: $\lim_{\alpha\to 255} P(\alpha) = 1$ (Fig.9.9-(b,c)).

Study of the sensitivity to the norm choice and the size of the structuring element

We recall that the sizes of the structuring elements are r and r' which measure the radius of the structuring element for the erosion and dilation, respectively. As mentioned before, $r' \leq r$ ensures that the mask M does not dilate further than the edge line, where the case $r' = r$ means that the mask contains both the uniform zones and the edge line. This latter example is shown in Fig.9.10.

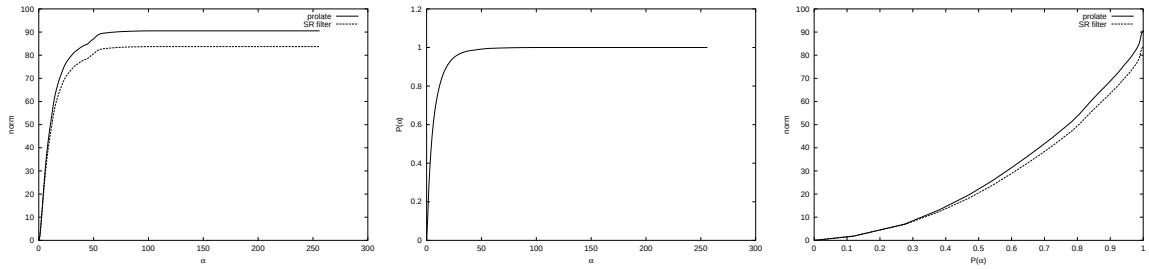

(a) (b) (c)

Figure 9.9: $r = r' = 2.5$ (a) $(\alpha, ||Z(u) - Z(u_P)||_1)$ and $(\alpha, ||Z(u) - Z(u_{SR})||_1)$ (b) $P(\alpha)$ (c) $(P(\alpha), ||Z(u) - Z(u_P)||_1)$ and $(P(\alpha), ||Z(u) - Z(u_{SR})||_1)$. $P(\alpha)$ is not linear with respect to α. The graph in (a) shows nearly constant value for $\alpha > 50$, which means that on this part of the graph the same number of pixels were considered. This indicates that the graph of $||Z(u) - Z(u_P)||$ should take into account the number of considered pixels for each value of α, which is done thanks to $P(\alpha)$ in (c).

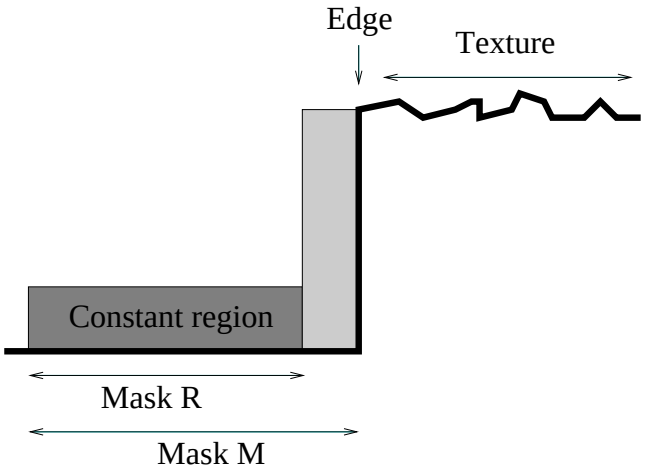

Figure 9.10: For $r = r'$, the final mask M contains edges and the nearby uniform zones (here on the left side of the edge). Texture regions are not selected because they have a high contrast level.

Since the SR filter is optimal for the blur/ringing trade-off, the evaluation of $||Z(u) - Z(u_P)||$ and $||Z(u) - Z(u_{SR})||$ should take into account both the blur and the ringing on the prefiltered images u_P and u_{SR}. Hence the mask obtained with $r' = r$ is the most appropriate since it contains uniform zones where the ringing can be measured and the edge line where the sharpness can be evaluated. The results shown in Fig.9.11 validate the optimality of the SR filter since the image prefiltered with the optimal filter is closer from the original image than the on prefiltered with the prolate filter

$$||Z(u) - Z(u_{SR})|| < ||Z(u) - Z(u_P)||$$

whatever the chosen norm (L^∞, L^1, L^2) and for all α $(P(\alpha) \in [0, 1])$. We recall here that u_{SR} and u_P are supposed by construction to have same ringing R_∞ and different sharpness values.

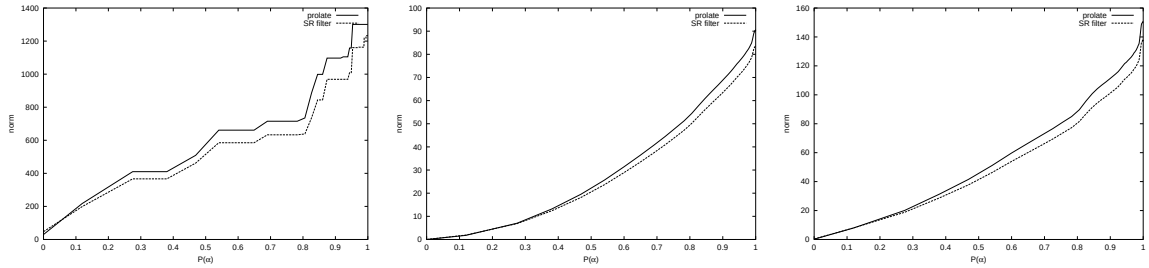

(a) (b) (c)

Figure 9.11: (a) L^∞ norm (b) L^1 norm (c) L^2 norm. All measures are done with $r = r' = 2.5$.

We obtain the same results independently of the size of the structuring element as long as $r = r'$. More tests with several r are shown in Fig.9.13 and 9.14. For $r' < r$, which means that the mask only contains constant regions and not edges, u_{SR} shows worst results than u_P for small α values, especially for the L^2 norm (Fig.9.12).

These results obtained here are not surprising for two reasons. First let us recall that u_{SR} and u_P have same ringing measure R_∞ and u_{SR} is supposed to be sharper than u_P. Let us now explain the two reasons.

- First, the optimality of the SR filter should be estimated in the vicinity of edges since u_{SR} and u_P have different sharpness levels. If $r' < r$, pixels near edges are not studied because the mask is not dilated enough to reach the edge line. This is also true for a small constrast measure α because an edge increases locally the contrast.
- Second, the comparison of u_{SR} and u_P with the L^2 norm may not show the optimality of u_{SR} since the SR filter may oscillate on his whole spatial support (Fig.6.2) and is more penalized by the L^2 norm than the prolate (even if for both filters, the ringing oscillations have same maximal amplitude R_∞).

9.4 Discussion on the norm to measure the ringing

To each norm corresponds a different ringing model. Measuring the ringing with the L^∞ norm focus on the overshoot, whereas L^1 or L^2 norms take into account the number of oscillations. Both models

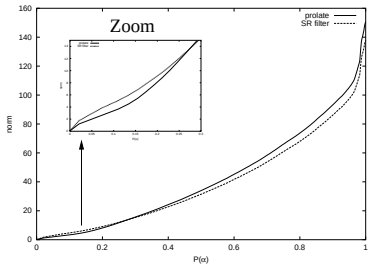

Figure 9.12: L^2-norm with $r = 5.5$ and $r' = 0$. For small α, u_P is closer to u than u_{SR} is. Since $r' < r$, the sharpness of the filtered image has not been measured.

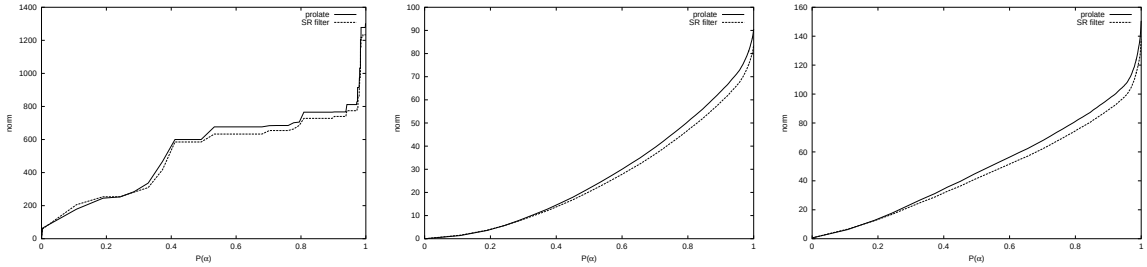

(a) (b) (c)

Figure 9.13: (a) L^∞ norm (b) L^1 norm (c) L^2 norm with $r = r' = 5.5$.

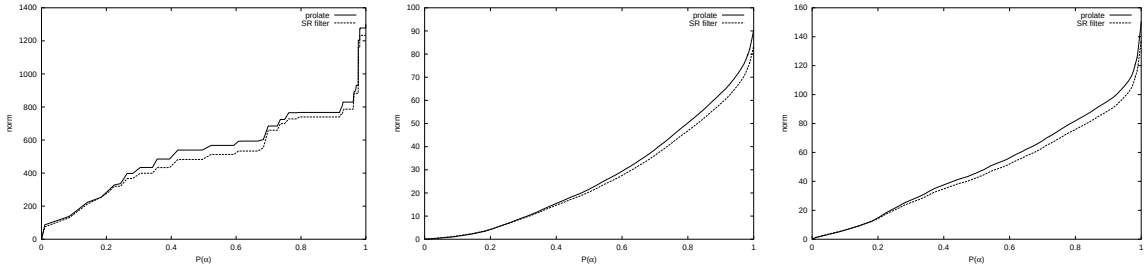

(a) (b) (c)

Figure 9.14: (a) L^∞ norm (b) L^1 norm (c) L^2 norm with $r = r' = 9.5$.

are reasonable from a perceptual point of vue. Big overshoots attract attention, as do long oscillations on a uniform zone. So a good model would consider both.
The previous section proved the good image quality of the image prefiltered with the optimal SR_∞ filter (u_{SR}) with respect to the image prefiltered with the prolate filter (u_P). Whatever the three tested norms, u_{SR} is definitely the closest to u. However, there is a theoretical optimal filter for the L^2 norm: the Shannon filter. Let us now study the image filtered with the Shannon filter, we note it u_S.

Remark on the Shannon filter: by construction, the sinc filter minimizes the L^2 norm of the energy loss. Indeed it preserves all frequencies up to the cut-off frequency. This filter adds a lot of ringing but the prefiltered image u_S is sharp. Fig.9.15 shows u_S for a reduction of the frequency domain by a factor 16.
From a theoretical point of vue, it is interesting to compare u_{SR} with u_S (Fig.9.16). We observe two cases.

- For small values of $P(\alpha)$, which represents up to half the number of points in the image on quasi uniform zones, u_{SR} is better than u_S. The very long oscillations of Shannon filter penalizes u_S on homogeneous zones.
- When $P(\alpha)$ tends to 1, the mask contains edges, which are sharp on u_S. This explains the poor results of u_S for small $P(\alpha)$, and the good results when $P(\alpha)$ tends to 1. As expected, when the whole image is considered, u_S performs better than u_{SR}:

$$\text{for } P(\alpha) = 1, \quad ||Z(u) - Z(u_S)||_2 < ||Z(u) - Z(u_{SR})||_2 \,.$$

Fig.9.17 displays images $Z(u)$ for three different values of $P(\alpha)$.

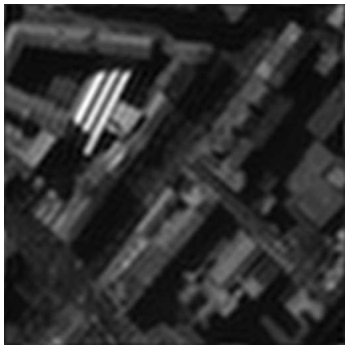

Figure 9.15: Town image u prefiltered with the sinc filter.

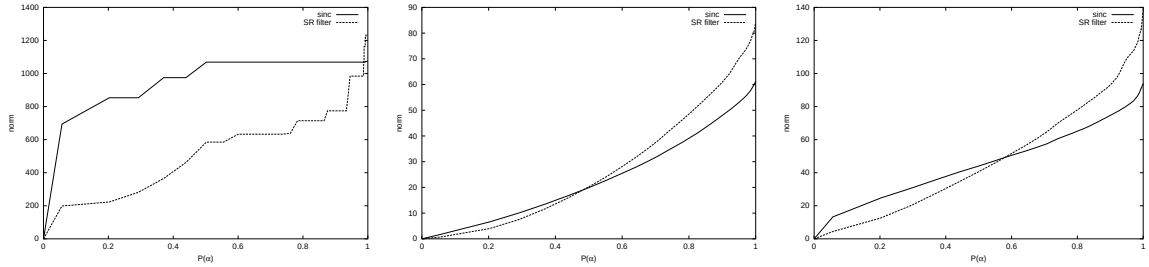

Figure 9.16: (a) L^{∞} norm (b) L^{1} norm (c) L^{2} norm with $r = r' = 3.5$. Shannon filter is optimal for the L^{2} norm when $P(\alpha) \geq 0.6$.

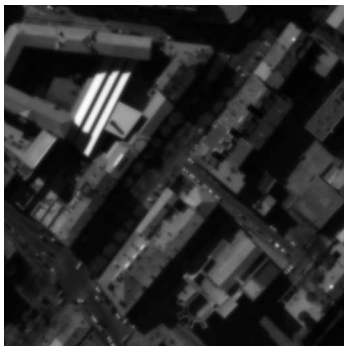

(a)

(b) (c) (d)

Figure 9.17: (a) Original image u (b-c-d) Mask M for $\alpha = 3, 11, 60$, which corresponds to $P(\alpha) \simeq 0.3, 0.7, 0.99$, respectively. The selected pixels are indicated by a white value $(M(u)(x) = 1)$. A small α selects small uniform regions, whereas a large one increases the mask area. When α is close to 1, most of the pixels are selected, as in (d).

Conclusion

This part was devoted to the study of the band-limitation of a signal with a low-pass filter. Band-limiting a signal is a common task in the image processing field required for example to enforce the hypothesis of the Shannon Sampling theorem in order to avoid the aliasing artifact. It is well known that the Shannon frequency cut-off filter degrades images with a strong ringing artifact, and should be replaced by some other filters given in the literature. However these filters also add blur. Since it is not clear how much artifact those filters introduce and which one should be chosen for a given application, we have proposed in this part a unifying approach that defines a measure for the artifacts and that allows to compare the performance of classical filters. Let us now successively recall the contributions of this part.

In the introduction of Part II, we recalled some classical low-pass filters of the literature, such as the Shannon filter, the Gaussian or the prolate. We also studied some other filters, the geometry of which has a simple expression in the Fourier domain.

We showed that the ringing and blur artifacts cannot be measured separately. Both measures have to be joined. Thus we proposed a new measure that simultaneously evaluates the level of blur and ringing introduced by a filter. The studt was done in one dimension. Since ringing occurs in the vicinity of sharp transition, we studied the Heaviside function H which represents a very sharp transition from 0 to 1. The artifacts are measured on the signal $\varphi \star H$, built by the convolution of the filter with H. The double measure of the blur and the ringing on $\varphi \star H$ results in the construction of the so-called *Spread-Ringing curve*, which characterizes the filter φ. This measure is useful for practical applications since it can be read in two ways: it gives either the level of ringing introduced by the filter for an accepted level of blur or the level of blur for a fixed level of ringing. The blur is measured by the spread of the transition, which is initially zero-valued on H. On the contrary, the ringing can be measured differently depending on whether we focus on its overshoots/undershoots or on the length of its oscillations. This is the reason why we proposed three norms, each one producing a different *Spread-Ringing curve*. The L^∞ norm is dedicated to the measure of the overshoots and undershoots, whereas the L^2 and L^1 norms penalize long oscillating curves.

This leads us to the filter classification using their *Spread-Ringing curve*, the major contribution of this part. We observed that when the ringing is measured with the L^∞ norm, the band-limited Gaussian filter is competitive for small blur values since it gives small ringing by comparison with the other tested filters. Moreover, we showed that the filter with a band-limited cosine shape in the Fourier domain and the prolate filter yield similar results, which was unexpected. Since the computation of a filter with a cosine Fourier transform is simple because it has an analytic expression, this filter has great advantages for practical and theoretical studies. These good results of the cosine filter with respect to the spread/ringing trade-off are confirmed when the ringing is measured with the L^2 or L^1 norms. But they are not better than the *optimal* ones obtained with the new class of filters built in Chapter 6 for one of the three considered norms. By construction, they outperform any other filter tested in the

first place. The best results of those so called *optimal* filters are confirmed when applied to images. As observed in Chapter 9 for an identical ringing value, the prolate filter adds more blur in the image than the *optimal* filter.

Chapter 7 gave the extension of the filters in two dimensions and Chapter 8 was devoted to a direct application of the *Spread-Ringing curve*. We considered the filter family of the optical system in one of the satellites launched by the CNES and we plotted its *Spread-Ringing curve*. We showed that this filter performs well when a small blur value is authorized during the filtering stage, i.e. a transition spread value in $[1.24, 1.5]$ pixels. But this filter is designed by the CNES to allow a small amount of aliasing so it would be interesting to define another measure that takes into account not only the ringing and blur artifacts but also the aliasing. This would lead to the criteria (Spread, Ringing, Aliasing) to characterize filters. This remains an open problem.

This part was devoted to the study of artifacts introduced by a filter. Let us now assume we do not know the filter, and we only have the degraded image. Some artifacts might reduce its quality, such as the blur, the ringing and the aliasing. In the next part, we propose one detector for each of the above-cited artifacts.

Part III

Image quality assessment

Introduction

In the image processing literature, the term *image quality* refers to the quality of an image, not in the sense of artistic beauty, but in the sense of artifact-free data. If the quality is low, it means that the image has been strongly deteriorated. Being able to evaluate the quality of an image is essential in most image processing applications. It gives information not only on the degradations during the image formation (for example the ones described in Part I), but also on the best adapted restoration procedure, the efficiency of which can again be evaluated by measuring the quality of the restored image. In this part, we propose several detectors to measure image quality. Each one is specific to the artifacts we have been studying in this thesis: blur, ringing and aliasing. Let us now briefly describe the three types of detectors:

- the first one is a sharpness detector, as opposed to blur. It is based on a frequential approach introduced by Morrone [37]: it states that phase coherence is high in a sharp image. The sinusoids of the Fourier transform have locally same phase on sharp contours. This comes from the ability of the Fourier transform to express a discontinuity by the sum of sinusoids. The small phase shift of a single sinusoid has a dramatic effect on the reconstructed edge, since the oscillations of this sinusoid are not compensated by the others. The oscillations are locally visible. We propose a detector that measures the effect of sinusoid small phase shift. We use the Total Variation since it is computed by adding the amplitude of all the transitions of the image and is then adequate for measuring oscillations, because the presence of oscillations increases the Total Variation. The detector is tested on the LIVE image database [46].

- the second one is a ringing detector devoted to the ringing resulting from blind deconvolution. We observe that oscillations around edges have the same period on the whole image, which makes them visually noticeable. We use this deviation to ringing-free images to build a detector that finds a highly represented oscillation period. For this purpose, we adopt a probabilistic approach. The probability that many pixels have same oscillation period is computed *a contrario*, based on the *a priori* statement that a white noise image has no particular oscillation period. This approach follows the general method proposed by Desolneux *et al.* [13] used to detect point alignments in image, but it is specific to the ringing artifact.

- the last one is an aliasing detector. Since the aliasing is defined in both the frequential and spatial domains, we propose here three detectors: the first one detects aliasing in the frequential domain, the second one in the spatial domain, and the last one combines both. We show that using the frequency approach is adequate for a restrained number of images, for example small images with a single edge. Since most natural images have more than one edge and have textures, it seems that the Fourier transform is too "global" to detect aliasing. The other two approaches give better results. They are based on studying the aliasing geometry, especially on the regularity

of the level lines around edges, and on the Shannon postulate, respectively. All detectors are tested on SPOT images.

Chapter 10

Sharpness detection

10.1 Classical measure of phase coherence

In the literature, the *phase coherence* defined by Morrone *et al.* in [35] [37] [36] to explain many perceptual phenomena such as the *Mach bands* (edge enhancement illusion) has been used by different authors. For example Kovesi detects different kind of image features like step edges or lines [22][21], and Simoncelli *et al.* detect blur thanks to the phase coherence measure [55]. They show that very localized features result in strong local phase coherence (calculated in the complex wavelet transform domain) across scale and space. The perception of blur would come from the disruption of local phase. This recent work shows that phase has a great influence on the perception of images and that the coherence of phase qualifies images. Before defining the phase coherence as given by Morrone, let us first recall the theoretical background. The idea that the Fourier components of sharp edges have same phase is not new. Euler showed that some discontinuous functions can be written as the infinite sum of cosine and sine functions. Some of them are recalled in [16].

For example, the square wave is the 2π-periodic function defined on $(-\pi, \pi)$ by

$$\forall x \in (-\pi, \pi), \quad SW(x) = \begin{cases} 1 & \text{for } x > 0 \\ -1 & \text{for } x < 0 \end{cases} . \tag{10.1}$$

Since it is an odd function, it can be written as an infinite sum of sines, given by $SW(x) = \sum_{n=0}^{\infty} \frac{\sin[(2n+1)x]}{2n+1}$ [22]. When the number of sines is restrained to $N+1$, we obtain the oscillating function $SW_N(x) = \sum_{n=0}^{N} \frac{\sin[(2n+1)x]}{2n+1}$ (Fig.10.1).
Morrone *et al.* define the phase coherence for each pixel x belonging to an image f by

$$PC(x) = \frac{|E(x)|}{\sum_n A_n(x)} \tag{10.2}$$

where

- $A_n(x)$ is the amplitude and $\Phi_n(x)$ the phase angle of the local Fourier transform of f in x. The subscript n indicates, that we are considering the amplitude and the phase angle of the n^{th} component of the local Fourier transform: $f_n(x) = A_n(x) \cdot e^{i\Phi_n(x)}$.
- $|E(x)|$ is the *Local Energy* at x. It is equal to the modulus of $E(x) = \sum_n f_n(x)$ (Fig.10.2).

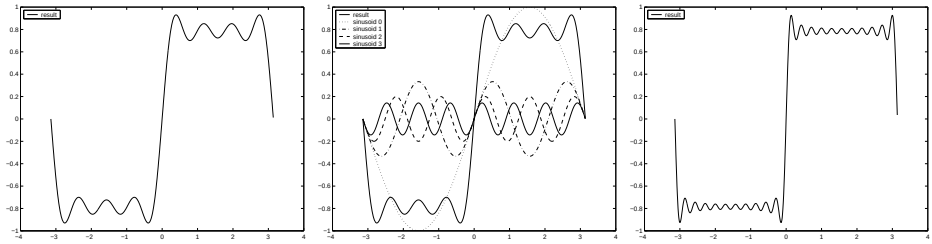

(a) (b) (c)

Figure 10.1: (a) Function SW_3 obtained with four sinusoids (b) Plot of SW_3 and the four sinusoids. (c) Function SW_{10}. The sinusoids are all centered in $x = 0$, they have same phase.

$PC(x)$ may take values from 0 to 1. If all sinusoids are in-phase ($\forall n$, $\Phi_n(x) = \Phi(x)$), then the phase coherence is maximal ($\sum_n A_n(x) = |E(x)|$ so $PC(x) = 1$). On the contrary, $PC(x)$ is minimal, i.e. close to zero, if all the sinusoids have different phase.

As defined by Morrone, the phase coherence is not a global measure, since it gives a different value at each pixel. It does not give the global sharpness of the image. This is the reason why we propose another measure, which is global.

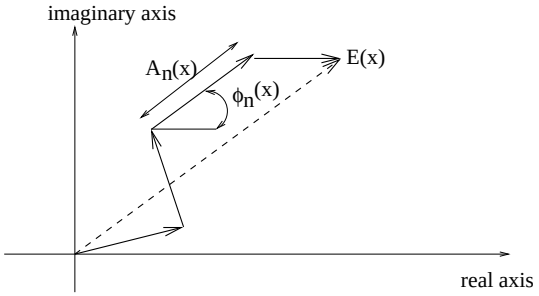

Figure 10.2: Representation of the elements to measure the phase coherence as defined by Morrone. The energy $|E(x)|$ is the modulus of $E(x) = \sum_n A_n(x) \cdot e^{i\Phi_n(x)}$.

10.2 New measure of phase coherence

10.2.1 Definition

In order to use the fact that phases are very coherent near sharp transitions, we consider the sensibility of the image total variation to phase shift. A sharp transition can be expressed as the sum of sinusoids which are in-phase. Even a small phase shift of a single phase would result in oscillations appearing on the whole signal. For example the sharp step function H is shown in Fig.10.4-(a). Its total variation is equal to 1 but it increases after the phase shift due to the oscillations of the dephased sinusoid. A sharp transition total variation is sensitive to the phase shift of its sinusoids. Conversely, a blurred

(a) (b)

Figure 10.3: a) Real image [46] (b) Its phase coherence image. White points indicates high phase coherence ($PC(x) \simeq 1$). It is large in sharp regions, such as the wings of the butterfly, whereas the blurred background has values close to zero.

transition is less sensitive. Only the first sinusoids of a blurred transition are in-phase. The high frequency components vanish, so their phase shift is of no consequence.

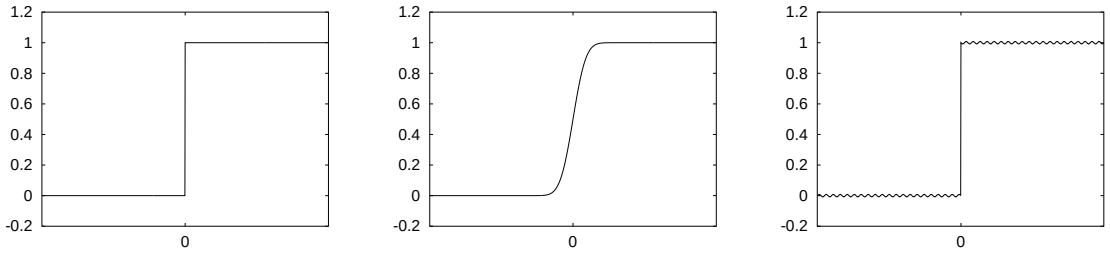

(a) (b) (c)

Figure 10.4: (a) sharp transition H (b) smooth transition (c) Example of the phase shift of one sinusoid of H. Signals (a) and (b) have the same total variation as they represent the same transition from 0 to 1. Note how the total variation increases for (c).

These remarks lead us to propose the following definition of the phase coherence. In order to be independent of the type of images and their normalizations, we define the coherence of phase in a probabilistic framework.

Definition 10.1 (randomly dephased) *Let $u(x)$ be an image, the Fourier transform of which is $\widehat{u}(\xi) = M(\xi)\, e^{i\Phi(\xi)}$. Let U_ε be the randomly dephased of u. It is a random field given by*

$$\widehat{U_\varepsilon}(\xi) = M(\xi) \cdot e^{i(\Phi(\xi) + \varepsilon \cdot R(\xi))} \tag{10.3}$$

where $R(\xi)$ are independent and identically distributed in $[-\pi, \pi)$ for

$$\xi \in \{(\alpha, \beta);\ \alpha > 0 \text{ or } (\alpha = 0 \text{ and } \beta > 0)\}$$

and

$$R(-\xi) = -R(\xi)$$

since phases are anti-symmetrical.

In the following, we use the classical notation where the upper-case and lower-case letter indicate the random field and one realization, respectively. For example here, U_ε is the random field and u_ε is one realization.

Property 10.2 *Image u_1 is a random phase image, which means that its phases are independent and uniformly distributed in $[-\pi, \pi]$.*

Proof: If $\varepsilon = 1$ then $R(\xi)$ has a uniform distribution in $[-\pi, \pi]$. As the phase is 2π-periodic and as the realizations of $R(\xi)$ (noted $r(\xi)$) have already a range of 2π in each frequency direction, a maximal phase shift of $\pm\pi$ is possible. The resulting image has then random phases.

□

Remark: the interesting values of ε are the ones such that $|\varepsilon| \leq 1$. An image, which phases are uniformly distributed in $[-\pi, \pi]$, is a random phase image (Fig.10.5). As a consequence, $\varepsilon > 1$ will not produce a "more random" image than the one obtained for $\varepsilon = 1$.

(a) (b) (c)

Figure 10.5: (a) Original image u (b) One image $u_{\varepsilon=0.2}$ (c) One image $u_{\varepsilon=1}$. This last image is a random phase image. Even if it has same modulus of the Fourier transform than u, its objects are no more recognizable.

Let us remark that for each fixed value of ε, there is an infinite number of images u_ε. Images of Fig.10.5 are one realization of U_ε. Now, the next step to measure the phase coherence of the image is to compare the total variation of the original image u to the total variation of its randomly dephased images.

Definition 10.3 (phase coherence) *Let u be an image and U_ε the associated random field. The phase coherence $F_\varepsilon(u)$ of u is defined by*

$$F_\varepsilon(u) = -\log_{10}\ \mathbb{P}\left(TV(U_\varepsilon) \leq TV(u)\right), \tag{10.4}$$

where $\mathbb{P}\left(TV(U_\varepsilon) \leq TV(u)\right)$ is the probability of the event "$TV(U_\varepsilon) \leq TV(u)$" and $TV(u)$ is the total variation of u defined by

$$TV(u) = \int |Du| .$$

Property 10.4 $F_\varepsilon(u) \in [0, \infty[$.

Proof: $\mathbb{P}\left(TV(U_\varepsilon) \leq TV(u)\right) \in [0, 1]$.

$\mathbf{F_\varepsilon(u) = \infty}$ represents the case of an infinite phase coherence. For sharp images, we expect large values of $F_\varepsilon(u)$. The total variation of such images typically increases with the random phase shift thus making $\mathbb{P}\left(TV(U_\varepsilon) \leq TV(u)\right) \simeq 0$. This increase is validated on Fig.10.5 where $TV(u) = 10.5\ <\ TV(u_{0.2}) = 12.3\ <\ TV(u_1) = 16.1$.

$\mathbf{F_\varepsilon(u)}$ **small** for blurred images. The random phase shift of such images changes the total variation but it may decrease.

10.2.2 Estimation of phase coherence

The estimation of the probability $\mathbb{P}\left(TV(U_\varepsilon) \leq TV(u)\right)$ in an empirical way is possible only if "$TV(U_\varepsilon) \leq TV(u)$" is not a rare event. If the event is rare, $F_\varepsilon(u)$ is expected to go to infinity but it cannot be estimated because one would need a huge number of u_ε images. However experimentally, we observed that when the size N of the image is large enough, the distribution of $TV(U_\varepsilon)_N$ has a Gaussian shape (Fig.10.6 and 10.7). We did not develop this theoretical aspect in this thesis, however we shall give now some related remarks.

Remarks : By definition, the inverse discrete Fourier transform of $\widehat{u}(\xi_m)$, $\xi_m \in \mathbb{Z}$, is

$$u(k) = \frac{1}{N} \sum_{m=0}^{N-1} \widehat{u}(\xi_m)\ e^{\frac{2i\pi\xi_m k}{N}}$$

for $k = 0 \ldots N-1$. We note U_ε the image of size N, the Fourier transform of which is dephased by $R(\xi_m)$ having uniform distribution in $[-\varepsilon\pi, \varepsilon\pi]$:

$$U_\varepsilon(k) = \frac{1}{N} \sum_{m=0}^{N-1} \widehat{u}(\xi_m)\ e^{\frac{2i\pi\xi_m k}{N}}\ e^{i\ R(\xi_m)} .$$

The difference between two values of u_ε in the vicinity of k is calculated by

$$D(U_\varepsilon)(k)\ =\ U_\varepsilon\left(k + \frac{h}{2}\right)\ -\ U_\varepsilon\left(k - \frac{h}{2}\right) . \tag{10.5}$$

But

$$U_\varepsilon\left(k + \frac{h}{2}\right) = \frac{1}{N} \sum_{m=0}^{N-1} \widehat{u}(\xi_m)\ e^{\frac{2i\pi\xi_m (k+\frac{h}{2})}{N}}\ e^{i\ R(\xi_m)}$$

$$U_\varepsilon\left(k-\frac{h}{2}\right)=\frac{1}{N}\sum_{m=0}^{N-1}\widehat{u}(\xi_m)\,e^{\frac{2i\pi\xi_m(k-\frac{h}{2})}{N}}\,e^{i\,R(\xi_m)}$$

By inserting these two expressions in (10.5), we get

$$\begin{aligned}D(U_\varepsilon)(k) &= \frac{1}{N}\sum_{m=0}^{N-1}\widehat{u}(\xi_m)\,e^{\frac{2i\pi\xi_m k}{N}}\,(e^{\frac{2i\pi\xi_m\frac{h}{2}}{N}}-e^{\frac{-2i\pi\xi_m\frac{h}{2}}{N}})\,e^{i\,R(\xi_m)}\\ &= \frac{1}{N}\sum_{m=0}^{N-1}\widehat{u}(\xi_m)\,e^{\frac{2i\pi\xi_m k}{N}}\,2i\sin(2\pi\xi_m\frac{h}{2N})\,e^{i\,R(\xi_m)}\end{aligned}$$

The perturbation $R(\xi_m)$ is a random phase shift. If $\varepsilon=1$, the distribution of R is uniform $\mathcal{U}([-\pi,\pi])$ with $\mathbb{E}(R(\xi_m))=0$ and $\mathrm{Var}(R(\xi_m))=\frac{\pi^2}{3}$. Since the discrete total variation of the signal u of size N is given by $TV(u)_N=\sum_{k=0}^{N-1}|Du(k)|$, the discrete total variation of U_ε is

$$\begin{aligned}TV(U_\varepsilon)_N &= \sum_{k=0}^{N-1}|D(U_\varepsilon)(k)|\,,\\ &= \sum_{k=0}^{N-1}\left|\frac{1}{N}\sum_{m=0}^{N-1}\widehat{u}(\xi_m)\,e^{\frac{2i\pi\xi_m k}{N}}\,2i\sin\left(\frac{h\pi\xi_m}{N}\right)\,e^{iR(\xi_m)}\right|\\ &= \sum_{k=0}^{N-1}\left|\frac{1}{N}\sum_{m=0}^{N-1}X_{k,m}\right|\end{aligned}$$

where

$$X_{k,m}=\widehat{u}(\xi_m)\,e^{\frac{2i\pi\xi_m k}{N}}\,2i\sin\left(\frac{h\pi\xi_m}{N}\right)\,e^{i\,R(\xi_m)}\,.$$

The Central Limit Theorem cannot be applied here to prove that the distribution of $TV(U_\varepsilon)$ has a Gaussian shape when N tends to infinity because the random variable $X_{k,m}$ are not independent and identically distributed. So we shall not prove here the Gaussian shape of the distribution of $TV(U_\varepsilon)$. However in practice, all the experiments showed that the distribution of $TV(U_\varepsilon)$ is very close to a Gaussian. Some examples are proposed in Fig.10.6 and 10.7, for which a million different phase shifts of the image from Fig.10.6(a) are done.

When $\mathbb{P}\left(TV(U_\varepsilon)\leq TV(u)\right)$ is estimated with a Gaussian model, the parameters of the model are estimated empirically. Here we use classical estimators for Gaussian laws.

Proposition 10.5 *Let u_ε^i be the i^{th} randomly dephased signal of ε, that is the i^{th} realization of U_ε. The estimator of the total variation mean of n dephased images is*

$$\widehat{\mu}=\frac{1}{n}\sum_{i=1}^{n}TV(u_\varepsilon^i)\,. \tag{10.6}$$

The unbiased estimator of the variance is

$$\widehat{\sigma^2}=\frac{1}{n-1}\sum_{i=1}^{n}\left(TV(u_\varepsilon^i)-\frac{1}{n}\sum_{i=1}^{n}TV(u_\varepsilon^i)\right)^2\,. \tag{10.7}$$

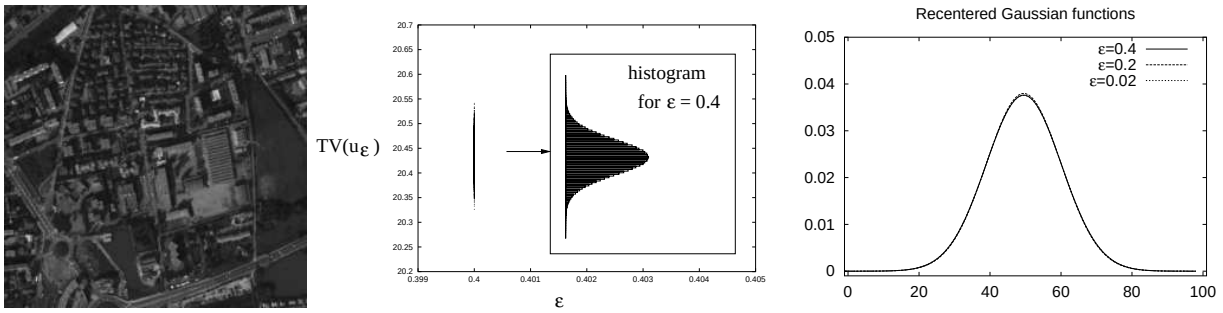

Figure 10.6: (a) Image u of size 256x256 (b) Histogram example with $\varepsilon = 0.4$ and 10^6 images $u_{0.4}$ (c) Comparison of the Gaussian shapes from Fig.10.7. Image u contains $N = 65536$ pixels, which is large enough to observe the Gaussian shape.

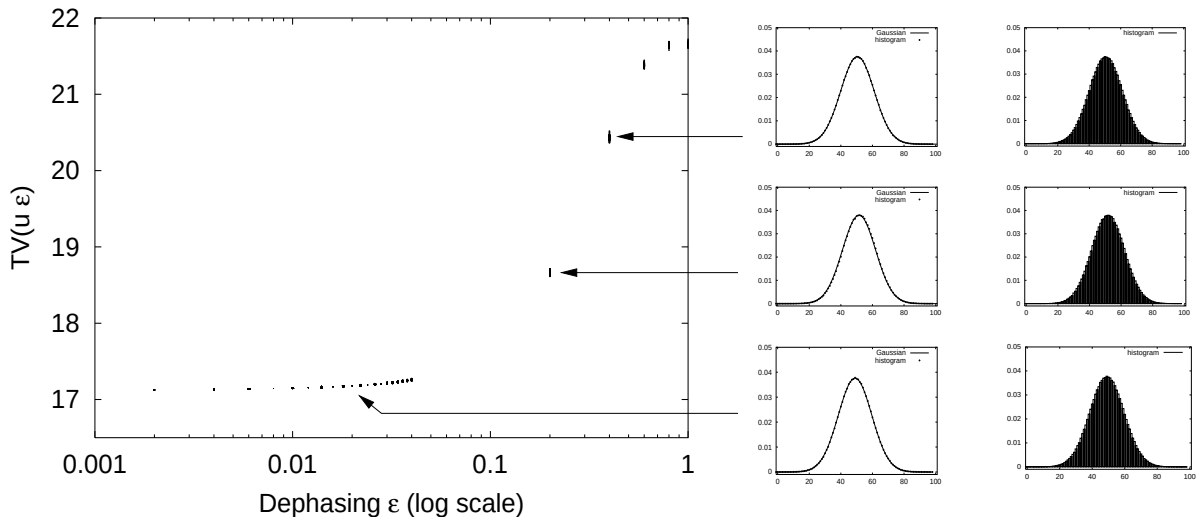

Figure 10.7: On the left: graph $(\varepsilon, TV(u_\varepsilon))$. $TV(u_\varepsilon)$ increases with ε. On the right: renormalized histograms of $TV(u_\varepsilon)$ for $\varepsilon = 0.02$, $\varepsilon = 0.2$ and $\varepsilon = 0.4$. Each one is calculated with 10^6 images u_ε. In the center: the corresponding Gaussian functions.

Proposition 10.6 *The estimator of the mean $\widehat{\mu}$ defined by (10.6) has normal cumulative probability function $\mathcal{N}(\mu, \frac{\sigma^2}{n})$.*

Proof: $\mathbb{E}(\widehat{\mu}) = \frac{1}{n}\sum_{i=1}^{n}\mathbb{E}(TV(U_\varepsilon^i))$. Since $\mathbb{E}(TV(U_\varepsilon^i)) = \mu$ for all i, we have $\mathbb{E}(\widehat{\mu}) = \mu$.
All $TV(U_\varepsilon^i)$ are independent because the U_ε^i are, hence $\sigma^2(\widehat{\mu}) = \frac{1}{n^2}\sum_{i=1}^{n}\sigma^2(TV(U_\varepsilon^i))$. Since $\sigma^2(TV(U_\varepsilon^i)) = \sigma^2$ for all i, then $\sigma^2(\widehat{\mu}) = \frac{\sigma^2}{n}$. The variance of the mean decreases with n.

□

The proposed definition of the phase coherence has the main advantage to use a probabilistic framework which avoids the difficult problem of defining parameters and the justification of the choice of their values.

10.2.3 Two estimation algorithms

Let u be the original image, the total variation of which is $TV(u)$. For ε fixed, the estimation of F_ε can be done from n different randomly dephased images u_ε, if n is large enough.

Algorithm 1 (Empirical estimation)

1. *Build n images u_ε^i, $i = 1 \dots n$*
2. *Compute $M = \{$number of u_ε^i such that $TV(u_\varepsilon^i) \leq TV(u)\}$*
3. *Estimate $\mathbb{P}(TV(U_\varepsilon^i) \leq TV(u)) \approx \frac{M}{n}$*
4. *Deduce $F_\varepsilon(u) = -\log_{10}\mathbb{P}(TV(U_\varepsilon) \leq TV(u)) \approx -\log_{10}\left(\frac{M}{n}\right)$*

Algorithm 2 (Gaussian estimation)
We suppose that $TV(u_\varepsilon) \sim \mathcal{N}(\mu, \sigma^2)$

1. *Build n images u_ε^i, $i = 1 \dots n$*
2. *Estimate $\widehat{\mu}$ and $\widehat{\sigma^2}$ empirically with (10.6) and (10.7).*
3. *Estimate $\mathbb{P}(TV(U_\varepsilon) \leq TV(u)) \approx \frac{1}{2}\left(1 + erf(\frac{TV(u)-\widehat{\mu}}{\widehat{\sigma}\sqrt{2}})\right)$*
4. *Deduce $F_\varepsilon(u) = -\log_{10}\mathbb{P}(TV(U_\varepsilon) \leq TV(u)) \approx -\log_{10}\left[\frac{1}{2}\left(1 + erf(\frac{TV(u)-\widehat{\mu}}{\widehat{\sigma}\sqrt{2}})\right)\right]$*

Let us remark that for both algorithms, the first step is the slowest one, as the process of the Fourier transform and the inverse Fourier transform for each image u_ε is time consuming. The complexity of the Fast Fourier Transform (FFT) algorithm is $O(N\log_2 N)$ [29], so in practice we are often limited to work with the images of small size. However the estimation of $F_\varepsilon(u)$ is all the better since n is large, which further increases the computational constraints.

10.2.4 Comparison of the proposed estimation methods

In Fig.10.9, we compare the empirical and Gaussian estimations on three real images, one sharp and two blurred, shown in Fig.10.8. Let us first consider the empirical estimation.

As announced in Subsection 10.2.2, the empirical estimation does not give correct values of the phase coherence if the probability $\mathbb{P}\left(TV(U_\varepsilon) \leq TV(u)\right)$ is too small, i.e. $F_\varepsilon(u)$ is large. So we cannot expect exact values of $F_\varepsilon(u)$ for sharp images with the empirical estimation, because such images have large phase coherence. This is observed in Fig.10.9(a). No image u_ε has a total variation such that "$TV(u_\varepsilon) \leq TV(u)$" (because the image u is so sharp that the phase shift increases its total variation and the event "$TV(u_\varepsilon) \leq TV(u)$" is so rare, that the empirical estimation requires many trials u_ε) so the empirical estimation yields $F_\varepsilon(u) = -\log_{10} 0 \to +\infty$, which has been thresholded to 100 for the numerical applications. One can improve the empirical estimation by increasing the number of trials of u_ε.

When the image is blurred Fig.10.9(b-c), "$TV(u_\varepsilon) \leq TV(u)$" is not a rare event and the empirical estimation gives satisfactory results, which are similar to the ones of the Gaussian estimation. Moreover for large $F_\varepsilon(u)$ the Gaussian estimation is robust, contrarily to the empirical estimation. This is the reason why the Gaussian estimation will be preferred to the empirical estimation in the next experiments.

(a) (b) (c)

Figure 10.8: (a) Image u of size 128x128 with no additive Gaussian blur (b-c) Additive Gaussian blur with standard deviation $std = 0.5$.

10.3 Probabilistic model for the sharpness of an image

In the previous section, we have proposed a definition and an estimation of the phase coherence of an image u. It is defined by

$$F_\varepsilon(u) = -\log_{10} \ \mathbb{P}\left(TV(U_\varepsilon) \leq TV(u)\right)$$

where $|\varepsilon| \leq 1$ is the parameter indicating the amplitude of the random phase shift of u.

Since we want to detect images which are sharp, we are not interested in all the values of $|\varepsilon|$, but only in the smaller ones. Indeed, the idea is to measure the image sharpness from the sensitivity to the random phase shift of the Fourier spectrum. Since the initial hypothesis is that a sharp image is very

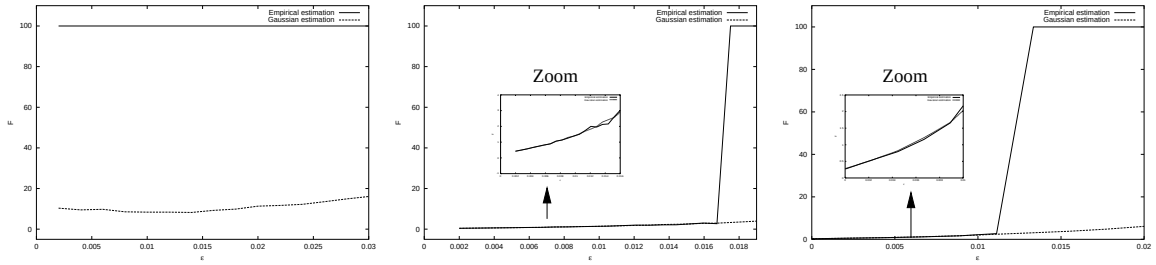

(a) (b) (c)

Figure 10.9: Comparison of the empirical and Gaussian estimation of $F_\varepsilon(u)$: the curves $(\varepsilon, F_\varepsilon)$ for both estimations associated to the images of Fig.10.8(a-b-c) are given with respectively 2000, 2000 and 1000 images u_ε tested for each value of ε. The results obtained with the empirical and the Gaussian estimation are similar when the value of $\mathbb{P}\left(TV(U_\varepsilon) \leq TV(u)\right)$ is large enough, that is for small values of $F_\varepsilon(u)$. For smaller values of $\mathbb{P}\left(TV(U_\varepsilon) \leq TV(u)\right)$, the empirical estimation fails because it requires a huge number of images u_ε to have at least one image u_ε such that $TV(u_\varepsilon) \leq TV(u)$. Note the thresholded curve for the empirical estimation for large $F_\varepsilon(u)$.

sensible to the phase shift, we shall test very small phase shift to evaluate this sensibility, which leads us to consider $\varepsilon \to 0$. The detection of the sharpness of an image is then related to the measure of

$$F_{0^+}(u) = \lim_{\substack{\varepsilon \to 0 \\ \varepsilon > 0}} F_\varepsilon(u)\,. \tag{10.8}$$

Lemma 10.7 and Proposition 10.8 give two results on the derivative of $TV(u_\varepsilon)$ when $\varepsilon \to 0$.

Lemma 10.7 *The local estimator of $TV(u_\varepsilon)$ is*

$$TV(u_\varepsilon) = TV(u) - \varepsilon < \mathit{curv}(u), \varphi > + o(\varepsilon) \tag{10.9}$$

where

- $|\varepsilon| \leq 1$ *is the parameter indicating the amplitude of the random phase shift of* u,
- $u(k,l)$, $k = 0 \ldots M-1$ *and* $l = 0 \ldots N-1$, *is the considered discrete signal,*
- a *and* b *are the images of the local phase shift, that is each pixel is the realization of a uniform distribution in* $[-\frac{1}{2}, \frac{1}{2}]$ *with the constraints*

$$\begin{aligned} a(-p,-q) &= -a(p,q) \\ b(-p,-q) &= -b(p,q) \end{aligned} \tag{10.10}$$

- φ *is the inverse Fourier transform of* $i\left(\frac{a(p,q)p}{M} + \frac{b(p,q)q}{N}\right) \cdot \widehat{u}(p,q)$, *with* $\widehat{u}(p,q)$ *the Fourier transform of* u, $p = 0 \ldots M-1$ *and* $q = 0 \ldots N-1$,

- *curv*(u) *is the curvature of* u *defined by*

$$\textit{curv}(u) = \ \textit{div}\ \left(\frac{Du}{|Du|}\right).$$

Proof: By definition, the inverse Fourier transform of $\widehat{u}$ is

$$u(k,l) \ = \ \frac{1}{M\cdot N}\sum_{p,q} e^{i\left(\frac{kp}{M}+\frac{lq}{N}\right)}\ \widehat{u}(p,q)\,.$$

By definition, u_ε is obtained after a random phase shift of the Fourier transform of u, that is

$$\widehat{u_\varepsilon}(p,q) \ = \ \widehat{u}(p,q)\ \ e^{i\varepsilon\left(\frac{a(p,q)p}{M}+\frac{b(p,q)q}{N}\right)}.$$

Approximating the exponential function at the first order when $\varepsilon \to 0$ yields

$$\begin{aligned}\widehat{u_\varepsilon}(p,q) &= \widehat{u}(p,q)\ \ \left(1+\varepsilon i\left(\frac{a(p,q)p}{M}+\frac{b(p,q)q}{N}\right)+o(\varepsilon)\right)\\ &= \widehat{u}(p,q)+\varepsilon\ \widehat{g}(p,q)\ \widehat{u}(p,q)+o(\varepsilon)\end{aligned} \tag{10.11}$$

where $\widehat{g}(p,q) = i\left(\frac{a(p,q)p}{M}+\frac{b(p,q)q}{N}\right)$. By linearity of the inverse Fourier transform, we deduce that

$$u_\varepsilon(k,l) = u(k,l)+\varepsilon\ \varphi(u)\ \ +o(\varepsilon) \tag{10.12}$$

where $\varphi(u)$ is the inverse Fourier transform of $\widehat{g}(p,q)\cdot\widehat{u}(p,q)$. Let us now compute the total variation of u_ε as given in (10.12).

$$TV(u_\varepsilon) = TV(u+\varepsilon\ \varphi(u)\ \ +o(\varepsilon))\,.$$

In order to compute $TV(u+\varepsilon\ \varphi(u)\ \ +o(\varepsilon))$, let us first compute the more general term $TV(u+\varepsilon\ v)$, where v is another image.

$$\begin{aligned}TV(u+\varepsilon\ v) &= TV(u)+\varepsilon\ <\nabla TV(u), v>+o(\varepsilon)\,.\\ \nabla TV(u)\cdot v &= \frac{d}{dt}TV(u+t\cdot v)_{t=0}\\ &= \frac{d}{dt}\int\left(\frac{\sqrt{|Du+tDv|^2}}{\sqrt{Du^2+2<Du,Dv>+t^2Dv^2}}\right)_{t=0}\\ &= \int\frac{<Du,Dv>}{|Du|} = \int v\cdot\ \textit{div}\ \left(\frac{Du}{|Du|}\right).\end{aligned} \tag{10.13}$$

By definition of the curvature of u we have

$$\begin{aligned}TV(u_\varepsilon) &= TV(u)+\varepsilon<\nabla TV(u),\varphi>+o(\varepsilon)\\ &= TV(u)-\varepsilon<\textsf{curv}(u),\varphi>\ +o(\varepsilon)\,.\end{aligned} \tag{10.14}$$

□

Now that a local estimator of $TV(u_\varepsilon)$ has been given, we study the behavior of $TV(u_\varepsilon)$ when ε tends to zero since we are interested in the sensitivity of the total variation for a very small phase shift.

Proposition 10.8 $\lim_{\varepsilon \to 0} \frac{\mathbb{E}(TV(u_\varepsilon)) - TV(u)}{\varepsilon} = 0$

Proof: From the proof of Lemma 10.7, we have

$$\widehat{u_\varepsilon}(p,q) = \widehat{u}(p,q) \;\; e^{i\varepsilon\left(\frac{a(p,q)p}{M} + \frac{b(p,q)q}{N}\right)},$$

where a and b are the images of the local phase shift, that is each pixel is the realization of a uniform distribution in $[-\frac{1}{2}, \frac{1}{2}]$. Let us note X the associated random variable $\vec{X} \sim \mathcal{U}[-\frac{1}{2}, \frac{1}{2}]^2$. From (10.9),

$$\begin{aligned} \mathbb{E}_X(TV(u_\varepsilon)) &= \mathbb{E}_X(TV(u) - \varepsilon < \text{curv}(u), \varphi > \; + o(\varepsilon)) \\ &= \mathbb{E}_X(TV(u)) - \varepsilon\, \mathbb{E}_X < \text{curv}(u), \varphi > + o(\varepsilon) \\ &= TV(u) - \varepsilon\, \mathbb{E}_X < \text{curv}(u), \varphi > + o(\varepsilon) \end{aligned} \tag{10.15}$$

since $TV(u)$ does not depend on X. Moreover we have

$$\begin{aligned} \widehat{\varphi}(p,q) &= \widehat{g}(p,q)\, \widehat{u}(p,q) \\ &= \frac{ip}{M}\widehat{u}(p,q)a(p,q) \; + \; \frac{iq}{N}\widehat{u}(p,q)b(p,q) \\ &= \left(\frac{ip}{M}\widehat{u}(p,q), \frac{iq}{N}\widehat{u}(p,q)\right) \cdot (a(p,q), b(p,q)) \\ \widehat{\varphi} &= \widehat{\nabla u} \cdot \vec{X} \end{aligned}$$

Hence

$$\mathbb{E}_X(TV(u_\varepsilon)) = TV(u) - \varepsilon\, \mathbb{E}_X < \text{curv}(u), IFT(\widehat{\nabla u} \cdot \vec{X}) > + o(\varepsilon) \tag{10.16}$$

where IFT is the inverse Fourier transform. To prove Proposition 10.8, we study now

$$\lim_{\varepsilon \to 0} \frac{\mathbb{E}(TV(u_\varepsilon)) - TV(u)}{\varepsilon}.$$

Thanks to (10.16), we have

$$\lim_{\varepsilon \to 0} \frac{\mathbb{E}(TV(u_\varepsilon)) - TV(u)}{\varepsilon} = \mathbb{E}_X < \text{curv}(u), IFT(\widehat{\nabla u} \cdot \vec{X}) > .$$

As $\vec{X} \sim \mathcal{U}[-\frac{1}{2}, \frac{1}{2}]^2$, we can replace $\vec{X}$ with $-\vec{X}$ in $< \text{curv}(u), IFT(\widehat{\nabla u} \cdot \vec{X}) >$, so that

$$\begin{aligned} < \text{curv}(u), IFT(\widehat{\nabla u} \cdot (-\vec{X})) > &= < \text{curv}(u), IFT(-(\widehat{\nabla u} \cdot \vec{X})) > \\ &= < \text{curv}(u), -IFT(\widehat{\nabla u} \cdot \vec{X}) > \\ &= - < \text{curv}(u), IFT(\widehat{\nabla u} \cdot \vec{X}) > \end{aligned}$$

by linearity of the inner product and the inverse Fourier transform. Hence $< \text{curv}(u), IFT(\widehat{\nabla u} \cdot \vec{X}) >$ is odd with respect to X. Since $\vec{X}$ is uniformly distributed in $[-\frac{1}{2}, \frac{1}{2}]^2$, the probability to have $< \text{curv}(u), IFT(\widehat{\nabla u} \cdot \vec{X}) >$ is equivalent to the probability to have $- < \text{curv}(u), IFT(\widehat{\nabla u} \cdot \vec{X}) >$, so that $\mathbb{E}_X < \text{curv}(u), IFT(\widehat{\nabla u} \cdot \vec{X}) >= 0$. This result is confirmed by numerical experiments (Fig.10.10). □

Proposition 10.8 shows that the behavior of $TV(u_\varepsilon)$ is regular when ε tends to zero, which means that the mean value of $TV(u_\varepsilon)$ decreases regularly to $TV(u)$. This result guarantees the stability of the computation of F_{0^+} in the numerical experiments.

In this section, the probabilistic model for the sharpness of an image has been presented and the associated detector F_{0^+} has been defined. It is based on the observation that the total variation of a sharp image is more sensitive to a small phase shift than the total variation of a smooth image. The following section presents some numerical experiments obtained with the detector F_{0^+}.

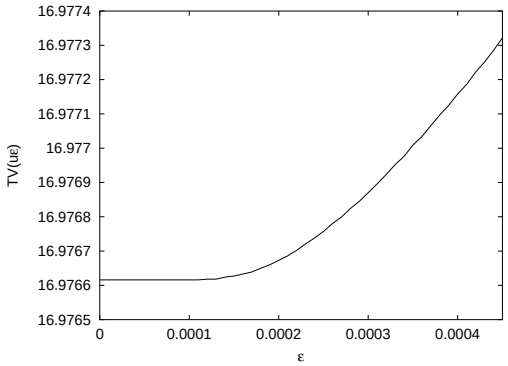

Figure 10.10: Visualization of $TV(u_\varepsilon)$. For ε fixed, the curve represents the mean over 10000 values of $TV(u_\varepsilon)$. As proved in Proposition 10.8, the derivative of $TV(u_\varepsilon)$ has zero mean when ε vanishes.

10.4 Numerical experiments

As the Gaussian estimation has shown better results than the empirical estimation (Fig.10.9), we will use this estimation in all the following experiments. In the first experiment, we compute the phase coherence of blurred images in order to check that blurred images are not detected as sharp. In the second experiment, we show that F_{0^+} is a good detector of sharp images.

Experiment 1

Fig.10.11 shows the relation between $F_{0^+}(u)$ and the image blur value. The original image u_0 is a subpart of a high-resolution satellite image. The studied images are built by convolution of u_0 with several Gaussian kernels G_σ with variance σ^2.

$$u = u_0 \star G_\sigma$$

The measure of F_{0^+} is sensitive to a small amount of blur. It allows to detect sharp images without measuring precisely the blur.

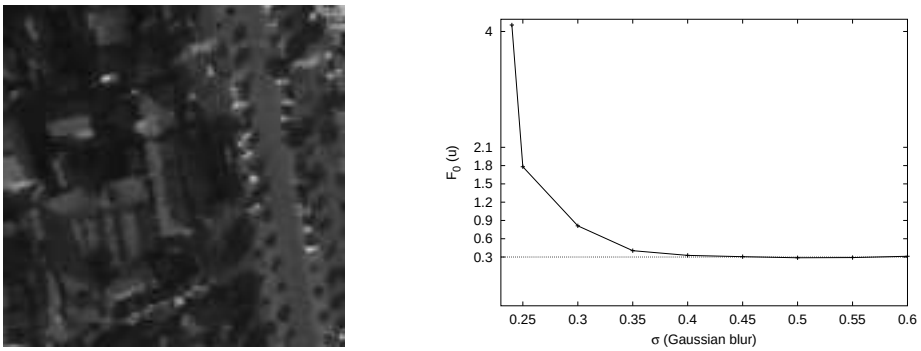

(a) (b)

Figure 10.11: (a) Sharp image u_0 of size 128x128 (b) Curve showing the relation between the level of blur of u and the value of the phase coherence $F_{0+}(u)$. The coherence of phase is estimated with 1000 images u_ε. The displayed limit value is $-\log_{10}(0.5) = 0.3010$ which corresponds to $\mathbb{P}\left(TV(U_\varepsilon) \leq TV(u)\right) = 0.5$.

Experiment 2

We present here a way to validate the detector F_{0+}. This study should be completed in future work. The ability of our sharpness model to detect automatically sharp images is tested on the image database [46]. It contains 174 images:

- 28 images are *reference images*, which are not globally sharp but they contain sharp zones,
- 146 images are *blurred images* obtained by convolution of the *reference images* with Gaussian kernels with different variances.

Let us first test the detector F_{0+} on the *reference images* and then on the *blurred images*.

Test on the reference images The *reference images* are sharp images, but they are not globally sharp since some out-of-focus zones, such as the background, may be blurred. In order to test the ability of F_{0+} to detect blurred zones in sharp images, the calculus of F_{0+} is done on sub-images of size 128x128. The choice of such a small sub-image size is motivated by a fast computation of F_{0+}. The sharpness model succeeds in classifying correctly both sub-images of Fig.10.12.

In order to take into account the disparity of the detector response for sharp and blurred zones of an image, all the *reference images* are studied on a sharp 128x128 subpart. 18 images out of the 28 are well classified by the detector since their chosen subpart have $F_{0+} \geq 100$, which indicates sharp images. Some examples are shown in Fig.10.13. The 10 other *reference images* have a smaller F_{0+} value as shown in Fig.10.14.

Figure 10.12: This image classified as sharp in [46] has effectively sharp zones (the focus has been done on the corpse of the butterfly) and some blurred zones (surrounding flora). The computation of sharpness on both windows classifies the 'flora' as blurred ($F_{0^+}(u_{\text{flora}}) = 2.03$) and the 'wing of the butterfly' as sharp ($F_{0^+}(u_{\text{wing}}) \geq 100$).

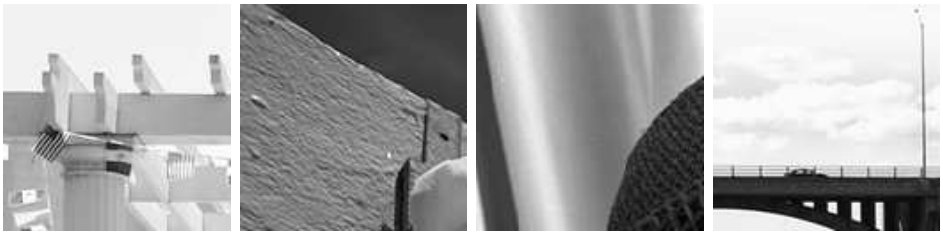

Figure 10.13: Some 128x128 subparts of sharp images well classified by the detector ($F_{0^+} \geq 100$).

(a) $F_{0+} = 2.9$ (b) $F_{0+} = 7.5$ (c) $F_{0+} = 2.3$ (d) $F_{0+} = 11.3$ (e) $F_{0+} = 12.8$

(f) $F_{0+} = 12.9$ (g) $F_{0+} = 0.87$ (h) $F_{0+} = 7.85$ (i) $F_{0+} = 4.3$ (j) $F_{0+} = 14.1$

Figure 10.14: 128x128 subparts of sharp images with smaller F_{0+}.

Test on the blurred images The sharpness detector is also tested on the *blurred images*. The image database [46] contains approximatively five blurred versions for each *reference image*. Here we study the five blurred versions of the butterfly image (Fig.10.12). Fig.10.15 shows the F_{0+} values obtained on the butterfly image blurred with a Gaussian kernel of standard deviation σ. As expected, the value of the phase coherence decreases with the level of blur, i.e. decreases as σ increases.

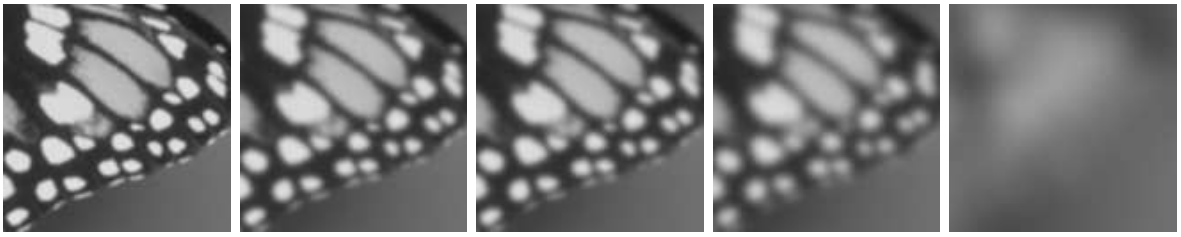

(a) $\sigma = 0.90$ and $F_{0+} = 8.6$ (b) $\sigma = 1.70$ and $F_{0+} = 7.9$ (c) $\sigma = 1.85$ and $F_{0+} = 7.6$ (d) $\sigma = 2.85$ and $F_{0+} = 5.9$ (e) $\sigma = 11.33$ and $F_{0+} = 3.1$

Figure 10.15: The five 128x128 subparts of the database [46]. They have a decreasing phase coherence as blur increases.

10.5 Conclusion

In this section, we have presented a new tool to detect sharp images. The detection is based on a new phase coherence measure. This approach is different from the one proposed by Morrone for two main reasons. First the measure proposed by Morrone is computed locally to detect edges: to each pixel is associated a phase coherence measure. On the contrary, the phase coherence defined in this thesis is measured globally, a unique value is assigned for a given image or image subpart. Second, the phase coherence, as defined by Morrone, is large if all the sinusoids of the Fourier transform have same phase. Here the phase coherence is measured with the sensitivity of the image to small phase shifts: the sharper the image is, the more sensitive to small phase shifts the image is. The sensitivity is measured with the increase of the total variation since the phase shift of a single sinusoid may add oscillations around sharp transitions.

The proposed sharpness detector has the nice parameter-free property which makes this detector useful for many applications. This detector is not dedicated to a unique kind of image. Let us give some examples of possible applications that may require automatic sharpness detection.

In the field of digital cameras, the detector could be useful to evaluate automatically the sharpness of the image. The photographer might want to know if the image is sharp or not in order to take another photograph if it is not sharp. To that aim, the detector should be put inside the camera and it should warn the photographer if the image is not sharp. Of course, for some specific applications, blurred images are also interesting and they should be kept. For example, blurred images may be artistically beautiful and they should be preserved. However, in everyday life blur is often an undesired effect of the bad stabilization of the camera during the image acquisition. A blurred image is often not satisfactory and in such cases the detector can help the photographer.

Another application is the image classification. Assume that an optical device provide a very large number of images and that only a small amount are sharp. The automatic detection of those sharp images would save time, moreover since the detector is universal, the classification is still possible even if the database contain different types of images (landscapes, indoor images, ...).

Another application of the detector is the automatic detection of the region of interest in an image, which are often the sharp zones. In most case, it is impossible to obtain a perfect focus for all scene objects since they do have not the same depth. So the sharp zones can be detected and consequently the regions of interest.

The last but not least application of the detector is the image restoration, especially the blind deblurring. Recovering the sharp image from its blurred version without knowing the blur kernel is a challenging problem. The restoration of a blurred image can be automatically done thanks to the sharpness detector. Both the sharp image and the blur kernel can be identified. This major image application in the image processing field will be studied in Part IV.

Chapter 11

Ringing detection

11.1 A description of classical methods

In the image compression literature, many papers refer to the measure of ringing, but they do not detect it specifically. They measure the distortion between the original and the processed images. In this thesis, we consider the more difficult problem of the ringing detection without a reference image. Nevertheless, we recall here some ringing measures developed in the image compression framework.

The peak signal-to-noise ratio (PSNR) or the mean square error (MSE) are often used as objective measures of image quality. However they are not adapted to measure the degradation introduced by artifacts, because artifacts have a structure which can be considered as information instead of noise by the PSNR measure. This remark is true for the ringing artifact, whose oscillatory structure is not well measured with the PSNR. In the literature, new ringing measures have been specifically developed. The underlying hypothesis is that the ringing appear near sharp edges of the image. The recent perceptual measures are

- the VRM measure (Visible Ringing Measure) defined by Oguz [39] and recently used by Yang *et al.* [58] to suppress ringing after a compression process. As the ringing appears as unexpected oscillations around edges, the idea of the VRM is to measure the variance locally on small size window (4x4) around edges. The regions near major edges are detected by a series of morphological operations. First of all, an edge map is generated by a Sobel operator. Then, this map is cleaned by applying successively a denoising filter and a line-curve linking algorithm. Finally, a binary closing followed by a dilatation of the edge map produces the final edge map.

- the measure defined by P.Marziliano [31] takes into account the length and the amplitude of the oscillations on each sides of the edge. The ringing measure is joined to the perceptual blur measure.

11.2 Ringing resulting from blind deconvolution

The blind deconvolution problem consists in the removal of blur from an observed image u. Any image acquisition system, which cuts off too many high frequencies, blurs images. Let us now model this system to describe the degradation of the original image. First, the low-pass filtering is generally modeled by the convolution of the "nice" and artifact-free original image u_0 with a filter k_0. Second,

as most acquisition systems add noise (n), this system can be modeled by

$$u = k_0 \star u_0 \ + \ n \ ,$$

or equivalently in the Fourier domain

$$\widehat{u} = \widehat{k_0} \cdot \widehat{u_0} \ + \ \widehat{n} \ .$$

The brutal deconvolution consists in the evaluation of u_0 by the inverse Fourier transform of $\frac{\widehat{u}}{\widehat{k_0}}$. But this method is not efficient to deblur an image because of the noise term. When $\widehat{k_0}(\xi)$ is small (we note ξ the frequency), the term $\frac{\widehat{n}}{\widehat{k_0}}(\xi)$ may become very large and then the image may have a predominant oscillation frequency ξ. In order to solve this ill-posed problem and to avoid those spurious oscillations, one must necessarily introduce some additional assumptions. One of the classical method is called Tikhonov regularization [52], which adds a regularization constraint on u_0 to penalize the oscillations. One of its simplest expression is given by the minimization of the energy

$$E(u_0) = \underbrace{\int |Du_0|^2}_{\text{smoothness constraint}} + w \underbrace{\int (u - k_0 \star u_0)^2}_{\text{data fidelity}}$$

where Du_0 is the differential of u_0, and $w \in \mathbb{R}^+$ is the weight on fidelity term. The solution of the minimization of $E(u_0)$ is given in the Fourier domain by

$$\forall \xi \in \mathbb{R}^2, \quad \widehat{u_0}(\xi) = \frac{\widehat{k_0}^*(\xi)}{\left|\widehat{k_0}(\xi)\right|^2 + \frac{|\xi|^2}{w}} \cdot \widehat{u}(\xi) \tag{11.1}$$

where $\widehat{k_0}^*$ is the conjugate complex of $\widehat{k_0}$. In the literature, (11.1) is a special case of *Wiener filtering*, and this is the case we will use in the experiments. Deblurring with such kind of filter may still introduce oscillations, which is what we call the ringing resulting from blind deconvolution. An example of the deconvolution with the Wiener filter is shown in Fig.11.1. As the convolution filter k_0 is unknown, we have tested the Gaussian filter

$$k_0 = e^{-2g^2\pi^2|\xi|^2}$$

with $g = 2$ and $w = 50$. As the choice of the Gaussian does not correspond probably to the real convolution filter and as the weight on fidelity term w is big, which penalizes more the fidelity term than the smoothness of u_0, it is not surprising to observe ringing on the deblurred image.

Our goal here is to define a detector for this kind of ringing. It is based on the important particularity that its oscillations have the same frequency modulus on the whole image.

11.2.1 Notations and definitions

We have observed that the oscillation frequency of the ringing occurring after a blind deconvolution is the same on the whole image. We will now use this observation to detect automatically the ringing. We want to detect the ringing by showing that its oscillations have same frequency, or equivalently same period. Let us define some useful variables. In an image with ringing, one can observe that edges are replicated into vanishing parallel edges. Even if some kind of oscillations are visible in the X and Y axes, ringing has clearly its own direction: the gradient direction Du, which is orthogonal to the object edges (Fig.11.2).

(a) (b)

Figure 11.1: (a) Image u (b) Image improperly deblurred with a Wiener filter. Ringing appears on the whole image.

Definition 11.1 (Ringing direction signal) *For each point $x \in \mathbb{R}^2$ of an image u, we define the ringing direction signal by*

$$\forall s \in \mathbb{R}\,, \quad v(s) \;=\; u\left(\, x \,+\, s\,\frac{Du}{|Du|}\,\right) \quad .$$

As a first approximation, we can use the nearest neighbor approximation to estimate u at $\left(\, x \,+\, s\,\frac{Du}{|Du|}\,\right)$. We note δ (integer number) the oscillation half-period. It represents the spread of either a fall or a rise between two extremal values (Fig.11.3). In practice, we consider $\delta \in [1, D]$, with D fixed to 20, which already represents a long distance between the extremal values. Indeed, in most images, when the distance between two points is 20 pixels then these points may not belong to the same object and can then be considered as independent.

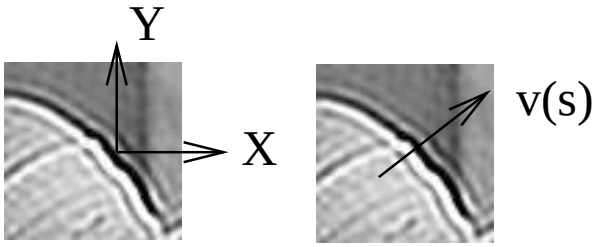

Figure 11.2: Subpart of Fig.11.1-(b). We study the ringing in the gradient direction and not along the X and Y axes. A cut v of the image is studied in the gradient direction.

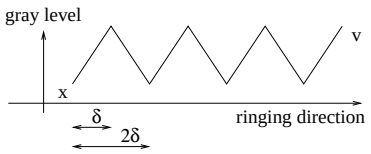

Figure 11.3: Example of an oscillating signal with half-period δ.

Now that the *ringing direction signal* has been defined, let us specify the term *oscillation*. Even if *oscillations* are perceptually clear on images, we formalize mathematically this word by using points of the ringing direction signal spaced by δ. We shall say that points of v oscillate if their gray level is alternatively larger or lower than the previous one.

Definition 11.2 (point oscillation) *Let $i \in \mathbb{N}$. Let $(\delta, a) \in \mathbb{N}^2$ and v be the ringing direction signal*

at pixel x belonging to image u. The points $v(0)\,,\ v(\delta)\,,\ v(2\delta)\,,\ \ldots\,,\ v(a\delta)$ oscillate if

$$\forall i \in [0, a-1],\ \ S_i \ \cdot\ S_{i+1} < 0\ ,$$

where $S_i = sign\,(v(i\delta) - v((i+1)\delta))$ is the sign of the difference between two consecutive point gray levels.

Notation: In this definition, the sentence "*the points $v(0)\,,\ v(\delta)\,,\ v(2\delta)\,,\ \ldots\,,\ v(a\delta)$ oscillate*" is long and it will be replaced in all the following by the convenient notation $\mathbf{E_a}$, where a is an integer. For a given pixel x belonging to the image u, with ringing direction signal v at x, we shall note E_a the event "$v(0)\,,\ v(\delta)\,,\ v(2\delta)\,,\ \ldots\,,\ v(a\delta)$ oscillate" if $a \geq 0$. Symmetrically if $a \leq 0$, E_a is the event "$v(0)\,,\ v(-\delta)\,,\ v(-2\delta)\,,\ \ldots\,,\ v(a\delta)$ oscillate". Hence depending on whether a is positive or negative, we study the forward or backward oscillations.

It is important to understand here that the definition of *oscillation* does only compare the gray level of points spaced by δ in the gradient direction v and not the points between those considered points. So there is no constraint on the monotonicity of v between two successive considered points. Perceptually the longer the oscillations are, the more perceptive the phenomenon is. So this model of the ringing should also take into account the length of the oscillations.

Definition 11.3 (maximal length of oscillation) *Let us note $N_\delta(x)$ the maximal length of oscillation at pixel x belonging to image u.*

$$N_\delta(x) \ = \ a_{\max} \ + \ b_{\max}\ ,$$

where $a_{\max} = \arg\max_{a \geq 0} E_a - 1$ and $b_{\max} = \arg\max_{b \leq 0} E_b - 1$.

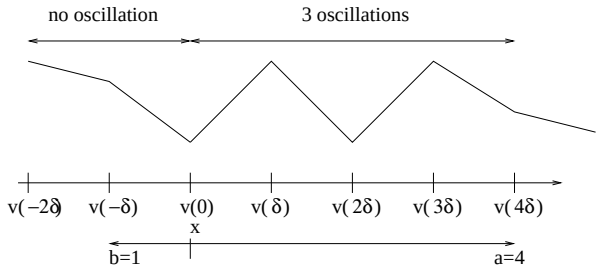

Figure 11.4: Example for the computation of $N_\delta(x)$. On the right side of x, there are three oscillations. first: $v(0), v(\delta), v(2\delta)$, second: $v(\delta), v(2\delta), v(3\delta)$, third: $v(2\delta), v(3\delta), v(4\delta)$. So $a_{\max} = 3$.

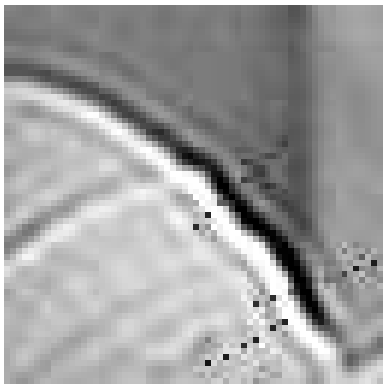

Figure 11.5: Subpart of Fig.11.1-(b). For three points x of the image belonging to the hat edge, we have $N_3(x) = 5$: the associated oscillations are shown in black.

An example in given in Fig.11.4 where $N_\delta(x) = 3$. Some oscillating points are represented in Fig.11.5. In order to detect the half-period of oscillation δ, we define

$$H(\delta) = \sum_x N_\delta(x) \tag{11.2}$$

which is high for δ associated to long oscillations, and the histogram

$$H(n, \delta) = \#\{x\,;\, N_\delta(x) = n\}\ , \tag{11.3}$$

where $\#$ should be read as "the number of". These two measures highlight the ringing frequency as shown in Fig.11.6 and 11.7 (image of Fig.11.1-(b)). These measures are visually convincing, but the ringing detector still has to be defined. Let us remark that no criterion has been given on x. All point of the image are studied. We could have selected points with high gradient to consider points near edges, where the ringing phenomenon is obvious in general. But we intend to build a parameter-free detector, that is without parameter on the gradient modulus.

See also on Fig.11.7 the two local maxima of the curve $H(\delta)$ in $\delta = \delta_0 = 3$ and $\delta = 9$. The first maximum of $H(\delta)$ corresponds to the oscillation period $P = 2 \times \delta_0 = 6$. It indicates that the distance between the local minimum and the next local maximum is δ_0 and that the distance between two local maxima (or two local minima) is P. The second maximum of $H(\delta)$ is linked to the first one by $\delta = \delta_0 + P = 3 \times \delta_0 = 9$, which is the distance between the local minimum and the second local maximum.

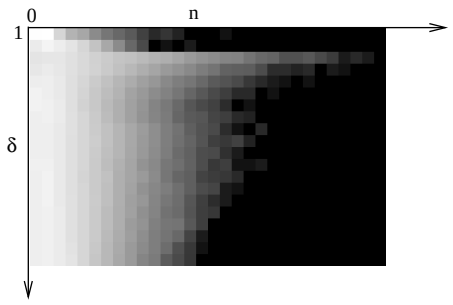

Figure 11.6: Histogram $\log(H(n, \delta))$ with $n \in [0, 30]$ and $\delta \in [1, 20]$. Line 3 ($\delta = 3$) highlights the oscillation half-period.

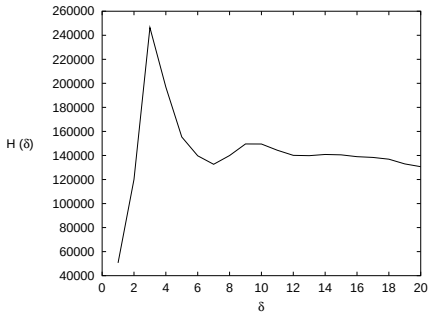

Figure 11.7: The maximum of $H(\delta)$ is in $\delta = 3$, which is the ringing oscillation half-period.

11.2.2 Statistical a contrario detection

Now that we have introduce some useful notations and definitions, let us describe the detector. Our approach is based on a statistical *a contrario* detection. We observed that ringing is a periodic phenomenon with the same frequency on the whole image. This particularity is used to detect such images with an *a contrario* approach: we detect ringing when one half-period δ of oscillation is highly represented, which is an unlikely event with respect to a naive random assumption of the distribution of the oscillation half-periods. As mentioned before, the oscillations are measured in the ringing direction. Given the gradient direction for each pixel, the problem boils down to the study of the cuts of an image. The length and the period of the oscillations of the gray levels along 1D lines are measured. We present here two possible approaches, which are based on some independence assumption that represents a simplified model of real images.

11.3 Naive model 1

The first model is based on the study of S_i with i integer. From Definition 11.2, S_i is the sign of the difference between two consecutive point gray levels:

$$S_i = \text{sign}\,(v(i\delta) - v((i+1)\delta))\ .$$

A positive and negative sign means a rise and a fall, respectively. This model is interesting since the oscillations are the succession of rise and fall. In this model, the S_i are assumed to be independent and identically distributed (i.i.d.) variables. We shall not make any assumption on the distribution of the $v(i\delta)$, since we only study S_i in this model. The study of $v(i\delta)$ will be done in the naive model 2. The i.i.d. assumption on S_i is a simplified model since in real images there is no distribution of v that ensures the independence of the S_i. However here we assume they are i.i.d., which means that S_i takes its value in the set $\{+,-\}$ independently of the values of S_j with $j \neq i$. The distribution of S_i is a Bernoulli distribution with $p = q = \frac{1}{2}$:

$$\mathbb{P}(S_i = +) = \mathbb{P}(S_i = -) = \frac{1}{2}\,.$$

For example the computation of $\mathbb{P}(E_2)$, which is the probability to have at least one oscillation, is immediate when assuming the independence of S_0 and S_1 (see Table 11.8).

$$\begin{aligned}\mathbb{P}(E_2) &= \mathbb{P}\left((S_0 > 0 \text{ and } S_1 < 0) \text{ or } (S_0 < 0 \text{ and } S_1 > 0)\right)\\ &= \mathbb{P}(S_0 > 0 \text{ and } S_1 < 0) \ + \ \mathbb{P}(S_0 < 0 \text{ and } S_1 > 0)\\ &= \left(\frac{1}{2}\cdot\frac{1}{2}\right) + \left(\frac{1}{2}\cdot\frac{1}{2}\right) \ = \ \frac{1}{2}\,.\end{aligned} \tag{11.4}$$

The negation of the previous assertion has same probability ($\mathbb{P}(\overline{E_2}) = 1 - \frac{1}{2}$), which is the probability to have no oscillation. Using the same reasoning, the probability to have one and only one oscillation is

$$\mathbb{P}(E_2 \text{ and } \overline{E_3}) = \frac{1}{4} \tag{11.5}$$

as show in Table 11.9.

S_0	S_1
+	+
-	-
+	-
-	**+**

Table 11.8: The four possible combinations of the signs of S_0 and S_1. The two last ones (in bold) show at least one oscillation. Hence $\mathbb{P}(E_2) = \frac{1}{2}$.

S_0	S_1	S_2
+	+	+
+	+	-
+	-	+
-	**+**	**+**
-	-	-
-	-	+
-	+	-
+	-	-

Table 11.9: The eight possible combinations of the signs of S_0, S_1 and S_2. The two lines in bold show one and only one oscillation. Hence $\mathbb{P}(E_2 \text{ and } \overline{E_3}) = \frac{1}{4}$.

Adapting definition (11.3) to the one-sided oscillation,we get the following definition.

Definition 11.4 (one-sided maximal length of oscillation) *Let us note $N_\delta^1(x)$ the maximal length of forward oscillation in $u(x)$. $N_\delta^1(x) = a_{\max}$, where $a_{\max} = \arg\max_a E_a - 1$.*

So we can reformulate the results of (11.4) and (11.5) by

$$(11.4) \quad \Leftrightarrow \quad \mathbb{P}(N_\delta^1(x) \geq 1) = \frac{1}{2}, \tag{11.6}$$

$$(11.5) \quad \Leftrightarrow \quad \mathbb{P}(N_\delta^1(x) = 1) = \frac{1}{4}. \tag{11.7}$$

The generalization of (11.6) and (11.7) yields the following proposition.

Proposition 11.5 *Let $n \in \mathbb{N}$ and x belong to a random image where the gray level are uniformly distributed in $\mathbb{R}$. The distribution of $\mathbb{P}(N_\delta^1(x) \geq n)$ is a geometric distribution with $p = 1/2$. The expectation value is $1/p = 2$. In particular, we have*

$$\mathbb{P}(N_\delta^1(x) \geq n) = \left(\frac{1}{2}\right)^n \tag{11.8}$$

and

$$\mathbb{P}(N_\delta^1(x) = n) = \left(\frac{1}{2}\right)^{n+1}. \tag{11.9}$$

We study now a more realistic model based on the random assumption for the $v(i\delta)$, by opposition to the random assumption for the S_i of the naive model 1. However the naive model 2 is not the best model for real images, since for small values of δ the random assumption for the $v(i\delta)$ is not true. Two close pixels may belong to the same object and may be linked. However the naive model 2 is more realistic than the naive model 1, and this is the model we describe now.

11.4 Naive model 2

The naive model 1, based on the random assumption for the S_i, is not realistic because it does not take into account that the gray level of an images are in $[0, 255]$ and not in $\mathbb{R}$. For the naive model 2, we assume that the distribution of $v(i\delta)$ is uniform in $[0, 255]$ and we assume that they are i.i.d. In fact, we assume here that gray levels are in $[0, 1]$ instead of $[0, 255]$ but this linear contrast change has no impact on the point oscillation. These assumptions change the probability calculus obtained with the previous model. In the naive model 1, the succession of two rises has same probability than the succession of a rise and a fall. But in real images, the finite range of gray levels makes the probability depends on the pixel gray level at the end of the first rise. If this value is too close to the upper bound of the gray level range then it is more likely to obtain a fall than a rise after the first rise. So the succession of two rises is less likely than the succession of a rise and a fall. This is considered in this new model. Let us give some theoretical results based on this remark.

We suppose that X_1, X_2, X_3 are 3 independent random variables uniformly distributed in $[0, 1]$. The associated probability density function is $\mathbb{1}_{[0,1]}$. Let us calculate the probability that the observed values x_1, x_2, x_3 are not oscillating, i.e. $\mathbb{P}(NR_\delta^1(x) = 0)$ (the additional letter R stands for **restricted** gray level interval).

Remark: we recall here that N_δ and N_δ^1 refer to the two-sided and one-sided oscillation model, respectively. In the following, NR_δ^1 refers to the one-sided oscillation model where gray level does not belong to $\mathbb{R}$, but to a restricted interval.

$$\begin{aligned}
\mathbb{P}(X_1 > X_2 > X_3) &= \int_{x_1=0}^{1}\int_{x_2=0}^{1}\int_{x_3=0}^{1} \mathbb{1}_{\{x_1>x_2 \text{ for } x_1 \text{ fixed}\}}\mathbb{1}_{\{x_2>x_3 \text{ for } x_2 \text{ fixed}\}}\, dx_3\, dx_2\, dx_1 \\
&= \int_{x_1=0}^{1}\int_{x_2=0}^{x_1}\int_{x_3=0}^{x_2} dx_3\, dx_2\, dx_1 \;=\; \int_{x_1=0}^{1}\int_{x_2=0}^{x_1} x_2\, dx_2\, dx_1 \;=\; \frac{1}{6} \\
\mathbb{P}(NR_\delta^1(x)=0) &= \mathbb{P}(X_1 > X_2 > X_3) + \mathbb{P}(X_1 < X_2 < X_3) \;=\; \frac{1}{3} \neq \frac{1}{2} \qquad (11.10)
\end{aligned}$$

The probability to have no oscillation is smaller in this restricted model, $\mathbb{P}(NR_\delta^1(x)=0)=\frac{1}{3}$, than in the previous model where $\mathbb{P}(\overline{E_2}) = \mathbb{P}(N_\delta^1(x)=0)=\frac{1}{2}$. The computation of $\mathbb{P}(NR_\delta^1(x)=n)$ has no exponential behavior with n as in Proposition 11.5. Some computations of some more values of $NR_\delta^1(x)$ are given here:

$$\begin{aligned}
\mathbb{P}(NR_\delta^1(x)=1) &= 2\cdot\mathbb{P}(X_1 > X_2 \text{ and } X_2 < X_3 < X_4) \\
&= 2\cdot\int_{x_1=0}^{1}\int_{x_2=0}^{x_1}\int_{x_3=x_2}^{1}\int_{x_4=x_3}^{1} dx_4\, dx_3\, dx_2\, dx_1 = \frac{1}{4} = 0.25 \qquad (11.11) \\
\mathbb{P}(NR_\delta^1(x)=2) &= 2\cdot\mathbb{P}(X_1 > X_2 \text{ and } X_2 < X_3 \text{ and } X_3 > X_4 > X_5) = \frac{3}{20} = 0.15 \qquad (11.12)
\end{aligned}$$

The computation of $NR_\delta^1(x)$ requires an iterative calculus. The unavoidable recursion formulae are easily implemented on a computer. The formulae is given in Proposition 11.6, but let us first introduce some notations. We note $P_{2n}(1)=\frac{1}{2}\mathbb{P}(NR_\delta^1(x)=2n)$ and

$$P_{2n}(t) = \int_{x_{2n}=0}^{t}\int_{x_{2n-1}=0}^{x_{2n}}\int_{x_{2n-2}=x_{2n-1}}^{1}\int_{x_{2n-3}=0}^{x_{2n-2}}\cdots\int_{x_3=x_4}^{1}\int_{x_2=0}^{x_3}\int_{x_1=0}^{x_2} dx_1 dx_2 dx_3 \ldots dx_{2n-1} dx_{2n}\,.$$

Proposition 11.6 *The recursion formula for the calculus of $P_{2n}(t)$ is*

$$\begin{aligned}
P_{2n+1}(t) &= \int_0^t -P_{2n}(s)\, ds \;+\; t\, P_{2n}(1) \qquad (11.13) \\
P_{2n+2}(t) &= \int_0^t P_{2n+1}(s)\, ds \qquad (11.14)
\end{aligned}$$

with $P_0=\frac{1}{6}$ and $P_1=\frac{1}{8}$. Moreover, one has

$$P'_{2n+1}(1)=0 \text{ and } P'_{2n+2}(0)=0\,. \qquad (11.15)$$

Proof: By definition

$$\begin{aligned}
P_{2n+1}(t) &= \int_{x_{2n+1}=0}^{t}\int_{x_{2n}=x_{2n+1}}^{1}\int_{x_{2n-1}=0}^{x_{2n}}\int_{x_{2n-2}=x_{2n-1}}^{1}\cdots\int_{x_3=x_4}^{1}\int_{x_2=0}^{x_3}\int_{x_1=0}^{x_2} dx_1 dx_2 dx_3 \ldots dx_{2n} dx_{2n+1} \\
&= \int_{x_{2n+1}=0}^{t} P_{2n}(1) - P_{2n}(x_{2n+1})\, dx_{2n+1} \qquad (11.16) \\
&= \int_{x_{2n+1}=0}^{t} -P_{2n}(x_{2n+1}) dx_{2n+1} + t\, P_{2n}(1) \qquad (11.17)
\end{aligned}$$

and

$$\begin{aligned} P_{2n+2}(t) &= \int_{x_{2n+2}=0}^{t} \int_{x_{2n+1}=0}^{x_{2n+2}} \int_{x_{2n}=x_{2n+1}}^{1} \dots \int_{x_3=x_4}^{1} \int_{x_2=0}^{x_3} \int_{x_1=0}^{x_2} dx_1 dx_2 dx_3 \dots dx_{2n} dx_{2n+1} dx_{2n+2} \\ &= \int_{x_{2n+2}=0}^{t} P_{2n+1}(x_{2n+2})\, dx_{2n+2}\,. \end{aligned} \tag{11.18}$$

The justification of (11.16) comes from the rewriting of

$$P_{2n+1}(t) = \int_{x_{2n+1}=0}^{t} \int_{x_{2n}=x_{2n+1}}^{1} q(x_{2n}) dx_{2n} dx_{2n+1}$$

where q is a polynomial in x_{2n} of order k: $q(x_{2n}) = \sum_{i=x_{2n+1}}^{k} a_i\,(x_{2n})^i$. The first integration is equal to

$$\int_{x_{2n}=x_{2n+1}}^{1} q(x_{2n}) dx_{2n} = \int_{x_{2n}=0}^{1} q(x_{2n}) dx_{2n} - \int_{x_{2n}=0}^{x_{2n+1}} q(x_{2n}) dx_{2n} = P_{2n}(1) - P_{2n}(x_{2n+1})\,.$$

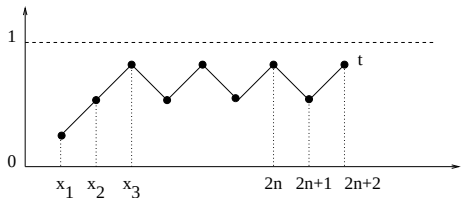

Figure 11.10: Schematic graph of the oscillation for the calculus of $P_{2n+2}(t)$.

We can deduce the formula from (11.17) and (11.18). The first terms are

$$P_0 = \frac{1}{2}\,\mathbb{P}(NR_\delta^1(x) = 0) = \frac{1}{6}\,,$$

$$P_1 = \frac{1}{2}\,\mathbb{P}(NR_\delta^1(x) = 1) = \frac{1}{8}\,,$$

and

$$P_2 = \frac{1}{2}\,\mathbb{P}(NR_\delta^1(x) = 2) = \frac{3}{40}\,.$$

We can also deduce by derivation of (11.13) and (11.14)

$$\begin{aligned} P'_{2n+1}(t) &= P_{2n}(1) - P_{2n}(t) \\ P'_{2n+2}(t) &= P_{2n+1}(t) \end{aligned}$$

from which (11.15) follows.

□

We will give the numerical values of $NR_\delta^1(x)$ in the following, but let us first remark here the link with a permutation counting problem.

11.4.1 Link with the Euler Zigzag Numbers

For example, the computation of $\mathbb{P}(X_1 < X_2 < X_3)$ is related to considering the number of permutations of three variables X_1, X_2, X_3 following the same law. Let us cite the $3!$ of them:

- $X_1 < X_2 < X_3$,
- $X_1 < X_3 < X_2$,
- $X_2 < X_3 < X_1$,
- $X_2 < X_1 < X_3$,
- $X_3 < X_1 < X_2$,
- $X_3 < X_2 < X_1$.

More generally, it is well known that the number of permutations of n elements is equal to $n!$. Consequently,

$$\mathbb{P}(X_1 < X_2 < \ldots < X_n) = \frac{1}{n!}\,.$$

Indeed, let us note σ a permutation, and σ_n the set of permutations of n elements. Let X be the random vector $X = (X_1, X_2, \ldots, X_n)$, the subset indicates the position of the considered component. Let X_σ be the permuted vector $X_\sigma = (X_{\sigma(1)}, X_{\sigma(2)}, \ldots, X_{\sigma(n)})$.

$$\forall \sigma \in \sigma_n, \quad X_\sigma \stackrel{\mathcal{L}}{=} X\,.$$

Hence

$$\forall \sigma \in \sigma_n, \quad \mathbb{P}(X_1 < \ldots < X_n) = \mathbb{P}(X_{\sigma(1)} < \ldots < X_{\sigma(n)})\,.$$

By summing over all permutations, we get

$$\begin{aligned} n!\,\mathbb{P}(X_1 < \ldots < X_n) &= \sum_{\sigma\in\sigma_n} \mathbb{P}(X_{\sigma(1)} < \ldots < X_{\sigma(n)}) \\ &= \mathbb{P}\left(\bigcup_{\sigma\in\sigma_n} [X_{\sigma(1)} < \ldots < X_{\sigma(n)}]\right) \end{aligned}$$

Since n elements are all different with probability one, $\mathbb{P}\left(\bigcup_{\sigma\in\sigma_n}[X_{\sigma(1)} < \ldots < X_{\sigma(n)}]\right) = 1$. Hence $\mathbb{P}(X_1 < \ldots < X_n) = \frac{1}{n!}$.

In our case, this result is interesting for the computation of $\mathbb{P}(NR^1_\delta(x) = 0) = \mathbb{P}(X_1 > X_2 > X_3) = \frac{1}{3!} = \frac{1}{6}$. For $\mathbb{P}(NR^1_\delta(x) = n)$ with $n > 0$, the model does not correspond since it only gives the probability of ordered numbers and not oscillating ones.

In the literature, this problem refers to the alternating permutations. These are permutations in which the difference between each successive pair of adjacent elements changes sign, that is each *rise* is followed by a *fall*. For example, for the list $\{1, 2, 3\}$, the permutation $\{1, 3, 2\}$ is alternating, while $\{3, 2, 1\}$ is not. Fig.11.11 and 11.12 illustrate the four alternating permutations and the two non-alternating permutations, respectively. So the probability of having an alternating permutation with 3 elements is $\frac{4}{3!}$. This number corresponds to the probability of having *at least one* oscillation: $\mathbb{P}(NR^1_\delta(x) \geq 1)$. Going back to previous notations, the four oscillating configurations are

- $X_3 < X_1 < X_2$,
- $X_1 < X_3 < X_2$,
- $X_2 < X_3 < X_1$,
- $X_2 < X_1 < X_3$.

They satisfy the conditions to have one oscillation, that is

- either X_2 is bigger than X_1 and X_3,
- either X_2 is smaller than X_1 and X_3.

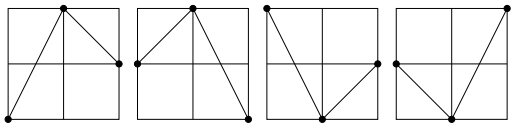

Figure 11.11: The two first alternating permutations begin with a *rise*, the two following ones begin with a *fall*.

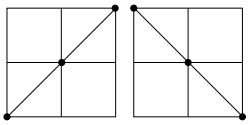

Figure 11.12: The two non-alternating permutations.

In the literature, the number of alternating permutations of n elements are called *Euler Zigzag Numbers*, a short table of which is given in Table 11.13. It has been shown that the *Euler Zigzag Numbers* are the coefficients of the expansion of $2 \times (\sec x + \tan x)$. The Maclaurin series of the secant and tangent functions are given by:

$$\begin{aligned} \sec(x) &= 1 + \frac{1}{2!}x^2 + \frac{5}{4!}x^4 + \frac{61}{6!}x^6 + \frac{1385}{8!}x^8 \ldots \\ \tan(x) &= x + \frac{2}{3!}x^3 + \frac{16}{5!}x^5 + \frac{272}{7!}x^7 + \frac{7936}{9!}x^9 + \ldots \end{aligned}$$

Multiplying both sides of the equations by two yields

$$\begin{aligned} 2\sec(x) &= 2 + \frac{2}{2!}x^2 + \frac{10}{4!}x^4 + \frac{122}{6!}x^6 + \frac{2770}{8!}x^8 \ldots \\ 2\tan(x) &= 2x + \frac{4}{3!}x^3 + \frac{32}{5!}x^5 + \frac{544}{7!}x^7 + \frac{15872}{9!}x^9 + \ldots \end{aligned}$$

We recognize here the *Euler Zigzag Numbers* given in Table 11.13. We note them $a(n)$. The computation of $\mathbb{P}(NR^1_\delta(x) = n)$ is given by the following Proposition.

n	1	2	3	4	5	6	7	8	9	10	11	12
$a(n)$	1	2	4	10	32	122	544	2770	15872	101042	707584	5405530

Table 11.13: Table of the first Euler Zigzag Numbers.

Proposition 11.7

$$\forall n \in \mathbb{Z}^+, \quad \mathbb{P}(NR^1_\delta(x) = n) = \frac{a(n+2)}{(n+2)!} - \frac{a(n+3)}{(n+3)!} \tag{11.19}$$

where $a(n)$ are the Euler Zigzag Numbers.

Proof: We note A_n, the event "n elements form an alternating permutation". The probability of such event is the ratio between the number of alternating permutations of n elements (this number is the *Euler Zigzag Number* $a(n)$) and the number of permutations of n elements:

$$\mathbb{P}(A_n) = \frac{a(n)}{n!}\,.$$

The computation of $\mathbb{P}(NR^1_\delta(x) = n)$ is the probability to have exactly n oscillations. The number of elements $v(i\delta)$ necessary to have exactly n iterations is $(n+2)+1$. The first $n+2$ elements correspond to have at least n iterations and the last element corresponds to the stop of the oscillation (two consecutive rises or two consecutive falls). For example, 4 elements can do exactly 1 oscillation: the three first elements make the rise and the fall, and the last element makes the second fall (Fig.11.14-left). Consequently, the computation of $\mathbb{P}(NR^1_\delta(x) = n)$ requires $n+3$ elements. For the computation of $\mathbb{P}(NR^1_\delta(x) \geq n)$, the number of elements is equal to $n+2$ since the last element is not considered.

$$\mathbb{P}(NR^1_\delta(x) \geq n) = \mathbb{P}(A_{n+2}) = \frac{a(n+2)}{(n+2)!}$$

Since $\mathbb{P}(NR^1_\delta(x) = n)$ is the probability to have exactly n oscillations, it is equal to the probability to have at least n oscillation minus the probability to have at least $n+1$ oscillations.

$$\begin{aligned}
\mathbb{P}(NR^1_\delta(x) = n) &= \mathbb{P}(NR^1_\delta(x) \geq n) - \mathbb{P}(NR^1_\delta(x) \geq n+1) \\
&= \mathbb{P}(A_{n+2}) - \mathbb{P}(A_{n+3}) \\
&= \frac{a(n+2)}{(n+2)!} - \frac{a(n+3)}{(n+3)!}\,.
\end{aligned}$$

This ends the proof of (11.19).

□

As an example, the values of $\mathbb{P}(NR^1_\delta(x) = 1)$ and $\mathbb{P}(NR^1_\delta(x) = 2)$ are now computed thanks to Property 11.7:

- $\mathbb{P}(NR^1_\delta(x) = 1) = \mathbb{P}(A_3) - \mathbb{P}(A_4) = \frac{a(3)}{3!} - \frac{a(4)}{4!} = \frac{4}{3!} - \frac{10}{4!} = 0.25\,,$
- $\mathbb{P}(NR^1_\delta(x) = 2) = \mathbb{P}(A_4) - \mathbb{P}(A_5) = \frac{a(4)}{4!} - \frac{a(5)}{5!} = \frac{10}{4!} - \frac{32}{5!} = 0.15\,.$

Remarks: It is important to observe here that we find the same results than the ones with the previous computations with the uniform distribution restrained on $[0,1]$: (11.11) and (11.12). Note also that the n^{th} *Euler Number* has the asymptotic expansion $4/\pi \cdot (2/\pi)^n \cdot n!$ (see [40]). Hence the coefficient $a(n)/n!$ has the asymptotic expansion $4/\pi \cdot (2/\pi)^n$.

Table 11.15 gives $\mathbb{P}(NR^1_\delta(x) = n)$ for $n \in [0, 10]$. Note that we check the same probabilities for the random image with uniform distribution: (11.10), (11.11) and (11.12). The results obtained with *Euler Zigzag Numbers* are interesting because they are general to any random image as long as pixels

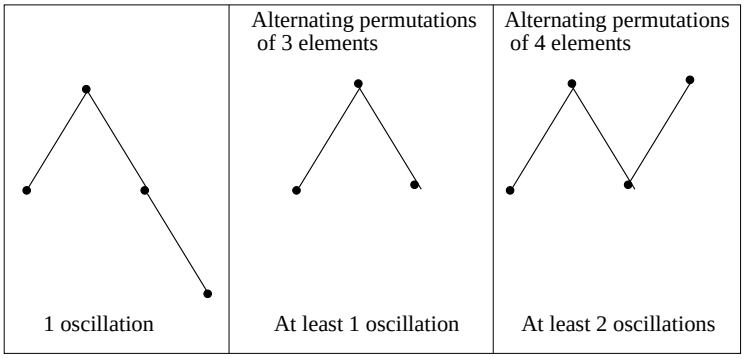

Figure 11.14: Representation of the configurations, the probability of which are computed, to calculate the probability to have exactly one-sided oscillation: $\mathbb{P}(NR_\delta^1(x) = 1)$. The probability to have exactly one oscillation is the probability to have at least one oscillation minus the probability to have at least two oscillations.

n	0	1	2	3	4	5
$\mathbb{P}(NR_\delta^1(x) = n)$	0.33	0.25	0.15	0.0972	0.0615	0.0392

n	6	7	8	9	10
$\mathbb{P}(NR_\delta^1(x) = n)$	0.0249	0.0158	0.0101	0.0064	0.0041

Table 11.15: Table of the first $\mathbb{P}(NR_\delta^1(x) = n)$.

have same distribution (for example uniform or Gaussian), as we will show in the next section. But this measure is also invariant under injective contrast change because the oscillations are considered as alternating gray level rise and fall so that the relative difference of the gray levels between two pixels are compared and not the absolute gray levels. This is perceptually relevant, since it is well known that our perception is insensitive to contrast change and contrast invariant algorithms are often seek in Computer Vision [15][33]. Let us give now some additive explanations of the reason why the computations of $\mathbb{P}(NR_\delta^1(x) = n)$ are distribution-free.

11.4.2 Distribution-free results

Let us now give the associated proposition.

Proposition 11.8 *Let u be a random image such that each pixel has a random value. Assume that the associated random variable X_i has probability density function f and that the X_i are i.i.d. Then the values of $\mathbb{P}(NR_\delta^1(x) = n)$ are independent of f.*

Proof : We prove here that the computation of

$$\mathbb{P}(NR_\delta^1(x) = n) = 2 \cdot \mathbb{P}(X_1 > X_2 < X_3 > \ldots < X_n > X_{n+1} > X_{n+2} > X_{n+3}),$$

where X_i has probability density function f, is f-free. To that aim, we consider the computation of a simpler case $n = 0$, which we generalize latter to any n. The computation of $\mathbb{P}(NR_\delta^1(x) = 0)$ requires the computation of $\mathbb{P}(X_1 > X_2)$, where X_1 and X_2 are i.i.d. random variables with probability density function f. We first recall that the cumulative density function F is defined by

$$F(t) = \int_{-\infty}^{t} f(x)\, dx,$$

and that we have the nice following property:

if f is the probability density function of the random variable X_i, then

$$F(X_i) \sim \mathcal{U}([0,1]).$$

We will prove that $\mathbb{P}(X_1 > X_2) = \mathbb{P}(F(X_1) > F(X_2))$ and since $F(X_i)$ has uniform distribution (that is f-free), we will conclude that the computation of $\mathbb{P}(X_1 > X_2)$ is also f-free. Let us now prove that $\mathbb{P}(X_1 > X_2) = \mathbb{P}(F(_1) > F(X_2))$. Since we have

$$\mathbb{P}(F(X_i) > F(X_j)) \;\leq\; \mathbb{P}(X_i > X_j) \;\leq\; \mathbb{P}(F(X_i) \geq F(X_j)),$$

we have to prove that $\mathbb{P}(F(X_i) = F(X_j)) = 0$ in order to prove that $\mathbb{P}(X_1 > X_2) = \mathbb{P}(F(_1) > F(X_2))$.

$$\begin{aligned}
\mathbb{P}(F(X_i) = F(X_j)) &= \int_0^1 \mathbb{P}(F(X_i) = F(X_j) | F(X_j) = t)\, dt \quad \text{because } F(X_i) \sim \mathcal{U}([0,1]) \\
&= \int_0^1 \mathbb{P}(F(X_i) = t)\, dt \\
&= \lim_{\varepsilon \to 0} \; \mathbb{P}(F(X_i) \leq t) - \mathbb{P}(F(X_i) \leq t - \varepsilon) \\
&= \lim_{\varepsilon \to 0} \; t - (t - \varepsilon) = 0
\end{aligned}$$

This last result implies that $\mathbb{P}(X_1 > X_2) = \mathbb{P}(F(_1) > F(X_2))$. Since F is f-free, $\mathbb{P}(NR^1_\delta(x) = 0)$ is f-free. The same reasoning can be applied for the computation of $\mathbb{P}(NR^1_\delta(x) = n)$ where the probability with respect to X_i can be replaced by the probability with respect to the f-free random variable $F(X_i)$.

□

Comparison of theoretical and experimental results

Fig.11.17-(a) displays the theoretical values of the naive model $\mathbb{P}(NR^1_\delta(x) = n)$ and $\mathbb{P}(N^1_\delta(x) = n)$ for $n \in [0, 30]$. We compare those values with experimental results on a random image u (512x512). The case $n = 1$ is the only value of n where both theoretical values are equal.

$$\mathbb{P}(N^1_\delta(x) = 1) = \mathbb{P}(NR^1_\delta(x) = 1) = \frac{1}{4}$$

The model NR^1_δ matches simulations. Two curves are displayed for the simulation on the random image: one for $\delta = 1$ and one for $\delta = 2$. Indeed we distinguish two cases.

- The cases $\delta > 1$ have similar results as pixels are independent.
- The case $\delta = 1$ has a particular behavior, not described by the model. This comes from the nearest neighbor interpolation of u. For some gradient values, the interpolation of points of v refers to the same point of u (Fig.11.16). A typical example is a diagonal gradient direction: $\frac{Du}{|DU|} = \left(\frac{1}{\sqrt{2}}, \frac{1}{\sqrt{2}}\right)$. The points $v(1)$ and $v(2)$ have the same interpolate $u(x_1 + 1, x_2 + 1)$. Indeed the nearest neighbor interpolation of $v(1) = u\left(x + \frac{Du}{|DU|}\right) = u\left((x_1, x_2) + \left(\frac{1}{\sqrt{2}}, \frac{1}{\sqrt{2}}\right)\right) \simeq u(x_1 + 0.7, x_2 + 0.7)$ and $v(2) \simeq u(x_1 + 1.4, x_2 + 1.4)$ yield both $u(x_1 + 1, x_2 + 1)$. This case suggests to use another kind of interpolation, which has not been done in this thesis.

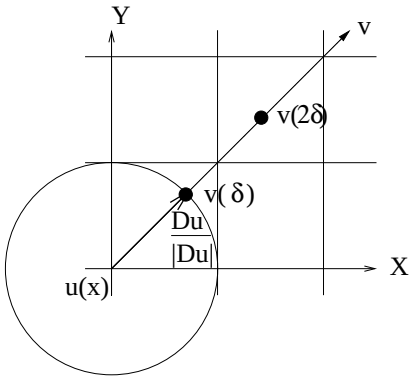

Figure 11.16: Example with $\delta = 1$ where $v(\delta)$ and $v(2\delta)$ have same interpolated value $u(x + \binom{1}{1})$.

Note that the two-sided oscillation model NR_δ can be deduced from the one-sided oscillation model NR^1_δ if oscillations are supposed independent on both sides of the edge (Fig.11.17-(b)):

$$\mathbb{P}(NR_\delta(x) = n) = \sum_{r+l=n} \mathbb{P}(NR^1_\delta(x) = r) \cdot \mathbb{P}(NR^1_\delta(x) = l)\,.$$

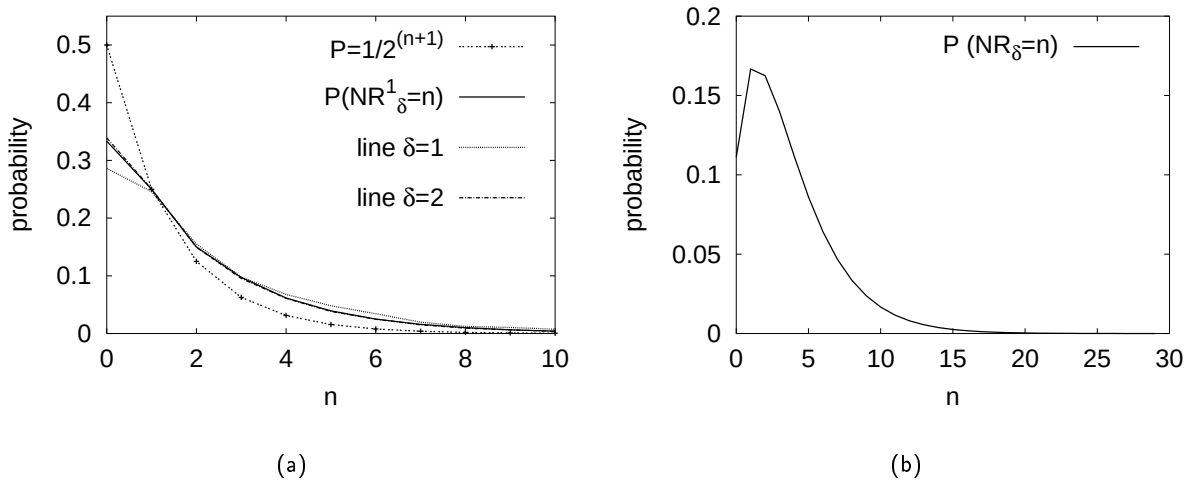

Figure 11.17: Probability values of the oscillation length under a random assumption (a) one-sided oscillations N_δ^1 and NR_δ^1. The curves for NR_δ^1 and $\delta = 1$ are not the same because of the nearest neighbor interpolation, but we check that the curves for NR_δ^1 and $\delta = 2$ are very close. (b) two-sided oscillations NR_δ.

Now that the theoretical values of $\mathbb{P}(N_\delta^1(x) = n)$ and $\mathbb{P}(NR_\delta^1(x) = n)$ have been given and checked by simulations, we propose to build *ringing detectors* based on these results. First, we have seen in Proposition 11.5 that the computation of $\mathbb{P}(N_\delta^1(x) = n)$ is easy, but does not totally match the cases of real images since their gray level are restrained to a given interval, generally linked to the sensor sensitivity in the optical chain. However since the mathematical computations are easy, we will propose four ringing detector based on $\mathbb{P}(N_\delta^1(x) = n)$. These detectors are presented in the Section 11.5. Then we will give another detector based on $\mathbb{P}(NR_\delta^1(x) = n)$, which was easily computed thanks to the *Euler Zigzag Numbers*. This detector is presented in the Section 11.6.

11.5 Detectors for the naive model 1

We propose here several detectors based on the naive model 1 (Proposition 11.5). Three detectors are defined. Each one is based on different models called model A, B and C. All try to detect the ringing oscillation half-period δ. The model A and B are based on the study of the histogram $H(n, \delta)$. Since H depends on two parameters, the detection with respect to a single one is not direct. This is the reason why we have had two approaches. The first one, called model A, consists in not detecting δ but any cell of $H(n, \delta)$ which has a high value with respect to the naive random model 1. In practice, it means testing each line of $H(n, \delta)$. The second approach is the global detection of δ with the information theory. The model C is based on the study of $H(\delta)$ (and not $H(n, \delta)$ as for model A and B) which has the advantage to depend on the single parameter δ, and then to detect directly the oscillation half-period.

11.5.1 Model A: definition of detector 1

Detection on $H(n,\delta)$ with δ fixed.

The aim is to detect high values of the histogram $H(n,\delta)$ with respect to the naive random model. Each line of $H(n,\delta)$ is analyzed independently. In order to detect the meaningfulness of the values of $H(n,\delta)$, we compute the probability to obtain those values, that is $\mathbb{P}(H(n,\delta)=k)$, with the random assumption described in the naive model 1.

We recall here that the probability that exactly k objects (independent and with Bernoulli distribution) out of the observed N have a considered quality is given by the binomial distribution

$$b(N,k,p) = \binom{N}{k} p^k (1-p)^{N-k}$$

where $0<p<1$ is the probability that one object has the considered quality. The probability that at least k objects out of the observed N have a considered quality is given by the tail of the binomial distribution

$$B(N,k,p) = \sum_{i=k}^{N} \binom{N}{i} p^i (1-p)^{N-i}.$$

By definition of the naive model 1, we have from Proposition 11.9

$$\mathbb{P}(N_\delta^1(x)=n) = 2^{-(n+1)}$$

so that the probability that a pixel x has the quality "$N_\delta^1(x)=n$" is equal to $p=2^{-(n+1)}$. Hence the probability that k points out of the N (number of points in the image) have the quality "$N_\delta^1(x)=n$" is equal to

$$\mathbb{P}(H(n,\delta)=k) = b\left(N,k,2^{-(n+1)}\right) = \binom{N}{k} 2^{-k(n+1)} \left(1-2^{-(n+1)}\right)^{N-k}.$$

The probability that at least k points have the quality is the tail of the binomial distribution, i.e.

$$\mathbb{P}(H(n,\delta)\geq k) = B\left(N,k,2^{-(n+1)}\right). \tag{11.20}$$

The Hoeffding's inequality [17] gives a bound to the tail of the binomial distribution.

Proposition 11.9 (Hoeffding's inequality) *Let $X_1,\ldots,X_l$ be independent random variables such that $0\leq X_i\leq 1$. We set $S_l=\sum_{i=1}^{l} X_i$ and $p=\mathbb{E}\left[\frac{S_l}{l}\right]$. Then for $pl<k<l$,*

$$\mathbb{P}[S_l\geq k] \leq \left(\frac{p}{k/l}\right)^{l(\frac{k}{l})} \left(\frac{1-p}{1-\frac{k}{l}}\right)^{l(1-k/l)}.$$

In other terms, setting $r=k/l$,

$$\mathbb{P}[S_l\geq k] \leq \exp\left[-r\left(r\log\frac{r}{p}+(1-r)\log\frac{1-r}{1-p}\right)\right].$$

From Proposition 11.9, we deduce a bound to (11.20):

$$\begin{aligned} B\left(N,k,2^{-(n+1)}\right) &\leq \exp\left[-N\left(\frac{k}{N}\log\frac{k}{N2^{-(n+1)}}+(1-\frac{k}{N})\log\frac{1-\frac{k}{N}}{1-2^{-(n+1)}}\right)\right] \\ -\log B\left(N,k,2^{-(n+1)}\right) &\geq N\left(\frac{k}{N}\log\frac{k}{N2^{-(n+1)}}+(1-\frac{k}{N})\log\frac{1-\frac{k}{N}}{1-2^{-(n+1)}}\right) \end{aligned} \tag{11.21}$$

The normalization of H by the number of pixels N of the image is $\tilde{H}(n,\delta)=\frac{H(n,\delta)}{N}$. Hence

$$(11.21) \quad \Leftrightarrow \quad -\log\mathbb{P}(H(n,\delta)\geq k) \;\geq\; N\left(\frac{k}{N}\log\frac{k}{N2^{-(n+1)}}+(1-\frac{k}{N})\log\frac{1-\frac{k}{N}}{1-2^{-(n+1)}}\right) .$$

Consequently, the "information" of $\tilde{H}(n,\delta)$ is

$$I(n,\delta) \;\simeq\; N\left(\tilde{H}(n,\delta)\log\frac{\tilde{H}(n,\delta)}{2^{-(n+1)}}+(1-\tilde{H}(n,\delta))\log\frac{1-\tilde{H}(n,\delta)}{1-2^{-(n+1)}}\right) .$$

Following the *a contrario* approach described in [12], we define the "number of false alarms" (NFA) of the event "$H(n,\delta)=k$". By definition, it measures the "meaningfulness" of the event, i.e. the smaller the NFA is, the more meaningful the event is. In other words, a small NFA shows that the event is unlikely to appear by chance. The meaningfulness is defined by $-\log NFA$, which is a more appropriate logarithmic scale.

Definition 11.10 (detector 1) *The number of false alarms of the event "$H(n,\delta)=k$" is*

$$NFA(n,\delta)=\#n\cdot\#\delta\cdot B\left(N,H(n,\delta),2^{-(n+1)}\right) , \tag{11.22}$$

where $\#n$ (resp. $\#\delta$) is the number of different possible values of n (resp. δ) that are tested. Their product represents the number of tests $N_{test}=\#n\cdot\#\delta$.

Remark on the calculus of the number of tests: N_{test} depends on the size of the image. As the NFA is computed on lines of the image (in the ringing direction), we shall estimate the number of tests in the 1D case. If we consider a square image u of size $N=\sqrt{N}\cdot\sqrt{N}=L^2$ then the one-dimensional signal has size in $[L,\sqrt{2}L]$. But as we interpolate with the nearest neighbor interpolation, we shall only consider here the length L (Fig.11.19).

As the image is discrete, the maximum number of oscillations n associated to a signal of size L depends on the value of δ. For a given value of $\delta\in\left[1,\left\lfloor\frac{L}{2}\right\rfloor\right]$, its value is

$$n(\delta)=\left\lfloor\frac{L-1}{\delta}\right\rfloor-1 \;. \tag{11.23}$$

For example, if $L=8$ then (Fig.11.18)

- $n(1)=\left\lfloor\frac{8-1}{1}\right\rfloor-1=6$: for $\delta=1$, the signal of length 8 contains 8 tested points, which can give up to $8-2=6$ oscillations,

- $n(3) = \left\lfloor \frac{8-1}{3} \right\rfloor - 1 = 1$: for $\delta = 3$, the signal of length 8 contains 3 tested points, which can give up to $3 - 2 = 1$ oscillation.

From (11.23), we deduce

$$N_{test} = \sum_{\delta=1}^{\lfloor \frac{L}{2} \rfloor} n(\delta) = \sum_{\delta=1}^{\lfloor \frac{L}{2} \rfloor} \left(\left\lfloor \frac{L-1}{\delta} \right\rfloor - 1 \right) . \quad (11.24)$$

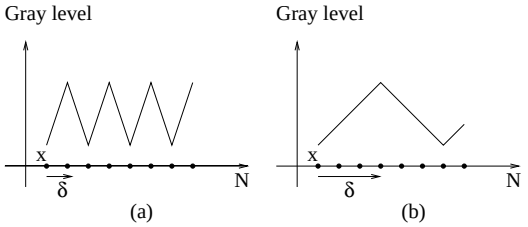

Figure 11.18: Calculus of N_{test} in the 1D case $L = 8$. a) $\delta = 1$ b) $\delta = 3$. The maximal number of possible oscillations (NR^1_δ) in both cases are respectively 6 and 1.

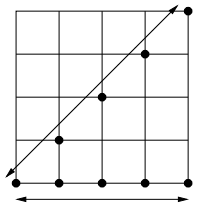

Figure 11.19: The horizontal and diagonal segments have different continuous length but the number of associated discrete points is identical ($L = 5$).

11.5.2 Model B: definition of detector 2

Detection on $H(n, \delta)$ with δ not fixed.

The first model detects ringing for each value of δ. But as we have seen in Fig.11.6, the detector should be global. Detector 2 is global because δ not fixed. It is based on the Kullback distance between the naive Bernoulli distribution and $\tilde{H}$.

Definition 11.11 (detector 2)

$$F(\delta) = \sum_{n \in [1,N]} \tilde{H}(n,\delta) \log \frac{\tilde{H}(n,\delta)}{2^{-(n+1)}} + (1 - \tilde{H}(n,\delta)) \log \frac{1 - \tilde{H}(n,\delta)}{1 - 2^{-(n+1)}} = \frac{1}{N} \sum_{n \in [1,N]} I(n,\delta)$$

As we will see in the numerical experiments, this distance is not adapted to our problem, because it is not precise enough to detect the ringing half-period. This result is not surprising since $F(\delta)$ is by definition the mean of $I(n, \delta)$, computed for the detector 1. Furthermore detector 2 has the disadvantage to be asymmetric.

Another model is studied now which is also valid for δ not fixed. We will see that model C is not precise enough to detect ringing oscillations, as model B. These results check that these approaches based on the naive model 1 are not realistic enough to be applied, and that they should be replaced by the naive model 2.

11.5.3 Model C: definition of detector 3

Detection on $H(\delta)$ with δ not fixed.

In the previous model, we tried to detect the oscillation half-period from the histogram $H(n, \delta)$. Here we try to detect from

$$H^1(\delta) = \sum_x N_\delta^1(x)\,.$$

We have seen in Proposition 11.5 that $\mathbb{P}(N_\delta^1 = n) = 2^{-(n+1)}$. If we note X_i the random variable associated to the number of oscillations N_δ^1 at pixel i, then

$$\mathbb{P}(X_i = n) = 2^{-(n+1)}\,, \tag{11.25}$$

and

$$H^1(\delta) = \sum_i X_i\,. \tag{11.26}$$

From (11.25), note that X_i has nearly a geometrical law $G\left(\frac{1}{2}\right)$ and that (11.26), which is the sum of X_i, has a simple expression if X_i is a geometrical law. For these reasons we chose to study a simplified version of the naive model 1 such that X_i has exactly a geometrical law $G\left(\frac{1}{2}\right)$:

$$\mathbb{P}(X_i = n) = 2^{-n}\,. \tag{11.27}$$

Hence, with our previous assumption, H^1 is the sum of independent random variables with geometric laws. Since the sum of N independent geometrical laws has Pascal distribution [43], then H^1 has Pascal distribution [43]. We recall here its definition and we give $\mathbb{P}(H^1 = k)$ for our special case.

Definition 11.12 *The Pascal law of order N has probability distribution function*

$$\mathbb{P}(Y = k) = \binom{k-1}{N-1} p^N (1-p)^{k-N} \tag{11.28}$$

with $p \in [0,1]$ and $k \in \{N, N+1, \ldots\}$.

In our case $p = \frac{1}{2}$, so that

$$\mathbb{P}(H^1(\delta) = k) = \mathbb{P}(\sum_i X_i = k) = \mathbb{P}(Y = k) = \binom{k-1}{N-1} 2^{-k} \tag{11.29}$$

with $k \in \{N, N+1, \ldots\}$ and N the number of points in the image.

In fact, the geometric distribution hypothesis on $N_\delta^1(x)$ is not true because the event "$N_\delta^1(x) = 0$" may appear (there might be no oscillation at pixel x) which is not possible with the geometric distribution. Let us now successively explain why the geometric distribution is not totally adapted to our case, define new variables to take into account this remark and propose a detector for the model C:

- **Remark on the geometric distribution:** by definition, the geometric distribution is the probability distribution of the number Z of Bernoulli trials needed to get one success, supported on the set 1, 2, 3, ... If p is the probability to get one success at each trial, then $\mathbb{P}(Z = z) = p(1-p)^{z-1}$ with $z = 1, 2, \ldots, \infty$. But in our experiments, the case $N_\delta^1(x) = 0$ may appear.

- **Notations:** the shift of 1 yields the following definitions:

  Definition 11.13 $N'_\delta(x) = N^1_\delta(x) - 1$.

  Definition 11.14 $H'(\delta) = \sum_x N'_\delta(x)$.

- **Detector:** as for detector 1 and 2, we propose an *a contrario* detector. The measured value $h'(\delta)$ of $H'(\delta)$ is meaningful if the probability that "$H'(\delta) \geq h'(\delta)$" is small.

  Definition 11.15 (detector 3)

  $$NFA(\delta) = \#\delta \cdot \mathbb{P}(H'(\delta) \geq h'(\delta))$$

  where $h'(\delta)$ is the observed value of $H'(\delta)$.

  The NFA is the product of the number of possible tests and the probability of the event. As in the first model, $\delta \in \left[1, \left\lfloor \frac{L}{2} \right\rfloor\right]$, so $\#\delta = \left\lfloor \frac{L}{2} \right\rfloor$.

With these new variables, (11.29) becomes for any value of N

$$\begin{aligned} \mathbb{P}(Y = k) &= \mathbb{P}(X'_1 + X'_2 + \ldots + X'_N = k) \\ &= \mathbb{P}(X_1 - 1 + X_2 - 1 + \ldots + X_N - 1 = k) \\ &= \mathbb{P}(X_1 + X_2 + \ldots + X_N = k + N) \\ &= \binom{k+N-1}{N-1} 2^{-(k+N)}. \end{aligned} \tag{11.30}$$

From (11.30), $\mathbb{P}(H'(\delta) = k) = \binom{k+N-1}{N-1} 2^{-(k+N)}$. This is the expression of a negative binomial law, because the Pascal distribution is linked to the negative binomial distribution, which is the law of $Y - N$. Since detector 3 is based on $\mathbb{P}(H'(\delta) \geq h'(\delta))$, its computation is the sum of negative binomial laws. We will now see why this model is not adapted to the ringing detection and why numerical experiments cannot be satisfactory.

First let us rewrite $\mathbb{P}(H'(\delta) \geq h'(\delta))$:

$$\mathbb{P}(H'(\delta) \geq h'(\delta)) = \sum_{k=h'(\delta)}^{M} \mathbb{P}(H'(\delta) = k) = \sum_{k=h'(\delta)}^{M} p_k \tag{11.31}$$

where M is the maximum value of $H'(\delta)$ and p_k is $\mathbb{P}(X = k)$ for any random variable X with negative binomial law. From (11.31), the detection of large values of $h'(\delta)$ (that is small values of $\mathbb{P}(H'(\delta) \geq h'(\delta))$) is possible only if $\mathbb{P}(H'(\delta) \geq h'(\delta))$ is sensitive to the measured values of $h'(\delta)$, which assume that there is no value of k such that p_k is far too large by comparison with other values of p_k. This hypothesis is not satisfied in reality, because there is a value of k bigger than the observed values $h'(\delta)$ in the experiments, such that p_k is very large by comparison with $p_{h'(\delta)}$. The following property states that the maximum of p_k is reached for $k = N - 2$.

Property 11.16 *Let X be a random variable with negative binomial law of order N with parameter $p = \frac{1}{2}$.*

$$\mathbb{P}(X = k) = \binom{k+N-1}{N-1} 2^{-(k+N)} = p_k.$$

Then p_k is maximum at $k = N - 2$.

Proof: Set $t_k = \frac{p_{k+1}}{p_k} = \frac{(N+k)!}{(N-1)!(k+1)!} \cdot 2^{-(N+k+1)} \cdot \frac{(N-1)!(k)!}{(N+k-1)!} \cdot \frac{1}{2^{-(N+k)}} = \frac{1}{2} \cdot \frac{N+k}{k+1}$.

$$p_{k+1} \geq p_k \Leftrightarrow tk \geq 1 \Leftrightarrow N - 2 \geq k$$

See the graph of p_k in Fig.11.20.

□

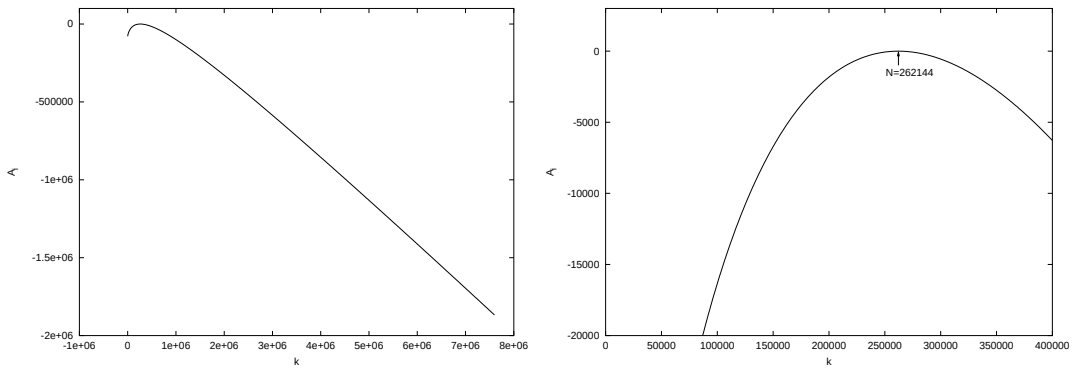

(a) (b)

Figure 11.20: (a) Curve of $A_i = \log_{10} \mathbb{P}(X = k) = \log_{10} p_k$ with $N = 512 \times 512 = 262144$ (b) zoom in. The maximal value of p_k is reached for $k \simeq N$.

As we will see now, the value $k = N - 2$ is smaller than M so the maximum value of p_k is always added in (11.31), which yields bad detection results. Let us estimate the value of M for an image of size $N = L^2$. Suppose that for a given value of δ, oscillations at each pixel have maximal length $\lfloor \frac{L}{2} \rfloor$, then $M = \left(\lfloor \frac{L}{2} \rfloor - 1 \right) \times N \gg N$. The numerical computation of H' shows values smaller than N. For example, in Fig.11.7, $H(\delta) \in [0, 246383]$ with $N = 256 \times 256 = 65536$.

So $H'(\delta) \in [0, 190168] \ll N$. Consequently, in the computation of $\mathbb{P}(H'(\delta) \geq h'(\delta))$, the main weight in $\sum p_k$ is given by p_{N-2} and the neighborhood values. The values of $p_{h'}$ are smaller than p_{N-2}. So $\forall \delta$, $\mathbb{P}(H'(\delta) \geq h'(\delta)) = Cte$. Consequently, this detector is not precise enough to differentiate the ringing half-period from other δ values. This is not really surprising since we used the nice properties of the sum of geometric distribution, even if our random variables do not have a geometric distribution.

11.5.4 Numerical experiments with the detectors 1 and 2

We have seen that the first and third detectors require a threshold value. The same problem occurs with detector 2. An example is given in Fig.11.21. Furthermore, the values of $F(\delta)$ for the random image (Fig.11.21-(b)) are very similar to the ones of the image with ringing (Fig.11.21-(a)). So this kind of detector would detect ringing in a random structure or no ringing at all. This major drawback is avoided by characterizing the ringing from noise or natural images. Natural images contain objects with smooth transitions, which reduces the number of oscillations especially for small δ. This produces small $H(\delta)$ (Fig.11.22). Random images have far more oscillations for all values of δ (Fig.11.23). These two kinds of images (natural and random) have histograms $H(n, \delta)$ nearly independent of δ.

By comparison, the histogram of an image with ringing has a larger value for the half-period of the ringing oscillations, than for other values of δ (Fig.11.6). The results of the detection with detector 1

$$NFA(n,\delta) = \#n \cdot \#\delta \cdot B\left(N, H(n,\delta), 2^{-n}\right)$$

are shows in Fig.11.24. The value of $H(n,\delta)$ is estimated by considering NR^1_δ and not NR_δ, because the theoretical values of NR^1_δ for random images are given in Section 11.4.1. The values of NR_δ could be as well written but it has not been done in this thesis.

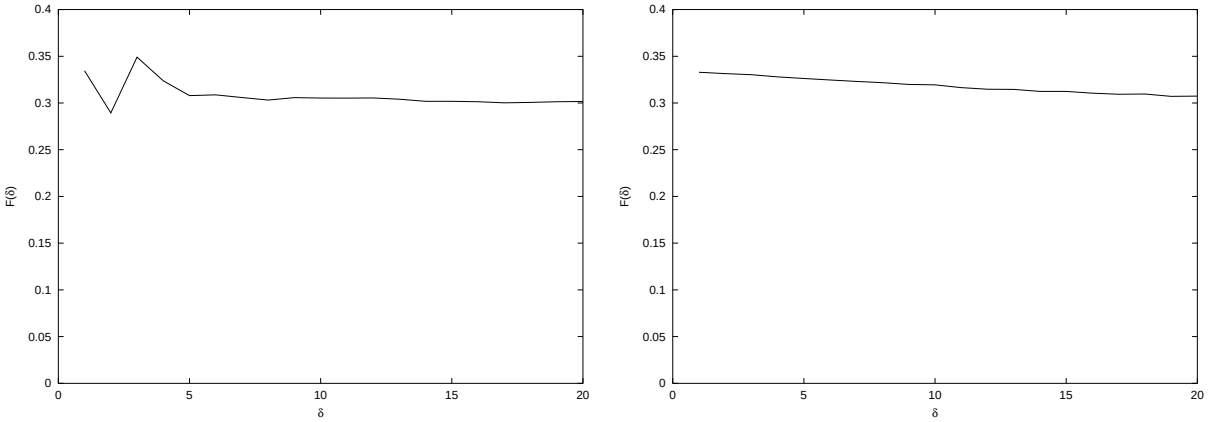

(a) (b)

Figure 11.21: (a) Curve $F(\delta)$ of the Fig.11.1-(b). The maximum is reached for $\delta = 3$ (b) Curve $F(\delta)$ of a random image of size 256×256.

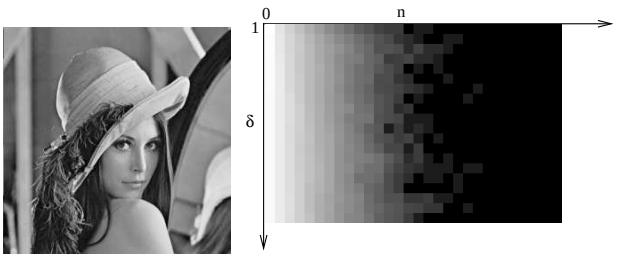

(a) (b)

Figure 11.22: (a) Natural image u (b) histogram $\log H(n,\delta)$. There is no value of δ for which the histogram has far more longer oscillations than for the other values of δ.

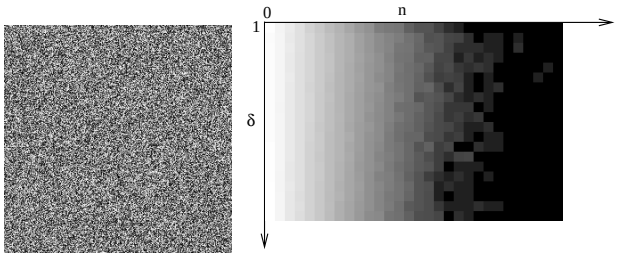

(a) (b)

Figure 11.23: (a) Image u with uniform random values in $[0, 255]$ (b) histogram $\log H(n,\delta)$. Random images have longer oscillations than natural images (Fig.11.22-b).

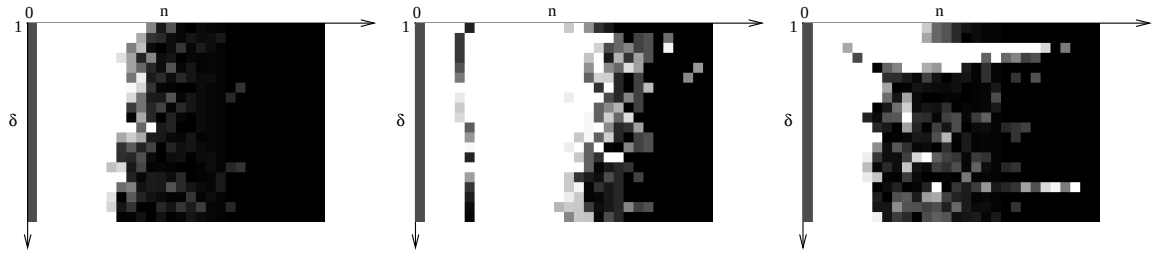

(a) (b) (c)

Figure 11.24: Detection associated to (a) the natural image (Fig.11.22), (b) the random image (Fig.11.23), (c) the image with ringing (Fig.11.1-(b)). The values of $-\log_{10} NFA(n,\delta)$ larger than 15 are thresholded (white pixels). We observe that for the image with ringing, the detection is meaningful for $\delta = 3$, nearly the whole line is meaningful.

11.5.5 Model D: improvement of model A and definition of detector 4.

In order to detect ringing neither in ringingless images nor in random images, we propose a last detector that takes into account the previous remarks. The new detector is based on the detector 1 built in Model A. In practice, the computation of $NFA(n,\delta)$ are done with the detector 1 and then they are compared to the values of $NFA(n,\delta)$ obtained for ringingless images. Let us define some variables.

Definition 11.17 *The proportion of meaningful points in the $NFA(n,\delta)$ image is defined by*

$$P_M = \frac{\textit{number of meaningful points in the } NFA(n,\delta) \textit{ image}}{\textit{number of points in the } NFA(n,\delta) \textit{ image}}\,.$$

Definition 11.18 *The proportion of meaningful points in each line of the $NFA(n,\delta)$ image is defined by*

$$P(\delta) = \frac{\textit{number of meaningful points in the line } \delta \textit{ of the } NFA(n,\delta) \textit{ image}}{\textit{number of points in the line } \delta \textit{ of the } NFA(n,\delta) \textit{ image}}\,.$$

Definition 11.19 *We define the curve of the difference with respect to the mean proportion value by*

$$C(\delta) = P(\delta) - P_M\,.$$

Definition 11.20 (detector 4) *We shall say that an image u has ringing with half-period δ if*

$$C(\delta)(u) > C_r$$

where

$$C_r = \max_{1\leq i\leq r} \max_{\delta} C(\delta)(R_i)$$

with r the number of tested random images R, r large.

The threshold value C_r is defined in this way in order to avoid the detection of ringing in random images. This is a very important criteria for our detector since we want to build a detector which does not depend on the level of noise in the image. The constant C_r is a threshold on $C(\delta)$ which is reached with very small probability when random images are considered. In practice, if this threshold exists, it is obtained when an infinite number of random images are tested ($r \to +\infty$).

11.5.6 Numerical experiments with detector 4

In this experiment, the ringingless image u is the Lena image blurred with a Gaussian kernel with standard deviation equal to 1. The images with ringing u_0 are built by deblurring u with a Wiener filter where k_0 is the Gaussian kernel with standard deviation equal to 2. We recall here the definition of a special case of the Wiener filter given in (11.1):

$$\forall \xi \in \mathbb{R}^2, \quad \widehat{u_0}(\xi) = \frac{\widehat{k_0}^*(\xi)}{\left|\widehat{k_0}(\xi)\right|^2 + \frac{|\xi|^2}{w}} \cdot \widehat{u}(\xi)\,.$$

Different values of the Wiener filter parameter have been tested. They introduce more or less ringing, depending on the value of w, weight of the fidelity term (Fig.11.25). Note that the computation of the NFA is done on the periodized version of the images in the X and Y directions, so the size of the window does not reduce artificially the number of oscillations for large δ.

(a) (b) (c) (d)

Figure 11.25: Images 256×256 (a) blurred image, (b-c-d) deblurred images with $w = 10, 20, 50$.

The estimation of C_r is done on random images of size 512×512. Points are considered as meaningful if $NFA < 10^{-15}$. We observed that we obtained similar results with other values of NFA-thresholds: 10^{-5} and 10^{-1}. We plot the values of C_r obtained for different $r \in [1, 1000]$, number of tested random images for the NFA-thresholds 10^{-15}. The maximum value of C_r for $r \in [1, 1000]$ is below 0.2, so that C_r is set to 0.2 (Fig.11.26).

For the NFA-threshold 10^{-5} and 10^{-1}, the C_r values are 0.2 and 0.21, respectively. Detector 4 succeeds in detecting the image with ringing (Fig.11.27). Furthermore, it gives the period of ringing in the images. For $w = 10$ and $w = 20$, we have $\delta = 4$. For $w = 50$, we have $\delta = 3$, which corresponds to the ringing half-period observed on images.

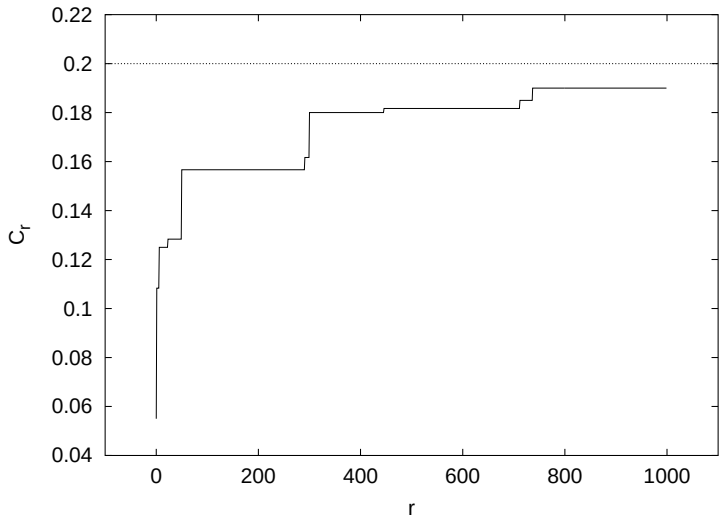

Figure 11.26: Estimation of C_r on 1000 random images of size 512×512 for $r \in [1, 1000]$. C_r increases with r because if $r' > r$ then $C_{r'} = \max\{C_r, \max_{r+1 \leq i \leq r'} \max_\delta C(\delta)(R_i)\}$. The value of $C(\delta)(R_i)$ is smaller than 0.2 for the 1000 tested random images, so that the reference value C_r is set to 0.2.

It is interesting to test detector 4 on a set of images having more and more ringing, i.e. for increasing values of w. Fig.11.28 shows the detection with $w \in [1, 14]$. For $w > 8$, the image is said to have ringing, which is perceptually convincing.

The last test checks if other kind of images without ringing are not detected by detector 4 (Fig.11.29). The detector classifies correctly those images except the image "room". This last image has an oscillatory texture (bottom part), which is detected as ringing. But a simple test on the locality of the detection avoids this kind of problem. The ringing is a global phenomenon on the whole image. A very localized detection is thus only a texture detection and is easily distinguished from ringing.

We also study the effect of noise on such images (Fig.11.30). We add a Gaussian noise with $\sigma = 2$ (the case $\sigma = 1$ has also been tested but we do not show here the results since they are similar to the ones obtained with $\sigma = 2$). Noise may add some extra oscillations which may increase $C(\delta)$. The proposed detection is globally robust to noise except on images with oscillatory textures. Images "room" and "house" have periodic structures (sweat-shirt in the room or bricks of the house) detected as ringing.

11.6 Detector for the naive model 2

We consider a random image with gray level restrained to a closed interval. The calculus of $\mathbb{P}(NR^1_\delta(x) = n)$ is explicitly given in Proposition 11.7 thanks to the *Euler Zigzag Numbers*. Using the same *a contrario* approach, we can define another detector, which has the advantage to be universal for any gray level distribution in the random image.

Definition 11.21 (detector 5) *For a given value of δ, the number of false alarms of the event "$H(n, \delta) = k$" is*

$$NFA(n, \delta) = \#n \cdot \#\delta \cdot B\left(N, H(n, \delta), \mathbb{P}(NR^1_\delta(x) = n)\right) . \tag{11.32}$$

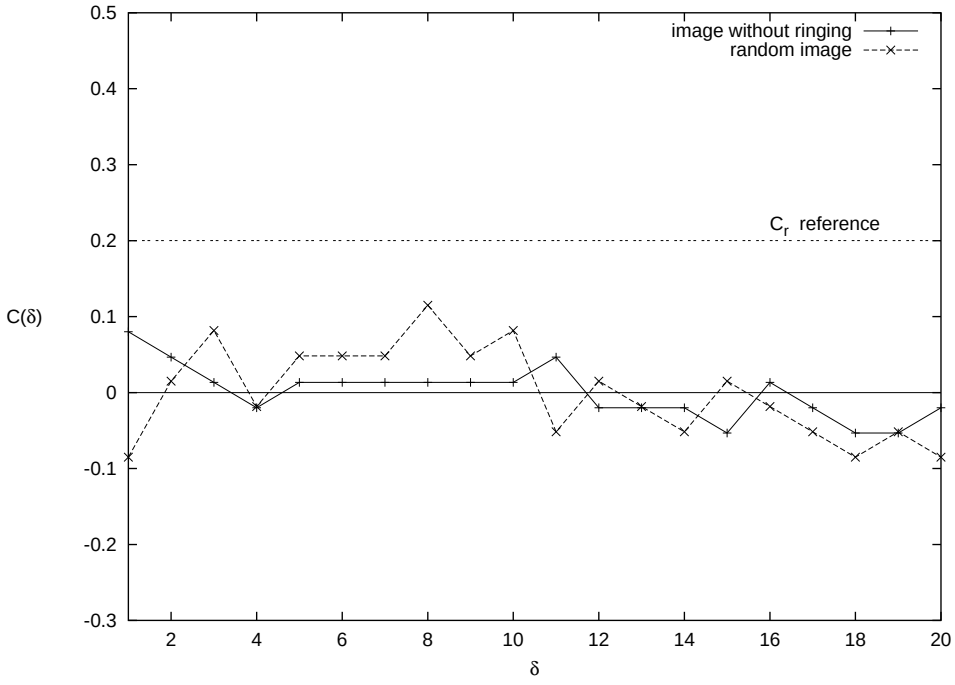

(a) No ringing detected

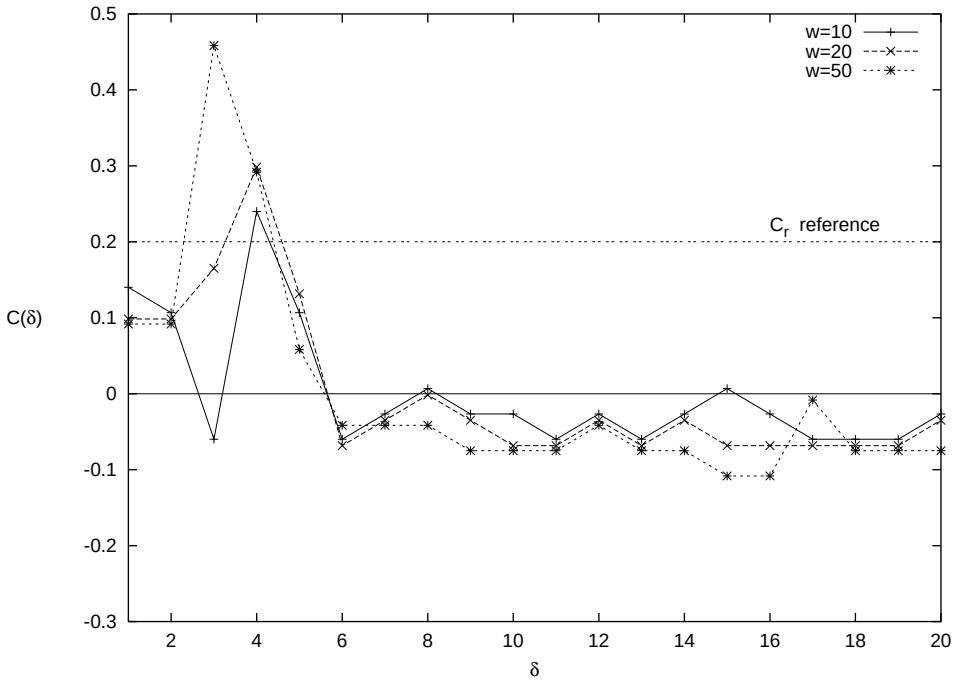

(b) Ringing detected

Figure 11.27: Curves $C(\delta)$. (a) The curve $C(\delta)$ of the blurred image and the random image is below C_r, which indicates no ringing. (b) The curve $C(\delta)$ of the images with ringing is above C_r. These images are detected as having ringing, which checks the validity of the detector.

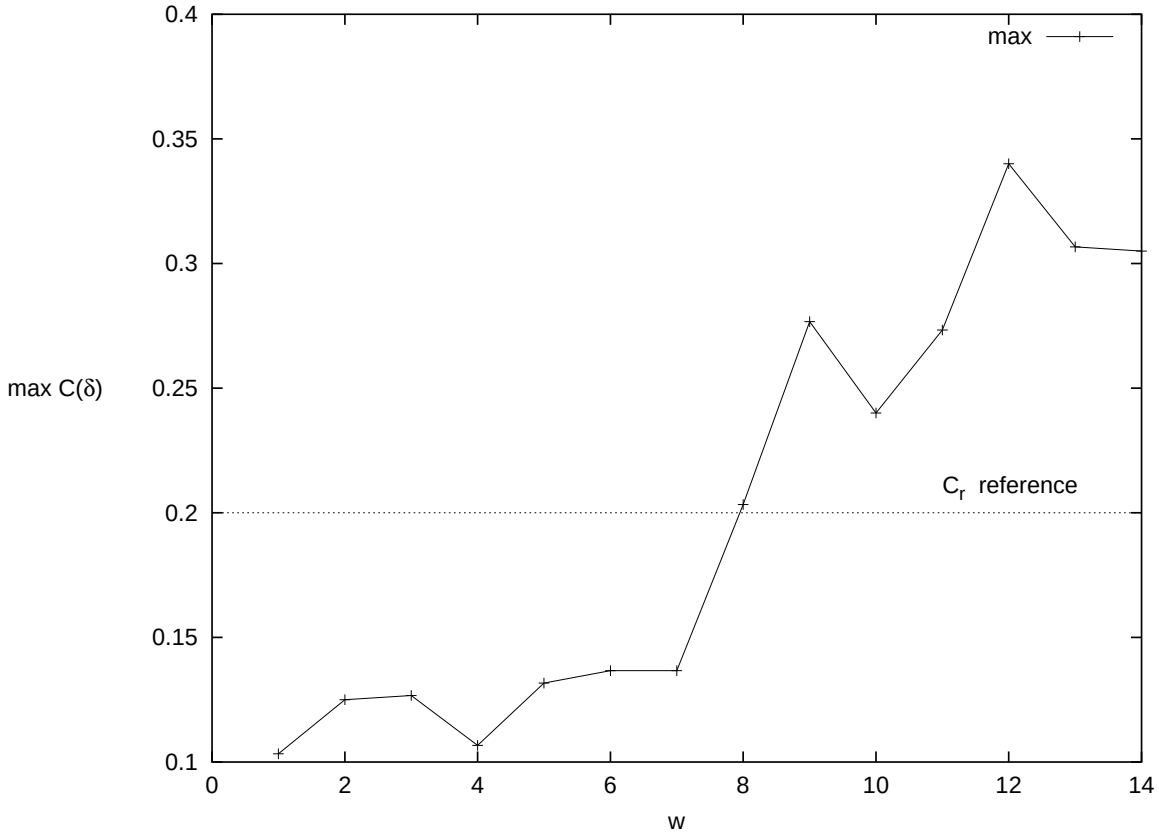

Figure 11.28: graph $(w, \max_\delta C(\delta))$ for deblurred images with different values of w. Note that this graph only takes into account the maximum value of $C(\delta)$, and not the number of δ such that $C(\delta) > C_r$. The ringing is detected if $\max_\delta C(\delta) > C_r$, which corresponds here to the images obtained with $w > 8$ with the Wiener filtering.

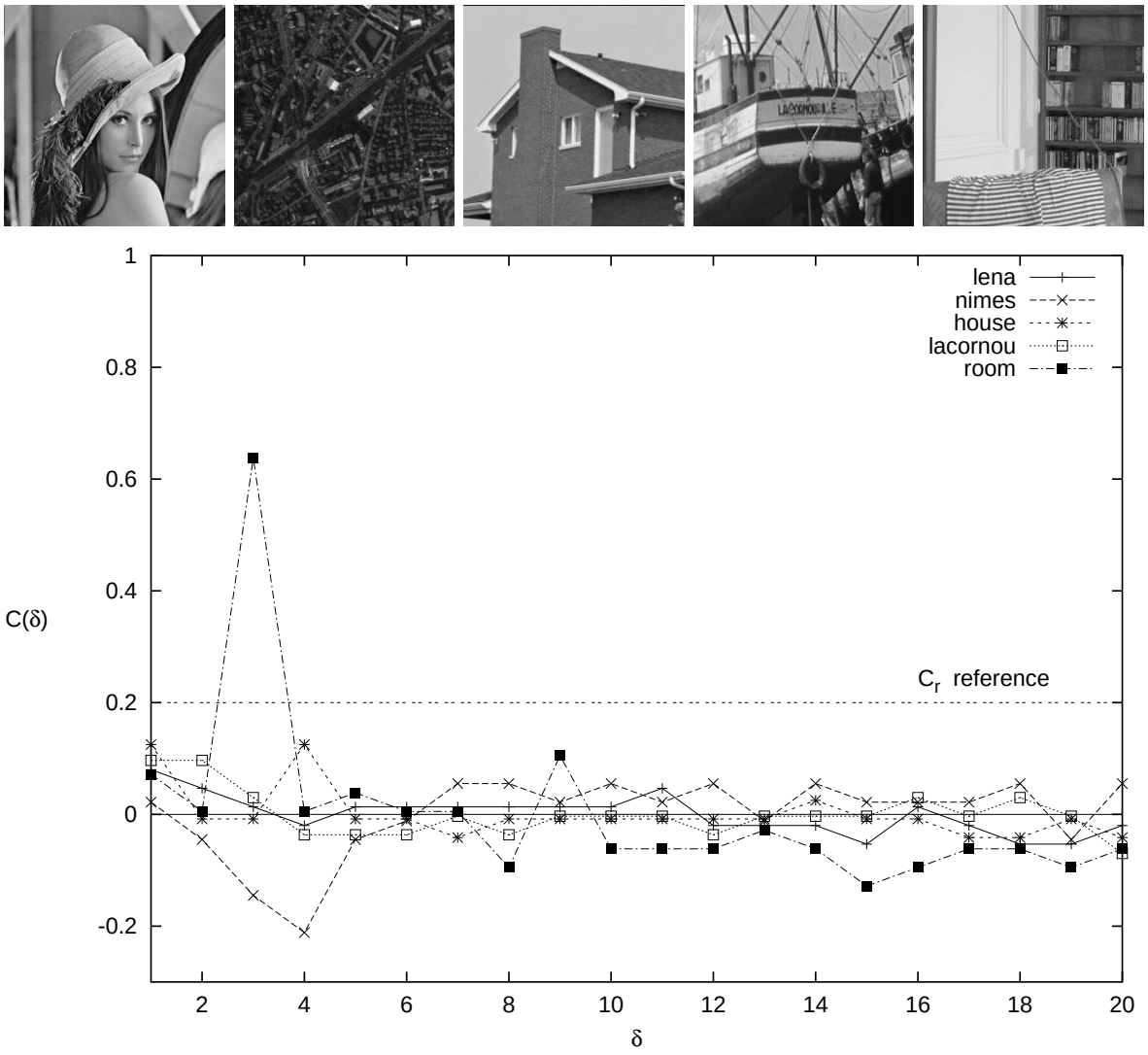

Figure 11.29: First line: images without ringing (lena, nimes, house, lacornou, room), second line: graphs $(\delta, C(\delta))$. Only the image "room" is detected as having ringing, because of its oscillatory structure in the lower part of the image. Others are correctly classified.

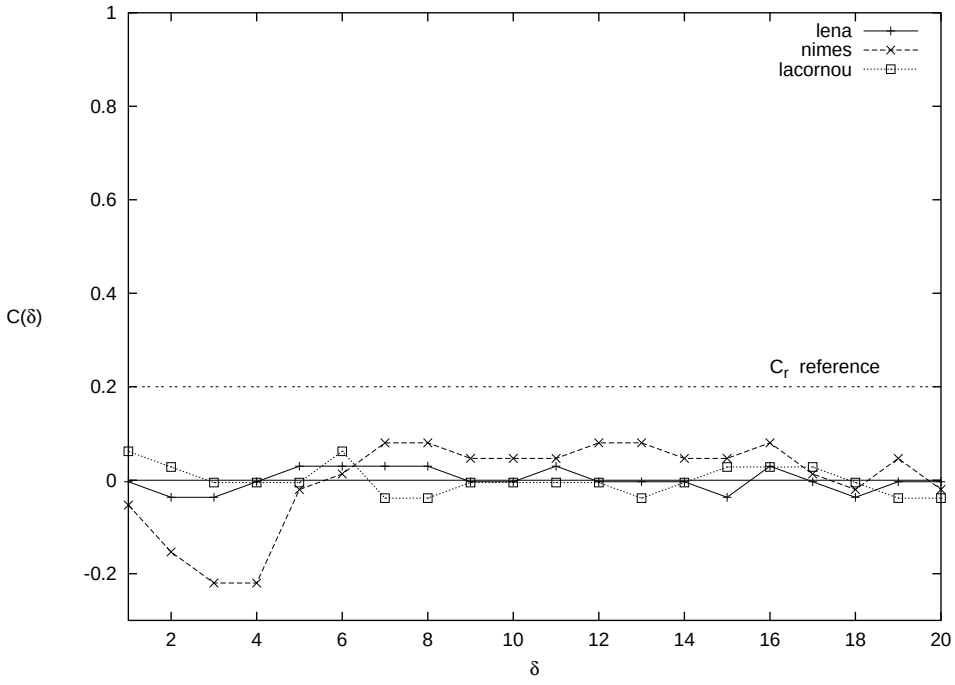

(a) No ringing detected

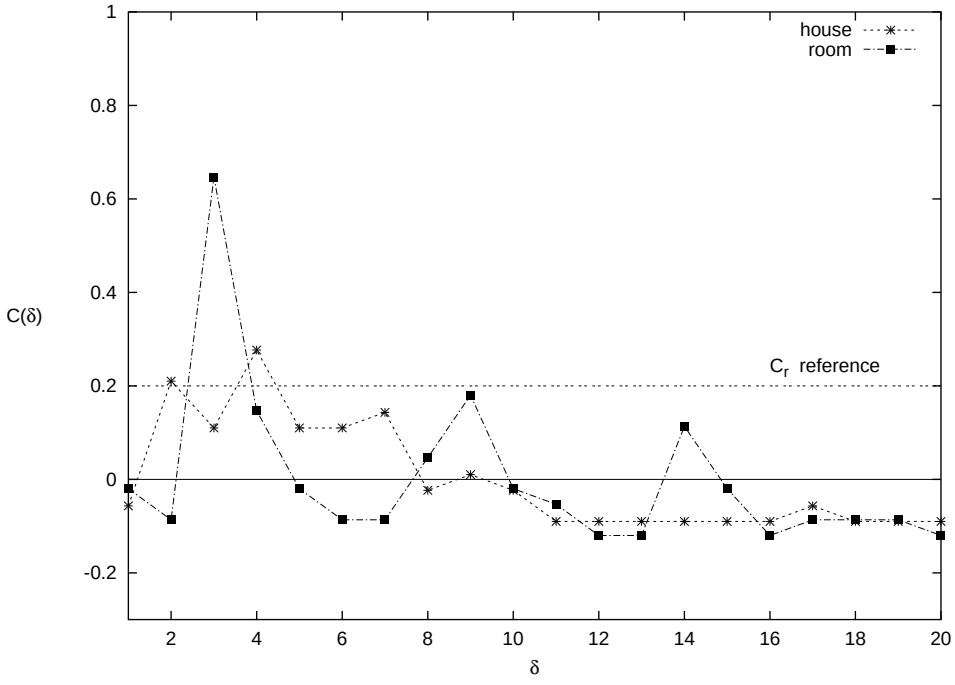

(b) Ringing detected

Figure 11.30: Graphs $(\delta, C(\delta))$ of the ringingless images with Gaussian noise with $\sigma = 2$. In (a), as expected there is no detection for the ringingless images. We obtain the same results than in the noiseless case (Fig.11.29), which shows that the noise has little impact on the detection results for these images. In (b), image "room" is detected as images with ringing because of its oscillatory texture, but we obtain the same detection as in the noiseless case (Fig.11.29). Image "house" is now detected as having ringing because the noise increases the oscillation length in the brick wall making the oscillation detectable.

Using the Hoeffding's inequality, we get

$$NFA(n,\delta) \leq \quad \#n \cdot \#\delta \cdot e^{-N\left(\frac{H(n,\delta)}{N}\log\left(\frac{H(n,\delta)}{N\cdot\mathbb{P}(NR_\delta^1(x)=n)}\right)+\left(1-\frac{H(n,\delta)}{N}\right)\log\left(\frac{1-\frac{H(n,\delta)}{N}}{1-\mathbb{P}(NR_\delta^1(x)=n)}\right)\right)}.$$

The detection is possible by setting a threshold value, which measures its meaningfulness. Here we set the same threshold value in all the experiments. They confirmed that there are no false detections in random images (Fig.11.31-a). The detector can be very sensitive to the level of ringing in the image, especially when the image contains edges surrounded by large uniform zones (Fig.11.31-b-c).

Another example is shown in Fig.11.32. For the images (a-b), some oscillations are detected for large value of δ. The structure of the shelves has a periodic pattern which is detected as oscillating. As the shelves are localized on a small part of the image, this detection is a false alarm. This kind of false detection can also be seen on the image with ringing (c-d), but the ringing phenomenon is predominant.

A last example is shown in Fig.11.33, which is the reference example in this chapter. Again the period $\delta = 3$ of the ringing is detected, which validates the coherent results of this detector.

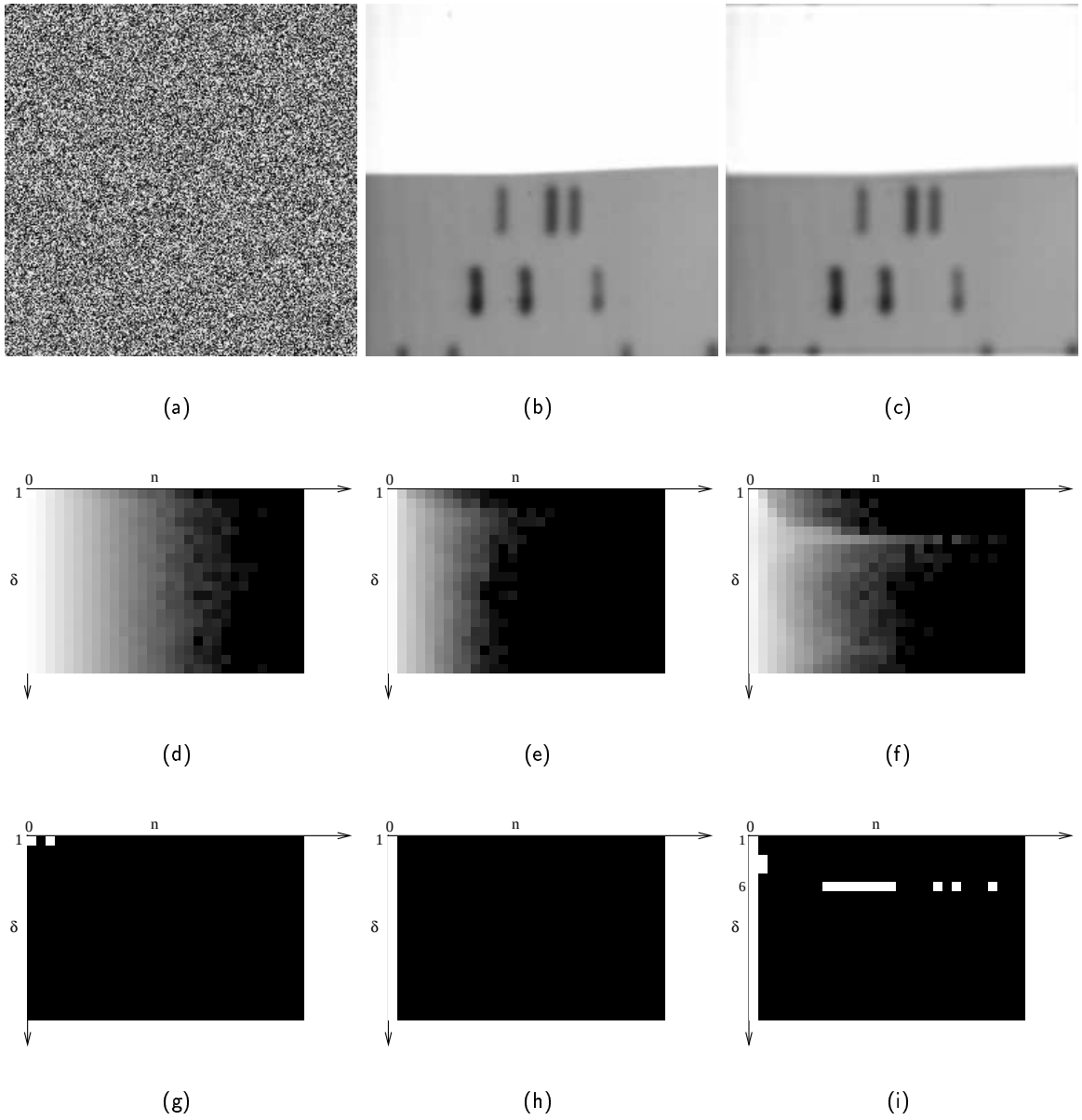

Figure 11.31: (a) random image with uniform distribution (b) original image without ringing (c) deblurred images with a Wiener filter $w = 0.2$ (d-e-f) associated images $\log H(n, \delta)$ (g-h-i) associated images $-\log_{10} NFA(n, \delta)$. The last image has ringing which is detected for $\delta = 6$.

(a) (b)

(c) $w = 1$ (d) $w = 5$ (e) $w = 25$

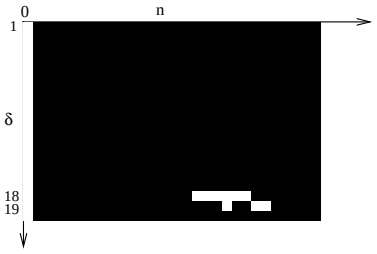

(f)

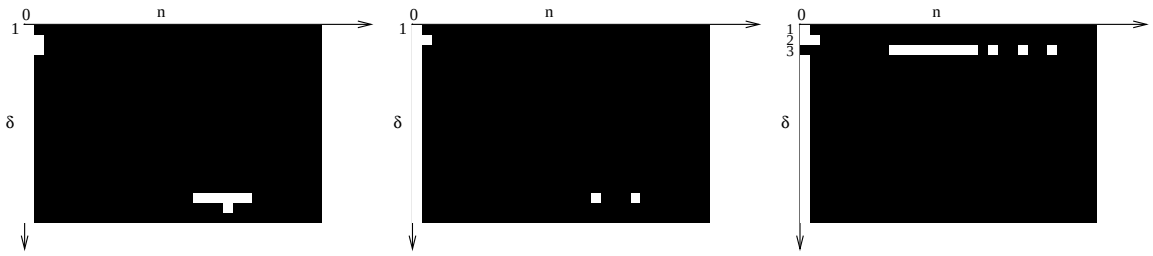

(g) (h) (i)

Figure 11.32: (a) original image u_0 (b) blurred image u without ringing: blurred version of (a) by a Gaussian with standard deviation 1 (c-d-e) deblurred versions of u with a Wiener filter $w = 1, 5, 25$ (f-g-h-i) images $-\log_{10} NFA(n, \delta)$ associated to (b-c-d-e). Image (b) has no ringing, the detection of the filter is for large δ, which corresponds to the oscillation half-period of the shelf texture ($36/2 = 18 = \delta$). Images (c-d) are not detected even if image (d) has some ringing. Image (e) has ringing and it is detected with oscillations of half-period $\delta = 3$.

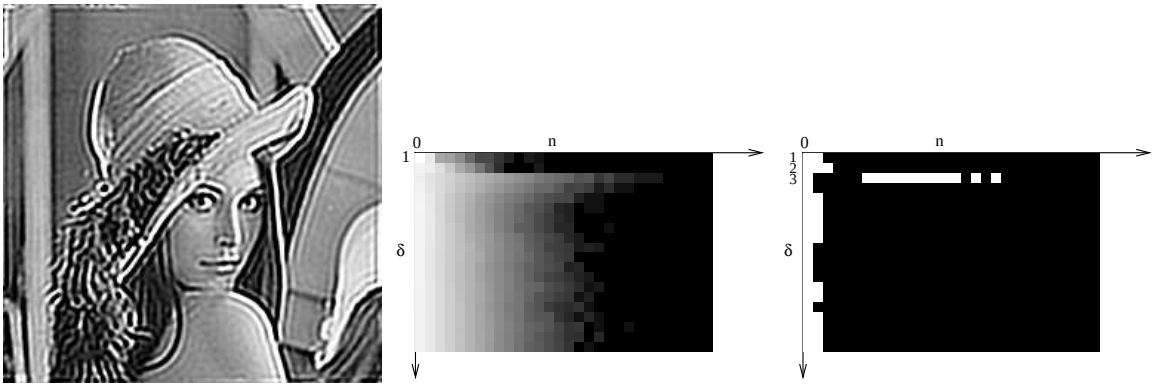

(a) (b) (c)

Figure 11.33: (a) Image with ringing Fig.11.1-b (b) $\log H(n,\delta)$ (c) $-\log_{10} NFA(n,\delta)$. The ringing is detected for $\delta = 3$.

11.7 Conclusion

We have proposed several new ringing detectors based on an *a contrario* approach. This kind of approach is really interesting since it generates parameter-free detectors and then is easy to use in all applications. Moreover it is a reference-free method, which is a great advantage when the original image is unknown.

The ringing studied in this chapter is the one issued from a deconvolution, i.e. which has oscillations with same period around edges. In the recommended detector (detector 5 in Definition 11.21), the detection is done by showing that there is a surprisingly large number of such oscillations on an image with ringing by comparison with an image without ringing. In order to be robust to weak noise, the latter image (the one without ringing) is generally modeled by a random image since the detector should not take noise for ringing.

We computed the theoretical value of $\mathbb{P}(NR^1_\delta(x) = n)$, the probability to have an oscillation of length n and period 2δ at the pixel x, for random images. We showed that the calculus of this probability is independent of the gray level distribution, as long as all pixels are independent and identically distributed, which makes this contrast invariant detector. In order to detect the ringing, we compared the theoretical value of $\mathbb{P}(NR^1_\delta(x) = n)$ obtained for random images to the number of pixels of the tested image satisfying "$NR^1_\delta(x) = n$". The ringing is detected when this number is much larger than theoretically expected. The proposed detector yielded good results in the numerical experiments. This proposed detector, being-parameter-free and robust to noise may be a good choice for all problems requiring post-deconvolution ringing detection.

Chapter 12

Aliasing detection

12.1 Using the frequential interpretation

We have seen that if the conditions of the Shannon sampling theorem are not satisfied before the downsampling of a signal, aliasing artifacts may occur. It results a spectral overlapping between high frequencies of the Fourier transform and low frequencies. This effect can be used to detect the artifact because it introduces an unnatural aspect in the image. The addition of the original frequency and its alias results in the superimposition of two waves on the object contours (Fig.12.1). An image is not constructed by the superimposition of two images, so our eyes detect aliased images because they cannot believe in the expression of two frequencies. For example, the grid pattern visible in Fig.12.1(b) is highly unlikely in the nature. The detection of such superimposed frequencies in the Fourier domain is difficult because of the global nature of the Fourier transform.

(a) (b) (c) (d) (e) (f)

Figure 12.1: Three original images of size 64x64 (a-c-e) and aliased versions: (b) texture change (d) thin structures are not preserved (f) contours have a *staircase* aspect. The aliased image is built by a spatial downsampling of factor two. In each case, we observe the superimposition of the original frequency and the aliased frequency.

For some special kind of images, it is possible to detect visually the aliasing artifact in the spectral domain. Fig.12.2-(b) shows a good example of aliasing. It contains an large oscillatory structure in the down left corner of the image. The associated oscillation frequency has a large Fourier transform modulus, as shown in Fig.12.2-(a). We see the large value of $|\hat{u}|$ for the fundamental frequency ξ_1 and the harmonics $\xi_i = i \cdot \xi_1$ for $i = 2$ and 3. We can say that the image has small aliasing, because ξ_3 is not contained in the spectral domain of u and we observe its alias. The overlapping of ξ_3 can be

easily shown by periodizing $\widehat{u}$ and noticing the extension (Fig.12.3)

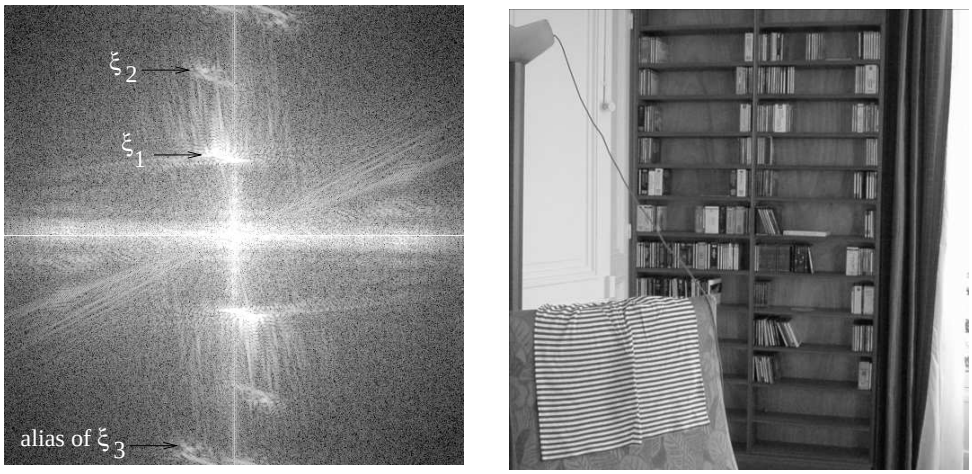

(a) (b)

Figure 12.2: (a) $|\widehat{u}|$ in log scale (b) the considered image u. The shirt on the couch has an oscillatory structure which can be detected in the Fourier domain by the large values of $|\widehat{u}|$ in $\xi = \xi_1, 2\xi_1, 3\xi_1$. The image has very small aliasing because the frequency $3\xi_1$ cannot be contained in the spectral support of u and we observe its alias.

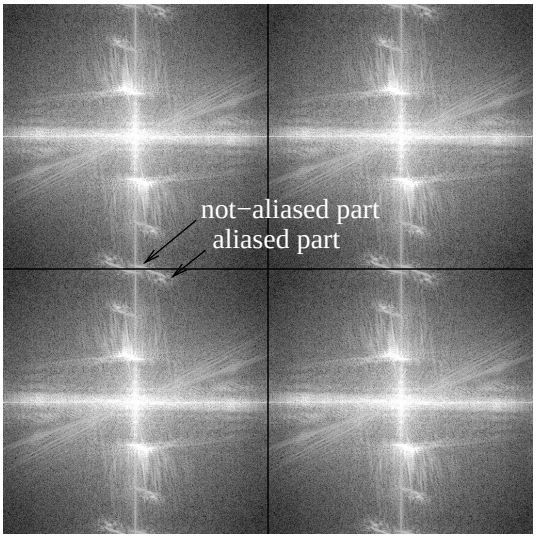

Figure 12.3: The periodization of $|\widehat{u}|$ from Fig.12.2 shows the extension of the line associated to $3\xi_1$ outside the spectral support of the image. This kind of aliasing is visually easily detected. This artifact could be removed if the spectral support was increased.

This kind of observation has already been done by Malgouyres [28] for the image restoration that preserves cylindric functions when frequencies are extrapolated out of the initial spectral domain. An example of application is the very special case of images containing a single edge. In this case, the

aliasing can be visually detected by periodizing the modulus of the Fourier transform of the image. We show some examples in Fig.12.4 and 12.5. The main frequency is clearly visible on the Fourier transform of the image: it is a line orthogonal to the edge direction. The aliases are also visible: they are lines parallel to the main one. The periodization of the Fourier transform shows immediately that the alias are the extension of the main line. This point has been discussed during the aliasing definition, see Fig.1.2. In log scale, the energy of the alias is bigger than the energy of the other frequencies. We immediately detect aliasing by comparing the energy of the main and aliased frequencies, which are close in log scale, to the energy of the background, which is small. Fig.12.5 shows two more examples. In the first one (a), aliasing can be easily detected because the image contains a single line. In the second one (c), the detection is difficult because it contains four line orientations, the alias of which interact and are hidden by the four main frequencies of each direction.

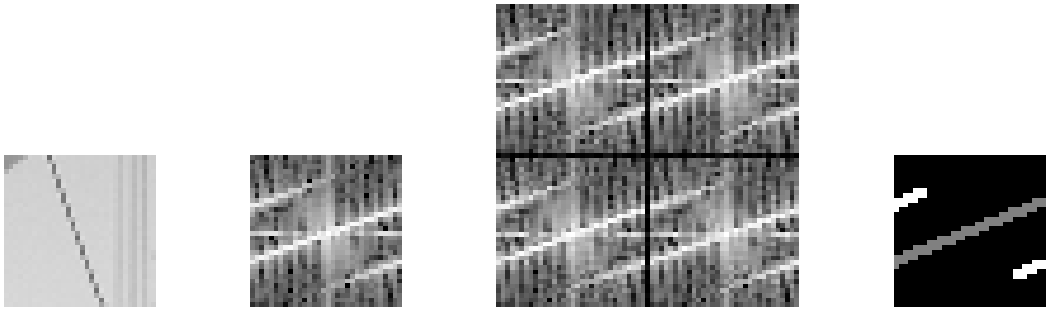

(a) (b) (c) (d)

Figure 12.4: (a) aliased image 32×32 (b) modulus of the Fourier transform in log scale (c) periodization of the modulus (d) mask of the main frequency (in gray) and of its aliases (in white). Aliases are visually detected on (c) by the line extensions.

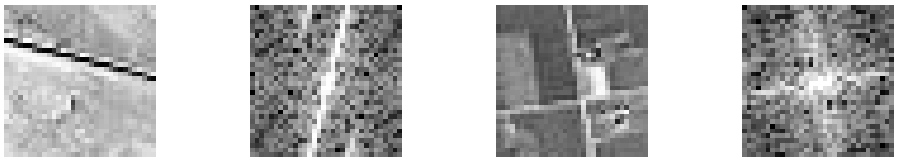

(a) (b) (c) (d)

Figure 12.5: (a) subpart of a SPOT 1 image 32×32 (b) modulus of its Fourier transform in log scale (c) an other subpart (b) modulus of its Fourier transform in log scale. On (b), aliases are visible since (a) contains a single line, but they are hidden in (d) since (c) has several edges.

As shown in Fig.12.5-d, the case of images which contain only one line is very special and the aliasing detection in the Fourier domain is not visually possible when an image contains more edges, as most natural images have. The problem of the aliasing detection in the Fourier domain comes from

the globality of the Fourier transform, so that aliases are often hidden by the frequential components of the other objects. Fig.12.6 shows an example of a very aliased image, the spatial image (b) is built by a down-sampling of a factor four in both direction of Fig.12.2-b. Our eyes detect aliasing in this image because of the unnatural shape of some objects. Some of the unnatural details are the electric wire is a dot line whereas the eye expect a continuous line, the irregular structure of some oblique books on the shelves and the stair-case effects along edges. The shirt on the couch still has an oscillatory structure which could be true. The change of orientation of the oscillatory textures cannot be detected without any other assumptions on the object geometry.

Even if our eyes detect aliasing in this image, the detection in the Fourier domain is not obvious. Fig.12.6-b does not contain lines which extension are clearly aliased. This shows that the aliasing detection should be done in the spatial domain. Such approach is presented in the next section.

(a) (b)

Figure 12.6: (a) $|\widehat{u}|$ in log scale (b) the aliased image u built by a downsampling of factor four of Fig.12.2-(b). The fundamental frequency of Fig.12.2 is aliased and the harmonics are hidden by low frequencies. The aliasing is visually detected in the image u and not in the image $|\widehat{u}|$.

12.2 Using the geometry

In the previous section, we have defined an aliasing detector based on the frequential characterization of this artifact. Now, we propose to detect the aliasing directly on the spatial image. One of the characterizations, which is called the *staircase* effect, is the degradation of the contours of objects. It reduces the regularity of the level lines. This is the reason why we propose to study the regularity of the level lines of an aliased image in order to detect aliasing.

12.2.1 The level line approach

The Coarea formula links the total variation of an image f to the length of its level lines [14]. And in a way, the longer the level lines are, the less regular they are. Before giving the Coarea formula, let us define the *level set* E_t.
Let U be an open set in $\mathbb{R}^n$, $BV(U)$ the space of functions of bounded variation and $\mathcal{L}^1$ the one-dimensional Lebesgue measure.

Definition 12.1 (Level set) *For $f : U \to \mathbb{R}$ and $t \in \mathbb{R}$, define*

$$E_t(f) \equiv \{x \in U \,|\, f(x) > t\}\,.$$

Theorem 12.2 (Coarea formula for BV functions) *Let $f \in BV(U)$. Then*

(i) *E_t has finite parameter for $\mathcal{L}^1$ a.e. $t \in \mathbb{R}$ and*

(ii) *$|Df|(U) = \int_{-\infty}^{\infty} |\partial E_t|(f)\, dt$.*

(iii) *Conversely, if $f \in L^1(U)$ and*

$$\int_{-\infty}^{\infty} |\partial E_t|(f)\, dt < \infty,$$

then $f \in BV(U)$.

Note: The expression "$\mathcal{L}^1$ a.e." means "almost everywhere with respect the measure $\mathcal{L}^1$," that is, except possibly on a set A with $\mathcal{L}^1(A) = 0$.

In this new approach, we try to prove that the level lines of aliased images have very special statistics.

12.2.2 Discussion

In aliased images, level lines are not regular. We observe this staircase structure along edges. Fig.12.7 shows the synthetic case of aliased and blurred steps with one level line. The level line discontinuity

(a) (b) (c) (d)

Figure 12.7: (a) Aliased image 128×128. (b) blurred image 128×128. (c) One level line on the zoomed version of (a). (d) One level line on the zoomed version of (b). Note the discontinuity and the regularity of the aliased and blurred image level lines, respectively.

is a direct consequence of the local configuration of the gray level values. In the case of the bilinear interpolation, level lines can be easily computed. Let us first recall the bilinear interpolation before describing the equation of the level lines. By definition, the interpolation of the discrete samples $u(i, j)$ (i, j integers) gives the continuous function $v(x, y)$ that coincide with u in (i, j). The computation of v is done on each 1×1 square with discrete coordinate (i, j), $(i + 1, j)$, $(i, j + 1)$ and $(i + 1, j + 1)$, the gray level values of which are a,b,c and d, respectively (Fig.12.8).

Definition 12.3 *The bilinear interpolation of the discrete image u on the domain*

$$S = [i, i + 1] \times [j, j + 1]$$

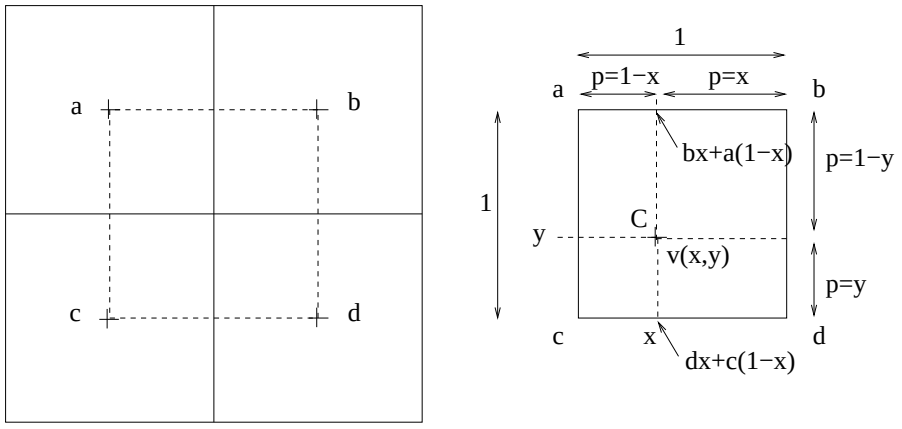

Figure 12.8: Bilinear interpolation. The value in (x, y) is obtained by giving a weight to the values of a, b, c and d as given by (12.1).

is the continuous image v defined $\forall (x, y) \in S$ by

$$\begin{aligned} v(x,y) &= (1-x+i, x-i)\begin{pmatrix} a & c \\ b & d \end{pmatrix}\begin{pmatrix} 1-y+j \\ y-j \end{pmatrix} \\ &= \big(a(1-x+i)+b(x-i)\big)(1-y+j)+\big(c(i+1-x)+d(x-i)\big)(y-j) \end{aligned}$$

where the discrete samples of u are

- $u(i, j) = a$,
- $u(i + 1, j) = b$,
- $u(i, j + 1) = c$,
- $u(i + 1, j + 1) = d$.

As expected, the corner values correspond to the discrete samples, that is

- corner 1: $v(i, j) = a$,
- corner 2: $v(i + 1, j) = b$,
- corner 3: $v(i, j + 1) = c$,
- corner 4: $v(i + 1, j + 1) = d$.

The level lines, defined in the regular case by $v(x, y) = k$ where k is a gray level in $[0, 255]$, are pieces of hyperbola with horizontal and vertical axes centered in $C = (x_c, y_c)$, where

$$x_c = \frac{a-c}{a+d-c-b} \quad \text{and} \quad y_c = \frac{a-b}{a+d-c-b} \quad \text{if} \quad a+d \neq b+c \ . \tag{12.1}$$

From (12.1), the value of v in C is $v(x_c, y_c) = \frac{ad-bc}{a+d-c-b}$. The position of C with respect to S modifies the level line smoothness within the pixel. Typically, we observe two positions of C:

P1: C in S (Fig.12.9-(a,b)). The level line curvature is large. The extreme case, where $C = (i, 0)$ is a corner of S, gives right angle. This case is observed in Fig.12.7-(a).

P2: C outside S (Fig.12.9-(c)). The level lines are parallel and the curvature is small. This case is observed in Fig.12.7-(b).

Definition 12.4 *The "**P1** points" are the points $C = (x_c, y_c) \in \mathbb{R}^2$, hyperbola center of the level lines of v defined on $S = [i, i+1] \times [j, j+1]$ by (12.1), such that C is in S.*

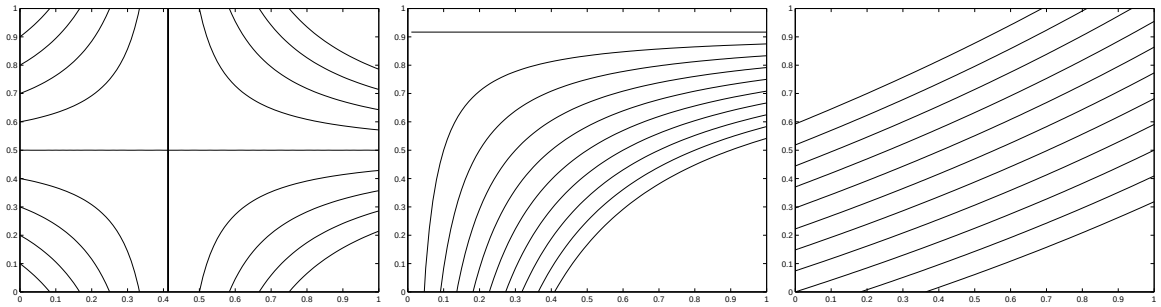

(a) (b) (c)

Figure 12.9: Level lines (a) **P1:** $C = (0.41, 0.50)$ (b) **P1:** $C = (0, 0.91)$ (c) **P2:** $C = (5.4, -2.2)$. The level line curvature is large when the center C of the hyperbola is within the pixel, that is in the $S = [0, 1]^2$ domain.

The number of points satisfying **P1** is generally large in aliased images. This comes from the local configuration along edges. In the example of synthetic aliased edge in Fig.12.10, S contains only one pixel of the edge, others belong to the background: $a = b = d$. The center C is a corner of S since

- $a = b$, so $y_c = 0$,
- $d = b$, so $x_c = \frac{a-c}{a+d-c-b} = \frac{a-c}{a-c} = 1$.

This example results in a top right corner position. The rotation of the black pixel among the four white ones, gives the four possible configuration associated to the four corner position of C.

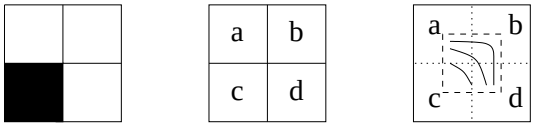

Figure 12.10: Example of **P1** configuration. Among the four pixels, three of them have very similar gray level values. They represents the background. The pixel from the edge has a different gray level value.

The fact that the number of points satisfying **P1** is generally large in aliased images can be useful to detect aliasing. But to build the detector we do not use this number but an other number we shall

define in the following that characterize the stair-case effect along edge, which is particular to the aliasing artifact. In the stair-case effect, two points **P1** with opposite corner position can be coupled as shown in Fig.12.11. Let us name

- C_1, C_2, C_3 and C_4 the corner position of S: they are the center of the pixels with gray level a, d, c and b, respectively.
- C'_1, C'_2, C'_3 and C'_4 the corner position of S', where S' is another square $[0,1]^2$ adjacent to S such that S and S' have one common boundary or only a common vertex.

Fig.12.12 shows an example of configuration of S and S'. The common boundary is such that $C_4 = C'_1$ and $C_2 = C'_3$.

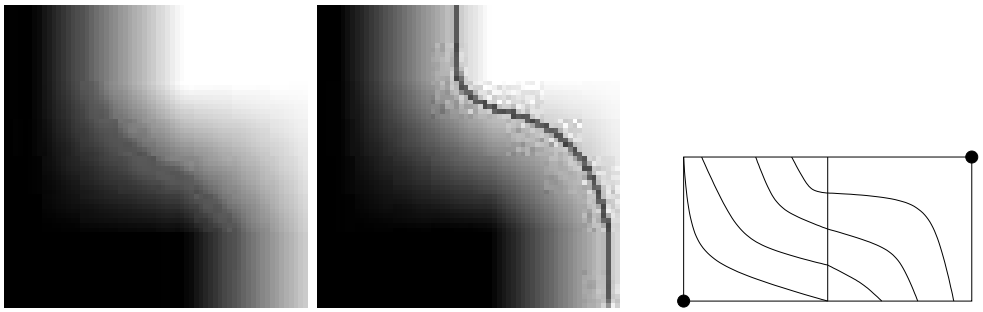

(a) (b) (c)

Figure 12.11: (a-b) Two level lines have opposite curvature. (c) The two associated hyperbola center C (marked by a •) have opposite corner position.

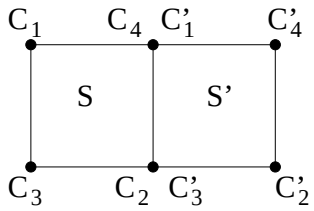

Figure 12.12: Both domains S and S' have four corner positions called C_1, C_2, C_3 and C_4 for S and C'_1, C'_2, C'_3 and C'_4 for S'. In such configuration of S and S', if there is **P1** points in opposite directions: (C_1, C'_2) or (C_3, C'_4), then the couple can be counted for the aliasing detection.

The coupled point are noted C_c and these are the points counted for the aliasing detection.

Definition 12.5 *Let S and S' be two different domains having at least one common vertex. The points C_c are the points for which S and S' have both a* **P1** *point and this couple of* **P1** *point should satisfy one of the six configurations of Fig.12.13.*

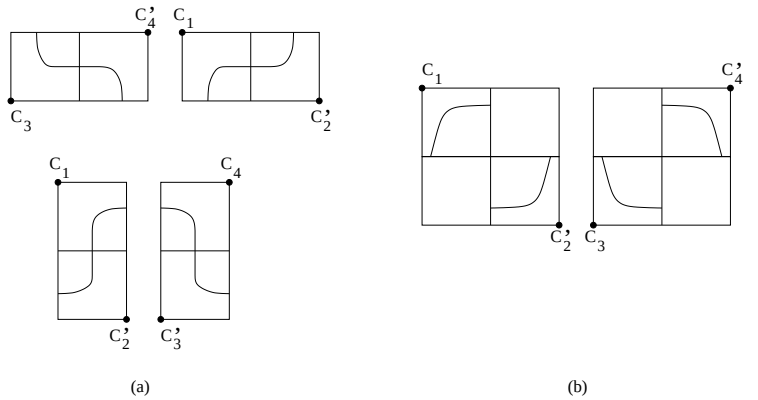

Figure 12.13: The six possible couples of **P1** points (a) 4 direct couples: S and S' have one common boundary (b) 2 diagonal couples: S and S' have one common vertex.

The number of points C_c can be useful to detect aliasing. Let us define the measure before defining the aliasing detector.

Definition 12.6 *The number of couples N_c is the number of C_c points in the image u.*
The proportion of couples $P(N_c)$ is defined by

$$P(N_c) = 100 \cdot \frac{N_c}{N},$$

where N is the number of tested pixels of u.

As we expect a large $P(N_c)$ for aliased images, we define the new following aliasing detector.

Definition 12.7 (Aliasing detector) *A given image u is aliased if*

$$P(N_c) \geq k,$$

where k is a threshold value.

The image is detected as *aliased* if the value of $P(N_c)$ is large. We introduce a threshold value k, which is not satisfactory. This is a preliminary work which should be improved by defining a parameter-free detector. As for the ringing detection, a probabilistic approach based on the NFA should be studied.

Now let us analyze the results obtained with the proposed aliasing detector in the numerical experiments.

12.2.3 Numerical experiments

Here we compute the values of $P(N_c)$ for two different sets of SPOT 5 image databases. The first database is used to set the parameter k and the detection is tested on the second database. The aliasing detector is also applied on a set of SPOT 1 image database. For all the tests, the computation of the values of $P(N_c)$ is not done for the whole image but on some subimages. So before doing these tests, a preliminary study of the stability of the $P(N_c)$ values on the subimages is done.

Preliminary study of the stability of the $P(N_c)$ values on subimages

We propose to compute the histogram of the values of $P(N_c)$ for 1000 randomly chosen 256×256 subimages of a SPOT 5 image of size 1280×960. The considered image is a non-aliased image with resolution 2.5 meters acquired above the town of *Canberra*. The values of $P(N_c)$ are in $[0.35, 1.47]$ with a large number of values in $[0.6, 0.8]$, which represents a small enough interval for the detection of aliasing since the spread is not bigger than the variability of the values of $P(N_c)$ for different kind of images: we will see in the test on the SPOT 5 image database that for non-aliased image, the value of $P(N_c)$ can range from 0 to 6.

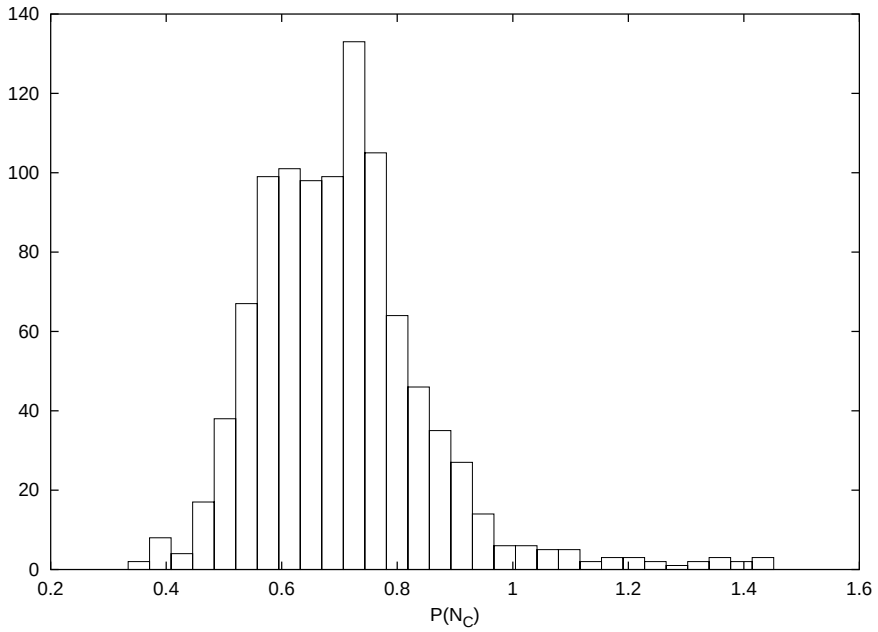

Figure 12.14: Histogram of the values of $P(N_c)$ for 1000 randomly chosen 256×256 subimages of *Canberra*. The histogram is narrow enough to chose either the median value or the maximal value of $P(N_c)$ as a good representative number for the aliasing detection.

In order to have a better understanding of the relation between the values of $P(N_c)$ and the kind of subimage, the subimages whose $P(N_c)$ values are extreme are analyzed in Fig.12.15. It shows that the lowest values of $P(N_c)$ correspond to images with a lot of uniform zones, such as the see. Since such kind of subimage does not characterize well the big image, the lowest values of $P(N_c)$ will not be considered as a representative value of the $P(N_c)$ of the big image. The same reasoning cannot be applied to the highest value since the associated images are very structured part of the image which contains useful information for the aliasing detection. The very geometrical structures have lines on which the stair-case effect might be detected.

These last results indicate that a big image subpart should always be preferred to a small one for at least two reasons. Firstly the problem of subimages containing only uniform zones has to be avoided. Secondly the subimage should contain enough information to be a good representative of the characteristics of the big image.

(a) image A (b) image B (c) image C

Figure 12.15: Three subimages (256×256) of *Canberra* for which the values of $P(N_c)$ belong to different parts of the histogram shown in Fig.12.14. Two extremal values of $P(N_c)$ are obtained for images A and B. For image A, which contains a lot of uniform zones due to the see, the value of $P(N_c)$ is small and belongs to the left part of the histogram: $P(N_c) = 0.49$, whereas image B contains many structure with geometrical parts so that the value of $P(N_c)$ is large and belongs to the right part of the histogram: $P(N_c) = 1.14$. On the contrary, image C is an example of the image for which the value of $P(N_c)$ belongs to the very central part of the histogram: $P(N_c) = 0.73$. It is a typical town image.

Test of the aliasing detector on a first SPOT 5 image database

We study three different SPOT 5 non aliased images with resolution 2.5 meters acquired above the town of *Canberra*, *Shanghai* and *Stockholm*. For each image, the aliasing detector is applied on four disjoint subparts of size 128×128 shown in Appendix (Section 12.5 Fig.12.33). Fig.12.16 displays the proportion of couples $P(N_c) = 100 \cdot \frac{N_c}{N}$ where N is the number of tested pixels for 12 subimages. The aliased images are built by downsampling the original image by a factor 2 and 3. N is smaller than the number of pixels in the image as we consider pixels with non zero gradient. We focus on pixels belonging to edges and we want to be noise independent. Fig.12.16 shows that $P(N_c)$ increases with the aliasing level. This information is not sufficient to classify correctly aliased images since texture may increase the value of $P(N_c)$. Hence some textured not aliased images may have large $P(N_c)$.

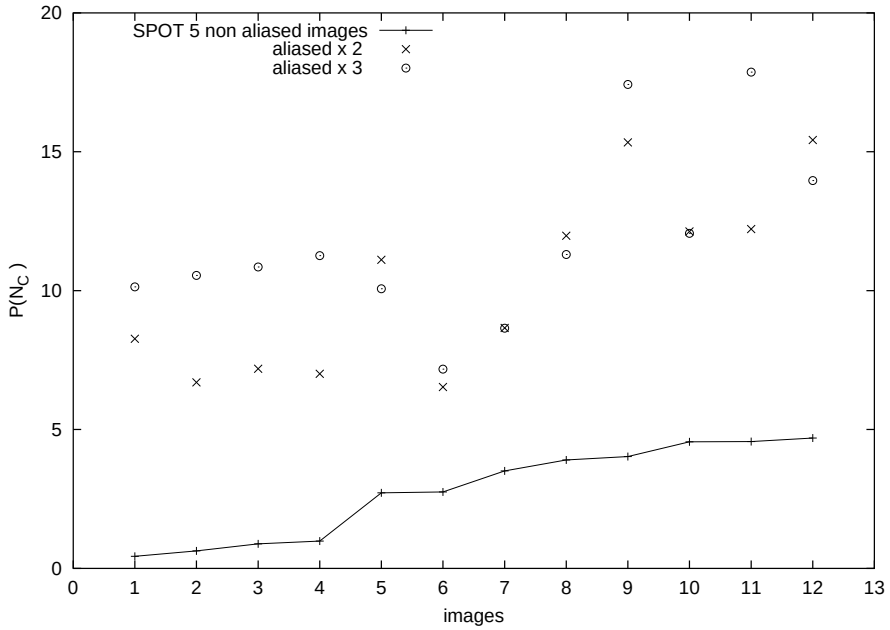

Figure 12.16: Proportion of couples $P(N_c)$ for 12 subparts of SPOT 5 images. Images are sorted along the X-axis such that their $P(N_c)$ values are in nondecreasing order. The $P(N_c)$ value of each original image is compared to the $P(N_c)$ value of the aliased images. The aliased versions are built by the downsampling of the original image by a factor 2 and 3. Original and aliased images have size 128×128. Note how $P(N_c)$ increases with the aliasing level.

Since we have seen that big image subparts are more representative of the image quality we do the same experiment with larger image subpart. The size of the image subpart is increased from 128×128 to 256×256. We also add another measure on the image called L, defined as the longer succession of C_c along an edge. This parameter is based on the visual observation that aliasing is more obvious when the aliased edge is long. This leads to the following procedure on each of the first SPOT 5 image database:

1. draw four disjoint random subparts of size 256×256,
2. compute $P(N_c)$ and L for each of the four subparts.

The algorithm for the aliased versions of the image is the same, except that the tested image is not the original image of the second database but its aliased version built by a downsampling of factor 2 of the original image. The $P(N_c)$ and L results of the three images of the database are shown in Fig.12.17. Experiments show that the aliasing detector with $k = 6$ is a good detector for the satellite images of the first database. The next test will check if this detector is not specific to the three tested images of the first SPOT 5 image database. To that aim we test the detector on a second database, which contains also SPOT 5 images but acquired at different places.

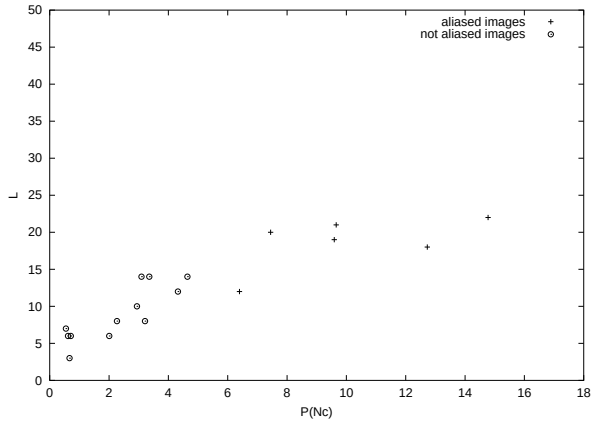

(a)

Figure 12.17: Graphs $(P(N_c), L)$ of four disjoint subparts of size 256×256 of the SPOT 5 images belonging to the first database: *Canberra*, *Shanghai* and *Stockholm*. The criteria $P(N_c) \simeq 6$ seems to be adequate for this learning basis since aliased images have $P(N_c) \geq 6$ and the original non-aliased images have $P(N_c) \leq 6$.

Test of the aliasing detector on a second SPOT 5 image database

We use the same experimental procedure than in the previous test but on the second SPOT 5 image database. We apply the aliasing detector from Definition 12.7 with $k = 6$. It shows that $P(N_c) \simeq 6$ seems to be a good delimiter between aliased and non-aliased images. The same criteria works for 2 others SPOT 5 tested images Fig.12.20-(a) and is confirmed for 21 others in Fig.12.20-(b). For both categories of images, aliased and non-aliased, some of them have results close to $P(N_c) \simeq 6$. We shall study now both categories to identify the corresponding images:

- the non-aliased image case: one can observe that some parts of non-aliased images have a high value of $P(N_c)$ close to 6. As indicated in Table 12.18, they belong to a single image: *Athens*. This is the only image with such a high value of $P(N_c)$. All the others have a value quite smaller than 6. This can be explained by the fact that there might be some aliasing in the diagonal direction on SPOT 5 images so the image of *Athens* has probably little aliasing. The subimage of *Athens* and *Amsterdam* that gave the maximal value of $P(N_c)$ are shown in Appendix in Fig.12.34.

Original image	*Athens*	*Amsterdam*	*Riga*	*Warsaw*	*Vienna*	*Madrid*	*Brussels*
$\max P(N_c)$ in %	5.71	4.82	4.37	4.15	4.12	3.95	3.83

Table 12.18: Table of the highest value of $P(N_c)$ among the four tested subparts of each non-aliased images. All values are bigger than 6, so that the original images are well classified.

- the aliased image case: some have a small $P(N_c)$ close to 6, such as *Washington* or *Tel Aviv* (Fig.12.35). However, the 19 others are clearly detected as aliased.

Aliased version of	*Washington*	*Tel Aviv*	*Toulouse*	*São Paulo*	*Istanbul*	*Budapest*	*Luxembourg*
$\min P(N_c)$ in %	**3.14**	**5.60**	6.10	6.12	7.14	8.09	8.53

Table 12.19: Table of the smallest value of $P(N_c)$ among the four tested subparts of each aliased images. The aliased versions of *Washington* and *Tel Aviv* have $P(N_c) \leq 6$, so they are badly classified.

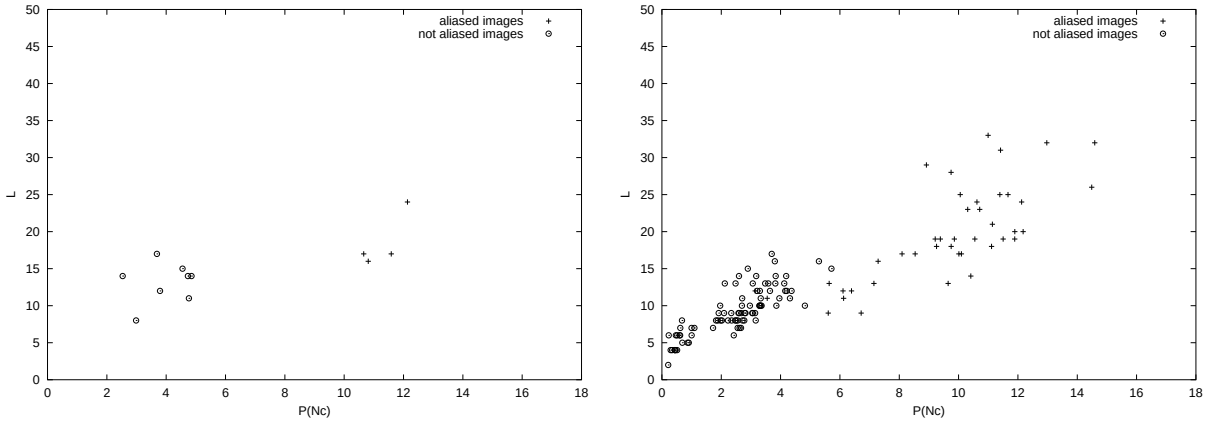

(a) (b)

Figure 12.20: Graphs $(P(N_c), L)$ tested on SPOT 5 image subparts of size 256×256 (a) *Berlin* and *Copenhagen* (b) *Toulouse*, *Brussels*, *Prague*, *Washington*, *Istanbul*, *Budapest*, *Rome*, *São Paulo*, *Valletta*, *Riga*, *Warsaw*, *Tel Aviv*, *Vilnius*, *Lisbon*, *Vienna*, *Amsterdam*, *Luxembourg*, *Athens*, *Bratislava*, *Nicosia*, *Madrid*. The only badly classified aliased image is the aliased version of *Washington* in (b), which is a smooth image, others have $P(N_c) \geq 6$.

We have not adopted a procedure for the analyze of the results. Each time we have plotted the $P(N_c)$ values of the four image subparts that have been tested. The preliminary study of the stability of the $P(N_c)$ values showed that we could followed a procedure that select for example the highest value among all $P(N_c)$ results obtained for the different subimages. We could have also considered a

median value if the number of tested images is large enough. These last considerations can be avoided by considering directly the whole image and not its subparts. The associated procedure is

1. extract the down 1201×881 subpart of SPOT 5 image (the upper part, which represents 80 lines, are crop because some text has been overimposed and then cannot be considered as reliable information),
2. compute $P(N_c)$ and L.

The results obtained on all the 26 images of the second SPOT 5 image database are presented in Fig.12.22: *Canberra*, *Shanghai*, *Stockholm*, *Berlin*, *Copenhagen*, *Toulouse*, *Brussels*, *Prague*, *Washington*, *Istanbul*, *Budapest*, *Rome*, *São Paulo*, *Valletta*, *Riga*, *Warsaw*, *Tel Aviv*, *Vilnius*, *Lisbon*, *Vienna*, *Amsterdam*, *Luxembourg*, *Athens*, *Bratislava*, *Nicosia* and *Madrid*. The results obtained on the whole image confirm the results obtained on subparts given in Table 12.19: three aliased images are badly classified:

Aliased version of	*Washington*	*Tel Aviv*	*Toulouse*	*São Paulo*	*Istanbul*	*Canberra*
$P(N_c)$ in %	**3.90**	**5.64**	**5.90**	6.09	6.86	7.18

Table 12.21: Table of the value of $P(N_c)$ for each aliased images. The only badly classified aliased images are the aliased versions of *Washington*, *Tel Aviv* and *Toulouse*. These results confirm the previous results given in Table 12.19, for which these three aliased images had already a $P(N_c)$ value smaller than 6 or very close to it.

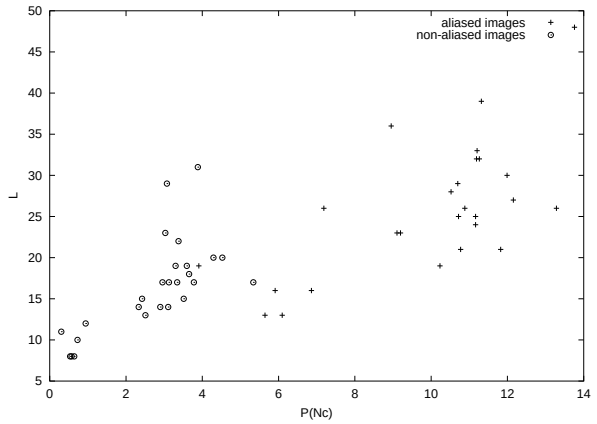

Figure 12.22: Graphs $(P(N_c), L)$ tested on 26 SPOT 1 images. The obtained results are very similar to the one obtained on the image subparts shown in Fig.12.20-(b). Again there is an aliased image with a very small value of $P(N_c)$, which corresponds to the *Washington* image. Two other aliased image have $P(N_c) \simeq 6$: *Tel Aviv* and *Toulouse*. These results obtained on the whole image confirm the results obtained on subparts given in Table 12.19.

Now that the validity of the results on image subparts has been checked with the results obtained on the whole image, the question of the detection of very small aliasing is analyzed. The aliased

images generated in the previous experiments were strongly aliased since only one pixel over two in each direction were preserved. The aliasing in satellite images might be more subtle. So the aliasing criteria is tested on already aliased images such as most images acquired by the satellite SPOT 1.

Test of the aliasing detector on a SPOT 1 image database

In the experiments, we chose subparts of SPOT 1 images, which are generally aliased. Fig.12.23 shows the results of three SPOT 1 images with resolution 20 meters. *Detroit* is a town image, whereas *Chile* and *Kuwait* are geologic images. These images are not town images such as tested on the SPOT 5 database. So it is not surprising that some 256×256 sub-images are not detected as aliased. They contain no sharp edge. However, the criteria performs well, as at least one of the sub-images detects that the image is aliased.

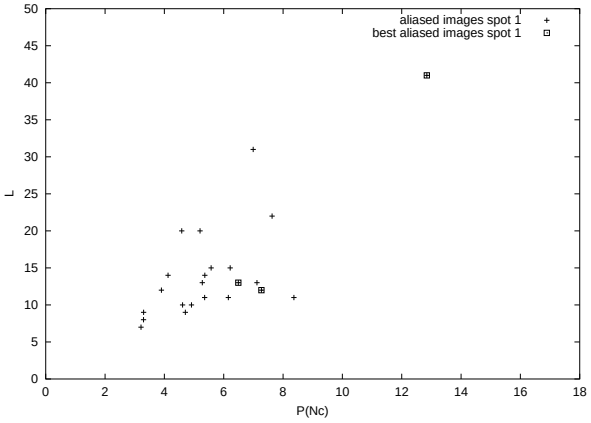

Figure 12.23: Graphs $(P(N_c), L)$ tested on SPOT 1 image subparts of size 256×256: *Detroit*, *Chile* and *Kuwait*. The square symbol indicates the highest $P(N_c)$ for each three images.

This method is based on the spatial characterization of the aliasing artifact, especially the stair-case effect and not the change of orientation for oscillating textures. We have seen that with the chosen threshold the detection is coherent on SPOT 5 images. However this method should be continued to propose a parameter free algorithm.

12.3 Using the Shannon postulate

12.3.1 Theory

The Shannon sampling theorem [45] is reformulated in [53] by

Theorem 12.8 (Shannon) *If a function $f(x)$ contains no frequencies higher than $\omega_{\max}$ (in radians per second), it is completely determined by giving its ordinates at a series of points spaced $T = \pi/\omega_{\max}$ seconds apart.*

The reconstruction formula that complements the Shannon theorem is

$$f(x) = \sum_{k \in \mathbb{Z}} f(kT)\,\mathrm{sinc}(x/T - k) \quad . \tag{12.2}$$

This reconstruction formula 12.2 is exact if f is band-limited with $\omega_{\max} \leq \pi/T$. We call a "Shannon image", a 2D signal satisfying the condition of Shannon theorem. An aliased image is built by downsampling a Shannon image by a factor δ. This discrete image has less samples than the discrete Shannon image. The reconstruction of the underlying continuous image f is then no more exact.

The formula 12.2 leads to the postulate which states that a Shannon image is *equivalent* to all its subpixel translations. Then this equivalence between translated images may allow to detect aliased images.

Definition 12.9 *Let $\mathcal{T}$ be the set of translated images*

$$\mathcal{T} = \{u_t \text{ such that } t = (t_x, t_y) \in [0,1]^2\}$$

where u_t is the image translated by t constructed from image u of size NxN:

$$u_t(k_1,k_2) = \sum_{m_1=0}^{N-1} \sum_{m_2=0}^{N-1} u(m_1,m_2)\ \textit{sincd}_N(k_1+t_x-m_1)\ \textit{sincd}_N(k_2+t_y-m_2)$$

or

$$\widehat{u_t}(p_1,p_2) = e^{\frac{-2i\pi}{N}(p_1 t_x + p_2 t_y)}\ \ \widehat{u}(p_1,p_2)\ .$$

We note sincd_N the discrete cardinal sine of order N the $N-$periodic function defined in [32] by

$$\forall t \in \mathbb{R} \setminus N\mathbb{Z}, \quad \text{sincd}_N(t) = \begin{cases} \frac{\sin(\pi t)}{N \sin(\pi t/N)} & \text{if } N \text{ is odd} \\ \frac{\sin(\pi t)}{N \tan(\pi t/N)} & \text{if } N \text{ is even} \end{cases} . \tag{12.3}$$

Let us recall that the subpixel translation of an image leads to ringing, which we will measure with the total variation. Fig.12.24 shows how a sharp edge increases more the total variation after a subpixel translation than a smooth transition. Ringing cannot affect images the same way. It is more visible on cartoon images than on textured images. The first ones have constant zones where ringing oscillations are very long whereas textures might hide the phenomenon (Fig.12.25).

We define an aliasing detector that compare the total variations of Shannon images to the ones of aliased images. In a way, this detector is very similar to the previous one that was using the geometry. We have seen in Section 12.2 that the Coarea formula links the total variation of an image f to the length of its level lines [14], so here we replace the measure of the level line regularity by the measure of the total variation. Moreover we replace the bilinear interpolation, which was necessary to estimate the sub-pixel regularity of the level lines, by the sub-pixel translations.

12.3.2 Detector definition

We propose now a new definition of the aliasing detector. As we defined a parameter-free sharpness detector based on a probabilistic model in Section 10.2

$$F_\varepsilon(u) = -\log_{10}\ \ \mathbb{P}\left(TV(U_\varepsilon) \leq TV(u)\right),$$

we define now a parameter-free aliasing detector based on a probabilistic model.

Definition 12.10 (Aliasing detector) *Let $TV(u)$ be the total variation of u and $TV(U_t)$ be the total variation of its translated version U_t where the translation is an uniform random variable in $[0,1)^2$. We define the aliasing detector by*

$$G(u) = -\log_{10}\ \ \mathbb{P}\left(TV(U_t) \leq TV(u)\right).$$

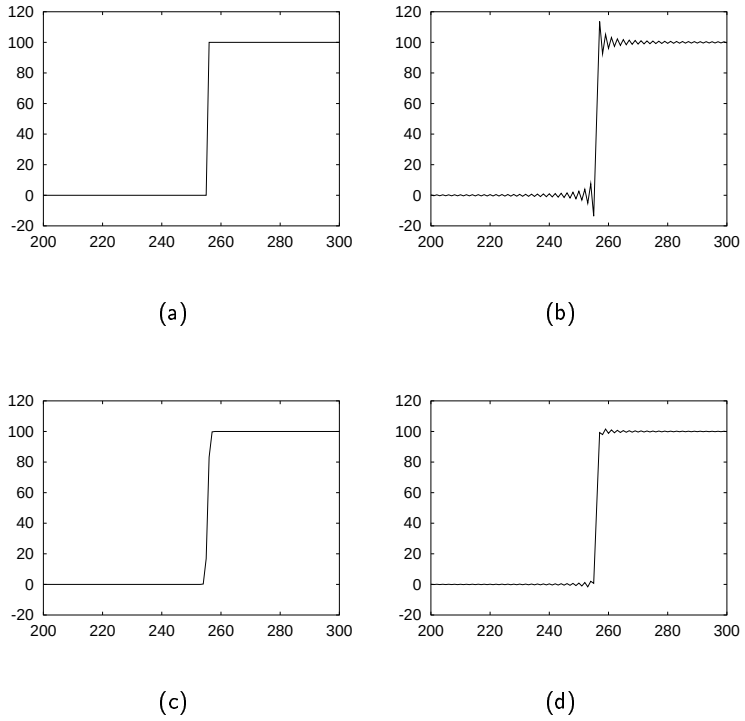

Figure 12.24: (a) sharp transition (b) result after the translation of 0.5 (c) smooth transition (b) result after the translation of 0.5. The original signals (a) and (c) have same total variation, which is equal to one. Note how the amplitude of the oscillations are larger for the sharp transition, yielding a larger increase of the total variation in (b) than in (d).

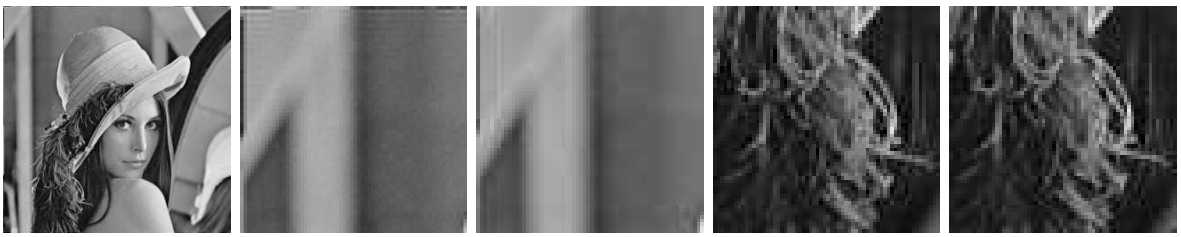

Figure 12.25: (a) Image u_t, translated version by $(t_x = t_y = 0.5)$ of the "lena" image u_0 (b-d) Sub-Images 64x64 of the upper left corner and the central down part of u_0. (c-e) Sub-Images from u_t. In (c), the ringing is clearly visible in the upper left corner. In (e), the ringing is hidden by hat's feathers textures.

The subpixel translation is done by the interpolation of the image with the Shannon filter. This step inevitably creates overshoot and undershoot The sharper the transitions are An aliased image has sharp edges, so that a subpixel translation increases the total variation. The interpolation with the Shannon filter adds high

Experimentally, the computations of G are done with the following algorithm:

Algorithm 3 (Empirical estimation)

1. *Build* n *images* u_t^i, $i = 1 \dots n$
2. *Compute* $M = \{$*number of* u_t^i *such that* $TV(u_t^i) \leq TV(u)\}$
3. *Estimate* $\mathbb{P}(TV(U_t) \leq TV(u)) \approx \frac{M}{n}$
4. *Deduce* $G(u) = -\log_{10} \mathbb{P}(TV(U_t) \leq TV(u)) \approx -\log_{10}\left(\frac{M}{n}\right)$

In practice for all experiments, we test 20 different translations along the X-axis, and 20 different translations along the Y-axis, which makes $n = 20^2 - 1 = 399$ translations (the translation $(t_x, t_y) = (0, 0)$ is not studied since in that case $TV(u_t) = TV(u)$). Numerically, we threshold G to 100 if $M = 0$.

12.3.3 Numerical experiments

Experiment 1

The first experiment studies the image of Fig.12.2 which has small aliasing. In order to reduce the computation times, we study a subimage of size 256×256 shown in Fig.12.26-b. For this image, we compute $G(u)$. For all tested u_t, we obtain no translation such that $TV(u_t) \leq TV(u)$, so that

$$M = 0 \quad \text{and} \quad G(u) = +\infty\,. \tag{12.4}$$

This result checks that u is aliased.

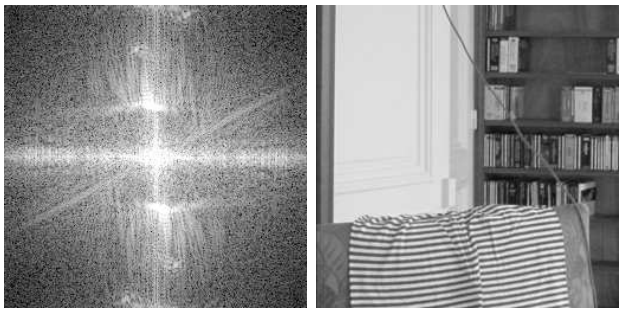

(a) (b)

Figure 12.26: (a) $|\widehat{u}|$ in log scale (b) the image u with small aliasing

Now we test the aliasing detector on degraded versions of u.

- First we study blurred versions of u obtained by the convolution of u with a Gaussian filter k_σ with standard variation σ:

$$u_\sigma = u \star k_\sigma \, .$$

The stair-case effects along edges decreases when σ increases, so that the image u_σ has less aliasing along edges and we intend a small value of G. In fact, if u_σ is not aliased, we expect $\mathbb{P}(TV(U_t) \leq TV(u_\sigma)) \geq 0.5$ which yields $G(u_\sigma) \leq 0.301$. Of course the blur does not cancel the low-frequency aliasing in u. Fig.12.27 shows the values of $G(u_\sigma)$ for $\sigma \in [0, 4]$. As expected, $G(u_\sigma)$ is small for large σ.

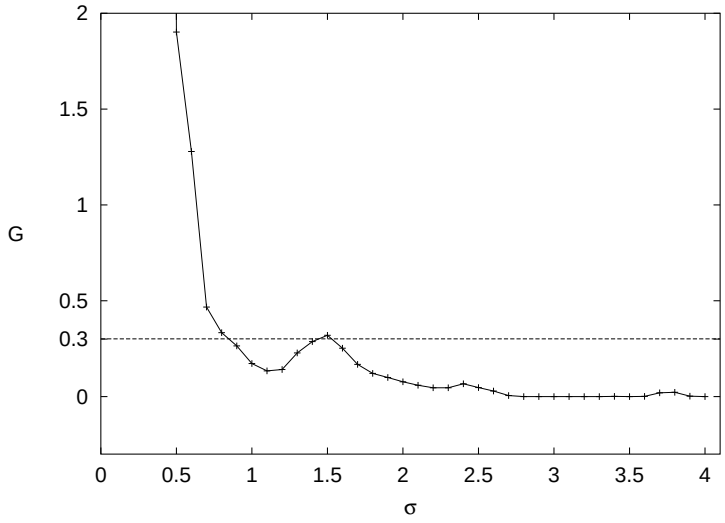

Figure 12.27: Graph $(\sigma, G(u_\sigma))$ for the Gaussian blur kernel with standard deviation $\sigma \in [0, 4]$. For $\sigma \geq 0.8$, there is no aliasing detected because $G(u_\sigma)$ is small. For $\sigma < 0.8$, no aliasing is detected because $G(u_\sigma) >> 0.301$. This result is coherent because when σ increases the stair-case effect, typical effect of the aliasing artifact, along edges is reduced.

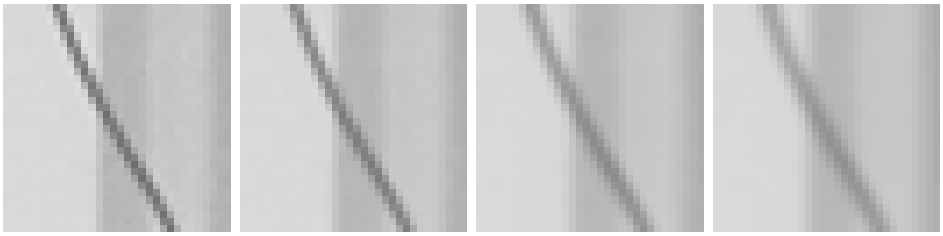

(a) $\sigma = 0$ (b) $\sigma = 0.5$ (c) $\sigma = 0.8$ (d) $\sigma = 1$

Figure 12.28: Subparts of the images $u \star k_\sigma$. Note how edges are very blurry for $\sigma \geq 0.8$, edges for which the stair-case effect is canceled.

- Second we study an aliased version u_d of u, which means that we downsample the image u by

a factor two. Of course, u_d will be aliased since u is already aliased. The image u_d is detected as aliased because

$$G(u_d) = +\infty\,.$$

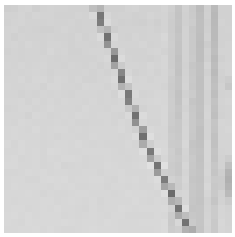

Figure 12.29: Subpart of the downsampled version u_d of image u. The staircase effect is important on this thin structure. This aliased image u_d is detected since $G(u_d) = +\infty$.

Experiment 2

The second experiment studies the 21 SPOT 5 images described in Section 12.2. The aliasing detector G is tested on these images and on their downsampled versions by a factor two in each direction. In order to have images with comparable size, for each image (original and downsampled images) the studied extract of the image is the largest central subpart of the image with dimensions power of two. For all images, the resulting image has size 512×256, and it is symmetrized in both directions in order to avoid the image boundary problems during the image translation. Moreover the total variation measure has to be independent of the boundaries, so that a large image size is favorable.

The Y-axis of the graph in Fig.12.30 shows the values of G obtained on these two groups of images. The aliasing detector allows the detection of two groups of images: one group with small values of G and one group with values of G larger than 100. As expected the group with large values of G corresponds to the group of aliased images: the total variation of the translated images is always larger than the total variation of the original image.

One aliased image, which is the downsampled version of *Lisbon* shown in Fig.12.31, has an unexpected small value of G. This could be explained by its large proportion of horizontal and vertical contours: the downsampling of this kind of contour looks often less aliased than diagonal ones.

Experiments showed that the characterization of the image with G does not completely solve the aliasing detection problem: some images are badly classified. However it has the great advantage to be a blind aliasing detection, i.e. without the reference non-aliased image, and to be parameter free.

Another interesting measure is the amplitude of the total variation with respect to the translations, that is

$$TV_{\max}(u) - TV_{\min}(u)\,,$$

where $TV_{\max}(u)$ and $TV_{\min}(u)$ are defined by

$$TV_{\max}(u) = \max_{t\in[0,1]^2} TV(u_t)$$

and

$$TV_{\min}(u) = \min_{t\in[0,1]^2} TV(u_t)\,.$$

We observe that the aliased images have a large amplitude of the total variation, contrarily to the non-aliased images. The value $TV_{\max}(u) - TV_{\min}(u)$ is the X-axis of the graph in Fig.12.30. This indicator is useful for the detection of aliased images, such as the downsampled version of *Lisbon* shown in Fig.12.31.

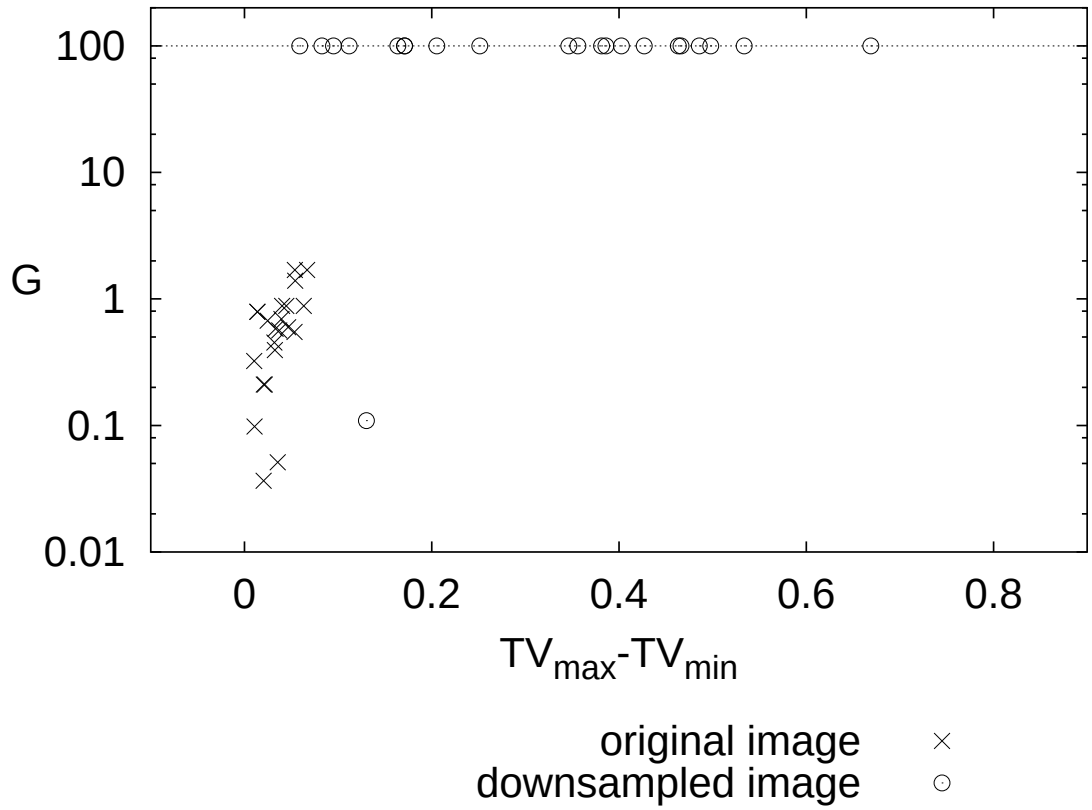

Figure 12.30: Graph $(G, TV_{\max} - TV_{\min})$ for 21 aliased and not aliased images with $n = 10$. The aliasing detector G classifies correctly most of the images: all original images have $G(u) \leq 1.7$, which indicates that images are not aliased, and all downsampled image except one (downsampled version of *Lisbon*) have $G(u) \geq 100$ which indicates that images are aliased. The computation of $TV_{\max} - TV_{\min}$ is also a good indicator since original images have a very small value of $TV_{\max} - TV_{\min}$, i.e. less or equal to 0.1, whereas most aliased images have a larger value, which classifies the downsampled version of *Lisbon* as aliased.

12.4 Conclusion

We have tested three new approaches to detect aliasing in an image. The first one was based on the frequential interpretation of this artifact. This approach seems natural since aliasing is defined in the Fourier domain by the overlapping of aliases. However it did not give satisfactory results because the Fourier transform is a global operation and the aliases are often hidden by other Fourier components.

Then we tested a new approach based on the effect of the aliasing in the spatial domain, especially

Figure 12.31: Subpart of size 512×256 of the downsampled version of *Lisbon*: $G = 0.11$ and $TV_{\max} - TV_{\min} = 0.13$. This image has a small value of G, but a sufficiently large enough value of the total variation amplitude so that the image could be detected as aliased.

Figure 12.32: Subpart of size 512×256 of the downsampled version of *Athens*: $G \geq 100$ and $TV_{\max} - TV_{\min} = 0.34$. The value of G is large enough to detect the image as aliased. This result is confirmed by the large value of the total variation amplitude.

along edges where it adds a staircase-like structure. This looks like a grid impression on the image. This effect lowers the regularity of the level lines and increases locally their length. The proposed detector counts the number of pixels $P(N_c)$ where the level lines are highly irregular, i.e. the level lines which follow the sampling grid. The numerical experiments showed that on SPOT 5 images, the $P(N_c)$ value is smaller for the original images than for the aliased images, built by a downsampling by a factor two of the original images in both X and Y directions. Note that the value of $P(N_c)$ at the frontier between the aliased and non aliased images has to be adapted to the type of images. In our examples, we studied images of town obtained by the SPOT 5 satellite and have chosen the frontier value of $P(N_c) \simeq 6$. For another type of images, this value will be different.

The third approach is based on the fact that if an image respects the Shannon theory then the image is equivalent to all its translated versions by the Shannon filter. The new detector is not designed specifically for the detection of aliased images but for the more global class of images that do not respect Shannon theory. The same approach than for the sharpness detection has been used to build the detector: the total variation of the translated versions of the image (and not the phase coherence as for the sharpness detector) is compared to the total variation of the original image. The total variation measure has been selected since translating an image produces ringing, due to the sinc interpolation

Now that we have defined some detectors for the three major artifacts studied in this thesis, let us discuss some applications of such detectors. The following part deals with two restoration problems: deconvolution and denoising, where the automatic detectors can be efficiently used to obtain a parameter-free process.

12.5 Appendix

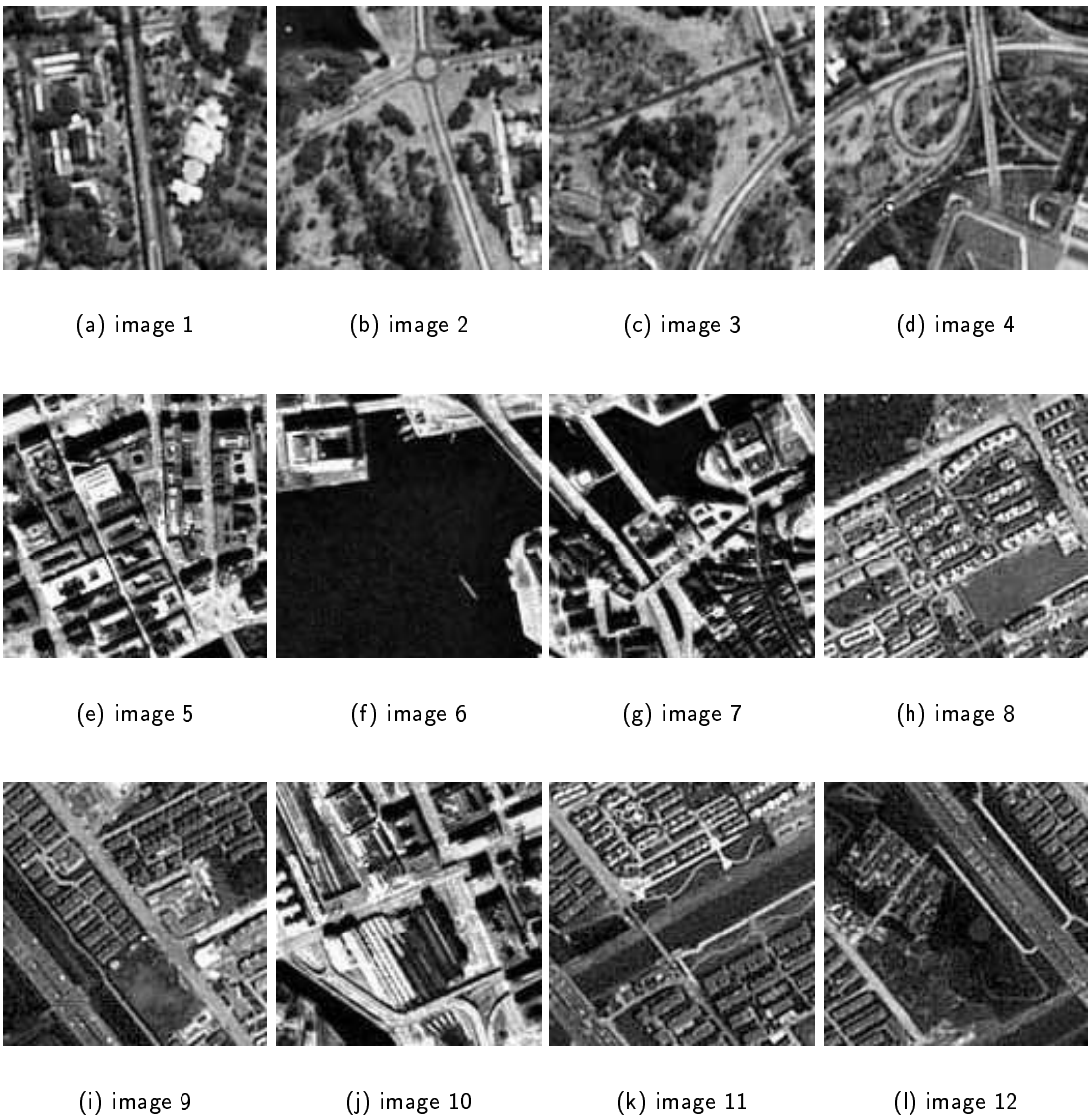

(a) image 1 (b) image 2 (c) image 3 (d) image 4

(e) image 5 (f) image 6 (g) image 7 (h) image 8

(i) image 9 (j) image 10 (k) image 11 (l) image 12

Figure 12.33: 12 subparts of SPOT 5 images of size 128×128 classified by the aliasing detector (Definition 12.7) sorted with an increasing order of $P(N_c)$. Images 1,2,3,4 are subparts of *Canberra*. Images 5,6,7,10 are subparts of *Stockholm*. Images 8,9,11,12 are subparts of *Shanghai*.

(a) *Athens* image subpart: $P(N_c) = 5.71$ (b) *Amsterdam* image subpart: $P(N_c) = 4.82$

Figure 12.34: Subparts of SPOT 5 images of size 256×256. Both images have $P(N_c) < 6$, so that no aliasing is detected.

(a) *Washington* image subpart: $P(N_c) = 3.14$ (b) *Tel Aviv* image subpart: $P(N_c) = 5.60$

Figure 12.35: Subparts of aliased SPOT 5 images of size 256×256. Both images have $P(N_c) < 6$, so that no aliasing is detected.

Part IV

Applications to image restoration without parameter

Introduction

The goal of restoration is to find a "*nice*" image, i.e. an artifact-free image, from its degraded version. In this part, we study two types of restoration: the deblurring and the denoising, which consist in removing the blur and the noise, respectively. The first chapter is devoted to the restoration of blurred images, and the second one considers the denoising problem. Artifact detectors can be used for such applications to obtain automatically the best parameter of the restoration method. In this part, we shall use only the sharpness detector F defined in Chapter 10, but the other detectors could be used as well for some other applications. Let us now describe the two approaches discussed in Chapter 13 and 15.

Chapter 13 refers to the blind deconvolution problem. The restoration of a blurred image without the knowledge of the blur kernel is not a new problem and there are already some methods in the literature. One of them is the Lucy-Richardson algorithm [27] [41]. This is an iterative algorithm well used in astronomy. Here we propose another method based on the deblurring with a Wiener filter and the criteria is given by the sharpness detector F. Here we consider two ways for the deblurring.

- The first one is the progressive deblurring. Some convolution filters are the iterated convolution product of the same filter or filter of the same family. We try to answer the question: is it possible to deblur the image continuously, that is by successive small deblurring steps? This refers to the idea that there might be a simple deconvolution path from the blurred image to the original sharp one. As an application to this question, we try to decompose the Shannon filter: $\xi \to \mathbb{1}_{[-W,W]}(\xi)$ into the convolution product of a single filter. We will give some necessary conditions for the progressive deconvolution with such a kernel. We also cite the results of Abramatic and Faugeras on the filter decomposition [1], but we will see that these results cannot be applied to our specific convolution model.

- The second type of deblurring is the complete one, that is one single convolution kernel between the original image and the restored one. Both types of deblurring are linked if the single convolution kernel of the direct deblurring belongs to one of the following family. The first family is the class of kernel with small support such as 3×3. Such a filter can be considered as an element step of a continuous deblurring since it has typically the size of the filter element of a decomposition. The second family contains the kernels which are intrinsically the convolution of filters of the same class, such as the product of Gaussian functions in the Fourier domain. Gaussian filters will be studied in this thesis because they are often used in practice to model the image degradation [18].

We show that the sharpness detector performs well on the two filter families (kernel with 3×3 support and Gaussian functions) since it detects the blur on the degraded image. It also allows the identification of the convolution filter since the corresponding deconvolved image is then detected as

sharp. For both types of filter, we also compare the sharpness detector with the total variation measure. It is adapted to measure the oscillations introduced by the deconvolution with a wrong filter, especially in some special cases with a lot of oscillations, but in most cases it is not adapted since it prefers smooth images to sharp ones.

Chapter 15 refers to the denoising problem. We do not propose a new denoising method. Instead, our goal is to provide tools for automatic denoising. Among numerous denoising algorithms in the literature, we have chosen a recent one called the NL-means [6]. Since it is a parametrized method, and since the choice of the parameters is not obvious (they can be chosen with the subjective perceptual evaluation), we propose here to use the sharpness detector to identify the best parameters. The best parameter is found when the obtained denoised image is detected as sharp.

Let us now study the restoration of blurred images.

Chapter 13

Restoration of blurred images

13.1 Blind deconvolution

Blind deconvolution is a term given to an image restoration technique in which both the blur kernel (or the point spread function of the imaging process) k and the original image u_0 are unknown. In the simplest case, image blurring is associated with the 2D convolution. The cumulative effects of noise during the acquisition process is very often modeled by an additional degradation. In the end,

$$u_c = k \star u_0 \, + \, n \, .$$

Some non linear techniques have been proposed in the literature to find u_0. Let us cite one example of iterative method of maximum likelihood called Lucy-Richardson (LR). The LR method is an algorithm of choice among optical astronomers because of the non-negativity constraint of u [27] [41]. It is also popular in the field of medical imaging. This method is not new (early 70'), however it is still competitive because of its robustness in the presence of noise. The algorithm proposed by Richardson assumes that u is unknown and k is known. The LR deconvolution has been extended by Ayers and Dainty by alternately iterating on each of the unknowns: the filter and the reconstructed image [4]. At each iteration k, the filter and the deblurred images are computed with the following formula

1. $(k(x))_{r+1} = (k(x))_r \cdot \left(\left[\frac{u_c(x)}{(u_0(x))_r \star k(x)} \right] \star (u_0(x))_{r-1} \right)$,

2. $(u_0(x))_{r+1} = (u_0(x))_r \cdot \left(\left[\frac{u_c(x)}{(u_0(x))_r \star k(x)} \right] \star (k(-x))_r \right)$,

where the recommended initial values of k and u_0 are the dirac function and the constant image having the mean value of u_c, respectively.

This algorithm will be used later in chapter 13.3 for the automatic deconvolution with filters having compact support and we will see how the sharpness detector can be added to this iterative algorithm. But before studying the deconvolution with filters having compact support, let us first define what we call progressive deblurring and let us see if the progressive deblurring of an image u is possible.

13.2 Blind deconvolution with progressive deblurring

13.2.1 Continuous blurring/deblurring

Blur interpolation

Consider an original image u with no blur which has been blurred by a filter $\tilde{k}$:

$$v = u \star \tilde{k} \,,$$

where v is the resulting blurred image. The idea of the blur interpolation is the existence of a path between u and v with an increasing value of blur (Fig.13.1). The image with intermediate blur is obtained by

$$u_{k_1} = u \star k_1 \,,$$

where k_1 is another filter. The difficulty is the constraint on the intermediate blur kernel k_1: the idea is not to give any kernel k_1 which produces less blur than $\tilde{k}$ after the convolution with u but the idea is to decompose the kernel k into the convolution of the filter k_1 and another filter k_2 (without excluding the possibility that $k_2 = k_1$)

$$\tilde{k} = k_1 \star k_2 \,.$$

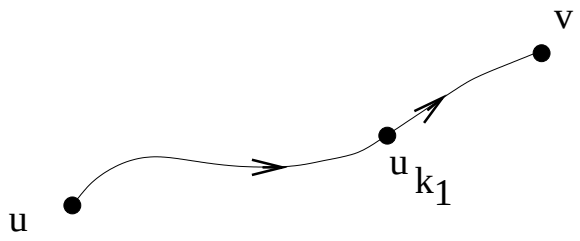

Figure 13.1: The path between u and v corresponds to an increasing blur value. The image u has no blur, on the contrary to v. Interpolating the blur assume the existence of an intermediate blurred version of u with less blur than v. We note $u_{k_1} = u \star k_1$ such image obtained with the filter k_1.

The blur interpolation is possible if the filter $\tilde{k}$ can be decomposed as the convolution of two or more filters. The idea is to decompose the filter $\tilde{k}$ in small filters, either with the multiple convolution of the same filter or with the convolution of several small different filters. For example, with n filters we would have the following decomposition of $\tilde{k}$:

$$\tilde{k} = k_1 \star k_2 \star \ldots \star k_n \,,$$

or

$$\tilde{k} = k \star k \star \ldots \star k \,, \tag{13.1}$$

if the small filters are identical: $k = k_1 = k_2 = \ldots = k_n$. From $\tilde{k}$, the idea is to give a continuous interpretation of the blur process. Pushing a little bit forward this idea, one could even wonder if the convolution with an infinite number of small kernels (n tends to infinity) has a sense ?

The iterative convolution of the same kernel as in 13.1 is studied now, where k is supposed to be a small kernel.

Let $(C_k)_{k\in\mathcal{M}_N}$ be the semi-group of translation invariant and linear operators. It is defined on images u of size $N\times N$ by

$$C_k(u) = u\star k\,.$$

If k blurs slightly u, then continuous blurring is obtained by iterating the convolution process

$$\begin{aligned} u_1 &= C_k(u) = u\star k\\ u_2 &= C_k(u_1) = u\star k\star k\\ u_3 &= C_k(u_2) = u\star k\star k\star k\\ &\dots \end{aligned}$$

Writing $u = u_0$ for the initial image, this set of images $u_0, u_1, u_2, ..u_N$ can be considered as the discretization of a continuous image flow $u(t)$ for $t\in[0,1]$. We note Δt the non-negative time step and Δx the space step in the two directions, so

$$u_n(i,j) = u(i\Delta x, j\Delta x, n\Delta t) = u(x,y,t)\,.$$

The process is equivalent to an evolution equation of u with respect to time t being the most "regular" as possible.

Proposition 13.1 *The following scheme*

$$u_{n+1} = u_n\star k_n = u_n\star(Id + k'_n) \tag{13.2}$$

is consistent with the PDE

$$\frac{\partial u}{\partial t}(.,.,t) = u\star K'(.,.,t) \tag{13.3}$$

where $K'(x,y,t) := \dfrac{k'(x,y,t)}{\Delta t}$ *and* $\int k(x,y,t)dx\,dy = 1$.

Note: all convolutions marked by $\star$ are with respect to space variables, that is (i,j) in the discrete space or (x,y) in the continuous space.

Proof: the consistency of (13.2) with (13.3) comes from the consistency of the scheme $\dfrac{u_{n+1}-u_n}{\Delta t}$ with the derivative operator

$$\frac{u_{n+1}(i,j)-u_n(i,j)}{\Delta t} = \frac{\partial u}{\partial t}(i\Delta x, j\Delta x, n\Delta t) + O(\Delta t)\,. \tag{13.4}$$

From (13.2), we have

$$\begin{aligned} u_{n+1}(i,j) &= u_n(i,j) + u_n\star k'_n(i,j)\\ \frac{u_{n+1}(i,j)-u_n(i,j)}{\Delta t} &= u_n\star\frac{k'_n}{\Delta t}(i,j)\\ &= u_n\star K'_n(i,j)\,. \end{aligned} \tag{13.5}$$

Combining (13.4) and (13.5), we have

$$\frac{\partial u}{\partial t}(.,.,t) = u\star K'(.,.,t)\,.$$

The other constraints on k' are set so that (13.3) has a unique solution. The equation (13.3) is a Partial Differential Equation with a term linear with respect to u, which has a unique solution if some constraints on k' are satisfied.

□

The solution of the PDE of Proposition 13.1 is given by the following proposition.

Proposition 13.2 *The explicit solution of (13.3) is given by*

$$u(.,.,t) = u(.,.,0) \star h(.,.,t)\,, \tag{13.6}$$

where

$$\widehat{h}(\xi_x,\xi_y,t) = \exp(\int_0^t \widehat{K'}(\xi_x,\xi_y,s)ds\ ) \tag{13.7}$$

with $\widehat{h}(\xi_x,\xi_y,t)$ the Fourier transform of $h(x,y,t)$.

Proof: Let us note v the image satisfying (13.6):

$$v(.,.,t) = u(.,.,0) \star h(.,.,t)\,.$$

To prove the proposition, we have to show that v also satisfies (13.3). To that aim, let us compute $\frac{\partial v}{\partial t}(x,y,t)$:

$$\frac{\partial v}{\partial t}(.,.,t) = \frac{\partial}{\partial t}\left(u(.,.,0) \star h(.,.,t)\right) = u(.,.,0) \star \frac{\partial}{\partial t}h(.,.,t)\,.$$

Let us now compute $\frac{\partial}{\partial t}h(x,y,t)$.

$$\begin{aligned} \widehat{h}(\xi_x,\xi_y,t) &= \exp(\int_0^t \widehat{K'}(\xi_x,\xi_y,s)ds\ ) \\ \frac{\widehat{\partial h}}{\partial t}(\xi_x,\xi_y,t) &= \widehat{K'}(\xi_x,\xi_y,t)\cdot\widehat{h}(\xi_x,\xi_y,t) \end{aligned} \tag{13.8}$$

Hence

$$\begin{aligned} \frac{\partial v}{\partial t}(.,.,t) &= u(.,.,0) \star K'(.,.,t) \star h(.,.,t) \\ &= u(.,.,0) \star h(.,.,t) \star K'(.,.,t) \\ &= v(.,.,t) \star K'(.,.,t) \end{aligned}$$

so that v satisfies (13.3). Moreover provided that u and v have the same initial conditions (i.e. u and v being equal at time $t=0$), we obtain $v=u$ since the PDE (13.3) has a unique solution.

□

Note that in the whole chapter, we will study only symmetric filters h.

Example

We study here the interpolation of the filter h between two moments:

- **time $\mathbf{t=0}$:** $h(0)=\delta_0$, which we will note with the discrete representation $h(0) = [\ 0\ ,\ 1\ ,\ 0\ ]$ in the following,
- **time $\mathbf{t=1}$:** $h(1) = \frac{1}{3}(\delta_{-1}+\delta_0+\delta_1)$, which we will note $h(1) = [\ \frac{1}{3}\ ,\ \frac{1}{3}\ ,\ \frac{1}{3}\ ]$ (the discrete averaging horizontal filter),

- with some regularity constraints: $\frac{\partial h}{\partial t}$ "smooth".

This formalization tries to answer the question: how to blur an image the most regularly as possible and reach in the end the image that would have been obtained by a direct convolution of the original image with a mean filter ?

$h(t) = [\ \frac{t}{3}\ ,\ 1-\frac{2t}{3}\ ,\ \frac{t}{3}\ ]$ and $\frac{\partial h}{\partial t} = [\ \frac{1}{3}\ ,\ -\frac{2}{3}\ ,\ \frac{1}{3}\ ]$. A closer look at the Fourier transform of $h(0)$ and $h(1)$ shows the difficulty of the existence of a smooth interpolation. Let us replace now the time variable t in the definition of h

$$h(t) = \left[\ \frac{t}{3}\ ,\ 1-\frac{2t}{3}\ ,\ \frac{t}{3}\ \right]$$

by the variable $a = \frac{t}{3}$ to simplify the writing by avoiding the division by 3, so that we have the new filter called g defined by

$$g(a) = [\ a\ ,\ 1-2a\ ,\ a\ ]\ ,$$

where $g(t/3) = h(t)$.

Property 13.3 *The Fourier transform of any filter* $g(a) = [\ a\ ,\ 1-2a\ ,\ a\ ]$ *is*

$$\forall \alpha \in \mathbb{R},\quad \widehat{g}(\alpha) = 1 - 4a\sin^2\frac{\alpha}{2}. \tag{13.9}$$

Proof: $\widehat{g}(\alpha) = ae^{-i\alpha} + (1-2a) + ae^{i\alpha} = 1 - 2a + 2a\cos\alpha = 1 - 4a\sin^2\frac{\alpha}{2}$.

□

We recall that the discrete Fourier transform of g of size N is the discrete signal defined by

$$\forall p \in \mathbb{Z}\ ,\quad \widehat{g}(p) = \sum_{k=0}^{N-1} e^{-\frac{2i\pi pk}{N}} g(k)$$

so that the discrete Fourier transform of g is obtained by replacing α by $\frac{2\Pi p}{N}$ in (13.9) yielding

- **time $\mathbf{t = 0}$:** set $a = \frac{t}{3} = 0$ in (13.9) then $\widehat{g}(p,0) = \widehat{h}(p,0) = 1$.
- **time $\mathbf{t = 1}$:** set $a = \frac{t}{3} = \frac{1}{3}$ then $\widehat{g}(p,\frac{1}{3}) = \widehat{h}(p,1) = 1 - \frac{4}{3}\sin^2\left(\frac{\Pi p}{N}\right)$.

The graphs of $\widehat{h}(p,0)$ and $\widehat{h}(p,1)$ are displayed in Fig.13.2. For $p = p_0$, $\widehat{h}(p,1) = 0$. For $|p| > p_0$, $\widehat{h}(p,1) < 0$. As interpolation between both filters has to be smooth, the filter Fourier transform should evolve regularly from a strictly positive function $(\widehat{h}(p,0))$ to a partially negative function $(\widehat{h}(p,1))$. But this is not possible because any zero value of the Fourier transform of the filter cannot evolve to a positive or negative value, it remains positive and stops the evolution of the Fourier transform of the filter at this point p_0: the result of the convolution of this filter with any other filter preserves the zero value of its Fourier transform at p_0.

Filter decomposition with a frequential approach

Let us consider the problem of decomposing a filter into the convolution of small filters g of size 3 (or 3×3 in 2D if the associated 2D-filter is built by the tensor product $g \otimes g$), where g is a 1D normalized filter defined by

$$g(a) = [\ a\ ,\ 1-2a\ ,\ a\ ].$$

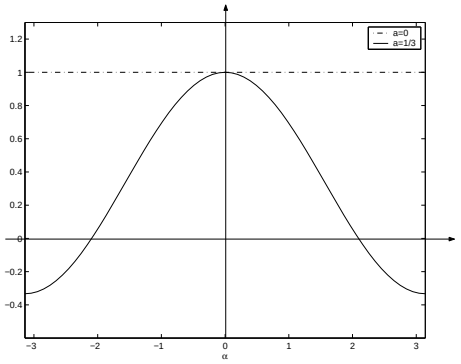

Figure 13.2: Graphs of $\widehat{h}(p,0) = \widehat{g}(p,0)$ and $\widehat{h}(p,1) = \widehat{g}(p,\frac{1}{3})$ for $N = 64$ and $p \in [-N/2, N/2]$, i.e. $\alpha \in [-\pi, \pi]$. Note that $\widehat{h}(p,1)$ is not positive and that $\widehat{h}(p,1) = 0$ for $\alpha \simeq \pm 2.09$.

Let $\alpha \in [-\pi, \pi]$. From Property 13.3, the Fourier transform of g is

$$\widehat{g}(\alpha) = 1 - 4a \sin^2 \frac{\alpha}{2} \,. \tag{13.10}$$

Here we use a frequential approach, which means that we will not study the decomposition of the filter in the space domain but in the Fourier domain. Since a convolution in space is equivalent to a product in frequency thanks to the property of the Fourier transform recalled in (1), we will study the existence of filters whose Fourier tranform is the product of the Fourier transform of small filters g:

$$\widehat{f}(\alpha) = \prod_{k \in \mathbb{Z}} (1 - 4a_k \sin^2 \frac{\alpha}{2}) \tag{13.11}$$

In the following, we shall answer to this question. But first let give us some notations. From (13.10), the right term of (13.11) can be rewritten $\prod_{k\in\mathbb{Z}} \widehat{g_k}(\alpha)$ where $\widehat{g_k}(\alpha) = 1 - 4a_k \sin^2 \frac{\alpha}{2}$. The existence of $\widehat{f}(\alpha)$ is proved in the following proposition.

Proposition 13.4 *Let f be a filter defined in the Fourier domain by (13.11):*

$$\widehat{f}(\alpha) = \prod_{k \in \mathbb{Z}} (1 - 4a_k \sin^2 \frac{\alpha}{2}) \,,$$

where the Fourier transform is positive ($\widehat{f}(\alpha) \geq 0$), regular ($\left(\widehat{f}\right)'(0) = 0$) and yields a normalized filter ($\widehat{f}(0) = 1$). Such filter exists if the decreasing of the coefficients a_k when k tends to infinity satisfies

$$a_k = o\left(\frac{1}{k^{(1+\varepsilon)}}\right) \,.$$

Proof: $\widehat{f}(\alpha)$ is defined as the product over $k \in \mathbb{Z}$. The product over k, when k tends to infinity, converges if the Riemann criteria is satisfied, that is $a_k = o\left(\frac{1}{k^{(1+\varepsilon)}}\right)$. Moreover the first values of a_k should be small enough, to preserves the positivity of the filter, since we have seen that the decomposition of the Fourier transform of a filter is possible only if all small kernels have a positive Fourier transform. The following property gives the condition on a_k to obtain the positivity of $\widehat{g_k}(\alpha)$ for all frequency α.

Property 13.5 *The filter g_k with $k \in \mathbb{Z}$, defined in the Fourier domain by*

$$\forall \alpha \in [-\pi, \pi], \quad \widehat{g_k}(\alpha) = 1 - 4a_k \sin^2 \frac{\alpha}{2}$$

is positive if $a_k \leq 1/4$.

Proof : $\forall \alpha \in [-\pi, \pi]$, $\sin^2 \frac{\alpha}{2} \in [0, 1]$. Consequently $1 - 4a_k \sin^2 \frac{\alpha}{2} \geq 0$ for all α if $a_k \leq 1/4$.

□

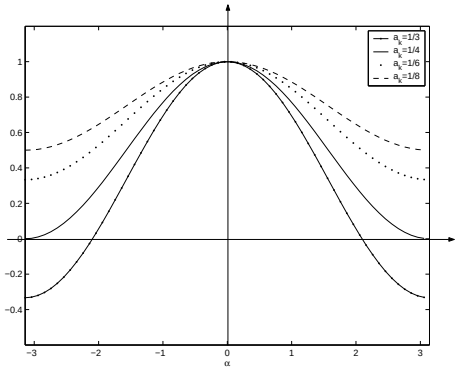

Figure 13.3: Graph $\widehat{f}(\alpha)$ for several a_k.

The frequential approach did give some constraints on the Fourier transform of the filters to obtain a continuous deblurring, more specifically the strong decreasing of the filter coefficient a_k. We propose now an new approach for the filter decomposition. It is based on the results in probability on the infinite divisible law, where we use the analogy between a filter and the law of a random variable.

Filter decomposition with a probabilistic approach

The problem of decomposing a low-pass filter can be studied in a probabilistic approach by using the analogy between the Fourier transform of a filter and the law of a random variable. Let us consider a filter that preserves low frequencies in $[-1, 1]$. We are interested in decomposing this filter as the convolution of two other filters. Using the afore mentioned analogy, the problem is equivalent to decomposing the law of the random variable X as the sum of two independent and identically distributed (i.i.d.) random variables. Hence the filter decomposition can be written with the probabilistic approach as the following problem:

Let X be a random variable taking values in $I = [-1, 1]$ such that

1. $X = Y_1 + Y_2$
2. Y_1 and Y_2 are i.i.d. random variables.

What is the law of X that can be obtained as close as possible to $\mathcal{U}([-1, 1])$?

It is a well-known fact that if Y_1 and Y_2 follow a uniform distribution $\mathcal{U}([-1/2, 1/2])$, then the distribution of their sum X is triangular on $2 \cdot [-1/2, 1/2] = I$. The triangle distribution is far from

the uniform distribution and we have seen in Chapter 2 and in the Introduction of Part II that the triangle filter is not satisfactory because it adds a lot of blur on the image. So we are interested in filters whose convolution is close to the Shannon filter. Hence the question is: can the distribution of the sum be closer from the uniform distribution than the triangular ?

The distance between those two distributions can be measured with the entropy of the random variable. The entropy evaluates the disorder of X in the sense of Information theory. Among all random variable defined on I, the uniform distribution has the highest entropy, because the distribution is uniform on I. On the contrary, the triangle distribution has a lower entropy since the distribution is bigger around zero than on the extrema of I (see Proposition 13.6 for the exact values and Fig.13.4 for the visualization). The differential entropy of a continuous random variable X is

$$H(X) = -\int_{-\infty}^{\infty} p(x)\log(p(x))\,dx \quad . \tag{13.12}$$

where p denotes the probability density function of X.

Proposition 13.6

(i) *If* $X \sim \mathcal{U}([-1,1])$, *then* $H(X) = \log(2)$.

(ii) *If* Y_1 *and* $Y_2 \sim \mathcal{U}([-1/2,1/2])$, *then* $H(Y_1+Y_2) = \frac{1}{2}$.

Proof:

(i) If $X \sim \mathcal{U}([-1,1])$,i.e. $p(x) = \frac{1}{2}\mathbb{1}_{[-1,1]}(x)$, then

$$H(X) = -\int_{-1}^{1} \frac{1}{2}\log\left(\frac{1}{2}\right)dx = \log(2) \simeq 0.69\,.$$

(ii) The probability density function associated to $\mathcal{U}([-1/2,1/2])$ is $p(y) = \mathbb{1}_{[-1/2,1/2]}$. Then, the probability density function associated to Y_1+Y_2 is

$$p \star p(y) = (1-|y|)\,\mathbb{1}_{[-1,1]}(y)\,.$$

Indeed

$$p \star p(y) = \int_{-1/2}^{1/2} \mathbb{1}_{[-1/2,1/2]}(y-t)dt = \int_{y-1/2}^{y+1/2} \mathbb{1}_{[-1/2,1/2]}(t)dt\,.$$

For $y \in [0,1]$,

$$p \star p(y) = \int_{y-1/2}^{1/2} (t)dt = 1-y\,.$$

So the entropy is

$$\begin{aligned} H(Y_1+Y_2) &= -\int_{-1}^{1}(1-|x|)\log(1-|x|)dx = -2\cdot\int_0^1 u\log(u)du \\ &= -\left[u^2(\log(u)-\frac{1}{2})\right]_0^1 = \frac{1}{2} \end{aligned}$$

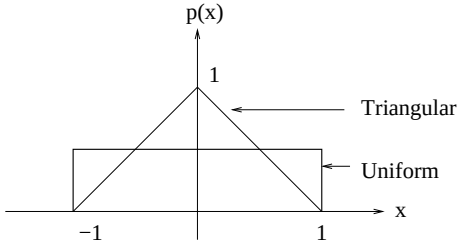

Figure 13.4: Probability density function associated to $\mathcal{U}([-1,1])$ and the triangular one on I.

□

The decomposition with a probabilistic approach refers to the more general problem of the partition of the uniform law.

Proposition 13.7 *The uniform law $\mathcal{U}([-1,1])$ is not divisible in law.*

proof: Let us use here a method of proof by contradiction. Assume that $X \sim \mathcal{U}([-1,1])$ is divisible in law. Then Y_1 and Y_2 i.i.d., such that $X = Y_1 + Y_2$, exist.

- If $X = Y_1 + Y_2$, then $\varphi(X) = (\varphi(Y))^2$, where $\varphi(X)$ (resp. $\varphi(Y)$) is the characteristic function of X (resp. Y).

  Indeed by definition $\varphi_Y(u) = \mathbb{E}[e^{iuY}]$. Moreover Y_1 and Y_2 are i.i.d.

  $$\begin{aligned}\varphi_{Y_1+Y_2}(u) &= \mathbb{E}[e^{iu(Y_1+Y_2)}] = \mathbb{E}[e^{iuY_1}\, e^{iuY_2}] = \mathbb{E}[e^{iuY_1}\, e^{iuY_2}] \\ &= \varphi_{Y_1}(u) \cdot \varphi_{Y_2}(u)\,.\end{aligned}$$

  The calculus of $\varphi(X)$ comes immediately

  $$\varphi(X) \quad = \quad \mathbb{E}[e^{iuX}] = \int_{-1}^{1} \frac{e^{iux}}{2} dx = \frac{1}{2}\left[\frac{e^{iux}}{ix}\right]_{-1}^{1} = \frac{\sin(u)}{u}\,.$$

  So the characteristic function of Y is

  $$(\varphi_Y(u))^2 = \frac{\sin(u)}{u}\,.$$

  As $\frac{\sin(u)}{u}$ has negative values for some u, $\varphi(Y)$ is necessarily a complex number.

- X is symmetrical as $X \overset{law}{=} -X$. Consequently, Y_1 and Y_2 have to be symmetrical too. But if Y is symmetrical then its characteristic function is real.

  (If Y is symmetrical then $-Y$ and Y have same law, and then same characteristic function.

  $\varphi_{-Y}(u) = \mathbb{E}[e^{-iuY}] = \overline{\mathbb{E}[e^{iuY}]} = \varphi_Y(u)$)

The two conditions on $\varphi(Y)$ are incompatible. This is a contradiction, so the initial assumption must be false. So $\mathcal{U}([-1,1])$ is not divisible in law.

□

Remark: note that Proposition 13.7 can be extended in the following way: the uniform law $\mathcal{U}([-1,1])$ is not infinitely divisible in law. We recall that by definition to say that a probability distribution F on the real line is infinitely divisible means that if X is a random variable whose distribution is F, then for every positive integer n there exist n i.i.d. random variables $X_1,\ldots,X_n$ whose sum is X. Usually the random variables $X_1,\ldots,X_n$ do not have the same probability distribution that X has. Now let us go back to the proof of "the uniform law $\mathcal{U}([-1,1])$ is not infinitely divisible in law". It is based on the following fundamental result: a distribution with bounded support is infinitely divisible if and only if it is degenerate ([50],p78). As the uniform law is not degenerate, then it is not infinitely divisible in law. We recall that a degenerate distribution is the probability distribution of a discrete random variable that assigns all of the probability, i.e. probability 1, to just one outcome of a random experiment. By extension the degenerate distribution of a continuous variable is described by the Dirac delta function.

In [10], Carasso studies the subclass G of the class of infinitely divisible densities. Its application is the direct blind deconvolution. He defines the class G as the class of blurring kernel $k(x,y)$ whose Fourier transforms satisfy

$$\widehat{k}(\xi,\eta) = e^{-\sum_{i=1}^{J}\alpha_i(\xi^2+\eta^2)^{\beta_i}}$$

with $\alpha_i \geq 0$ and $0 < \beta_i \leq 1$. The overall kernel corresponds to the convolution product of the individual components kernels. Such individual component is a symmetric Lévy stable density $k(x,y)$. The Gaussian case corresponds to $\beta = 1$. It occurs in diverse contexts (such as undersea imaging, nuclear medicine, computed tomography scanners, ...) which makes the class G interesting to study. Note that $\widehat{k}(\xi,\eta)$ is positive which makes possible a evolution equation, contrarily to the previous example with $h(1) = [1/3, 1/3, 1/3]$.

We have seen three approaches (spatial, frequential and probabilistic) for the filter decomposition for the continuous blurring/deblurring. The decomposition of a filter in elementary filters has already been studied in the literature. Let us cite the paper of Abramatic and Faugeras on the *small generating filters* [1]. We will see that the results on the *small generating filters* can be applied only for the continuous deblurring of separable filters since the decomposition of 1D filters or for 2D separable filters is always possible. We will not use this decomposition in this thesis since we want to study a large class of 2D filters (not only separable), anyway we recall the method of Abramatic *and al.* for the construction of *small generating filters*.

13.2.2 Generating filters

Abramatic and Faugeras showed interesting results on the decomposition of 1D-filters in [1], which we recall in the following proposition.

Proposition 13.8 *Let $h(k)$ be any real valued impulse response of a 1D-filter and $H(z)$ its z-transform*

$$H(z) = \sum_{k=-Q}^{Q} h(k)\, z^{-k}\,. \tag{13.13}$$

H can be decomposed as

$$H(z) = \prod_{i=1}^{Q} P_i(z)\,, \tag{13.14}$$

where

$$P_i(z) = a^i_{-1} z^{-1} + a^i_0 + a^i_1 z^1 \ . \tag{13.15}$$

In other words, this means that h can be expressed as the convolution of n generating filters, the z-transform of which is defined by (13.15). This is really useful for practical applications. The decomposition of large kernel into the convolution of small kernels saves computation time.

The result comes from the fundamental theorem of algebra: it states that a polynomial of degree n with real coefficients can be decomposed into the product of n polynomials with real or complex coefficients. (13.14) comes from the gathering of conjugate complex coefficients and of pairs of real coefficients. For example, the filter defined by $h = [\ a\ ,\ 1-2a\ ,\ a\ ]$ has the following z-transform

$$\begin{aligned} H(z) &= \sum_{k=-1}^{1} h(k) z^{-k} && (13.16)\\ &= a z^{-1} + (1-2a) + a z^1 && (13.17)\\ &= P_1(z)\ . && (13.18) \end{aligned}$$

In the case of unilateral z-transform

$$H(z) = \sum_{k=0}^{Q} h(k)\, z^{-k} = \prod_{i=1}^{Q} \tilde{P}_i(z) = \prod_{i=1}^{Q} P_i(x) \tag{13.19}$$

with $x = \frac{1}{z} = \frac{1}{a+ib} = \frac{a-ib}{a^2+b^2} = \frac{1}{a^2+b^2} z^*$, $x \in \mathbb{C}$ and $P_i(x) = x - a^i$. Coefficients a^i may be complex conjugate. In that case

$$\begin{aligned} P_i(x).P_{i+1}(x) &= (x-a^i)(x-a^{i+1}) && (13.20)\\ &= (x-(a+ib))(x-(a-ib)) && (13.21)\\ &= x^2 - 2ax + a^2 + b^2 && (13.22) \end{aligned}$$

is associated to the filter $h = [\ a^2+b^2\ ,\ -2a\ ,\ 1\ ]$. To obtain real coefficients, there are two categories of generating filters depending on the form of their unilateral x-transform

- $P_i(x) = x - a^i$ for a^i real,
- $P_i(x) = x^2 + c^i_1 x + c^i_0$ for a^i and $\left(a^i\right)^*$ complex conjugate. The coefficients are given by (13.22)

$$c^i_1 = -2\mathcal{R}(a^i) \qquad \text{and} \qquad c^i_0 = \left(\mathcal{R}(a^i)\right)^2 + \left(\mathcal{I}(a^i)\right)^2$$

where $\mathcal{R}$ denotes the real part and $\mathcal{I}$ the imaginary part of the complex number a^i.

Conclusion: if the number of roots of the z-transform of a filter h is even, then the filter is obtained by the convolution of filters of size 3 with real coefficients. If the number of roots is odd, it suffices that there is at least one real root to build the filter by the convolution of filters of size 2 or 3 with real coefficients.

Remark: Abramatic and Faugeras define the term *small generating kernel* (SGK) for the 2D-case. These small filters generate filters with large size impulse responses.

Even if the decomposition is possible, there is no condition on the generating filter properties. In practice, we may require generating filters with positive Fourier transform or a normalized filter. These conditions are generally not satisfied by generating filters. For example,

- a filter of size 2 with the following z-transform

$$H(z) = z^{-1} - a^i$$

is defined by

$$h = [\, -a^i \,,\, 1 \,] \,,$$

where $\sum h \neq 1$.

- a filter of size 3 with the following z-transform

$$H(z) = z^{-2} - a_1^i z^{-1} - a_0^i$$

is defined by

$$h = [\, -a_0^i \,,\, -a_1^i \,,\, 1 \,] \,,$$

where $\sum h = -a_0^i - a_1^i + 1$ is not *a priori* equal to one, but the normalization is possible.

This decomposition can be used for 1D filters or separable 2D filters. But the decomposition of other 2D filters is in general not available because 2D-polynomials of degree n cannot be written as a product of polynomials with small degrees. This problem would force us to restrict our study to separable filters, which is not what we want to do here. This is the reason why we will not consider in this thesis the decomposition with the SGK.

In this chapter, we have studied some possible approaches for the blind deconvolution with progressive deblurring. We have seen that the sign of the Fourier transform of the filter and the number of its zeros indicate if the deblurring is possible. In Chapter 13.3, we study the deconvolution with the special class of small filters with a compact spatial support of size 3×3, for which we give a global analyze of the sign of its Fourier transform according to the sign of the filter coefficients.

13.3 Deconvolution with filters having compact support

13.3.1 Definition of the filters

In this part, we consider the ringing phenomenon occurring after a deconvolution process. The deblurring with a wrong filter may introduce oscillations that may dominate by far the true part of the reconstructed image. (These oscillations are called *ringing* in the literature [24] and there are some proposed methods that reduce this kind of ringing [56][57][24].) The mismatch between the convolution and the deconvolution filter has clearly a frequential explanation. In order to understand the phenomenon, we first study a restricted class of filters: the ones with small spatial support 3×3. The convolution process is defined by

$$u_c = k \star u_0 \, + \, n \,.$$

where u_0 is the initial image of size $N \times N$, and n is an additive Gaussian noise. We note u the reconstructed image.

Definition 13.9 *The isotropic filter k of size $N \times N$ is defined by*

$$\begin{bmatrix} (0) & \cdots & (0) \\ \vdots & \boxed{\begin{matrix} c & a & c \\ a & e & a \\ c & a & c \end{matrix}} & \vdots \\ (0) & \cdots & (0) \end{bmatrix}.$$

The constraints on k are the following

$$\begin{cases} 4c + 4a + e = 1, \\ 8c + 4a = \sigma^2, \\ a,\ c,\ e \geq 0. \end{cases} \tag{13.23}$$

The constraints (13.23) are traditional in the literature [9]. The first equation imposes a normalized filter. The second one defines the variance of the filter. This value is linearly related to the amount of blur introduced by the filter. The third equation preserves the positivity of the filtered image if the input image is positive and also ensures that the filter blurs the image. Moreover the filter is chosen isotropic in order to reduce the number of parameters. The physical counterpart is that we only consider the blur due to the focusing operation and not the motion blur. But this modeling remains general enough for our problem.

From the definition of k, we specify the range of the variables σ^2, a, c, e in the following proposition. We also characterize the Fourier transform $\widehat{k}$ in order to study its sign (we recall the change of sign of $\widehat{k}$ may introduce oscillations on the image during the deconvolution process since a null value of $\widehat{k}$ may yield large frequency modulus after inverse filtering). The proof of Proposition 13.10 is given in Appendix (Subsection 13.3.5)

Proposition 13.10 *Assume k is the filter of Definition 13.9.*

(i) *The variance σ^2 of k is restricted to*

$$\sigma^2 \in [0, 2]\,.$$

(ii) *The discrete Fourier transform of k is*

$$\hat{k}(\alpha, \beta) = 4c(\alpha - l)(\beta - l) + 1 - \sigma^2 + 4c - 4cl^2, \tag{13.24}$$

with $(\alpha, \beta) \in [-1, 1]^2 = \Omega$ and

$$l := 1 - \frac{\sigma^2}{8c}. \tag{13.25}$$

(iii) *Assume σ is fixed. c ranges in $[c_{\min}(\sigma), c_{\max}(\sigma)]$, where*

$$\begin{cases} c_{\min}(\sigma) = \max\left(0, \frac{1}{4}(\sigma^2 - 1)\right), \\ c_{\max}(\sigma) = \frac{\sigma^2}{8}. \end{cases} \tag{13.26}$$

Consequently, a ranges in $[a_{\min}(\sigma), a_{\max}(\sigma)]$, where

$$\begin{cases} a_{\min}(\sigma) = 0, \\ a_{\max}(\sigma) = \frac{\sigma^2}{4} + \min\left(0, \frac{1}{2}(1 - \sigma^2)\right) \end{cases} \tag{13.27}$$

and e ranges in

$$E = \left[1 - \sigma^2, 1 - \frac{\sigma^2}{2}\right] \cap [0, 1] \ . \tag{13.28}$$

(iv) $l \leq 0$

(v) *The branch of the hyperbola defined in (13.24) changes quadrants for*

$$c = c_{crit} = \frac{\sigma^4}{16} \ . \tag{13.29}$$

Remark: The formulation (13.24) is interesting because the parameters a and e are no more in the equation of $\widehat{k}$. Furthermore the value of c depends on σ as given by Proposition 13.10-(iii).

From this proposition, we will distinguish different categories of filters. First we see that there are two cases for l that lead to two types of filters.

case A: filters with $l \in [-1, 0]$. The asymptotes of the hyperbola intersect in Ω. An example with $l = -0.3$ is shown in Fig.13.5-(a).

case B: filters with $l < -1$. The asymptotes of the hyperbola do not intersect in Ω. An example with $l = -1.5$ is shown in Fig.13.5-(b).

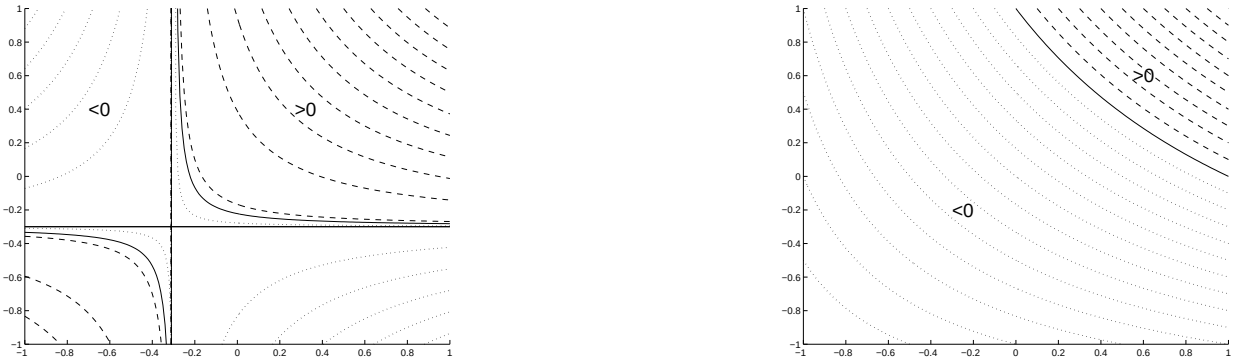

Figure 13.5: Level lines of the hyperbola $\widehat{k}(\alpha, \beta)$ (13.24) in the domain Ω
(a) case A: $\sigma^2/8c = 1.3 < 2$ with $l = -0.3$, $c = 0.15$ and $\sigma^2 = 1.56$.
(b) case B: $\sigma^2/8c = 2.5 > 2$ with $l = -1.5$, $c = 0.1$ and $\sigma^2 = 2$.

These two types of filters will be used in the proof of the following proposition, which shows that the quantity $\sigma^2 = 1$ is a very specific value, which divides the class of possible variances in two groups yielding the class of filters with strictly positive Fourier transform and the class of filters with a Fourier transform with some positive and negative values.

Proposition 13.11 *Assume k is the filter of Definition 13.9 and $\widehat{k}$ its discrete Fourier transform.*

(i) *for* $\sigma^2 < 1$, $\forall (n,p) \in \left[-\frac{N}{2}, \frac{N}{2}\right]^2$, $\widehat{k}(n,p) > 0$.

(ii) *for* $\sigma^2 > 1$, $\exists (n,p) \in \left[-\frac{N}{2}, \frac{N}{2}\right]^2$ *such that* $\widehat{k}(n,p) < 0$.

Remark: the filter is normalized so $\widehat{k}(0,0) = 1$. So (ii) implies that $\widehat{k}$ may be negative.
Proof: as $\widehat{k}(0,0) = 1 > 0$, let us first calculate the minimum value of $\widehat{k}$ in order to determine if the kernel remains positive or if it changes sign for some frequencies. The study is done on the two previous cases:

case A:

$$\hat{k}_{\min} = \min_{\alpha,\beta} \hat{k}(\alpha,\beta) = \hat{k}(-1,1) = \hat{k}(1,-1) = 1 - \sigma^2 .$$

case B:

$$\hat{k}_{\min} = \min_{\alpha,\beta} \hat{k}(\alpha,\beta) = \hat{k}(-1,-1) = 4c \cdot (1+l)^2 + 1 - \sigma^2 + 4c - 4cl^2 .$$

From (13.25), we have $8cl = 8c - \sigma^2$, thus $\hat{k}_{\min} = 16c - 2\sigma^2 + 1$. But in case B, $\sigma^2/8c > 2$, then $\hat{k}_{\min} < 1 - \sigma^2$.

Cases A and B show that $\sigma^2 = 1$ determines the sign of $\widehat{k}$ (Fig.13.6).

- For $\sigma^2 < 1$, (case A) $\hat{k}_{\min} > 0$ and (case B) $\hat{k}_{\min} < C$ with $C > 0$. In order to prove (i), we still need to show that in case B, $\hat{k}_{\min} > 0$.

  Proof: The quantity $\sigma^2 \in [0,2]$, so $16c - 2\sigma^2 + 1 \in [16c - 1, 16c + 1]$.

  $$\begin{aligned} \hat{k}_{\min} > 0 &\Leftrightarrow 16c - 1 > 0 \\ &\Leftrightarrow 16c > 1 \end{aligned} \tag{13.30}$$

  Since case B defines the group of filters such that $\sigma^2 > 16c$, so from (13.30), we have $\sigma^2 > 16c > 1$. To conclude, $\widehat{k}$ is positive for $\sigma^2 > 1$. This ends the proof of **(i)**.

- For $\sigma^2 \geq 1$, the filter of case A already has negative values in $\widehat{k}$ because $\hat{k}_{\min} = 1 - \sigma^2 \leq 0$. This ends the proof of **(ii)**.

□

Remarks: as shown in Fig.13.6, the sign of the filter also depends on the sign of $16c - 1$. We study here the case $16c < 1$ in order to complete our understanding of the sign of $\widehat{k}$.

- For $\sigma^2 \in [16c, 1]$

  $$\hat{k}_{\min} = 16c - 2\sigma^2 + 1 \tag{13.31}$$
  $$\hat{k}_{\min} \in [16c - 1, 1 - 16c] . \tag{13.32}$$

  As $16c < 1$, $\hat{k}_{\min}$ may be positive or negative.

  $$\begin{cases} \hat{k}_{\min} > 0 \text{ for } \sigma^2 \in [16c, \frac{16c+1}{2}], \\ \hat{k}_{\min} < 0 \text{ for } \sigma^2 \in [\frac{16c+1}{2}, 1] \end{cases} \tag{13.33}$$

- For $\sigma^2 > 1$, results are similar as before: $\hat{k}_{\min} < 0$. Indeed if $\sigma^2 > 1$ then $16c - 2\sigma^2 + 1 < 16c - 1$ (Fig.13.7).

Figure 13.6: (a) Case A: $1 - \sigma^2 > 0$ means a positive $\widehat{k}$. (b) Case B: $\sigma^2 > 16c$. The sign of $\widehat{k}$ depends whether $16c$ is larger or smaller than 1.

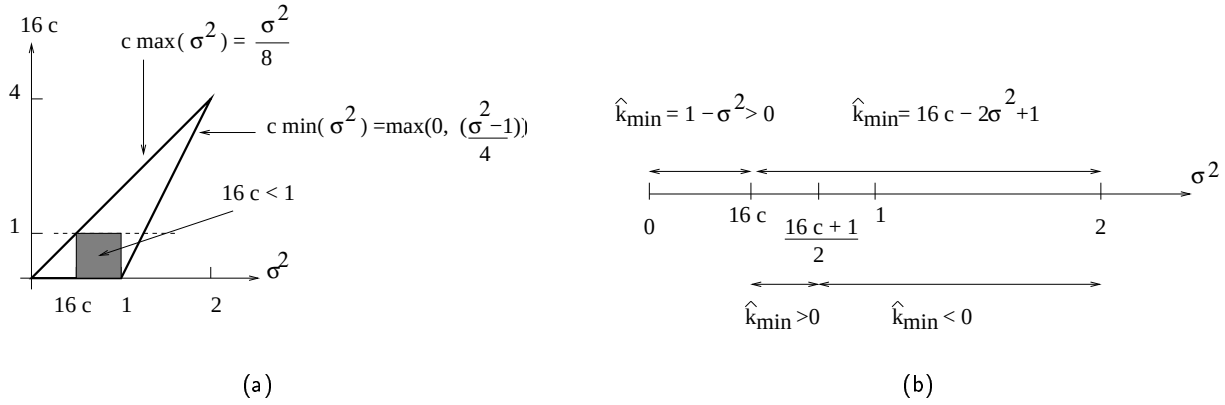

Figure 13.7: (a) Case $16c < 1$ (b) Associated sign of $\hat{k}_{\min}$

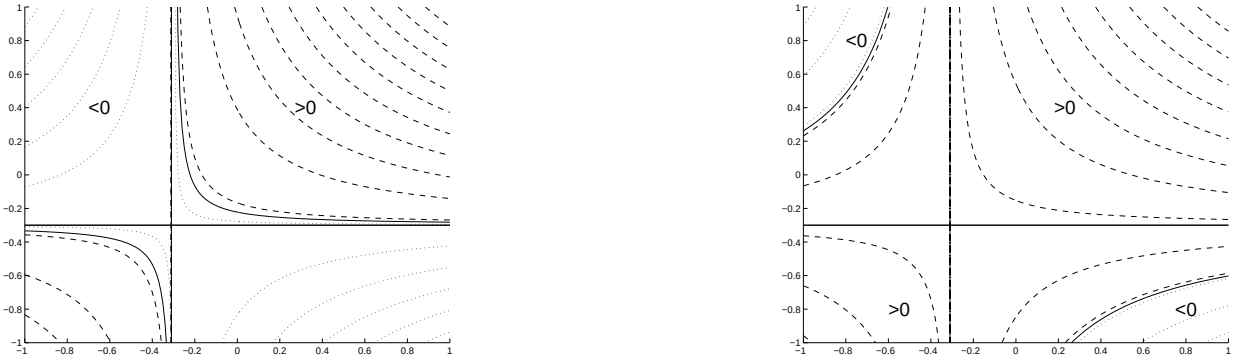

(a) (b)

Figure 13.8: Level lines of the hyperbola $\widehat{k}(x,y)$ (13.24) in the domain $\mathbf{\Omega}$: case A with $l=-0.3$
(a) $\sigma^2=1.56$ and $c=0.15<c_{\text{crit}}=0.1512$ [configuration 1],
(b) $\sigma^2=1.24$ and $c=0.12>c_{\text{crit}}=0.0961$ [configuration 2].
Note that the branch of the hyperbola changes quadrants between configuration 1 and 2.

For case A, the critical value c_{crit} defined in Proposition 13.10 represents the value of c for which the branch of the hyperbola changes quadrants. An example is given in Fig.13.8. For a fixed value of l, we show the level lines of two hyperbola.

- for the first hyperbola $c<c_{\text{crit}}$ [configuration 1],
- for the second hyperbola $c>c_{\text{crit}}$ [configuration 2].

For $c>c_{\text{crit}}$ values (Fig.13.9-(c)), the frequential area, where $\hat{k}$ is positive, is larger. On the one hand, only high frequencies Fourier transform may vanish, introducing high frequency ringing. This kind of ringing is less visible than a low frequency one. On the other hand, the restored image will be less sharp than if $c<c_{\text{crit}}$.

So a blind deconvolution, that tests the ringing artifact with σ^2 fixed, gives better results for large values of c.

Conclusion: the critical value c_{crit} is very important. As we will see in the numerical experiments, it classifies the filters in two groups, one group generating a lot of ringing [configuration 1] and one other group generating little ringing [configuration 2].

13.3.2 Construction of the filters

Definition 13.12 *We define K_σ the set of filters k with variance σ.*

In order to compare the impact of the filter after a deconvolution process, we analyze the results of the filters $\tilde{k}$ with a variance σ' which may be different from the variance σ of the convolution filter k: $\tilde{k}\in K_{\sigma'}$. The values of the coefficients of $\tilde{k}$ are chosen randomly while respecting constraints (13.23). We propose here an algorithm to compute the coefficients.

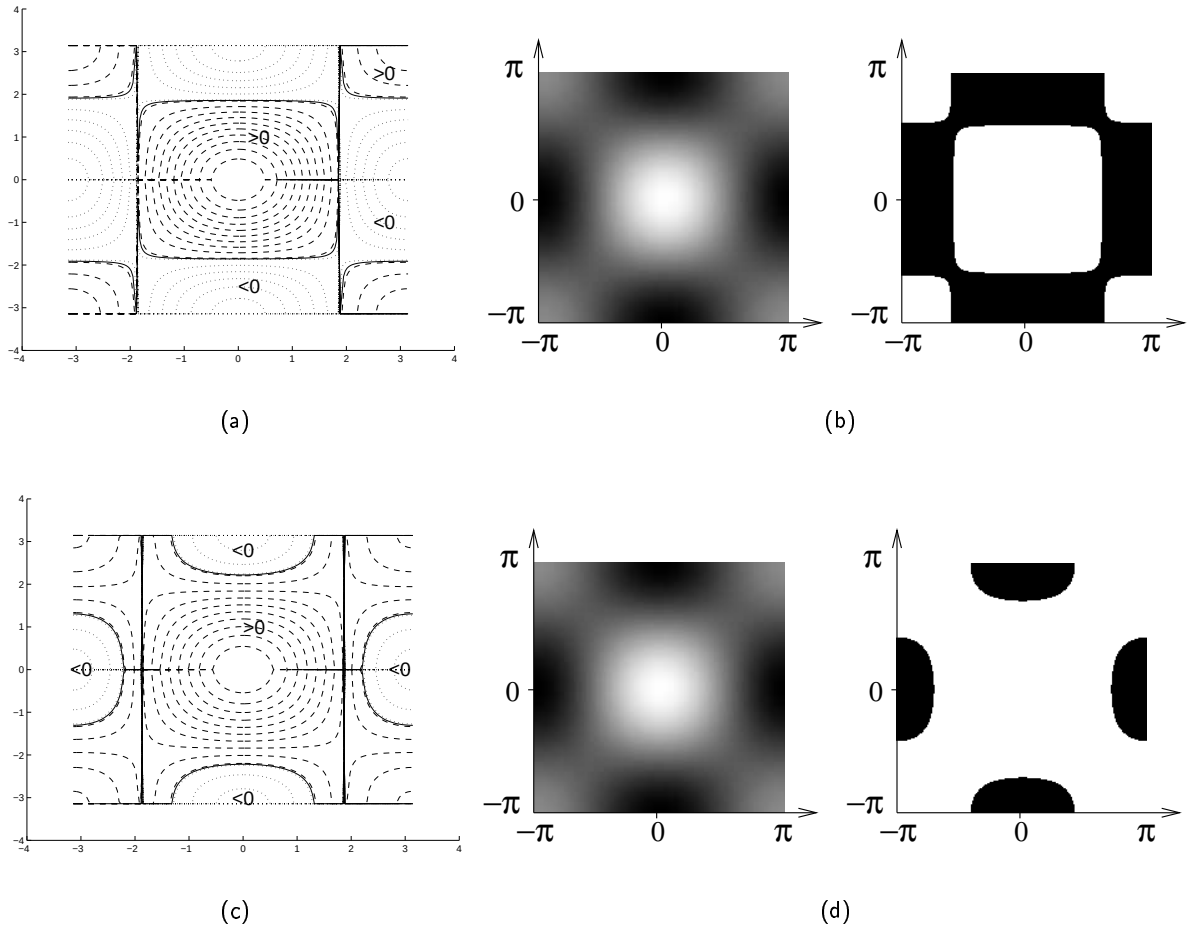

Figure 13.9: Level lines of the hyperbola $\widehat{k}(n,p)$ in the domain $[-\pi,\pi]^2$: case A with $l=-0.3$
(a) $\sigma^2=1.56$ and $c=0.15<c_{\text{crit}}=0.1512$ [configuration 1],
(b) image $\widehat{k}(n,p)$ and the thresholded image where $\widehat{k}(n,p)<0$ is a black pixel,
(c) $\sigma^2=1.24$ and $c=0.12>c_{\text{crit}}=0.0961$ [configuration 2],
(d) image $\widehat{k}(n,p)$ and the thresholded image where $\widehat{k}(n,p)<0$ is a black pixel.
Note the difference between configuration 1 and 2:
the diagonal direction of the Fourier transform of the filter has negative values in the configuration 1.

Proposition 13.13 *Let $\tilde{k}$ be the isotropic filter defined by*

$$\begin{bmatrix} (0) & \cdots & (0) \\ \vdots & \boxed{\begin{matrix} c' & a' & c' \\ a' & e' & a' \\ c' & a' & c' \end{matrix}} & \vdots \\ (0) & \cdots & (0) \end{bmatrix} \tag{13.34}$$

with the following constraints

$$\begin{cases} 4c' + 4a' + e' = 1, \\ 8c' + 4a' = (\sigma')^2, \\ a',\ c',\ e' \geq 0. \end{cases} \tag{13.35}$$

The following algorithm samples the uniform law of the set of filters $\tilde{k}$ as defined by (13.34) and (13.35).

Algorithm 4 (random filter trial)

1. *Draw a random number e' from a uniform distribution, whose support is* $E = \left[1 - (\sigma')^2, 1 - \frac{(\sigma')^2}{2}\right] \cap [0, 1]$.
2. *Compute*
   $a' = \frac{1}{4}\left(2 - (\sigma')^2 - 2e'\right)$,
   $c' = \frac{1}{4}\left(e' + (\sigma')^2 - 1\right)$.

Proof : The variance of the filter is equal to $(\sigma')^2$, so that the range of e' is given by (13.10)-(iii): $e' \in E$. Hence the initialization of e' with a trial having a uniform distribution in E is adapted. This explains the first step of the algorithm. Let us now explain the second step. As Fig.13.24 shows, the constraints defined by (13.35) make a line in the 3D space (e', a', c'), so that the values of the three random variables e', a' and c' are linked. Consequently if e' and σ' are fixed, then the values of a' and c' are determined. First the value of a' is obtained with the second equation of the system (13.35). Second the value of c' is obtained by substituting the obtained values of e' and a' in the first equation of the system (13.35).

□

13.3.3 Numerical experiments

The deconvolution with compact support filter is tested on images of size 128×128. We note u the reconstructed image. Following our approach of the ringing detection (chap.11), the ringing of u is measured with the total variation. We also add another criterion. Following the notations of chapter 12 we define the average amplitude of the total variation of an image after a random phase shift.

Definition 13.14

$$\Delta TV(u) := \mathbb{E}(TV(u_\varepsilon) - TV(u))$$

As is chapter 12, in order to have stable results, the mean value is computed and not the maximal value of the difference over several trials. In the experiments, we set $n = 100$, where n is the number of trials, and $\varepsilon = 0.4$. This value of ε gives a good idea of the slope of $TV(u_\varepsilon)$ with respect to ε (Fig.13.10).

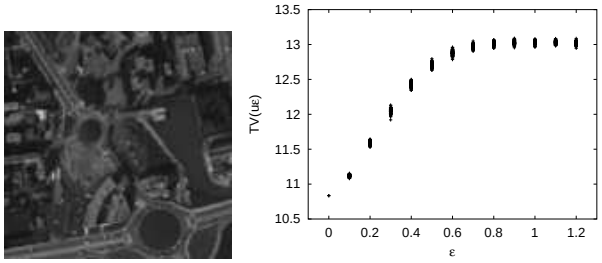

(a) (b)

Figure 13.10: (a) Image u of size 128×128 (b) Graph $(\varepsilon, TV(u_\varepsilon))$. For each value of the phase shift ε, we plot $TV(u_\varepsilon))$ with $n = 100$, number of tested images u_ε. As explained in chapter 12, a phase shift of $\varepsilon > 1$ is useless. $\varepsilon = 1$ build a random phase image.

Experiment procedure

We note k_σ the convolution filter k with variance σ. We recall that the blurred image u_c is the result of a convolution by k_σ.

$$u_c = k_\sigma \star u_0 \, + \, n \, .$$

In blind deconvolution, the filter k_σ is supposed unknown. So the *a contrario* approach consists in being surprised of the good quality of the reconstructed image u for a randomly tested deconvolution filter. As σ is unknown, the tested deconvolution filters $\tilde{k}_{\sigma'}$ may have a different variance. So there are two problems in the blind deconvolution process:

- the identification of σ,
- the identification of $\tilde{k} \in K_\sigma$.

Results

a) Illustration of the critical c value

The blurred image is simulated from a initial image u_0 with the formula

$$u_c = k_\sigma \star u_0 \, + \, n \, .$$

The aim is to estimate k from the blurred image u_c. In this experiment we set $\sigma = 4/3$ for the convolution filter and we add a Gaussian noise n of standard deviation 1. The tested deconvolution filters $\tilde{k}$ does not have the same variance than the convolution filter, since in practice the variance of the kernel is not known. Here we set $\tilde{k} \in K_{\sigma'}$ with $(\sigma')^2 = 0.85$. From Proposition 13.29, we deduce the critical value of c

$$c_{\text{crit}} = \frac{(\sigma')^4}{16} = \frac{0.85^2}{16} = 0.04515 \, .$$

Fig.13.11 shows the graph $(TV(u), \Delta TV(u))$ with $\varepsilon = 0.4$ and u_0 image of Fig.13.10-(a). It shows three groups of images u. The first group has little ringing (small $TV(u)$). This group is named "left

group" on the image. It corresponds to large values of c [configuration 2]. On the opposite, the "right group" has a lot of ringing [configuration 1]. Between those two groups is the "transition group" with $c \simeq c_{\text{crit}}$.

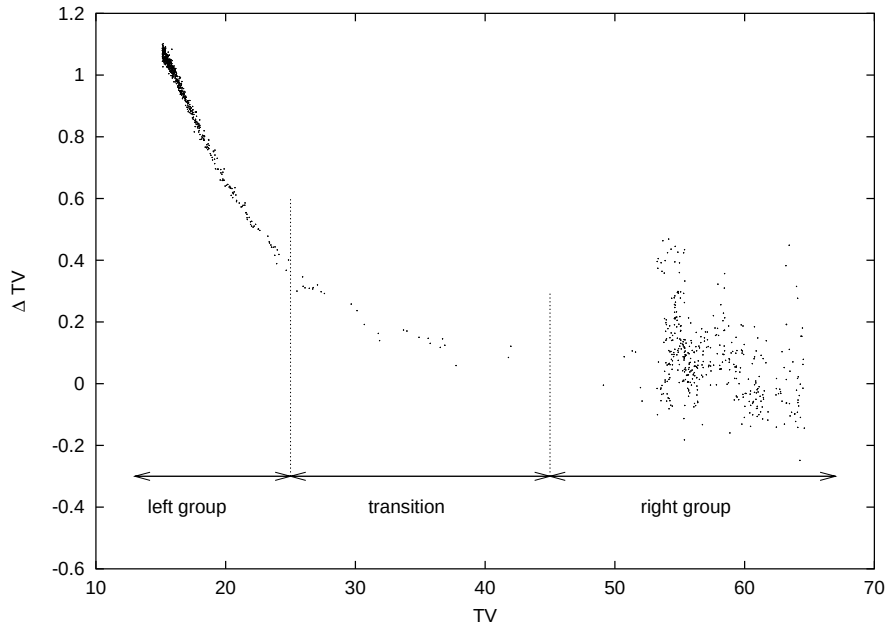

(a)

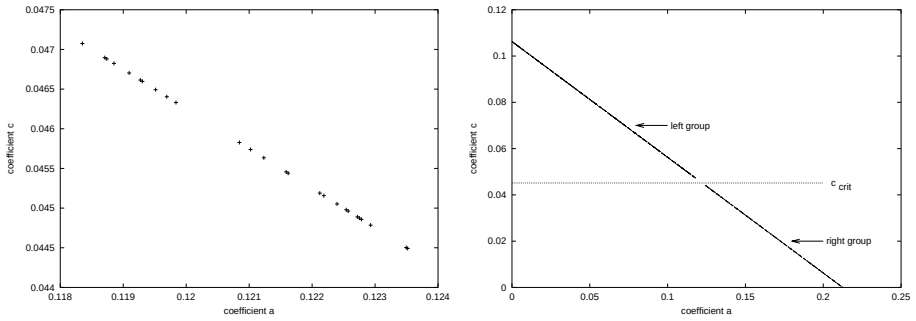

(b) (c)

Figure 13.11: (a) Points $(TV(u), \Delta TV(u))$ with $(\sigma')^2 = 0.85 < \sigma^2 = 4/3$. We test 1000 random filters $\tilde{k} \in K_{\sigma'}$. (b-c) coefficient values of $\tilde{k}$: (b) values for the "transition group" (c) Values for the "right group" and "left group". Note the range of c and a satisfying (13.26) and (13.27).

b) Blind deconvolution experiments without noise: $u_c = k_\sigma \star u_0$.

The deconvolution is done with the special case of the Wiener filter already mentioned in (11.1):

$$\forall \xi \in \mathbb{R}^2, \quad \widehat{u_0}(\xi) = \frac{\widehat{k_\sigma}^*(\xi)}{\left|\widehat{k_\sigma}(\xi)\right|^2 + \frac{|\xi|^2}{w}} \cdot \widehat{u_c}(\xi)\,, \tag{13.36}$$

which allows a "regularized deconvolution" parametrized by w. The "deconvolution filter" called $\widetilde{k_w}$ is a regularized version of the filter k^{-1} and $\widetilde{k_w}$ is defined by

$$\frac{\widehat{k_\sigma}^*(\xi)}{\left|\widehat{k_\sigma}(\xi)\right|^2 + \frac{|\xi|^2}{w}}$$

so that

$$\forall \xi \in \mathbb{R}^2, \quad \widehat{u_0}(\xi) = \widehat{\widetilde{k_w}(w)} \cdot \widehat{u_c}(\xi)\,.$$

In order to validate the criterion F_{0^+} to restore images, we compare the results with a very simple criterion: TV. First let us study this criterion. Fig.13.12 and 13.13 yield the following conclusion.

Conclusion 13.15 *In the case of blind deconvolution without noise*

(i) *for $\sigma^2 < 1$, the TV criterion does not detect k.*

(ii) *for $\sigma^2 \geq 1$, the TV criterion detects k. It is the filter that minimizes $TV(u)$, total variation of the restored image. σ^2 is the value for which the regularity of the TV minimum is maximal.*

Remark: assertion (i) can be explained by Proposition 13.11(i). As the Fourier transform of the filter is positive, only little ringing occurs so images are either blurred or sharp. TV favors blurred images (small TV) over sharp ones (large TV). Consequently, the filter that minimizes the restored image TV gives the most blurred image: it is not k.

Assertion (ii) can be explained by Proposition 13.11(ii). The convolution filter k may vanish for some frequencies. To compensate $\tilde{k}$, a large weight should be given to those frequencies. Ringing may occur if wrong frequencies are magnified.

In Fig.13.12 and 13.13, the coefficients are not chosen randomly, but linearly. That is, for fixed σ^2, c is regularly sampled in $[c_{\min}(\sigma), c_{\max}(\sigma)]$. In the experiments, we set $w = 100000$. This large value of w permits to give more weight on the fidelity term, which permits to evaluate the filter itself, than on the regularity term. u_0 is the image of Fig.13.10-(a).

We will see later that the nice properties of the TV criterion are no longer valid in the presence of noise. Now let us compare the results with F_{0^+}. We test the case $\sigma^2 < 1$, which is unresolved with the TV criterion. We set $\sigma^2 = 0.6$ with $a = 0.025$, $c = 0.0625$ and $e = 0.65$. The reference image u_0 is shown in Fig.13.16-(a). It is an extract of "lacornou" of size 64×64. The phase coherence are $F_{0^+}(u_0) = 1.94$ and $F_{0^+}(u_c) = 0.33$. This criterion detects the convolution filter even in the case $\sigma^2 < 1$. The precision in the detection is shown Fig.13.15. Furthermore, we tested filters $\tilde{k} \in K_{\sigma'}$ with $\sigma' \neq \sigma$ in order to check that filters with wrong variance give small F_{0^+}. Indeed for $(\sigma')^2 = 0.55 < \sigma^2$, $F_{0^+} \in [0.28, 0.36]$. And for $(\sigma')^2 = 0.65 < \sigma^2$, $F_{0^+} \in [0.27, 0.37]$.

Conclusion 13.16 *In the case of blind deconvolution without noise, the F_{0^+} criterion detects the convolution filter k independently of σ.*

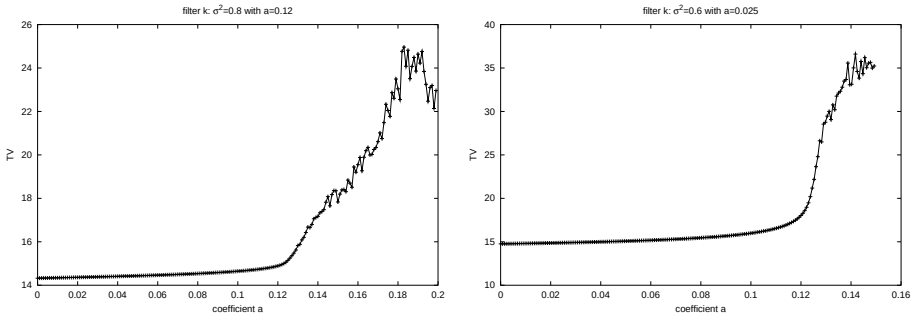

(a) (b)

Figure 13.12: Illustration of assertion (i). $\tilde{k} \in K_\sigma$. (a) $\sigma^2 = 0.8$ (b) $\sigma^2 = 0.6$. The convolution filter is not detected. The minimal value of TV is reached for small a, i.e. large c, as discussed above.

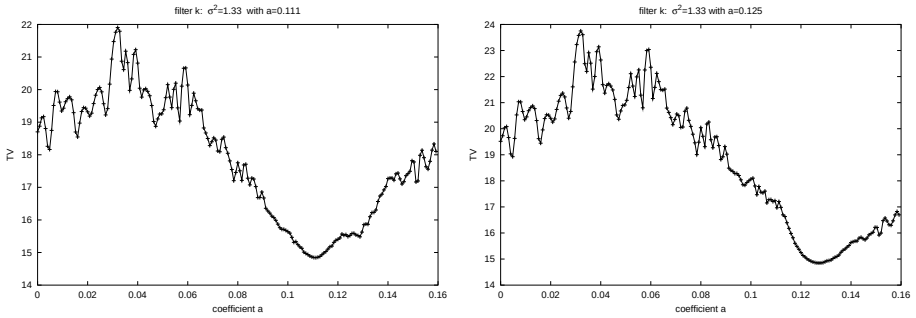

(a) (b)

Figure 13.13: Illustration of assertion (ii). $\tilde{k} \in K_\sigma$ with $\sigma^2 = 4/3$. (a) $a = 1/9$ (b) $a = 1/8$. The convolution filter is detected because the correct value of a minimizes $TV(u)$. Note the regularity of the curve near the minimum which allows the detection of the convolution kernel.

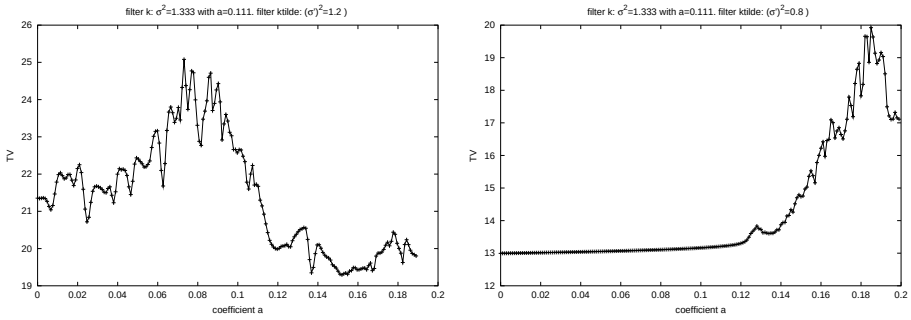

(a) (b)

Figure 13.14: Results for $\tilde{k} \notin K_\sigma$. (a) $(\sigma')^2 = 1.2 \geq 1$. $TV(u)$ has local minima where the curve is not regular. (b) $(\sigma')^2 = 0.8 > 1$. The variance of the filter is too small, so the global minimum is reached for $c = c_{\mathsf{max}}(\sigma)$, i.e. $a = a_{\mathsf{min}}(\sigma)$.

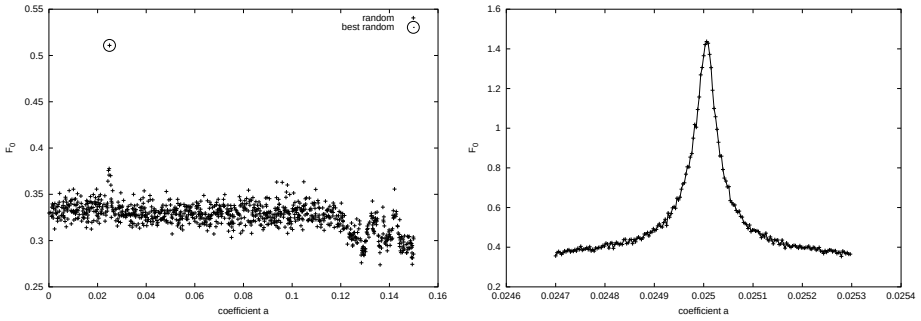

(a) (b)

Figure 13.15: Graph (a, F_{0^+}). (a) 1000 filters $\tilde{k} \in K_\sigma$ randomly chosen are tested. The best result $(F_{0^+}(u) = 0.51)$ is for $a = 0.0249$, $c = 0.06254$ and $e = 0.6501$, which is a kernel very similar to k. (b) Zoom around the best random filter. Two hundred new filters are tested. Their coefficient a are regular samples in $[0.0247, 0.0253]$. The filter k is detected if there is at least one sample of a in $[0.0249 - 5.10^{-4}, 0.0249 + 5.10^{-4}]$.

(a) (b) (c) (d)

Figure 13.16: (a) u_0 (b) u_c (c) restored image with the correct kernel ($a = 0.025$) (d) restored image with the wrong kernel ($a = 0.1$). The mismatch between both kernels k and $\tilde{k}$ produces ringing as shown in (d) whereas the restoration with the correct kernel in (c) produces a sharper image.

F_{0+} detects k for $\sigma^2 < 1$. Now let us study the case $\sigma^2 \geq 1$. We have seen that the total variation criterion identifies the convolution kernel. But let us check that the F_{0+} criterion gives coherent results. We show here that the criterion identifies the convolution kernel, since the deconvolved image is detected as sharp, but we also show that this criterion has to be coupled to the total variation criterion for some deconvolution filters for which the deconvolved image has a pattern (which has a large value of TV) that could be taken for a sharp image.

The associated experiment is now described: the convolution kernel is fixed to $\sigma^2 = 4/3$, $a = 0.1111$ and 200 deconvolution filters are tested. The blurred image u_c is shown in Fig.13.19-(a) and the weight on fidelity term in the Wiener filter to $w = 10^{14}$ is increased to have results very specific to the filters. Fig.13.18 shows the F_{0+} measures of the deconvolved images. It shows that most images are not detected as sharp (one example is shown in Fig.13.19-(d) obtained with $a = .11006$ which is not sharper than u_c and even worse it is degraded by an oscillatory pattern), except two of them:

- one is the expected sharp image which has been deconvolved with the correct filter ($a = 0.1111$). Observe in Fig.13.19-(b) that this image has less blur than u_c.
- one is an unexpected image which has not been deconvolved with the correct filter ($a = 0.1107$). Observe in Fig.13.19-(c) that this image is very degraded. The very oscillating pattern is detected as a sharp image.

As announced the detection of the convolution filter is done by computing also the total variation of the deconvolved image. As showed in Table 13.17, the degraded image detected as sharp with the F_{0+} criterion could be rejected because of its large total variation. Note that the same convolution filter is identified if a larger range of a is tested, i.e. for $a \in [a_{\min}, a_{\max}]$.

c) Blind deconvolution experiments in the presence of noise: $u_c = k_\sigma \star u_0 + n$.

We test here the detector sensitivity to noise addition. We analyze first the TV detector then the F_{0+} detector. We have seen that the TV detector is effective in the case $\sigma^2 \geq 1$. So in the first experiments, we set

- $\sigma^2 = 4/3$ with $a = c = 1/9 \simeq 0.11111$,
- the standard deviation of the Gaussian noise n to $\sigma_n = 1$.

	Coefficient of $\tilde{k}$		
	$a = .11110$	$a = .11007$	$a = .11006$
F_{0^+}	0.50	0.55	0.31
$TV(u)$	14	84	23

Table 13.17: Sharpness and ringing in reconstructed images. As expected the deconvolution with the correct filter ($a = .11110$) builds a sharp image (large F_{0^+}) with a small total variation ($TV(u)$). The other tested filters are not selected because they give either a too large value of ($TV(u)$) or a blurred image ($F_{0^+} \simeq 0.3$).

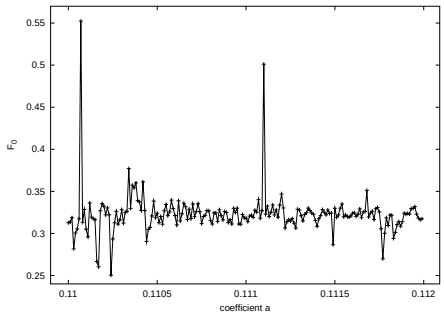

Figure 13.18: Graph (a, F_{0^+}). 200 filters are tested. Their coefficient a are regular samples in $[0.11, 0.112]$. Two restored images have a large value of F_{0^+} (see Table 13.17). They are obtained with $a = .11110$ and $a = .11007$. The correct value of a, i.e. $a = .11110$, is detected as $a = .11007$ introduces too much oscillations in the restored image as shown in Fig.13.19-(c).

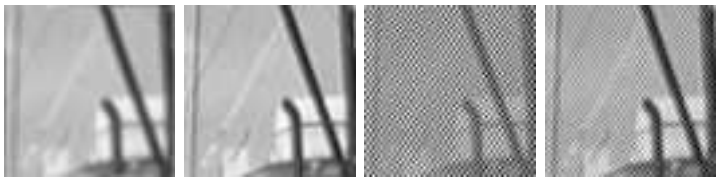

(a) (b) (c) (d)

Figure 13.19: (a) blurred image u_c. Restored image with (b) the correct filter $a = 0.11110$: the image is sharper than u_c, it as been well restored (c) $a = 0.11007$ (d) $a = 0.11006$. On images (c) and (d), the oscillations dominate the true image: the image has been degraded.

Of course, as noise changes $\widehat{u_c}$, deconvoling u_c with $\left(\widehat{k_\sigma}\right)^{-1}$ does not give the optimal result. Furthermore, we decrease w, weight on fidelity term in the Wiener filter, to minimize the ringing coming from the noise. Obviously, the value of w has to be adapted to the level of noise n. Let us compare the results obtained with different values of w. Fig.13.20 shows that

- for large w ($w = 10^{14}$), the total variation is very large. The oscillations hide the true image.
- for smaller w ($w = 10^2$), the value $a = 0.112$ is a local minimum of $TV(u)$. The filter $\tilde{k}$ with $(\sigma')^2 = 4/3$ and $a = 0.112$ is the "good" deblurring filter. This result is confirmed by Fig.13.21. For $w = 10^2$, $a = 0.112$ is also a local minimum of $||u - u_0||_2$, i.e. the reconstructed image is the closest from the original among all the restored images with $\tilde{k} \in K_\sigma$.
- for even smaller value ($w = 10$), we cannot detect k.

Remark: the smaller w is, the more important the regularization with the Wiener filter is. Consequently the more regular the graph $(a, TV(u))$ is.

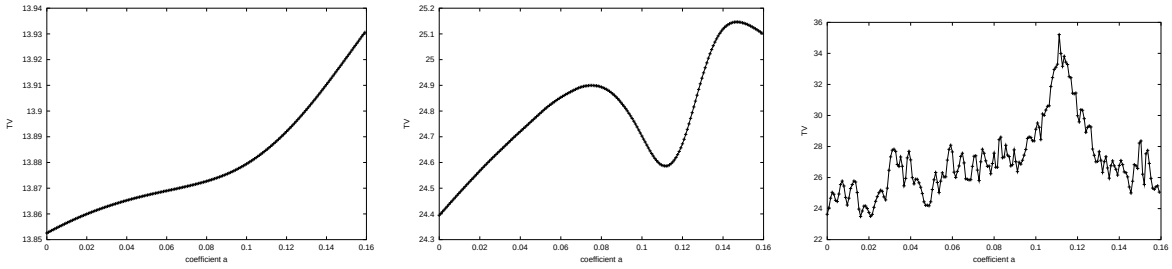

(a) (b) (c)

Figure 13.20: Graph $(a, TV(u))$ with $\sigma^2 = 4/3$, $a = 0.11111$ and $\tilde{k} \in K_\sigma$ (a) $w = 10$ (b) $w = 10^2$ (c) $w = 10^{14}$. The detection of the blur filter is possible only in (b) where the total variation reaches a local minimum for $a \simeq 0.11111$. It corresponds to a smaller value of w than in the previous experiments, but a too small value of w, which means more regularization, does not allow to detect the convolution filter k.

We have seen that the TV criterion detects the convolution kernel only for $\sigma^2 \geq 1$. The case $\sigma^2 < 1$ should be done with the F_{0^+} criterion. We discuss this case in the next part.

13.3.4 Comparison with the Lucy-Richardson method

We compare the previous results with the Lucy-Richardson method. It is all the more interesting since this algorithm is fast for small kernel. The tested filter has support 3×3 and variance $\sigma^2 = 0.6$. The initial image u_0 is shown in Fig.13.22 and the blur kernel is the same than in the case studied in Fig.13.15.

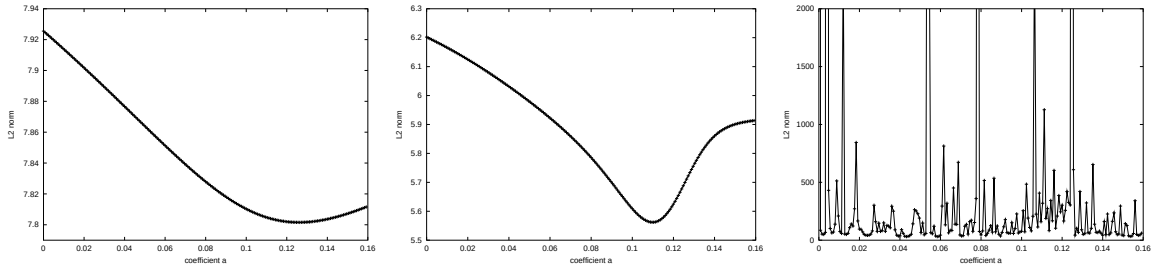

Figure 13.21: Graph $(a, ||u - u_0||_2)$ corresponding to Fig.13.20. This graph validates for $w = 10, 10^2$ that $a \simeq 0.11111$ is the good filter parameter since $||u - u_0||_2$ reaches a minimum. However the detection with the total variation parameter as shown in Fig.13.20 was not possible.

$$k_\sigma = \begin{pmatrix} c & a & c \\ a & e & a \\ c & a & c \end{pmatrix} = \begin{pmatrix} 0.0625 & 0.025 & 0.0625 \\ 0.025 & 0.65 & 0.025 \\ 0.0625 & 0.025 & 0.0625 \end{pmatrix}$$

Figure 13.22: Image u_0 of size 128×128

We used the function *deconvblind* implemented in Matlab. It is the adapted version of the Lucy-Richardson algorithm when the convolution filter is unknown. For a reasonably small amount of iterations, it respects the constraint $4c + 4a + e = 1$ and the positivity of the filter (Fig.13.23). We tested $i \in [1, 10]$ iterations and we plot the output filter of the Lucy-Richardson algorithm. At iteration i, it is characterized by the filter coefficients a_i, c_i and e_i. From these values, we compute $s_i = 4c_i + 4a_i + e_i$ and $\sigma_i = 8c_i + 4a_i$. We note u_i the reconstructed image at iteration i. The initial kernel is set very close to the objective $a_0 = 0.026$, $c_0 = 0.064$, $e_0 = 0.652$ and $\sigma^2 = 0.616$.

As expected, the closest image u_i from u_0 is obtained by deconvoling with a filter very close to k_σ. Iteration 4 gives the smallest difference in the L^2 sense between u_i and u_0. The corresponding filter has $a_i = 0.0256$, $c_i = 0.0626$, $e_i = 0.6472$ and $\sigma_i^2 = 0.6034$. However obviously the algorithm has not converged a the fourth iteration. We note that the variance σ_i tends to decrease with i, which is not surprising because in this algorithm we only impose the spatial spread of the filter but the constraints on the filter given 13.23 are not included in the algorithm. So we cannot expect the LR algorithm to

find the convolution kernel k. More precisely the blur added with $k\sigma$ is probably superimposed with the original blur of the tested image u_0. So the LR algorithm may deblur both the original blur of u_0 and the additive blur obtained with the convolution with k_σ. This test cannot really compare the results of the coherence detector F_{0+} and the LR method. Even if we cannot really conclude on the comparison, we can say that F_{0+} determines precisely k_σ, as shown in Fig.13.15, because the class of possible kernel is fixed (the blur of the original image is probably not obtained with a 3×3 kernel), whereas the LR algorithm as not converged in four iterations. However it would be interesting at this stage to detect if the output image at each iteration of the LR algorithm is sharp. Applying the sharpness detector would give additive information on the resulting images of the LR algorithm.

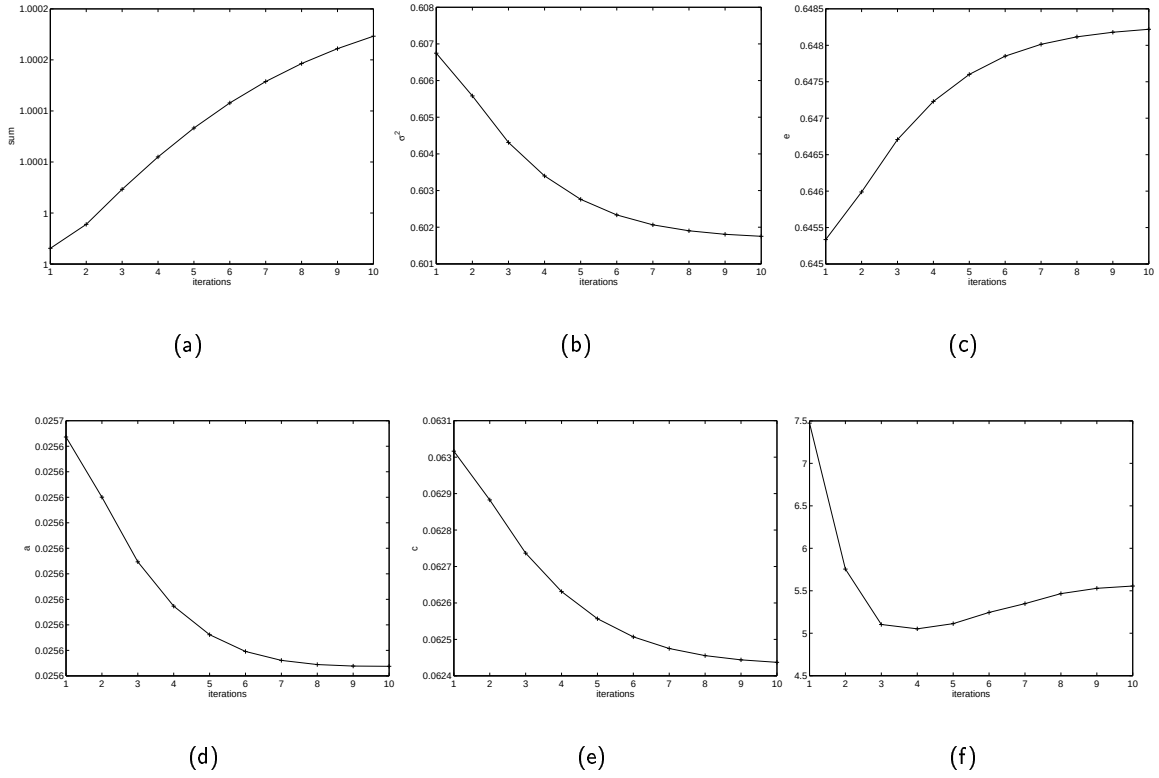

Figure 13.23: Graphs (a) (i, s_i) (b) (i, σ_i) (c) (i, e_i) (d) (i, a_i) (e) (i, c_i) (f) $(i, ||u_i - u_0||_2)$. The graphs (a-b-c-d-e) are direct outputs of the LR algorithms and the graph (f) allows the comparison of the restored image obtained with the LR algorithm with the true original image u_0. The convergence of the algorithm is not reached in 10 iterations. The constraints on k are not respected since for example in (b) the curve of σ^2 is always decreasing. However the LR method may deblur more than expected because of the blur on the original image u_0, so we cannot expect the algorithm to stop at k_σ.

13.3.5 Appendix

Proof of Proposition 13.10

(i) the proof of Proposition 13.10-(i) follows from the constraint equations of k. We have $8c+4a=\sigma^2$ and $a, c \geq 0$, so $\sigma^2 \geq 0$. From $8c+4a=\sigma^2$, the value of σ^2 is maximum when c is maximum too., i.e. when a is minimum. Let $a=0$ in $8c+4a=\sigma^2$, so $8c=\sigma^2$. And let also $e=0$ in $4c+4a+e=1$, so $4c=1$. Consequently, $\sigma^2=8c=2$.

(iii) the discrete Fourier transform of k is

$$\hat{k}(n,p) = \sum_{k_\alpha,k_\beta=0}^{N-1} k(k_\alpha,k_\beta) e^{-2i\pi\left(\frac{k_\alpha n}{N}+\frac{k_\beta p}{N}\right)},$$

where (n,p) is the frequential discretization in the space domain and (k_α,k_β) in the Fourier domain. Injecting the coefficients of the filter implies

$$\hat{k}(n,p) = 4c\cos\left(\frac{2\pi n}{N}\right)\cos\left(\frac{2\pi p}{N}\right)+2a\left(\cos\left(\frac{2\pi n}{N}\right)+\cos\left(\frac{2\pi p}{N}\right)\right)+e.$$

From (13.23), we have

$$\begin{cases} 2a=\frac{\sigma^2}{2}-4c, \\ e=1-\sigma^2+4c. \end{cases} \tag{13.37}$$

Then

$$\hat{k}(n,p) = 4c\cos\left(\frac{2\pi n}{N}\right)\cos\left(\frac{2\pi p}{N}\right)+\left(\frac{\sigma^2}{2}-4c\right)\left(\cos\left(\frac{2\pi n}{N}\right)+\cos\left(\frac{2\pi p}{N}\right)\right)+1-\sigma^2+4c.$$

By defining $\alpha=\cos\left(\frac{2\pi n}{N}\right)$ and $\beta=\cos\left(\frac{2\pi p}{N}\right)$, we get the reduced Cartesian equation, with the coordinate axes as its asymptotes, of an equilateral hyperbola

$$\hat{k}(\alpha,\beta) = 4c\alpha\beta+\left(\frac{\sigma^2}{2}-4c\right)(\alpha+\beta)+1-\sigma^2+4c.$$

The announced result in Proposition 13.10-(ii) will follow immediately by setting $l=1-\frac{\sigma^2}{8c}$.

(iii) Let $a=0$ in $8c+4a=\sigma^2$ (13.23). As σ is fixed, we get the maximal value of c. That is $c_{\max}(\sigma)$. The minimum value of c is deduced from (13.23). The associated geometric problem is shown in Fig.13.24. For $\sigma^2 \leq 1$, $c_{\min}(\sigma)=0$. For $\sigma^2>1$, $c_{\min}(\sigma)=\frac{1}{4}(\sigma^2-1)$. The range of a comes directly from the constraints on k (13.23), where $a=\sigma^2/4-2c$.

The minimal and maximal values of e are noted $e_{\min}$ and $e_{\max}$. From (13.37), we have

$$e=1-\sigma^2+4c.$$

and from (13.26) we have (see Fig.13.25)

$$\begin{cases} c_{\min}(\sigma)=\max\left(0,\frac{1}{4}(\sigma^2-1)\right), \\ c_{\max}(\sigma)=\frac{\sigma^2}{8}, \end{cases}$$

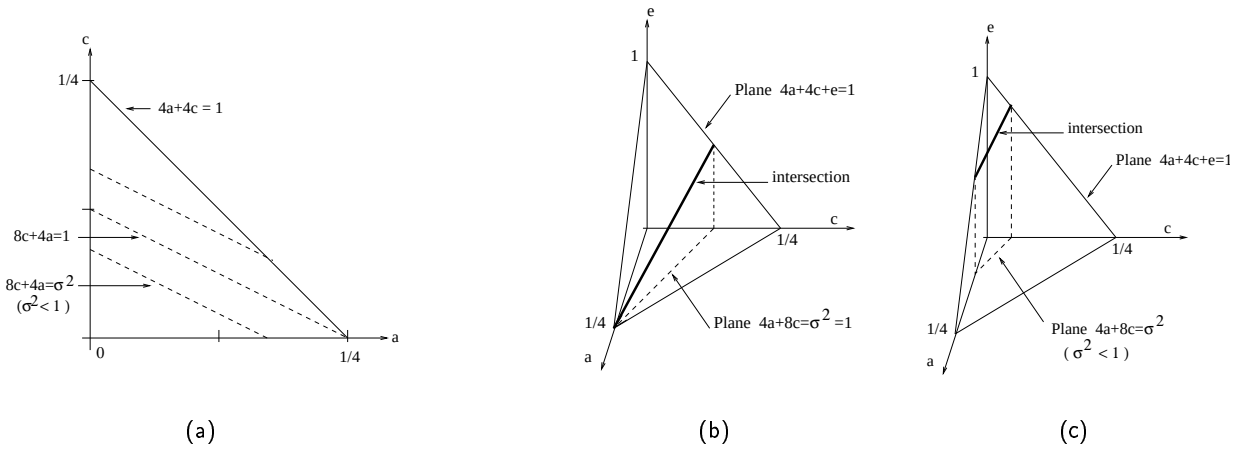

(a) (b) (c)

Figure 13.24: (a) Projection of the constraints (13.23), on the plane $e = 0$ (b-c) 3D visualization of the constraints.

so that

$$\begin{cases} e_{\min}(\sigma) = 1 - \sigma^2 + 4c_{\min}(\sigma)\,, \\ e_{\max}(\sigma) = 1 - \sigma^2 + 4c_{\max}(\sigma)\,. \end{cases}$$

The value of $e_{\max}$ is immediate since $c_{\max}(\sigma) = \frac{\sigma^2}{8}$ so that

$$\begin{aligned} e_{\max}(\sigma) &= 1 - \sigma^2 + 4c_{\max}(\sigma) && (13.38) \\ &= 1 - \sigma^2 + 4\frac{\sigma^2}{8} && (13.39) \\ &= 1 - \frac{\sigma^2}{2}\,. && (13.40) \end{aligned}$$

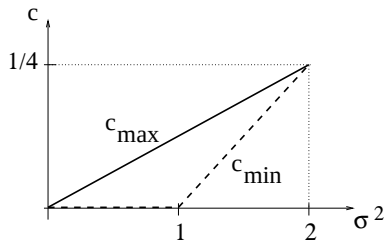

Figure 13.25: Visualization of $c \in [c_{\min}, c_{\max}]$.

The value of $e_{\min}$ depends on the value of σ^2:

- if $\sigma^2 \in [0, 1]$, then $c_{\min}(\sigma) = 0$. Hence

$$e_{\min}(\sigma) = 1 - \sigma^2\,.$$

- if $\sigma^2 \in [1,2]$, then

$$c_{\min}(\sigma) = 1 - \sigma^2 + 4 \cdot \frac{1}{4}(\sigma^2 - 1) = 0\,.$$

To summarize

- if $\sigma^2 \in [0,1]$, then $c \in \left[1 - \sigma^2, 1 - \frac{\sigma^2}{2}\right]$,
- if $\sigma^2 \in [1,2]$, then $c \in \left[0, 1 - \frac{\sigma^2}{2}\right]$,

so that we obtain the general equation

$$\forall \sigma^2 \in [0,2]\,, \quad e \in E = \left[1 - \sigma^2, 1 - \frac{\sigma^2}{2}\right] \cap [0,1]\ .$$

(iv) As $c_{\max}(\sigma) = \frac{\sigma^2}{8}$ (Proposition 13.10-(iii)), then from (13.25), $l \leq 0$.

(v) The critical value of c corresponds to Cte $= 0$ in (13.24) if (13.24) is rewritten

$$\hat{k}(\alpha, \beta) = 4c(\alpha - l)(\beta - l) + \text{Cte}.$$

Then

$$\begin{aligned} Cte = 0 \quad &\Leftrightarrow \quad 1 - \sigma^2 + 4c - 4cl^2 = 0 \\ &\Leftrightarrow \quad 1 - \sigma^2 + 4c(1 - l^2) = 0 \\ &\Leftrightarrow \quad 1 - \sigma^2 + 4c(1 - (1 - \frac{\sigma^2}{8c})^2) = 0 \\ &\Leftrightarrow \quad \sigma^4 = 16c. \end{aligned}$$

□

Chapter 14

Deconvolution with filters having non compact support

Now let us consider a more challenging blind deconvolution. The filters are no more 3×3 compact support filters, but Gaussian filters. This kind of filter is interesting because it has a positive Gaussian Fourier transform. The inversion of such Fourier transform do not vanish, so the deconvolution introduces only little ringing. It is an analogy with the previous case $\sigma^2 < 1$.

The original image u_0 (Fig.13.16-(a)) is blurred with a Gaussian filter. As the convolution in space is equivalent to a product in Fourier domain, we use this equivalence to speed up computations. We note p the standard deviation parameter of the Gaussian filter in Fourier domain.

- First test: the Gaussian filter in Fourier domain has standard deviation $\sigma_b = 0.5$. The blind deconvolution is done with a Wiener filter with $w = 10^6$.
- Second test: $\sigma_b = 0.8$ and $w = 10^{14}$.

Results of the TV and F_{0^+} detectors are displayed in Fig.14.1, 14.2 and 14.3. It shows that the total variation is increasing with p. So the particular case $p = \sigma_b$ is not detected. Whereas F_{0^+} is locally maximal for $p = \sigma_b$, which coincide with the convolution filter. Consequently, F_{0^+} is a good detector of sharp images in a blind deconvolution problem.

Remark: the increasing of w between both experiment produces a curve $(p, F_{0^+}(u))$ more discontinuous as the regularity term in the Wiener filter has low weight.

In the presence of noise, i.e. $u_c = k_\sigma \star u_0 + n$, the restored image with $p = \sigma_n$ is not always the sharpest one. It depends on the level of noise. For small noise values, we intend to find a filter very close to the convolution filter. For larger values, the filter might be very different from the convolution one. Fig.14.4 shows the results obtained with

- an additive Gaussian noise $\sigma_n = 1$,
- a Gaussian filter k with standard deviation $\sigma_b = 0.5$,
- a Wiener filter $w = 10^{10}$ for the image restoration.

As observed before, total variation is not a good criterion for blind deconvolution. It increases with p (Fig.14.4-(b)). On the contrary, F_{0^+} is more informative, as some images deblurred with $p \in [0.4, 0.6]$ are detected as sharper than the others (Fig.14.4-(a)). This is coherent with the convolution kernel

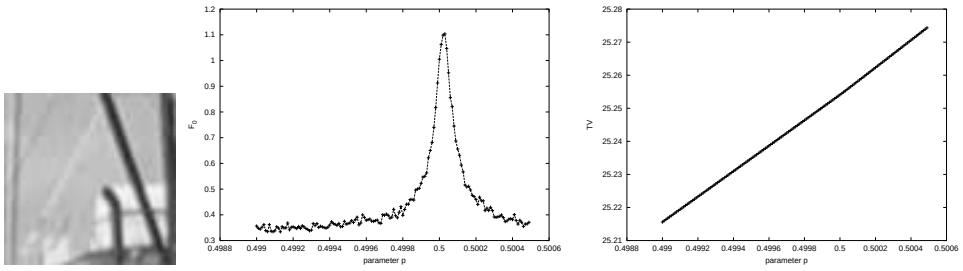

(a) (b) (c)

Figure 14.1: Case $\sigma_b = 0.5$ (a) blurred image u_c (b) graph $(p, F_{0^+}(u))$ (c) graph $(p, TV(u))$
The value of p is regularly sampled in $[0.499, 0.50049]$. 150 samples.
The sharpest image u is obtained for $p = \sigma_b$.
The total variation criteria does not allow the detection of $p = \sigma_b$ as $TV(u)$ increases with p:
there is no minimum of $TV(u)$ for $p \simeq \sigma_b = 0.5$.

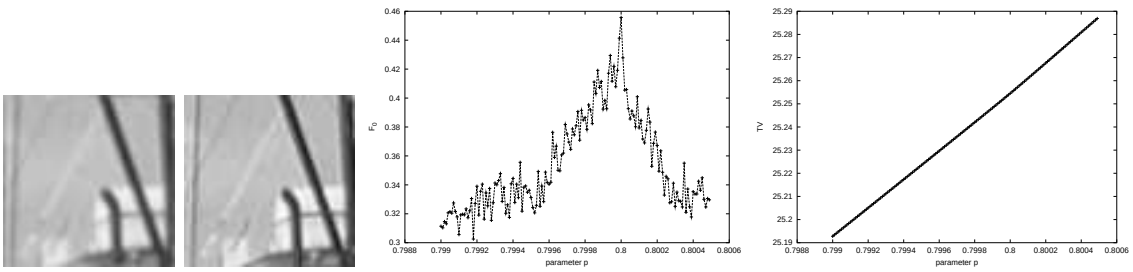

(a) (b) (c) (d)

Figure 14.2: Case $\sigma_b = 0.8$ (a) blurred image u_c (b) restored image u with $p = 0.8$ (c) graph $(p, F_{0^+}(u))$ (d) graph $(p, TV(u))$. p is regularly sampled in $[0.799, 0.80049]$. 150 samples.
The sharpest image u is obtained for $p = \sigma_b$.
The total variation criteria does not allow the detection of $p = \sigma_b$ as $TV(u)$ increases with p.

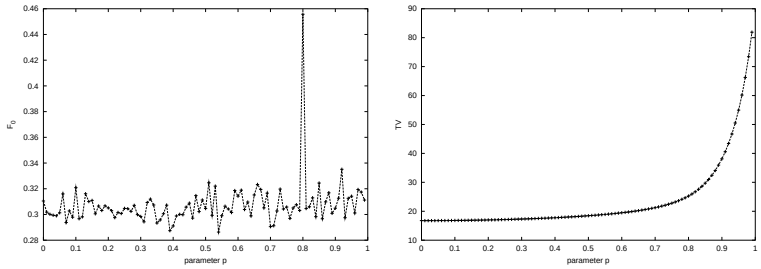

Figure 14.3: Same experiment than in Fig.14.2 for a larger parameter range. p is regularly sampled in $[0, 1]$. 100 samples. Even for a wider range of p, the restored image u obtained for $p = \sigma_b$ is detected as the sharpest. The total variation criteria does not allow the detection of $p = \sigma_b$ as $TV(u)$ increases with p.

$\sigma_b = 0.5$. To prove that such filters give "good" images, we plot the difference between the original image u_0 and the restored image: $||u - u_0||_2$. In practice, u_0 is unknown, but here it confirms the results obtained with F_{0^+}: images restored with $p \in [0.4, 0.6]$ are the closest from the original one among all images restored with $p \in [0, 1]$.

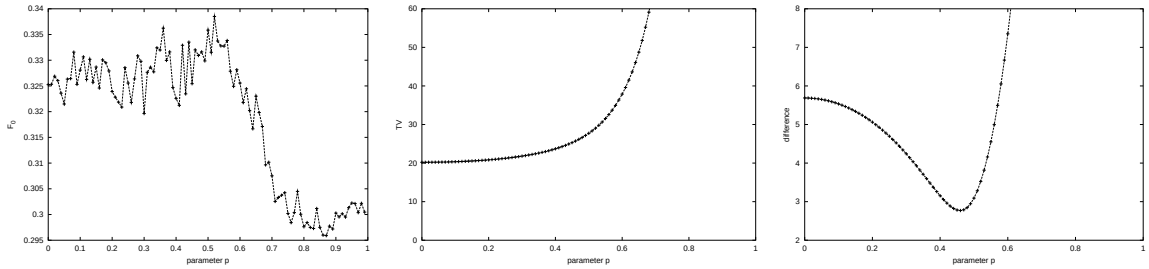

(a) (b) (c)

Figure 14.4: Graphs (a) $(p, F_{0^+}(u))$ (b) $(p, TV(u))$ (c) $(p, ||u - u_0||_2)$. The graph (c) is the reference and it indicates as expected that $p \simeq 0.5$ produces the best reconstructed image. The graph (b) shows that $TV(u)$ does not allow the detection since there is no minimum of the curve for $p \simeq 0.5$. The graph (a) shows that images obtained with $p > 0.5$ are not sharp (small value of $F_{0^+}(u)$) but it makes no difference between the images obtained with $p \leq 0.5$.

Remark: the phase coherence of the original image is $F_{0^+}(u_0) = 1.94$. For the noisy blurred image, $F_{0^+}(u_c) = 0.32$. The restored image with $p = 0.5$ is not as sharp as u_0. It comes from the regularity term in the Wiener filter (even if it is nearly zero) and mainly from the noise component.

When the level of noise increase, $p = \sigma_b$ is not the best filter parameter as noise may introduce ringing. Fig.14.5 shows the results for $\sigma_n = 3$. Restored images with $p \simeq 0.3$ are closer from u_0 than with $p = 0.5$. As observed before, the TV criterion only favors smooth images. The F_{0^+} criterion

proposes several sharp images, some of them could be rejected because of their high TV.

Fig.14.6 shows some reconstructed images. They have the highest phase coherence F_{0+}. The two first can be accepted. The third and the forth ones have too much ringing. These results confirm that in the presence of noise, restoring images with $p = \sigma_b$ is not optimal (Fig.14.6-(c)).

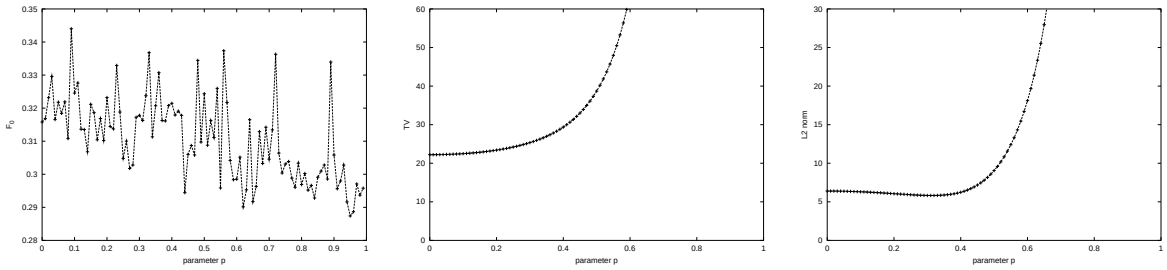

(a) (b) (c)

Figure 14.5: Graphs (a) $(p, F_{0+}(u))$ (b) $(p, TV(u))$ (c) $(p, ||u - u_0||_2)$. In the presence of noise $(\sigma_n = 3)$, restoring images with $p = \sigma_b = 0.5$ is not optimal as shown in Fig.14.6. None of the variables (F_{0+} or TV) allow the detection of $p = 0.5$.

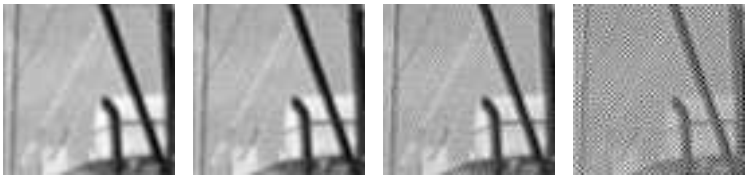

(a) (b) (c) (d)

Figure 14.6: Restored images with (a) $p = 0.09$ (b) $p = 0.33$ (c) $p = 0.5$ (d) $p = 0.72$. With $p = \sigma_b = 0.5$, the restored image has ringing. A smaller value of p produces images with less ringing.

Conclusion

We have studied in this chapter the deblurring of an original image with a regularized deconvolution. It is well known that if the reverse operation is done with a wrong filter, images are highly degraded and the restoration becomes impossible. On the contrary, when the correct convolution filter is used for the deconvolution, the resulting image has better quality than the original blurred one.

Here, we proposed to use the sharpness detector, defined in the previous part, to deblur the image in an automatic way, i.e. to detect the convolution filter. In all the experiments, we assumed that the unknown filter belongs to a given class of filters. We tested the class of filters with compact support and the class of filters with a Gaussian Fourier transform, which do not have a compact support. In both experiments, we showed that the correct convolution filter can be found automatically, even when the original image is degraded by a very small noise (typically a small noise has an amplitude smaller or equal to the quantization step size when the discrete image is converted to a digital image). The comparison with another approach of the literature was difficult since our tests are done on a special class of filters (for example 3×3 filters satisfying some normalization and variance constraints) which is a good indication of the blur filter, whereas most approaches in the literature do not make assumptions on the filter. For example the Lucy-Richardson algorithm does not have the normalization and variance constraints. We observed that the proposed detector makes automatic deblurring possible. No real study on the sensitivity of the detector to the noise level was done here, but the experiments showed that the filter detection is possible provided that the level of noise is small enough.

Another possible image restoration application of the sharpness detector is the denoising. Most denoising methods are parametrized. Let us cite as an example the NL-means denoising method recently defined by Buades *et al.* in [6] [7], which has four parameters. In most methods, the parameter choice is often a problem, so the coherence measure could be used for an automatic parameter selection. We propose some denoising results obtained with the sharpness detector in Chapter 15. This chapter is not meant to be a detailed study of the denoising problem, since we will use the NL-means algorithm and apply the sharpness detector as an additive tool to a restoration process. We will see in this chapter how the sharpness detector coupled with the NL-means algorithm can help propose a coherent denoised image.

Chapter 15

Towards automatic denoising

Most denoising methods are parametrized. The parameter choice is often a problem. The coherence measure can be used in such a purpose. We propose here an automatic parameter selection for the NL-means denoising method defined by Buades *et al.* in [6]. This algorithm is designed for image denoising. It gives good results by comparison with other denoising algorithm because it preserves image features (textures, edges ...). This method takes advantage of the high degree of redundancy of any natural image. It estimates the value of a pixel i as an average of the values of all the pixels whose Gaussian neighborhood looks like the neighborhood of i. Let us recall here the computation of the average value as given in [6].

"Let Ω be the image domain, u be the original image denoted by $u(\mathbf{x})$ for $\mathbf{x} = (x, y) \in \mathbb{R}^2$ and u_n the noisy image, the NL-means algorithm estimates the value of $\mathbf{x}$ by

$$NL(u_n)(\mathbf{x}) = \frac{1}{C(\mathbf{x})} \int e^{-\frac{(G_a \star |u_n(\mathbf{x}+.) - u_n(\mathbf{y}+.)|^2)(0)}{h^2}} v(\mathbf{y})\, d\mathbf{y}\,,$$

where G_a is a Gaussian kernel with standard deviation a, $C(\mathbf{x}) = e^{-\frac{(G_a \star |u_n(\mathbf{x}+.) - u_n(\mathbf{z}+.)|^2)(0)}{h^2}} d\mathbf{z}$ is the normalizing factor and h acts as a filtering parameter."

This algorithm is Non Local since pixels belonging to the whole image are used for the estimation of i. However in practice, in order to reduce the computation time, the seek of the neighborhood is limited to a window around the pixel to be estimated, which may reduce the quality of the denoising. The NL-means method has four parameters:

- the size of the window: $(2w_s + 1) \times (2w_s + 1)$. It is a subpart of the image where similar neighborhoods are seek,
- the size of the neighborhood: $(2p + 1) \times (2p + 1)$. In [6], they suggest a patch of size 7×7 or 9×9 (that is $p = 3$ or $p = 4$) for gray level images,
- the standard deviation of the Gaussian kernel a,
- the decay of the exponential function h: decay of the weights in the similarity measure.

Experimentally, the method restores very well images when the four parameters are appropriately chosen. Buades proposes a perceptual evaluation of the parameters. He made some suggestions about the size of the patch p and the value of h. He proposes a patch of size $p = 3$ or $p = 4$ and h of the order of noise standard deviation σ [6] (note that in [7], Buades *et al.* have seen experimentally that

h can take values between $10 \cdot \sigma$ and $15 \cdot \sigma$). However, this recommendation depends on the type of considered images and on the other parameter values. Experimental results showed that textures are better preserved when considering a smaller value of p, for example $p = 2$. Moreover, the value of a, the standard deviation of the Gaussian kernel in the similarity measure, may change the optimal value of h. Such h restores the best as possible the noisy image. The modeling of this image is

$$u_n = u + n_\sigma$$

where u is the original nice image, n_σ is a Gaussian noise with variance σ^2 and u_n is the resulting image. We shall call u_r the reconstructed image by the NL-means algorithm:

$$u_r = NL(u_n)\,.$$

As we shall test different values of h in the NL-means algorithm, let us add a subscribe h at u_r. It yields $u_{r,h}$.

Experiments:

We propose here to study the case of a patch size 5×5 (that is $p = 2$) with $a = 2$ and $w_s = 15$. Several noise variances are tested $\sigma = \{3, 5, 10\}$ (Fig.15.1). For each fixed σ, we plot the phase coherence of $u_{r,h}$ ($F_0(u_{r,h})$) as a function of h. To simplify the notations, $F_0(u_{r,h})$ is noted F_0. Results are compared with the mean square error E between u and $u_{r,h}$ (Fig.15.2). We have chosen here the mean square error but other criteria could be tested.

The argmin of $E(h)$ gives the true optimal value of h. Let us note

- h_E the optimal h given by E, the mean square error between u and $u_{r,h}$
- h_F the optimal h given by F_0

The original image has size 128×128 (Fig.15.1). We summarize the h_E and h_F values for different values of σ in Fig.15.5.

Remarks:

1. We measured the added noise with its standard deviation σ. However the noise impact also depends on u. This is the reason why the signal noise ratio (SNR) is also an interesting measure. It takes into account both the standard deviation of the noise (σ) and the standard deviation of the image u denoted by $\sigma(u)$.

   $$SNR = \frac{\sigma(u)}{\sigma}$$

   The empirical standard deviation of u is calculated by

   $$\sigma(u) = \left(\frac{1}{N} \sum_{i,j} (u(i,j) - \bar{u})^2 \right)^{1/2}$$

   where N is the number of pixels in u and u is the average gray value: $\bar{u} = \frac{1}{N} \sum_{i,j} u(i,j)$. For example, u in Fig.15.1 has standard deviation 60. This represents a good quality image [6]. The SNR of the noisy images are simply $SNR = \frac{60}{\sigma}$. This means $SNR = 20$ when $\sigma = 3$.

2. The sharpness measure F_0 detects the optimal value of h. Its value is maximal when the restored image is the closest to the original (E minimal). Note that on the graphs, F_0 is thresholded to 100.

3. For large values of h the coherence is also maximal as the restored image suppresses the "granularity" of the image. Flat zones seem more flat than on u. Edges are preserved which increases the image sharpness perception.

4. h_F is larger than the true one h_E for large σ. This comes from the fact that F_0 is very sensitive to the image sharpness whereas E really measures the proximity to u. F_0 privileges sharp images even if it means suppressing some textures or the granularity of flat zones. Whereas the loss of these characteristics increases E. An example is given in Fig.15.6 where the initial noise is set to $\sigma = 2$ and the corresponding optimal values h are $h_E = 10$ and $h_F = 14$. We observe that with h_F (Fig.15.6-(d)) the image has lost more granularity than with h_E (Fig.15.6-(c)).

   For large σ, the noisy image has already lost too much details. Even the NL-means algorithm can not reconstruct them.

5. the optimal value of h in the L^2 sense (mean square error between the original image u and $u_{r,h}$) is shown by h_E in Fig.15.5. Note how the curve of $h_E(\sigma)$ is close to a line. It is coherent that the value of h increases with the noise level σ. Indeed if the image is very noisy, there is good reconstruction, i.e. enough regularization of the image, if many points are used to compute the average, even points with a slightly different neighborhood than the neighborhood of the considered point. We do not give an explanation of the linear behavior of h_E with σ. It would be interesting to check this characteristic for different kinds of image and to see how the line slope depends on the images and the other parameter choices.

(a) (b) (c)

Figure 15.1: Images (a) u (b) u_5 ($SNR = 12$) (c) u_{10} ($SNR = 6$)

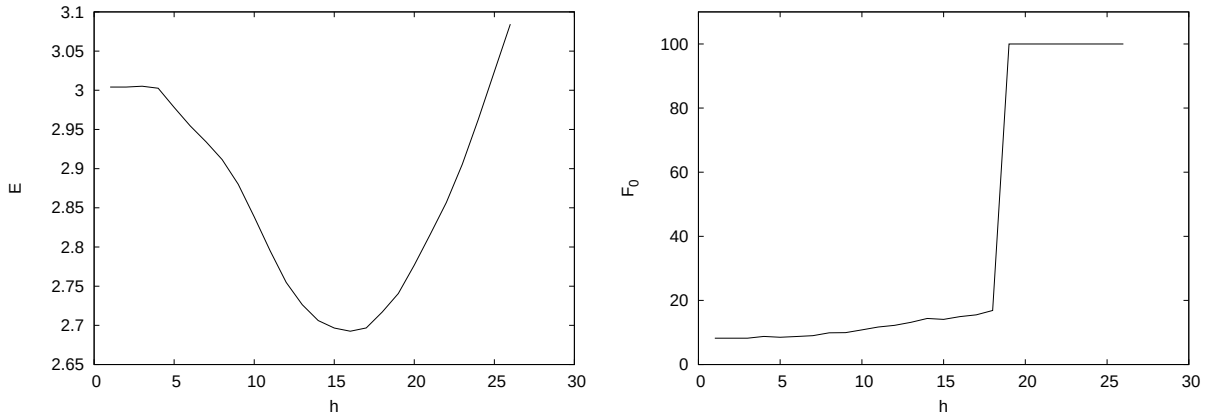

(a) (b)

Figure 15.2: Noise variance: $\sigma = 3$ (a) (E, h) (b) (F_0, h). The value of h that gives a sharp image (jump of F_0) is very close to the argmin of E, i.e. $h_E \simeq h_F$.

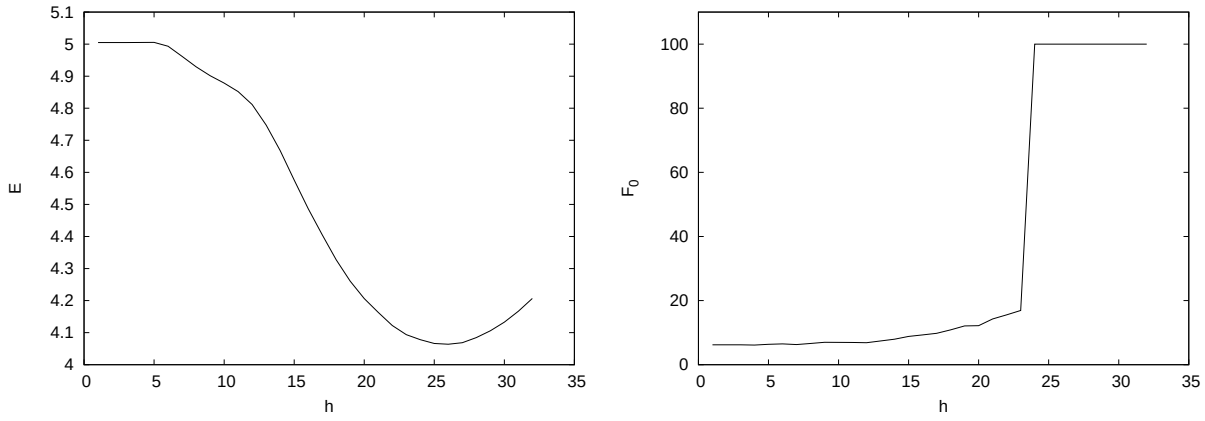

(a) (b)

Figure 15.3: Noise variance: $\sigma = 5$ (a) (E, h) (b) (F_0, h). Same comment as in Fig.15.2

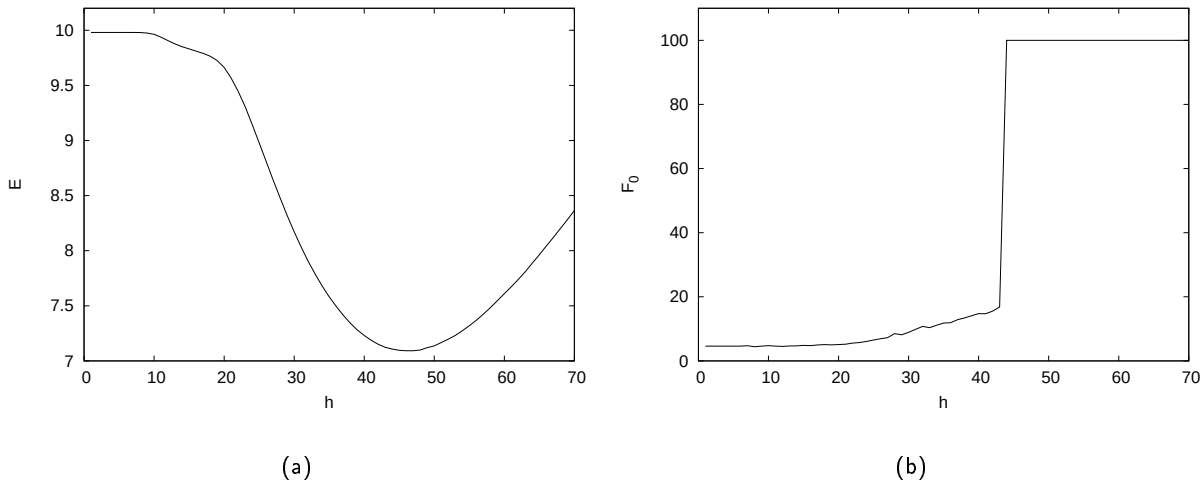

Figure 15.4: Noise variance: $\sigma = 10$ (a) (E, h) (b) (F_0, h). Same comment as in Fig.15.2

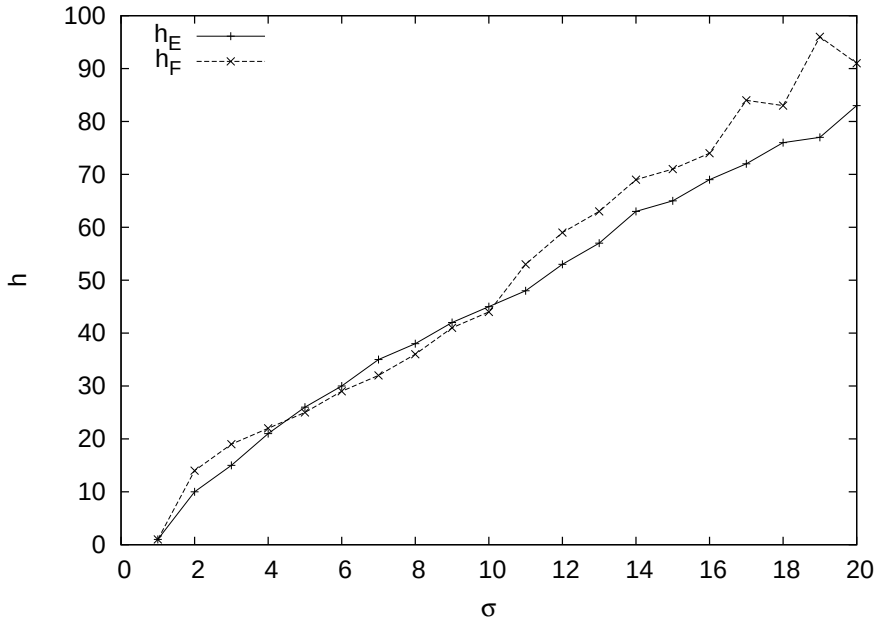

Figure 15.5: Comparison of h_E and h_F for $\sigma \in [0, 20]$. The phase coherence measure detects images very close to the optimal image (the optimality being measured in the L^2 sense). Note also how $h_E(\sigma)$ is close to a line.

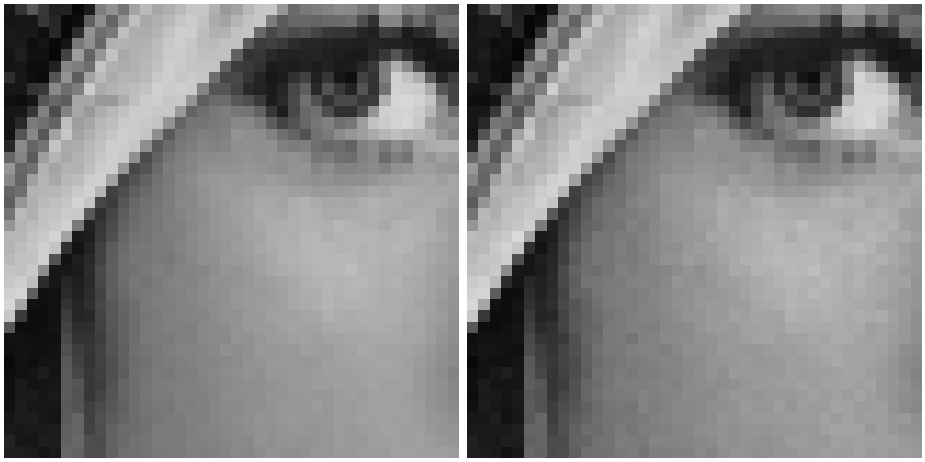

(a) (b)

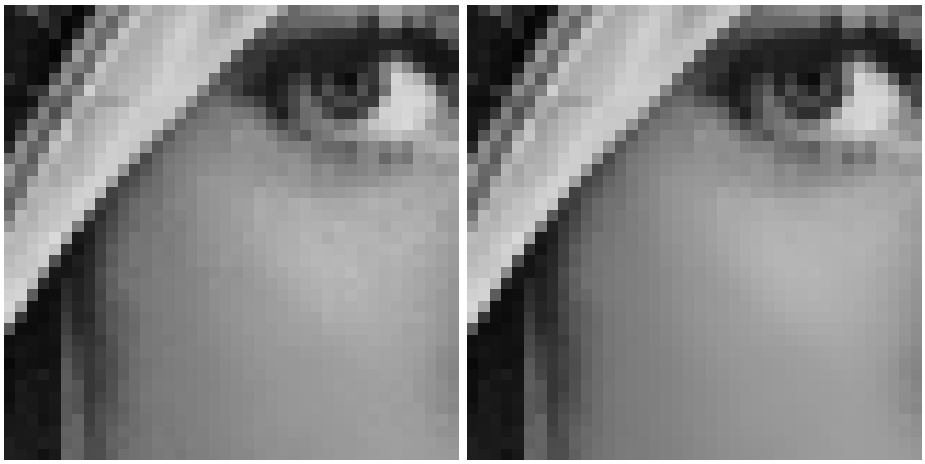

(c) (d)

Figure 15.6: Images (a) u (b) u_2 (c-d) denoised with $h_E = 10$ and $h_F = 14$. I mage (d) has lost more granularity than image (c).

Conclusion and perspectives

This thesis studies the question of the image quality. The quality of a numerical image is inherent to its formation, i.e. to the production of a discrete version of the continuous world. All formation processes are constrained to degrade the image quality by introducing some artifacts, so it is paramount to reduce the amount of artifacts on the image. The major difficulties are the characterization and the detection of such artifacts in images. Previous works in image quality showed that the question of the evaluation of these artifacts is not solved. Some solutions already exist for the blur control of an image formation process when the sampling grid of the image and the noise introduced by the instruments are given. Firstly with the satellite SPOT 5, a global approach in the Shannon kingdom was performed, where the sampling has been adapted to the support of the MTF. But the other artifacts have not been studied simultaneously.

The objective of this thesis was precisely to study these artifacts directly linked to the formation of a numerical image. Two major difficulties of the image quality question, which are the characterization and the detection of artifacts, have been studied. They have been formalized for the three artifacts directly related to the formation of a numerical image: the blur, the ringing and the aliasing. Contrarily to some solutions of the literature, the question of the instrumental noise has not been analyzed for the moment. In this work the focus was on the image degradation by the artifacts and not by the noise because these two degradations have an essential difference. The noise has no structure, whereas the studied artifacts have a characteristic structure: the ringing adds spurious oscillations, aliasing destroys the regularity of the edges of the image and blur is a structured degradation which smoothes the image. Since the framework has been the characterization and the detection of the artifacts in the presence of a little amount of noise, the question of the stability of our results in the presence of moderate or large noise would have to be studied. The evaluation of the noise impact on the perception of the artifacts and the possible masking effect of the noise could also be considered in future work.

The underlying theory used in the whole thesis is the Shannon theorem, which is the foundation of the understanding of the formation of the artifacts. Obtaining an artifact-free image is a difficult problem because physically a real image acquisition device with numerical images is often an approximation of the filter defined by Shannon, and mathematically the quasi-compacity in both the space and the Fourier transform domain is difficult. We showed that there is often a trade-off between these artifacts yielding to the idea of the study of the three artifacts in a united way.

Here this unified approach of the three artifacts was concretely expressed by first a methodology to design an *optimal filter* given a sampling grid in the aliasing-free image context. The idea of a blur/ringing trade-off has been pushed forward. Second new detectors have been proposed for each of the artifacts. The detection is adapted to the artifact characterization and it is based on a statistical *a contrario* approach following the work of Desolneux *et al.* [13], which has the advantage to be parameter-free. This statistical approach has been used repeatedly all along this thesis.

Beginning with a formal definition of the ringing artifact, we discussed that the ringing artifact is

neither a consequence of the Gibbs theorem nor a consequence of the Bôcher theorem. To show the difference, an example has been given where the projection onto the band-limited space of a given C^∞ function oscillates. A general theorem that would identify the class of continuous functions whose projection onto the band-limited space oscillates would be interesting. Knowing the position and the amplitude of the overshoots and undershoots would also be a useful indication for the applications of image low-pass filtering.

Following with the low-pass filter characterizations, the context of aliasing-free image reduction has been studied. A new joint measure of the blur and ringing artifacts has been defined. This measure was developed after realizing that ringing and blur are intimately linked around a low-passed sharp transition and that it is not possible to measure the spread of the transition due to the blur without considering the impact of the ringing oscillations on the perceived blur. The blur/ringing measure was realized by a so called *Spread-Ringing curve*, assuming no aliasing, which completely characterizes a filter or a filter family. The *Spread-Ringing curves* of classical low-pass filters have been compared so that any user can objectively chose the best filter for the image reduction depending on its visual constraints and the initial image quality. A table of the filter parameter with respect to the blur/ringing measure has been proposed for an immediate application of the comparison results. With respect to the *Spread-Ringing curve* the associated *optimal filters* have been proposed, which means that the filter gives the best blur/ringing trade-off for our joint blur and ringing measure.

In many cases, the filter is unknown so that the filter characterization with respect to the artifacts is not possible requiring a direct evaluation of the artifacts on the images. The evaluation on the image is also useful to check the validity of a post-processing. Three new detectors have been proposed for the three image qualifiers: sharpness, ringing and aliasing. Although the most straightforward approach would be to consider only the spatial domain, the proposed sharpness detector considers both the spatial and frequential domains. A new definition of the phase coherence has been proposed. In this definition there is no direct test to know if the Fourier components are in-phase around sharp transitions, as proposed by Morrone [37], but the estimation of the coherence of the transitions is done by estimating the sensitivity of the total variation of the image after small random phase-shifts of its Fourier transform components. The idea is that a sharp transition can be decomposed in in-phase sinusoids, and a small phase-shift increases strongly the total variation of the image since the sinusoids do not compensate anymore. Experiments showed that the detection of sharp images is possible with the associated sharpness detector. For some special image cases, blurred images may be detected as sharp if they are deteriorated by a very structured artifact. This observation has shown that the detector response does not always match the visual criterion and that some other measures, such as the total variation, can detect such unnatural images. For the ringing detection, the approach is an *a contrario* method based on the detection of oscillations, which are specific to ringing in the spatial domain. Moreover, this detector has three great advantages: it is parameter-free, robust to noise and invariant under contrast change. For the aliasing, some approaches have been tested based on the spatial domain or on the frequential one. The most promising approach we have proposed and tested is a new method based on the fact that an aliased image is not described by Shannon theory and that the postulate that the image is equivalent to its sub-pixel translations is not true for an aliased image. The detectors have been tested on satellite images and still need to be tested on a larger image database. Two possible applications of the detectors have been presented in the blind deconvolution and denoising problems.

This review of the main points of the thesis has shown that the study is not close. We present now some possible improvements. The characterization of a low-pass filter with its *Spread-Ringing curve* is well adapted in the aliasing-free context. A nice generalization of the measure could take into account

other possible image degradations such as aliasing and noise. So the first possible generalization of the *Spread-Ringing curve* could be the addition of a third degree of freedom by substituting the curve of two parameters (spread,ringing) by a curve of three parameters (spread, ringing, aliasing). The associated *Spread-Ringing-Aliasing measure* would have practical applications. The first possible application would be the image formation by an acquisition device. The instruments used in an optical chain have intrinsic physical constraints that cannot always be changed. The physical constraints may yield an image with at least one of the three artifacts. The *Spread-Ringing-Aliasing measure* would be a tool adapted to the characterization and the specification of the acquisition devices. The second possible application would be the post-processing of a discrete image, such as in the image reduction case. In this application, the filter is not fixed by the instrumental constraints but by the application and the *Spread-Ringing-Aliasing measure* would be useful to chose the most appropriate filter to obtain an image that is the best adapted to the visual constraints. A possible refinement of the measure is the addition of the noise measure, yielding maybe to a *Spread-Ringing-Aliasing-Noise measure*.

Some possible applications of the artifact detectors have been given in restoration. The idea is not only to validate a restoration algorithm by checking its image output quality, for which the artifact detector is already a nice automatic tool, but it is also the coupling of the detectors to the restoration procedure. First, it could offer some nice perspectives for all parametrized algorithms, for which the detector could help for the choice of the best parameters. Second, it could also be coupled to an iterative algorithm, such as the well-known Lucy-Richardson algorithm, for which the detector could help to stop the procedure when the output image has no artifact. More generally, the use of the detectors as decision tools for the choice of the best filter/image could be coupled to any restoration procedure.

This wide range of applications of the artifact detectors comes from the global approach that has been adopted in this thesis. The artifacts have been characterized and studied simultaneously and the detectors have been defined in a very general way, based on both the Shannon theory and the spatial characterization of the artifacts, without any application specification. This new approach of the image quality domain seems to yield interesting perspectives for the automatic image quality assessment. This is the first time that a statistical *a contrario* approach has been used in the image quality domain and it seems to be adapted. The second idea of coupling the spatial and frequential characterization of the artifacts could be pushed forward in future works to measure and detect other types of artifacts that should be taken into account in a more precise and global modelling of perfect image quality.

Bibliography

[1] J. F. Abramatic and O. D. Faugeras. Sequential convolution techniques for image filtering. *IEEE Trans. Acoust., Speech, Signal Processing*, 30(1):1–10, 1982.

[2] A. Almansa. *Échantillonnage, interpolation et détection. Applications en imagerie satellitaire*. PhD thesis, École Normale Supérieure de Cachan, 2002.

[3] M. Ayer, H. D. Brunk, G.M. Ewing, W. T. Reid, and E. Silverman. An empirical distribution function for sampling with incomplete information. *Ann. Math. Statist.*, 26:641–647, 1955.

[4] G. R. Ayers and J. C. Dainty. Iterative blind deconvolution method and its applications. *Optics Letters*, 13(7):547–549, 1988.

[5] J-M. Bony. *Théorie des distributions et analyse de Fourier*. Éditions de l'école Polytechnique, 2001.

[6] A. Buades, B. Coll, and J.-M. Morel. On image denoising methods. *Preprint CMLA №2004-15*, 2004.

[7] A. Buades, B. Coll, and J.-M. Morel. A review of image denoising algorithms, with a new one. *Multiscale Modeling and Simulation*, 4(2):490–530, 2005.

[8] J. Buzzi and F. Guichard. Uniqueness of blur measure. In *(long version) unpublished communication*.

[9] J. Buzzi and F. Guichard. Uniqueness of blur measure. In *ICIP*, pages 2985–2988, 2004.

[10] A.S. Carasso. Direct blind deconvolution. *SIAM J. Applied Math.*, 61:1980–2007, 2001.

[11] A. Desolneux. *Événements significatifs et applications à l'analyse d'images*. PhD thesis, École Normale Supérieure de Cachan, 2000.

[12] A. Desolneux, L. Moisan, and J.-M. Morel. Meaningful Alignments. *International Journal of Computer Vision*, 40(1):7–23, 2000.

[13] A. Desolneux, L. Moisan, and J.-M. Morel. *From Gestalt Theory to Image Analysis - A Probabilistic Approach*. Preprint MAP5 №2006-9, 2006.

[14] L.C. Evans and R.F. Gariepy. *Measure Theory and Fine Properties of Functions*. CRC-Press: Boca Raton, 1992.

[15] J. Froment. Perceptible level lines and isoperimetric ratio. In *International Conference on Image Processing*, volume 2, pages 112–115, September 2000.

[16] E. Hewitt and R. Hewitt. The Gibbs-Wilbraham phenomenon: an episode in Fourier analysis. In *Arch. Hist. Exact Sci. 21*, pages 129–160, 1980.

[17] W. Hoeffding. Probability inequalities for sums of bounded random variables. *Journal of the American Statistical Association*, 58:13–30, 1963.

[18] R. Hummel, B. Kimia, and W. Zucker. Deblurring Gaussian Blur. *Computer Vision, Graphics and Image Processing*, 38:66–80, 1987.

[19] P. Jansson. Deconvolution of Images and Spectra. Academic Press, New York, 1997.

[20] A. J. Jerri. *The Gibbs Phenomenon in Fourier Analysis, Splines and Wavelet Approximations*. Kluwer Academic, Boston, 1998.

[21] P. Kovesi. Phase congruency: A low-level image invariant. *Psychological Research*, 64:136–148, 2000.

[22] P. Kovesi. Edges are not just steps. *ACCV2002: The 5th Asian Conference on Computer Vision, Melbourne, Australia*, pages 822–827, January 2002.

[23] S. Ladjal. *Flou et quantification dans les images numériques*. PhD thesis, École Normale Supérieure de Cachan, 2005.

[24] R. Lagendijk, J. Biemond, and D. Boekee. Regularized iterative image restoration with ringing reduction. *IEEE Transactions on Acoustics, Speech, and Signal Processing*, 36(12), 1988.

[25] H. J. Landau and H.O. Pollak. Prolate spheroidal wave functions, Fourier analysis and uncertainty-II. *Bell System Techical Journal*, 40:65–84, 1960.

[26] H. J. Landau and H.O. Pollak. Prolate spheroidal wave functions, Fourier analysis and uncertainty-III: The dimension of the space of essentially time-and band-limited signals. *Bell System Techical Journal*, 41:1295–1336, 1962.

[27] L.B. Lucy. An iterative technique for the rectification of observed images. *The Astronomical Journal*, 79(6):8–37, 1974.

[28] F. Malgouyres. *Augmentation de résolution d'images digitales: Théorie variationelle et applications*. PhD thesis, École Normale Supérieure de Cachan, 2000.

[29] S. Mallat. *Une exploration des signaux en ondelettes*. Editions de l'école Polytechnique, 2000.

[30] P. Marziliano, F. Dufaux, S. Winkler, and T. Ebrahimi. A no-reference perceptual blur metric. In *International Conference on Image Processing*, volume 3, pages 57–60, Rochester, NY, September 22–25, 2002.

[31] P. Marziliano, F. Dufaux, S. Winkler, and T. Ebrahimi. Perceptual blur and ringing metrics: Application to JPEG2000. *Elsevier Signal Processing: Image Communication*, 19(2):163–172, February 2004.

[32] L. Moisan. Modeling and image processing. *polycopié de cours du D.E.A. M.V.A.*, 2005.

[33] P. Monasse and F. Guichard. Fast computation of a contrast invariant image representation. In *Cahiers de l'ENS Cachan*, 1998.

[34] J.M. Morel and S. Ladjal. Analyse de Fouier et théorie de Shannon. In *Analyse de Fourier et traitement d'images. Journées X-UPS 1998. Centre de Mathématiques de l'École Polytechnique. France.*

[35] M.C. Morrone and D.C. Burr. Feature detection in human vision: a phase-dependent energy model. *Proc. Roy. Soc.*, pages 221–245, 1988.

[36] M.C. Morrone and R.A. Owens. Feature detection from local energy. *Pattern Recognition Letters*, 6(5):303–313, 1987.

[37] M.C. Morrone, J.R. Ross, D.C. Burr, and R.A. Owens. Mach bands are phase dependent. *Nature*, pages 250–253, November 1986.

[38] A. Muñoz Barrutia, T. Blu, and M. Unser. Least-squares image resizing using finite differences. *IEEE Transactions on Image Processing*, 10(9):1365–1378, September 2001.

[39] S.H. Oguz. *Morphological post-filtering of ringing and lost data concealment in generalized lapped orthogonal transform based image and video coding.* Ph.D. dissertation, Univ. of Wisconsin, Madison, 1999.

[40] R. R.Ehrenborg. The asymptotics of almost alternating permutations. *Adv. in Appl. Math.*, 28(3-4):421–437, 2002. Special issue in memory of Rodica Simion.

[41] W. Richardson. Bayesian-based iterative method of image restoration. *Journal of the Optical Society of America*, 62:55–59, 1972.

[42] B. Rougé. Théorie de la chaîne image et restauration d'image optique à bruit final fixé. Mémoire d'habilitation à diriger des recherches. Option: Mathématiques appliquées. 1997.

[43] G. Saporta. *Probabilités, analyse des données et statistique.* Editions Technip, Paris, France, 1990.

[44] J. Serra. *Image Analysis and Mathematical Morphology*, volume 1. Academic Press, London, England, 1982.

[45] C. E. Shannon. Communications in the presence of noise. In *Proceedings of the Institute of Radio Engineers*, volume 37, pages 10–21, 1949.

[46] H.R. Sheikh, Z. Wang, L. Cormack, and A.C. Bovik. *LIVE Image Quality Assessment Database Release 2.* http://live.ece.utexas.edu/research/quality, 2005.

[47] D. Slepian. Prolate spheroidal wave functions, Fourier analysis and uncertainty- IV: Extensions to many dimensions; Generalized prolate spheroidal functions. *Bell System Techical Journal*, 43:3009–3057, 1964.

[48] D. Slepian. Prolate spheroidal wave functions, Fourier analysis, and uncertainty- V: The discrete case. *Bell System Technical Journal*, 57:1371–1429, 1978.

[49] D. Slepian and H.O. Pollak. Prolate spheroidal wave functions, Fourier analysis and uncertainty-I. *Bell System Techical Journal*, 40:43–64, 1961.

[50] J. Stoyanov. *Counterexamples in Probability, Second Edition*. Wiley, 1996.

[51] P. Thévenaz, T. Blu, and M. Unser. Image interpolation and resampling. In I.N. Bankman, editor, *Handbook of Medical Imaging, Processing and Analysis*, chapter 25, pages 393–420. Academic Press, San Diego CA, USA, 2000.

[52] A. N. Tikhonov. Regularization of Incorrectly Posed Problems. *Soviet Math.*, 4:1624–1627, 1963.

[53] M. Unser. Sampling—50 Years after Shannon. *Proceedings of the IEEE*, 88(4):569–587, April 2000.

[54] M. Unser, A. Aldroubi, and M. Eden. Enlargement or reduction of digital images with minimum loss of information. *IEEE Transactions on Image Processing*, 4(3):247–258, March 1995.

[55] Z. Wang and E.P. Simoncelli. Local Phase Coherence and the Perception of Blur. In Sebastian Thrun, Lawrence Saul, and Bernhard Schölkopf, editors, *Advances in Neural Information Processing Systems 16*, pages 1435–1442. MIT Press, Cambridge, MA, May 2004.

[56] P. H. Westerink, J. Biemond, and P.H.L de Bruin. Digital color image restoration. *Proc. European Signal Processing Conference EUSIPCO, The Hague*, 1986.

[57] J. W. Woods, J. Biemond, and A. M. Tekalp. Boundary value problem in image restoration. *Proceedings, ICASSP*, 1985.

[58] S. Yang, Y. Hu, T. Nguyen, and D. Tull. Maximum-likelihood parameter estimation for image ringing-artifact removal. In *IEEE Trans. on Circuits and Systems for Video Tech., vol. 11*, pages 963–973, 2001.

[59] Y. Yang and N. Galatsanos. Removal of compression artifacts using projections onto convex sets and line process modeling. *IEEE Trans. on Image Processing*, 6(10):1345–1357, Oct 1997.

Étude des artefacts de flou, ringing et aliasing en imagerie numérique. Application à la restauration.

Résumé : Cette thèse aborde les problèmes liés à la formation des images numériques. L'étape d'échantillonnage nécessaire à la formation d'une image discrète à partir d'une image continue peut introduire différents types d'artefacts qui constituent des dégradations majeures de la qualité de l'image. La motivation principale de cette thèse a été l'étude de ces artefacts que sont le flou, le ringing et l'aliasing. Dans la première partie, nous rappelons tout d'abord le processus de formation des images numériques puis nous proposons des définitions de ces artefacts. Dans la deuxième partie, nous définissons une mesure conjointe du flou et du ringing dans le cadre d'un filtrage passe-bas précédant l'échantillonnage. La troisième partie est dédiée à la détection automatique de ces artefacts dans les images. Enfin, en quatrième partie, la détection automatique est testée dans des applications concrètes de la restauration d'images : la déconvolution aveugle et le débruitage.

Mots-clefs : échantillonnage, artefacts, ringing, aliasing, flou, filtrage linéaire, déconvolution aveugle, Gibbs, détecteur.

Study of the blur, ringing and aliasing artifacts in numerical imaging. Application to restoration.

Abstract : This thesis deals with the problems related to the formation of numerical images. Sampling, which is a necessary stage for the formation of a discrete image from a continuous one, may introduce some artifacts that degrade the image quality. These artifacts are called blur, ringing and aliasing. The main motivation in this thesis was the study of these three artifacts. In the first part, we recall the image formation process and we define these artifacts. In the second part, we propose a new measure of both the ringing and blur artifacts associated to a low-pass filtering prior to sampling. The third part is dedicated to the automatic detection of these artifacts in images. In the fourth part, the automatic detection is tested on two real restoration applications: the blind deconvolution and the denoising.

Keywords : sampling, artifacts, ringing, aliasing, blur, linear filtering, blind deconvolution, Gibbs, detector.